Towards the experimental realization of a strongly interacting 1D Fermi gas

Cédric Enesa

PSL
UNIVERSITÉ PARIS

THÈSE DE DOCTORAT
DE L'UNIVERSITÉ PSL

Préparée à École Normale Supérieure

Towards the experimental realization of a strongly interacting 1D Fermi gas

Soutenue par
Enesa Cedric
Le 13 Décembre 2019

École doctorale n°564
Physique en Ile-de-France

Spécialité
Physique Quantique

Composition du jury :

Roberta Citro University of Salerno	*Rapporteuse*
Giacomo Roati University of Florence	*Rapporteur*
Robin Kaiser CNRS	*Examinateur*
Jook Walraven Universiteit van Amsterdam	*Président du Jury*
Frédéric Chevy École Normale Supérieure	*Directeur de thèse*
Christophe Salomon CNRS	*Membre invité*

1794
ENS | PSL

Abstract

This thesis reports on the recent results of the FerMix experiment, which is dedicated to the study of fermionic quantum many-body systems at ultralow temperatures using ensemble of ^{40}K. The main achievements are twofold.

First, we describe the experimental apparatus and the successive stages leading to the preparation of a deeply degenerate Fermi gas of 1.5×10^4 atoms of ^{40}K at a temperature of $T/T_F = 0.14$, just below the critical temperature of superfluidity. The key steps to achieve this essential milestone, such as the loading of the main optical dipole trap and the ensuing phases of evaporative cooling, are presented. We also report on the main upgrades implemented on the machine over the course of this thesis.

Second, we summarize our progress towards the exploration of the dimensional crossover between the Tomonaga-Luttinger liquid in 1D and the Landau-Fermi liquid in 3D. To that end, we confine our ultracold Fermi gas in a large spacing optical lattice. The experimental considerations regarding the tunability of the dimensionality of our system as well as the apparatus used to generate the 2D lattice are described in detail. Following the characterization of the optical periodic potential, the strategy employed to adiabatically transfer atoms into a single 1D lattice before loading them into the 2D standing wave is discussed. The loading of the 1D lattice represents the final milestone presented in this work: the realization of a degenerate Fermi gas in two dimensions composed of 250 atoms per spin state at a temperature $T/T_F = 0.34$.

Résumé

Cette thèse décrit les récents résultats de l'expérience FerMix, expérience dédiée à l'étude des systèmes fermioniques quantiques à N corps à ultra basse température. Pour cela, des ensembles d'atomes de ^{40}K sont utilisés. Nous présentons ici deux principaux résultats.
En premier lieu, nous décrivons le dispositif expérimental ainsi que les étapes menant à la préparation d'un gaz fermionique fortement dégénéré composé de 1.5×10^4 atomes de ^{40}K à une température de $T/T_F = 0.14$, soit juste en-dessous de la température critique de superfluidité. Les étapes clés permettant la réalisation de ce jalon essentiel, telles le chargement des pièges optiques dipolaires ou encore les différentes phases de refroidissement évaporatif, sont présentées. Les principales améliorations apportées à l'expérience tout au long de cette thèse sont également résumées.
En second lieu, nous rapportons nos progrès pour explorer le croisement dimensonnel entre les liquides de Tomonaga-Luttinger à 1D et ceux de Landau-Fermi à 3D. Pour ce faire, nous confinons notre gaz de Fermi ultrafroid au sein d'un réseau optique à grand pas. Les considérations expérimentales concernant l'ajustabilité de la dimensionalité de notre système de même que le dispositif utilisé pour générer le réseau optique 2D sont décrits en détail. Après la caractérisation du potentiel optique périodique, nous discutons de la stratégie mise en oeuvre pour d'abord transférer adiabatiquement les atomes dans le réseau 1D puis au sein de l'onde stationnaire 2D. Le chargement du réseau 1D représente l'accomplissement final présenté dans ce manuscrit : la réalisation d'un gaz de Fermi dégénéré à deux dimensions, composé de 250 atomes par état de spin et à une témperature de $T/T_F = 0.34$.

Table of contents

Chapter 1

Introduction

Universality is a remarkable concept of physics. It refers to the similar behaviour of vastly different systems and has strong fundamental and technological implications. In 1675, while designing bridges, Robert Hooke faced the complication of calculating the perfect arch, when he realised: "As hangs the flexible line, so but inverted will stand the rigid arch". This constitutes an early example of a *simulation*, where an experiment of a simpler system can provide information about a complex problem that is otherwise inaccessible via analytical or numerical approaches. As pointed out by Yuri Manin in 1980 [1], in many cases of quantum physics, simulators can provide a more accurate representation of the original system than numerical computation [2]. Nowadays, such quantum simulators are realized with systems of neutral atoms [3], ions [4] or even photons [5]. They can be used to investigate phenomena ranging from electronic transport [6] to black-holes [7]. Within this context, ultracold atoms epitomize the concept of quantum simulation envisioned by Richard Feynman in 1982 [8].

The quantum degenerate regime

A non-interacting gas is characterized by its temperature T and density n. Quantum effects become increasingly relevant at lower temperatures and higher densities, when the thermal de-Broglie wavelength $\lambda_{\mathrm{dB}} = \mathrm{h}/\sqrt{2\pi m \mathrm{k_B} T}$ and the inter-particle spacing $n^{-1/3}$ reach the same order of magnitude. Here, m denotes the mass of the atoms, h the Planck constant and $\mathrm{k_B}$ the Boltzmann constant. Formally, this condition can be expressed through the phase space density, which is defined as $PSD = n\lambda_{dB}^3$. For a $PSD \ll 1$, the gas is classical and its statistics are described by the Boltzmann distribution. However, for a $PSD \geq 1$, it is in the degenerate regime and the statistics depend on the spin of its particles [9]. The spin-statistic theorem states that particles in 3D can either have an integer or a half-integer spin. Constituent, such as photons, with an integer spin obey Bose-statistics, while half integer spin particles such as electrons follow Fermi-statistics. In high-energy physics, elementary bosons mediate the interaction[1]

[1] For instance, photons mediates the electromagnetic interaction.

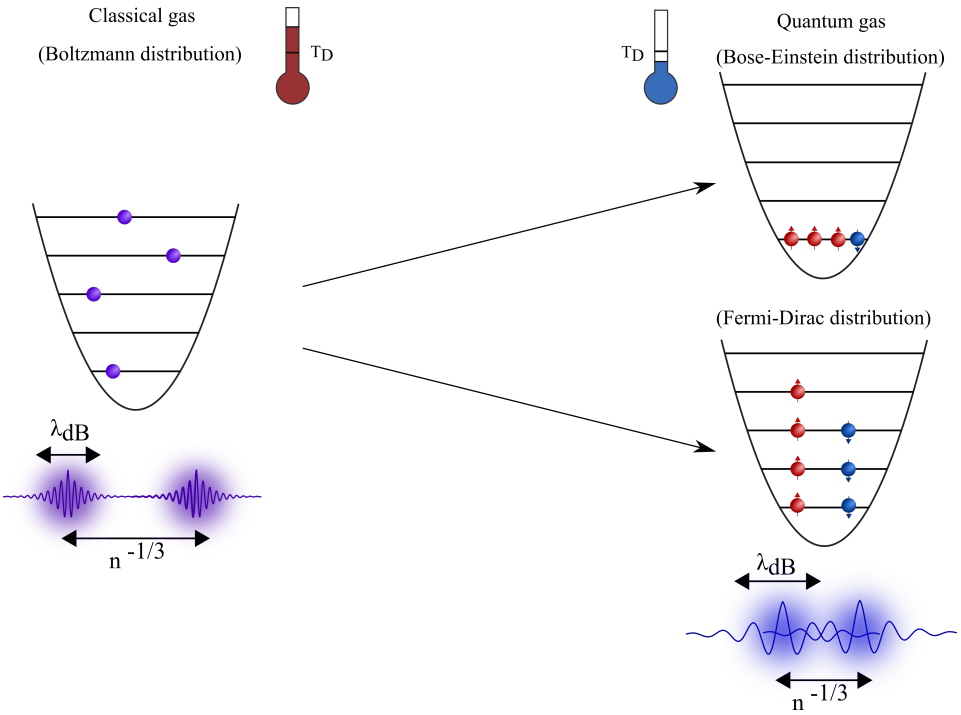

Fig. 1.1 **Statistics of an ideal gas of bosons and fermions in a harmonic trap**. (Left) At high temperatures, the interparticle distance is very large compared to the de Broglie wavelength. The cloud follows a classical Boltzmann distribution, regardless of the statistics of its constituents. (Right) At low temperatures, the particle wavelength becomes comparable to the interparticle distance and the behavior of the ensemble depends on the statistics of the atoms. While bosons will accumulate in the groundstate of the system, identical fermions will form a Fermi sea and populate all the energy levels up to the Fermi energy. T_D denotes the degeneracy temperature.

while matter is exclusively made up of elementary fermions such as electrons and quarks [10]. Composite particles such as atoms, are thus an ensemble of elementary fermions. If the sum of all its elementary constituents is an even or odd number, an atom will, respectively, be a boson or a fermion. For instance, of the three isotopes of Potassium with the highest natural abundance, two are bosonic (^{39}K and ^{41}K) and one is fermionic: the ^{40}K.

A Bose gas undergoes a second order phase transition in the low-temperature limit. The resulting Bose-Einstein condensate features a macroscopic occupation of the single-particle ground state [11, 12]. This transition does not rely on interactions and is purely a statistical effect. A Fermi gas, by contrast, displays no phase transition. At zero temperature, Pauli blocking leads to unity population of all energy levels up to the Fermi energy E_F. Figure 1.1 illustrates the classical and quantum regimes for both bosons and fermions.

The absolute temperature scale at which the quantum regime is reached strongly depends on the respective system. On one hand, for electrons in a typical metal, the characteristic Fermi

temperature $T_F = E_F/k_B$ is around 10^4 K, while for the crust of a neutron star it is on the order of 10^{10} K [13]. On the other hand, for liquid Helium-3 it is on the order of 1 K and for bosonic Helium-4, the critical temperature for condensation in the same temperature range [14].

Strongly correlated quantum systems

In addition to the statistics of the particles, the presence of interactions can strongly alter the properties of a many-body system. In metals, they can lead to superconductivity and pairing between electrons. Pairing in metals is not a two-body effect and arises from the restricted phase-space due to Pauli blocking, as was first discovered by Cooper [15]. The length scale of these Cooper pairs is large compared to the inter-particle spacing, highlighting the many-body character of the pairing. Superconductivity in weakly-interacting fermionic states of matter, for example through phonon-mediated interactions, is well understood in the context of Bardeen-Cooper-Schrieffer (BCS) theory [16].
Despite important theoretical breakthroughs, such as the BCS theory or the Landau-Fermi liquid theory [17–19][2], the understanding of strongly correlated matter remains an open challenge of many-body physics. Due to the large amount of memory required to store the states of the system, numerical simulations using classical computers are very challenging. For a simple gas of N particles with spin-$1/2$, even if the external degrees of freedom were ignored, the exact diagonalization of the system requires a $2^N \times 2^N$ matrix to be solved to calculate its time evolution and 2^N states must be stored in memory. This causes an unavoidable exponential explosion with the size of the system and quickly renders computational capacities insufficient. As a result, approximation methods such as Monte-Carlo, were developed [21]. However, sensible approximations are not always possible and present limitations for the simulation of fermionic systems (the sign problem [22] for instance). These problems, combined with the difficulty to interpret direct observations of many strongly correlated systems due to their inherent complexity, such as high-T superconductors [23], frustrated magnets [24] or quantum chromodynamics [25], motivated analog quantum simulation using ultracold atoms.

Early experiments with ultracold atoms

Atomic gases are dilute, which, in turn, sets an extremely low temperature scale for degeneracy. For typical experimental settings, temperatures on the order of 10^{-7} K or even below need to be reached. Taking advantage of the progress of laser technology, pioneering results regarding cooling [26] and trapping [27–29] of atoms were achieved during the 1980s. In 1995, the first

[2] Landau liquid theory maps strongly interacting many-body systems and their properties onto weakly interacting fermionic quasi-particles. Liquid Helium-3 and most metals in their normal state are two of the most prominent examples where the theory can be applied [20].

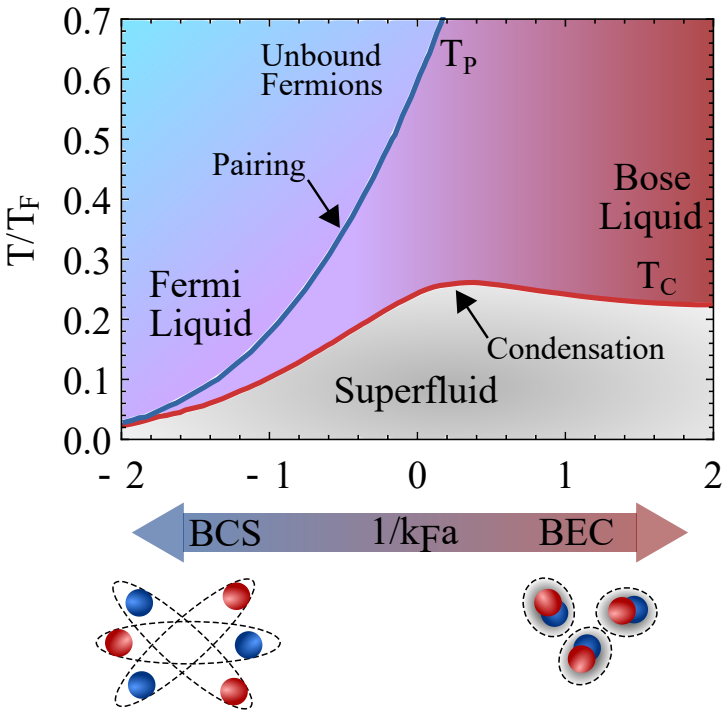

Fig. 1.2 **Mean field diagram of the BEC-BCS crossover in a balanced Fermi mixture in 3D**. Evolution of the ground state from the BCS limit with large overlapping cooper pairs to the BEC limit of tight molecules. At unitarity ($1/k_F a = 0$), the size of the pairs is comparable to $1/k_F$. As the attraction increases, the pair formation crossover scale T_P diverges away from the condensation temperature T_C. Figure adapted from [41, 42].

Bose-Einstein condensates of ^{87}Rb and ^{23}Na were realized, confirming theoretical predictions of Bose [11] and Einstein [12] made 70 years earlier. The confirmation of this quantum phase transition was soon followed by other remarkable results [30], such as matter-wave interference [31], solitons [32, 33] and superfluidity [34, 35]. In 1999, the first degenerate Fermi gas was obtained at Jila using ^{40}K [36], opening the door for the simulation of fermionic quantum many-body systems [37, 38].

A striking feature of ultracold atoms is the ability to freely tune their interactions via scattering resonances to either create a non interacting gas, a strongly interacting one, or anything in between. Owing to the absence of net electric charge and low densities, the many-body interactions are usually short-ranged and typically dominated by few-body collisions. At low energy, two body elastic collisions can be described by a single scalar parameter a, called the scattering length. In absence of additional collision processes, the many-body interacting system can be completely described by this two-body parameter [37]. The strength of the interaction can be changed using the so-called Feshbach resonances, which directly modify the scattering length by coupling to external magnetic fields. [39, 40].

Tuning the scattering strength

This tunability of the scattering length has enabled a hallmark result of Fermi gas experiments: the experimental realization of the BEC-BCS crossover [43], which has been the subject of numerous theoretical and experimental works of research [42, 44–46]. The mean-field diagram

of this smooth crossover is represented in figure 1.2 for a spin-balanced Fermi mixture. For the understanding of the phase diagram it is helpful to recall that the scattering length is an effective parameter and that the Van-der-Waals interaction potential between two atoms is always attractive. The crossover from BCS to BEC can therefore be viewed as an increase in attraction between atoms, which leads to a bound state at unitarity and on the BEC side. On the BCS side, superfluity arises from loosely bound cooper pairs, while on the BEC side, deeply bound two-body bosonic molecules make up the gas. Between those two situations, when $1/k_F|a|< 1$, one enters the strongly interacting regime.

Building on this highly tunable experimental platform, many groundbreaking results were obtained, such as superfluidity of fermions below a critical temperature [47–49], phase separation between paired and unpaired fermions in imbalanced Fermi mixtures [50]. For imbalanced Fermi mixtures, Fermi liquid behavior was also reported above the Chandrasekhar-Clogston limit of polarization [51]. The unitary regime of the phase diagram, where the scattering length diverges, is of particular interest. Here, the scattering cross section becomes independent of the scattering length and the only remaining length scales are identical to those of non-interacting fermi gases: λ_{dB} and the inter-particle spacing $n^{-1/3}$. This leads to scale invariance and universal thermodynamcis [52, 53]. While bosons have a short lifetime in the vicinity of a Feshbach resonance, two-component Fermi gases are protected from three-body recombination losses due to Pauil blocking. In the unitary limit, all thermodynamic quantities solely depend on density and temperature. A set of universal functions of T/E_F is thus sufficient to characterize the unitary Fermi gas. For instance, its pressure P at zero temperature is given by [42]:

$$P = \frac{2\xi}{5} E_F \tag{1.1}$$

with $\xi = E/E_0 = 0.37$ [49]. E_0 denotes the energy of the non-interacting system, E the total energy of the unitary gas and ξ the universal Bertsch parameter [54]. After having been the main subject of numerous theoretical studies [55, 56], it was recently measured using ultracold atom experiments [49]. The unitary regime is also expected to play a role in exotic matter such as the quark-gluon plasma and the crust of neutro stars [55]. Anolog simulators are crucial to mimic the dynamics of strongly interacting systems that are difficult to tackle theoretically due to the absence of small interaction parameters [57] but also difficult to directly observe experimentally. In this spirit, recent studies of non-equilibrium dynamics of unitary Fermi gases have enabled a better understanding of the transport properties of this extreme state of matter [58–61].

Tailoring dimensionality

In contrast to most experimental realisations of many body ensembles, such as condensed matter systems, atom trapping offers a lot of flexibility to design custom external potentials. This can be used to tune the dimensionality of the system at hand. It is well known that reducing the dimensionality of a system can strongly alter its properties and lead to unique behaviors. For instance, true long-range order and spontaneous symmetry breaking cease to exist in reduced dimensions due to the increased impact of thermal fluctuations [62]. This phenomenon, embodied by the Mermin-Wagner theorem [63], notably prevents the formation of a BEC in both one and two dimensions in the thermodynamic limit. Additionally, in one dimension the low energy excitations are collective and as a result, the Landau liquid theory breaks down. As a consequence, analog quantum simulation of strongly correlated systems in low dimensions, such as carbon nanotubes or electrons in semi-conductors in respectively one- and two-dimensions, also requires one to confine ultracold atoms in reduced dimensions [64]. By shining in a strongly anisotropic potential, such as an optical lattice [65], one can freeze out the atomic motion in one or several dimensions, effectively confining the atoms in either $2, 1$ or even 0 dimensions. Numerous breakthroughs followed the first use of an optical lattice, such as the phase transition between the superfluid and the Mott insulator phase [66], the observation of the BKT transition in 2D [67] and the realization of a Tonks-Girardeau gas [68] as well as a Luttinger liquid [69] in 1D.

Outline of this thesis

This manuscript presents the recent progress of the FerMix experiment. The main achievements are twofold: first, we produced a deeply degenerate quantum gas of ^{40}K around $T/T_F \simeq 0.15$. Second, in order to study the dimensional crossover of this Fermi gas in the strongly interacting regime, we implemented a 2D lattice with large spacing to directly control the (effective) dimensionality. The optical lattice spacing and transverse frequencies were measured and a deeply degenerate Fermi gas in two dimensions was produced, which constitutes an important milestone towards reaching the 1D regime. The main text of this work is structured in the following way:

1. The chapters 2 and 3 present the experimental setup and the different steps leading to the realization of a quantum degenerate Fermi gas of ^{40}K.

2. In schapter 4, the theory of degenerate Fermi gases in 3D and 1D in the normal state will be presented. The realization of the dimensional crossover from 3D to 1D will also be discussed as well as a potential characterization of the crossover through the exploration of the system's transport properties.

3. Finally, chapters 5 and 6 summarize the progress towards the realization of the dimensional crossover. The experimental apparatus will be described in detail as well as the calibration of the 2D lattice and the preparation of a degenerate Fermi gas confined in two dimensions.

Chapter 2

Overview of the experimental setup

The FerMix experiment was first started in 2008 under the drive of Frédéric Chevy and Christophe Salomon. Given the fact that earlier stages of the experiment have already been described in great details (see for example [70–73]), this chapter will be mainly focused on the current status of our experimental apparatus and the recent changes implemented during

this thesis and to a large extend also reported in [74]. FerMix initial goal was to explore the properties of the fermionic isotope of the Potassium and Lithium alkali (^{40}K and ^{6}Li) in the quantum degenerate regime. To this end, several milestones were reached, such as the implementation of a gray D1 molasses [75, 76]. Over the course of this thesis, we realized a deeply degenerate gas of ^{40}K as well as implemented a large-spacing two dimensional optical lattices required to study the properties of a strongly correlated Fermi gas confined in one dimension.

2.1 General description of the FerMix experiment

An overview of our experiment is provided in fig. 2.1. A typical sequence takes about 60 s. A magneto optical trap (3D-MOT) is first loaded during 20 s, capturing typically 1.5×10^9 atoms coming from an atomic beam of ^{40}K. This atomic flux is created by a two dimensional magneto optical trap which is combined with a longitudinal molasses and a push beam (2D-MOT). After fully loading the 3D-MOT, the 2D-MOT is switched off, the optical power of the 3D-MOT decreased and the magnetic confinement risen in order to increase the spatial density of the atomic cloud (CMOT phase). The magnetic field is then switched off and a brief phase of 8 ms of gray molasses significantly increases the phase-space density by using the Alkali D1 Lines (D1 molasses). This stage of cooling is crucial to ensure a high efficiency for the magnetic transport of the ^{40}K from the MOT chamber to the science cell (see figure 2.1) and as a result for the rest of the sequence. Prior to the transport, the atoms are optically pumped to low-field seeking states and transferred into a magnetic trap. An ensemble of partially overlapping coils allows the transport of the atoms to the science cell which is located 65 cm away from the MOT chamber. Once in the science cell, a microwave evaporation is performed before loading 1×10^7 atoms in an optical dipole trap. After 800 ms of loading, the trap depth is lowered to force the evaporative cooling of the confined atoms of ^{40}K, which eventually reach quantum degeneracy. During the optical evaporation, the atoms are transferred into the lowest Zeeman states and a second optical dipole trap is added in order to increase the spatial density by forming a crossed dipole trap. Upon reaching the quantum degeneracy, the atoms are either kept into the dipole traps or transferred into a periodic potential created by an optical lattice. Finally, standard absorption imaging is employed to record the integrated profile of the atoms using highly sensitive CCD cameras.

In the following, we will first briefly present our vacuum ensemble before addressing the laser system necessary for trapping, cooling and the imaging of our atomic sample as well as the software used to operate the experiment. After this short introduction, we will describe in more detail the FerMix experiment as well as the key steps of the machine up to the magnetic transport of the ^{40}K into the science cell and the ensued microwave evaporation. Since the

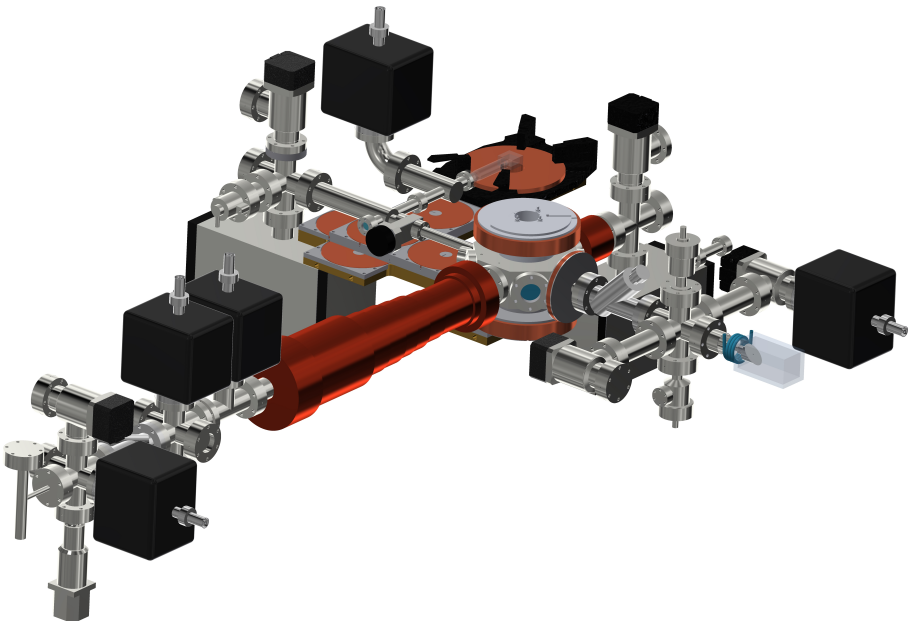

Fig. 2.1 **Overview of the vacuum assembly**.A 2D-MOT and a Zeeman slower are used as sources for a dual spieces MOT. After a transfer into a quadrupole trap, an array of partially overlapping pair of coils are used to route the atoms from the MOT chamber to the science cell, making use of the better optical access. Once in the science cell, multiple stages of evaporation take place to reach quantum degeneracy and then load the optical lattice.

loading of the optical dipole traps as well as the evaporation up to quantum degeneracy required major changes and upgrades of the setup around the science cell, they will be the main topic of the following chapter of this thesis.

2.2 Vacuum chambers

The density window for observing fermions in the deep quantum regime is typically between $10^{11}\,\mathrm{cm}^{-3}$ and $10^{15}\,\mathrm{cm}^{-3}$ to ensure sufficiently high collision rate and thermalization while avoiding three body losses [30, 37]. As a consequence, the corresponding temperature to achieve the quantum degeneracy is comprised between 100 nK and 50 µK [37]. Upon reaching those temperatures, a trap depth of few hundreds of µK is perfectly adequate to efficiently confine the atomic cloud. Therefore, collisions between the atomic cloud and the background gases, in thermal equilibrium with the exterior of the vacuum chamber at room temperature, will lead to heavy losses from the trap, which will reduce the collision rate and ultimately limit

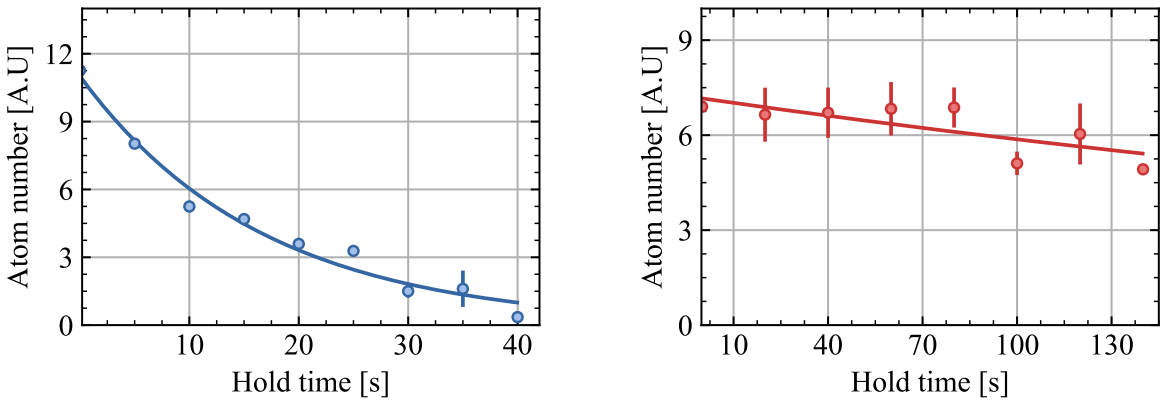

Fig. 2.2 **Lifetime in the two main vacuum regions**. While the lifetime in the MOT chamber is of only 15 s (a), the better vacuum quality of the science cell offers lifetime of more than 180 s (b). Additional details regarding the vacuum quality of the experiment can also be found in [70, 77].

our ability to reach low temperatures. Pressures below 10^{-11} mbar are thus required to obtain lifetimes of up to several minutes [1]. Even though such lifetimes seem rather long, one has to remember that an experimental sequence such as described in section 2.1 takes around 60 s with more than 10 s of optical evaporation in the science cell taking place in a dipole trap with a trap depth below 100 µK.

However, one problem arises when trying to maintain such pressures inside the vacuum enclosure. In order to obtain a reasonably high atomic flux around 2×10^8 atoms.s^{-1} that will then be captured by the 3D-MOT, the potassium's vapor pressure needs to be much higher than 10^{-11} mbar (between 10^{-8} mbar and few 10^{-7} mbar). As a result, differential pumping is necessary to keep large pressure differences between the different regions of the experiment. In FerMix, the differential pumping stages are tubes of reduced apertures that connect adjacent vacuum regions. Their small diameter limits the communication between regions with different pressures. Unequal pressure levels are maintained thanks to medium ion pumps from Varian (with pumping capacities between 20 L.s^{-1} and 40 L.s^{-1}) [78, 70].

A CAD drawing depicting the vacuum assembly of FerMix is given in figure 2.1. The first region consists of the two zones of elevated vapor pressure used to generate the atomic jets of ^{6}Li and ^{40}K by means of a Zeeman slower and a 2D-MOT respectively. In the central octagon, located at the intersection of the two atomic beams, the potassium MOT is loaded. The vacuum quality in those regions is ensured thanks to several ion pumps as well as non-evaporable getter material (St707). In the MOT chamber, the lifetime of the ^{40}K is around 15 s in the

[1] for a non-interacting gas optically trapped

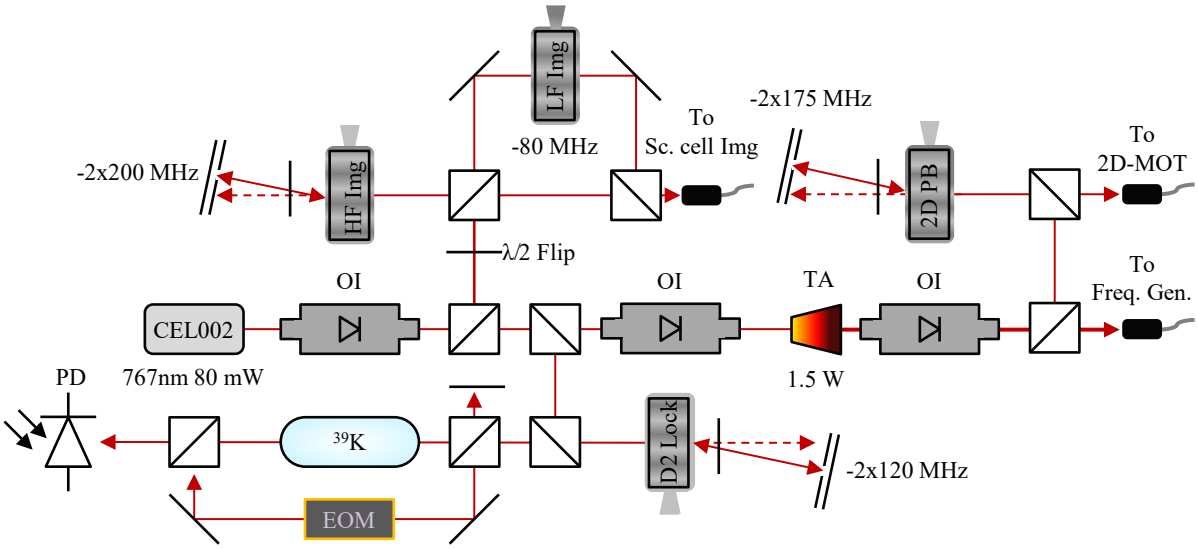

Fig. 2.3 **Master laser setup for ^{40}K.** After a first optical isolator, a small portion of the main laser light is used as a reference to lock our main laser on the ^{39}K D2 crossover while another small fraction of the optical power serves for the imaging in the science cell at both high and low magnetic field. Finally, most of the power is used as an input source for a tapered amplifier. The output of the amplifier is then additionally split. The first part, after a double pass AOM and a single-mode polarization maintaining fiber, is used as a push beam for our 2D-MOT while the other part is directly injected into a single mode fiber, which will eventually be further split to generate all necessary frequencies for our D2 laser system (see fig. 2.4). Figure style adapted from [74].

magnetic-optical trap as presented in figure 2.2a. After being confined in a magnetic trap, the atoms are magnetically transported inside a 65cm L-shape tube, with a turning point at 30 cm from the MOT chamber, to the rectangular science cell, that offers a much better optical access [71, 72]. The glass cell is made of uncoated Vycor, a fused silica dioxide. Manufactured by Hellma GmbH, it has internal dimensions of 23 mm × 23 mm × 10 mm with a wall thickness of 4 mm. The L-shape of the transport reduces parasitic effect from the atoms remaining inside the MOT chamber and from the optical beams used for the earlier stage of the experiment (such as the push beam and the D1 molasses for example). It also provides a better optical access along the transport direction. In contrast to the relatively low lifetime in the MOT chamber, the lifetime of the ^{40}K in the science cell while captured by an ODT exceeds 180 s (figure 2.2b).

2.3 Master laser system

Coherent laser light can be an extremely versatile tool to drive electric dipole transitions and thus can be used to perform laser cooling, imaging and modifying the internal degree of

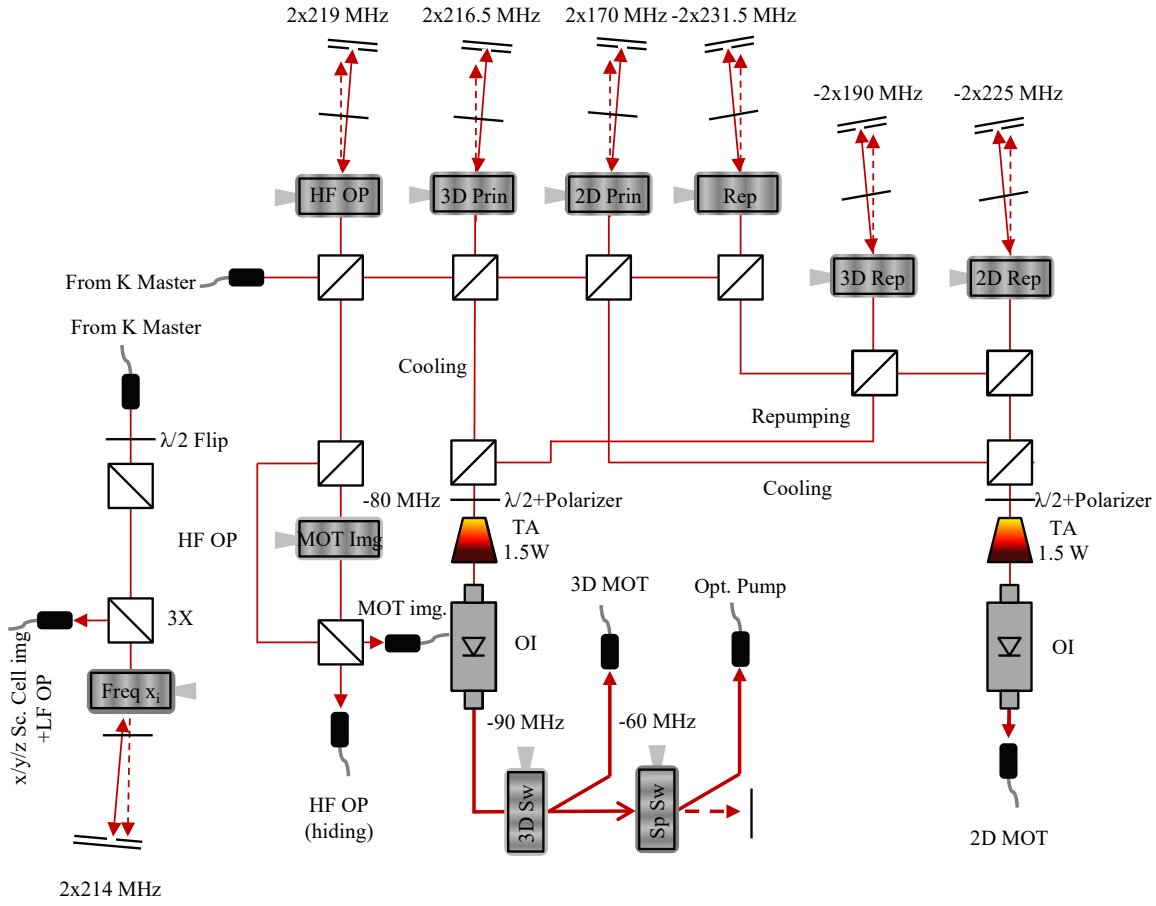

Fig. 2.4 ^{40}K **optical table.** Light from the master laser (see fig. 2.3) is split and rerouted towards several double pass AOMs. Light from the principal and the repumper AOMs of the 2D MOT and 3D MOT are overlapped and directed towards the 2D and 3D MOT tapered amplifier respectively. After the amplifiers, the MOTs lights are send to the main table through single mode optical fibers where they will be used for the 2D-MOT, the 3D-MOT and the optical pumping in the MOT chamber. Optical isolators are placed to avoid damaging the TA chips due to back reflections. After the high field optical pumping AOM, the light is directed towards two fibers: one for the optical pumping at high field in the science cell and one for the MOT imaging. Finally, light from the main D2 laser is also used for the imaging in the science cell. Figure style adapted from [74].

freedom of an atomic cloud. In order to do so, the intensity, the frequency and the polarization of the light must be generated in a tunable and controlled way. The figures 2.3 and 2.4, as well as [70, 78], depict our D2 laser system for the manipulation of ^{40}K. For the optical pumping and the three stages of cooling (2D-MOT, the 3D-MOT and the D1 molasses), this table is used to produce the appropriate powers and frequencies of the repumping and cooling beams. Moreover, for greater efficiency and easier alignment, before being sent to the main table, the repumper and the cooling beams of each steps are overlapped. This optical table is also used to

produce the fitting intensity and the frequency of the imaging beams, the push beam and the optical pumping at high field to transfer the atoms into a dark state with respect to the resonant imaging light (see sec. 3.6).
Following a MOPA-principle (for Master Oscillator Power Amplifier), a diode laser is frequency stabilized via modulation transfer spectroscopy on a Doppler-free absorption signal of the D2 or D1 groundstate crossover line and is used to inject a homebuilt tapered amplifier [79]. The light is then being mode cleaned owing to a polarization maintaining single mode optical fiber from Thorlabs. The use of optical fibers to propagate light coming from the tapered amplifier also facilitate the realignment of the optical table after the exchange of a TA chip. Due to the extremely low natural abundance of ^{40}K (around 0.01%), the detection of the absorption signal is technically very challenging. Consequently, the absorption lines of the ^{39}K are used as references for the two diode lasers. A fixed offset, created by an AOM (Acousto-Optic Modulator), is added to address the ^{40}K D2 and D1 transitions. Before going through several additional tapered amplifiers (see fig. 2.4), light from the main laser is split into several beams. Each of those beams are then directed towards separate AOMs from Gooch&Housego in double pass with cat's eye configuration [80] to be frequency shifted towards their respective transitions (see table. 2.1). Finally, each of those beams are sent into their dedicated tapered amplifiers.
At that stage, the required optical powers for the MOT, the 2D-MOT and the optical pumping in the MOT chamber are available. The three bichromatic [2] laser beams corresponding to the MOT, the 2D-MOT and the optical pumping are therefore finally being sent to the main table via single mode optical fiber from Oz Optics. In order to prevent unwanted light from being transmitted to the main table, several commercial (from Uniblitz) and homemade shutters are installed in front of each fibers. While those shutters are relatively slow, the Uniblitz shutters can be closed in 0.6 ms [3] and the closing time of our homebuilt shutters can reach 100.0 ms [4], they can completely block any parasitic light. When faster speed is required, additional single pass AOMs serve as fast switches with a fall time of typically 30 ns. For the D1 path, light from the tapered amplifier is directed into a single pass AOM and a single mode fiber that transmits the D1 light to the main table. The "repumping" frequency of D1 is generated by an Electro-Optic Modulator (EOM) located between the diode laser and the tapered amplifier [71, 77].
Over the course of this thesis, several modifications of the laser table were carried out in order to improve the overall performance of the machine as well as its stability. The first major change was the replacement of the D2 main diode laser. Originally a homemade diode laser, technical specification can be found in [70], it was replaced by a commercial one (MogLabs CEL002) to increase its output power and its stability. Thanks to the increase in power, a

[2] For the cooling and the repumping frequencies.
[3] But they have a delay of roughly 5.0 ms.
[4] This long closing time is caused by the vibrations generated by the shutters when they are switched off.

portion of the outgoing light is used to generate the imaging light at low and high magnetic bias field in the science cell (see fig. 2.3). A new stage of double pass AOMs was also added in order to facilitate the imaging of multiple spin state at high field. This new setup, after the cleaning fiber, also provides an independent push beam for the 2D-MOT (see sec. 2.6 and [74]). Cleaning cubes were also added in front of each fibers as the last optical element in order to prevent any potential polarization drift as well as shutters, thus allowing us to maintain the different TAs seeded during the entire sequence instead of unseeding them to prevent parasitic light from being sent to the main table. This increased the TAs lifetime and the experiment overall stability.
Furthermore, the RF sources of the AOMs were vastly exchanged. Primarily made up of an ensemble of VCO (Voltage Control Oscillator) and VVA (Variable Voltage Attenuator) (specific details can be found in [73]), they were exchanged for DDS (Direct Digital Synthesizer) modules (MixNV and SynthNV from WindFreak as well as SG4400L from DS Instruments) which reduced the fluctuation of frequency due to the lab's air conditioning unit as well as the cross talk between two RF sources close to one another.
Finally, to stabilize the temperature of the potassium table and the lab as much as possible, all RF amplifiers' power supplies, used to amplify the intensity of the RF signal for the AOMs, were kept on at all time. The heat generated by the amplifiers is dissipated by a cooling plate that is water cooled by a chiller (Termotek P1020). A mechanical relay, connected to the interlock pin of the chiller, was also installed in order to switch off the amplifiers in case of a chiller breakdown, thus preventing them from overheating.

2.4 Computer control of the experiment

Our entire experimental apparatus is controlled and operated thanks to Cicero Word Generator, an open source software developed by Aviv Keshet at MIT specifically designed for cold atoms experiments. It is composed of two applications with a server-client architecture. The client Cicero is used to design the experimental sequences owing to its intuitive graphic interface. The sequences are a succession of steps of variable duration. In each of those steps, one can set the value of all the digital and analog channels. Being compatible with GPIB and RS232 communication, one can also separately assign the control parameters of the different frequency generator signals and DDS thanks to the dedicated panel and simply trigger them when necessary with a TTL signal. We replaced all LAN based communication between frequency generator and Cicero with GPIB connection which allowed us more programming flexibility. Additionally, all DDS were incorporated into Atticus and communication via RS232 implemented. The value of the different parameters used can be stored into dedicated variables and can be then retrieved and stored in a text file via a snippet server. Once the sequence

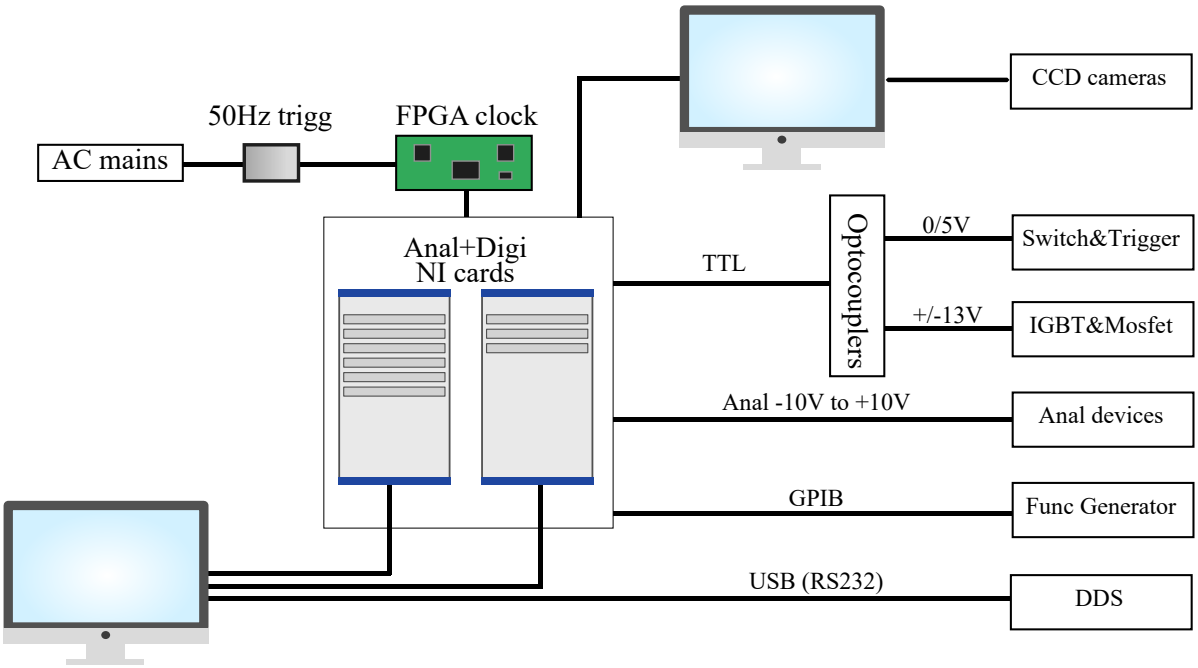

Fig. 2.5 **Schematics of the experiment control hardware**.

designed, the Atticus server translates it into output buffers and send them to a PXI system made by Nationals Instruments.

This system is composed of several digital (model NI PXI-6533 and NI PXI-6536) and analog (model NI PXI-6713) cards which provide all the digital (0 V or +5/+3.3 V), analog (from −10 V to +10 V with a 12−bit resolution) and GPIB signals necessary to operate all the devices of the experiment (such as shutter, drivers for AOMs, power supplies or signal generator for example). The current drained by each of those cards independently shouldn't exceed 10 mA. To protect the system from current drops, voltage spikes or even ground loops, several analog and digital optocoupling devices were installed between the NI cards and the controlled devices [73]. They allow fast switching of up to 0.5 µs and 20.0 µs in the case of the digital and analog optocouplers respectively and should consequently be used every time faster switching is not necessary.

The duration of a sequence is fixed by the maximum number of buffers than can be generated. To optimize this number, one can adapt the resolution of the different steps. To this end, an external FPGA with a variable clock speed (model XEM 3001 from OpalKelly) is used as a reference clock, which allows us to set each step of a sequence with a specific resolution. Thanks to an arduino-based program, the sequence is also synchronized with the mains, such that each sequence starts at a fixed point of the oscillation waveform of the mains-supply [73].

A second computer is used to control the various camera of the experiment. A new Python

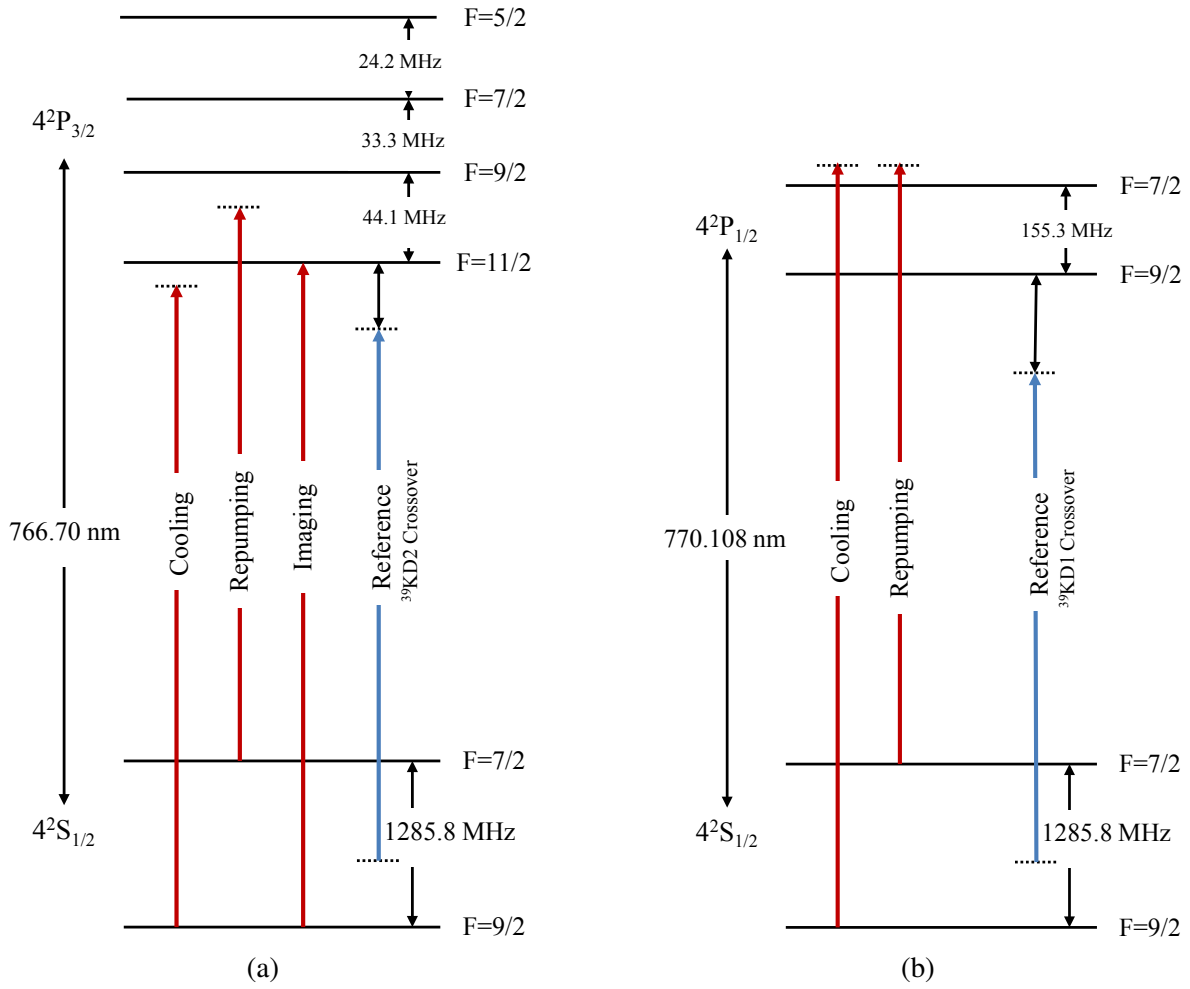

Fig. 2.6 **Optical transitions and hyperfine structure for the D2 (a) and D1 (b)-lines of ^{40}K at zero magnetic field**. The detuning of the various cooling and repumping transitions with respect to their respective main transition is available in table 2.1.

based graphic interface as well as a new imaging program were developed by Clément De Daniloff to communicate with the different cameras, visualize the picture taken and perform quick analysis (such as the estimation of the atom number or the ratio T/T_F for example). A schematic description of the control system of the experiment is presented in figure 2.5

2.5 Atomic properties of ^{40}K

An overview of the optical transitions of ^{40}K used in the experiment is presented in figure 2.6 and in table 2.1. The main and strongest transitions from the ground state are the D2: $4^2S_{1/2} \rightarrow 4^2P_{3/2}$ and D1 :$4^2S_{1/2} \rightarrow 4^2P_{1/2}$ lines, which are separated by 3 nm. The D2 and D1 spectral line have a respective wavelength of 767 nm and 770 nm. The associated linewidth of the two

Transition	Reference Transition	detuning ($\Gamma/2\pi$)
2D MOT cooling	$\|9/2\rangle \rightarrow \|11/2\rangle$	-2.5
2D MOT repumping	$\|7/2\rangle \rightarrow \|9/2\rangle$	-5.1
3D MOT cooling	$\|9/2\rangle \rightarrow \|11/2\rangle$	-2.0
3D MOT repumping	$\|7/2\rangle \rightarrow \|9/2\rangle$	-8.4
D1 "cooling"	$\|9/2\rangle \rightarrow \|7/2\rangle$	4.0
D1 "repumper"	$\|7/2\rangle \rightarrow \|7/2\rangle$	4.0
Imaging	$\|9/2\rangle \rightarrow \|11/2\rangle$	0.0

Table 2.1 **Optical transition for our ^{40}K experiment**. The linewitdh of the D2 (resp. D1)-line is $2\pi \times 6.03$MHz (resp. $2\pi \times 5.96$MHz)

transitions is $\Gamma = 2\pi \times 6.03\,\text{MHz}$ for the D2 transtion and $\Gamma = 2\pi \times 5.96\,\text{MHz}$ for D1 [81]. Moreover, as all alkali metal, ^{40}K has a single valence electron with an electronic spin $S = 1/2$. Since the ground state value of the electron orbital angular momentum $L = 0$, the total electronic angular momentum J=1/2, where J is the quantum number associated with the total electronic spin $\mathbf{J} = \mathbf{L} + \mathbf{S}$. Due to the hyperfine interaction between the electron's magnetic field and the nuclear spin I= 4, the total electron angular momentum $\mathbf{J}$ and the nuclear spin $\mathbf{I}$ are coupled and form the total atomic angular momentum $\mathbf{F} = \mathbf{J} + \mathbf{I}$. As a result, the ground state splits into the two hyperfine manifolds with total atomic angular momenta $F = 9/2$ and $F = 7/2$, separated by an energy splitting of $h \times 1285.80\,\text{MHz}$ (h being Planck's constant). Contrary to most metal alkali, due to the negative value of the magnetic dipole constant $a_{hf} = -h \times 285.7\,\text{MHz}$ [82, 83], the hyperfine structure of the potassium 40 groundstate is inverted with the hyperfine level $F = 9/2$ being energetically lower than the level $F = 7/2$. For the first excited state, the total electronic (resp.atomic) angular momentum can take all the half integer values that fulfill the relation $|\,L - S\,| \leq J \leq |\,L + S\,|$ (resp. $|\,J - I\,| \leq F \leq |\,J + I\,|$). Since $L = 1$ for the excited state, the 4^2P level gives rise to the two excited levels $4^2P_{3/2}$ and $4^2P_{1/2}$. Thus, for the $4^2P_{3/2}$ level, the total atomic angular momentum can take the values $F = 5/2, 7/2, 9/2$ and $11/2$. Due to the absolute value of the magnetic dipole constant being much smaller for the two excited states ($a_{hf} = -h \times 34.5\,\text{MHz}$ and $-h \times 7.6\,\text{MHz}$ for the level $4^2P_{1/2}$ and $4^2P_{3/2}$ respectively) than the groundstate's one [81], the energy splitting between the lowest and highest hyperfine level is only $h \times 101.6\,\text{MHz}$. For the $4^2P_{1/2}$ level, the total atomic angular momentum can take the values $F = 7/2$ and $9/2$ and the energy splitting between the two levels is $h \times 155.3\,\text{MHz}$. Laser cooling and imaging are performed on the $F = 9/2 \rightarrow F' = 11/2$ transitions while the transition $F = 7/2 \rightarrow F' = 9/2$ is used for the repumpers.

Thanks to its large total angular momentum, the two hyperfine groundstates split into numerous (respectively 10 and 8 for the $F = 9/2$ and the $F = 7/2$ levels) Zeeman sublevels in the presence

of an external magnetic field (see figure 2.11). In particular, atoms in a sublevel with a positive slope, called low-field seeker, will preferably explore region with a minimum of magnetic field and can be magnetically trapped. Due to Pauli's principle, two fermions in the same state cannot collide at low temperature (for ^{40}K, p-wave collisions start to be heavily suppressed around 20 µK [84, 85]). As a consequence, fermions in at least two spin states must be trapped for an efficient evaporation and thermalization. Moreover, in order to avoid producing untrappable high-field seeking atoms after a collision between two atoms, atoms must be prepared in a stable mixture of magnetically trappable states. While most metal alkali do not possess such combination of state,^{40}K can be trapped in a mixture of maximum internal momentum $|F = 9/2, m_F = 9/2\rangle$ and $|F = 9/2, m_F = 7/2\rangle$, which is stable against spin relaxation.

2.6 A 2D-magneto-optical trap for ^{40}K

Contrary to the ^{6}Li for example, ^{40}K has a very low natural abundance (0.01%) [86] and obtaining a strong enrichment is necessary to efficiently load a 3D-MOT. In 1999, B. DeMarco, H. Rohner and D.S Jin developed a novel strategy to produce a highly enriched source of ^{40}K [87]. Using an slightly ^{40}K enriched 5:1 molar mixture of calcium and potassium chloride, they were able to produce a 9% enriched source of ^{40}K and load a ^{40}K MOT of 2×10^8 atoms. Another solution, used in FerMix, is to buy directly an ampule of enriched ^{40}K. We bought from Technical Glass Inc, Aurora, USA a 100 mg sample of potassium containing 4 mg of ^{40}K [5]. The low abundance of ^{40}K with respect to its bosonic counterparts renders the use of a potassium oven combined to a Zeeman slower challenging. By raising the oven's temperature to load a sufficiently large 3D-MOT, one would increase the vapor pressure of the two unwanted bosonic isotopes of potassium on top of the fermionic one's. This would lead to an increase of unwanted particles in the MOT chamber, which would greatly degrade the quality of the vacuum in the MOT chamber. Furthermore, since loading a 3D-MOT from a Zeeman slower only works on atoms within a certain velocity class, one would have to frequently replenish the pricey atomic source. As a consequence, a 2D-MOT was implemented to serve as an atomic source for our 3D-MOT of ^{40}K.

2.6.1 Generation of a vaporous phase of ^{40}K

Our potassium sample is stored in two reservoirs. The main reservoir, which contains in a solid state most of the potassium sample. The second one consists in a cold point and is located next to the 2D-MOT glass cell [77]. The cold point acts as an intermediate source that gets heated

[5] The precise composition was 4 mg of ^{40}K, 89.5 mg of ^{39}K and 6.5 mg of ^{41}K, for 4000 $. Unfortunately, the price for enriched potassium increased and can reach up to 10000 $. Moreover, nowadays very few companies sell enriched potassium ampule.

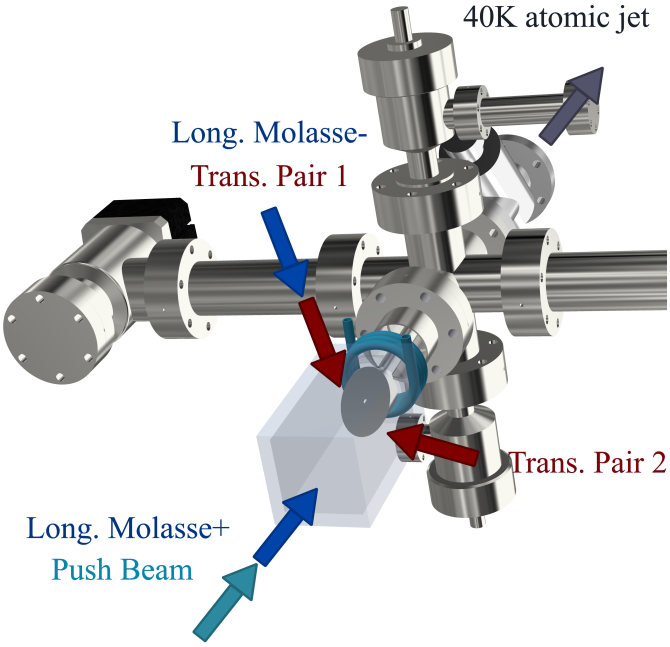

Fig. 2.7 **CAD drawing of the 2D-MOT region of the FerMix apparatus**

during the day to create the vaporous phase of ^{40}K used to load the 3D-MOT from the 2D-MOT and cooled down during the night to store the atoms in a solid phase. This auxiliary source, once depleted, can be easily replenished by heating the main reservoir to migrate atoms from the main source to the cold point (more details about the procedure can be found in [74]). It is made up of three windings of a small PVC hose encircling the 2D-MOT's "throat" in which circulate a temperature regulated anti-freeze coolant (see fig. 2.7). The coolant temperature is controlled by the Coherent ThermoTek T257P-30 210W chiller whose regulation range extends from 0 °C to 45 °C. Since the 2D-MOT glass cell as well as the surrounding vacuum assembly are kept at more than 60 °C, the cold point, once the chiller is set to low temperatures, acts as an efficient pump that can collect all the potassium vapor residing in the 2D-MOT enclosure. Moreover, by increasing this additional reservoir temperature, one can evaporate the solid sample stored on the cold point, creating a vaporous phase of potassium that will fill the 2D-MOT chamber. The ^{40}K vapor pressure can then be easily changed by tuning the chiller's setpoint. A set of three UV-LEDs (LED395-66-60-110 of Roithner LaserTechnik), shining up to 1.4 W of incoherent light at 395 nm can increase further the vapor pressure. Located around the 2D-MOT glass cell, they can be used to induce atomic desorption from the inside walls of the 2D-MOT vacuum chamber [88, 89], increasing the atomic flux by up to 50 %. Since

the UV-LEDs can disturb the MOT loading if permanently switch on, we only activate them during the first two seconds of the MOT loading. Additional characterization of the UV-LEDs performance can be found in [73]. In case of a chiller's failure (due to an electrical shutdown for example), due to the elevated temperature of the vacuum chamber, the cold point might heat up, vaporizing the accumulated potassium and destroying this intermediate source. As a consequence, in order to preserve it, the chiller is hooked up to an UPS (**U**ninterruptible Power Supply) from Riello Ups (model Sentinel Dual 10000VA) which can supply the chiller for more than 10 hours which is much longer than the necessary time for the entire vacuum system to cool down to room temperature [74].

2.6.2 Performance and characterization of the ^{40}K 2D-MOT

As mentioned ealier (see sec. 2.6.1), we load a ^{40}K 2D-MOT from the ambient potassium vapor. Unfortunately, due to collisions with the two much more abundant isotopes of potassium, the 2D-MOT atomic flux decreases when the vapor pressure becomes too high. While this phenomenon would still occure with a pure sample of ^{40}K, the maximum attainable flux would be much higher. Our optimal conditions are reached for a total potassium vapor pressure of 2.3×10^{-7} mbar [70], which corresponds to a temperature of roughly 50 °C [90]. The 2D-MOT is composed of two pairs of retro-reflecting beams (called "Trans. Pair 1" and "Trans. Pair 2"), propagating in the two transverse directions (with respect to the direction of propagation of the atoms) and cooling the ^{40}K in those directions. In the longitudinal one, a pair of beams increases the effect of the molasses. One of those beams ("longitudinal molasses -") hit a one inch 45 ° elliptical mirror with a hole in the center. As a consequence, the central part of this beam is not reflected and atoms in the shadow region will only be addressed by the other longitudinal beam ("longitudinal molasses +"), experiencing a resulting force pushing them towards the central hole and inside the MOT chamber, located 55 cm away from the 2D-MOT (see fig. 2.1). The frequency of both the cooling and repumping components of the longitudinal molasses as well as the transverse cooling beams are red-detuned (by 2.5Γ and 5.0Γ respectively) with respect to their respective transition ($|\,F = 9/2\rangle \rightarrow |\,F' = 11/2\rangle$ for the cooling component and $|\,F = 7/2\rangle \rightarrow |\,F' = 9/2\rangle$ for the repumping one). The typical total power required for all three pairs of beams is 350 mW and the optimal power ratio cooling/rempumping 3.3. The magnetic field necessary for the gradient of the 2D-MOT is created by a set of four coils, whose arrangement generates a gradient of 11 G.cm^{-1} in the transverse direction [78].

In addition to the longitudinal molasses, a small push beam is used to accelerate the atoms from the 2D-MOT towards the 3D-MOT chamber and further increase the atomic flux [72]. Depending on the condition of the cold point the push beam can increase the atomic flux by up

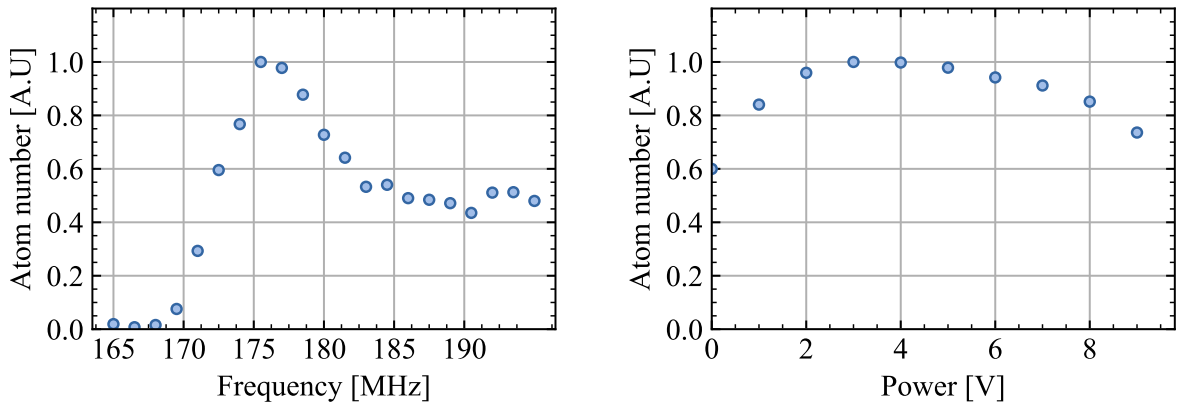

Fig. 2.8 **Optimization of the push beam parameters**. Both frequency (a) and amplitude (b) of the push beam can be optimized offering a better tunability and control of the 2D-MOT performance.

to an order of magnitude. Originally, a small amount of light from the 2D-MOT was deviated far from the vacuum chamber to generate the push beam. The first drawback arising from this design is the lack of tunability of the push beam: since both its intensity and its frequency were set by the 2D-MOT optimal parameters, it couldn't be tuned with our computer control system. Furthermore, due to the small beam size of the push beam (in combination with the long path that it traveled), we observed large fluctuations of the atomic flux (due to the fluctuations of the beam pointing) which leads to large fluctuations of the number of atoms loaded into the 3D-MOT. As a consequence, a new setup was built to replace the push beam [74]. Part of the light generated by the main TA is deviated towards a double-pass AOM and sent to the 2D-MOT thanks to a single mode fiber, offering both frequency and power tunability (see fig. 2.3). Optimization of both parameters (see fig. 2.8) leads to an atomic flux of typically 2.0×10^8 atoms.s^{-1} and a loading of 1.5×10^9 atoms in the 3D-MOT.

2.7 3D-magneto-optical trap and compressed MOT

Once pushed by the push beam and the longitudinal molasses, the atoms are transferred from the 2D-MOT to the MOT chamber where they are captured by a MOT (Magneto-Optical Trap), standard trapping and cooling technique implemented in most cold atoms experiment [91, 27]. At sufficiently low laser intensity (compared to the saturation intensity of the cooling transition), the temperature of the atoms trapped in MOT is ultimately limited by the linewidth of the addressed optical transition[6] [92]. For ^{40}K, this Doppler temperature corresponds to $k_B T_D =$

[6] A simple model consist in considering the atoms' behaviour as a random walk as they absorb and re-emit photons. The cooling limit is then related and set by the spontaneous emission rate Γ

$\hbar\Gamma/2 = k_B \times 145\,\mu K$. This limit, despite ignoring sub Doppler cooling mechanism such as Sisyphus cooling, gives us an initial estimation of the reachable temperature at the end of the MOT loading. Built in a similar fashion as the 2D-MOT, our MOT is composed of three pairs of counter-propagating bichromic beams and a magnetic quadrupole field. The frequency of the cooling (resp. repumping) part of the MOT beams is red-detuned by 2Γ (resp. 8.4Γ) with respect to the transition $|\,F = 9/2\rangle \rightarrow |\,F' = 11/2\rangle$ (resp. $|\,F = 7/2\rangle \rightarrow |\,F' = 9/2\rangle$). The decoupled control of the RF source of their respective AOMs (see fig. 2.4) allows one to tune their power and intensity independently. In the optimal configuration, the power ratio cooling/repumping is equal to 33.8. The typical total power at the output of the MOT fiber (before being equally split between all three bicromatic beams) is 200 mW, which, given the beam size of 22 mm for our MOT beams, gives us an intensity $I = 2.50 \times I_{sat}$ per pair of beam (where $I_{sat} = 1.75\,mW.cm^{-1}$ represents the saturation intensity of the D2 transition). The magnetic confinement is created by a pair of coils separated by 13.0 cm in anti-Helmholtz configuration [72]. During the loading of the 3D-MOT, they create a gradient of $8.0\,G.cm^{-1}$ along their axis of symmetry (and $4.0\,G.cm^{-1}$ in the transverse direction), trapping up to 2.0×10^9 atoms in 18 s at a temperature of 140 µK. At that stage of the sequence both the temperature and the density of the cloud do not allow for an efficient magnetic transport from the MOT chamber to the science cell. To this end, a D1 molasses was implemented (see sec. 2.8). In order to increase the transfer efficiency to the D1 molasses, prior to the molasse stage and after the loading of the 3D-MOT, the magnetic gradient is rapidly increased from $8.0\,G.cm^{-1}$ to $45.0\,G.cm^{-1}$ in 8.0 ms [7] and the optical power decreased and tuned closer to resonance, increasing the spatial density by a factor 5 [79, 73].

2.8 Enhanced gray molasses on the D1 transition

As mentioned earlier, after the 3D-MOT, the temperature and density of the atomic cloud do not allow efficient transport to the science cell. While one could directly load the magnetic trap and perform evaporative cooling, our experiments proved that the initial elastic collision rate was too small for the evaporation to be efficient in the MOT chamber [77]. Another solution to reach reach sub-doppler cooling is to use Sisyphus cooling. In this section we will first introduce the principle of sub-Doppler cooling before discussing of the implementation of the D1 gray molasses, its performance and the transfer of the cloud from the D1 gray molasses to the magnetic trap.

[7] The recompression of the 3D-MOT is kept as short as possible in order to limit the losses due to the increased density.

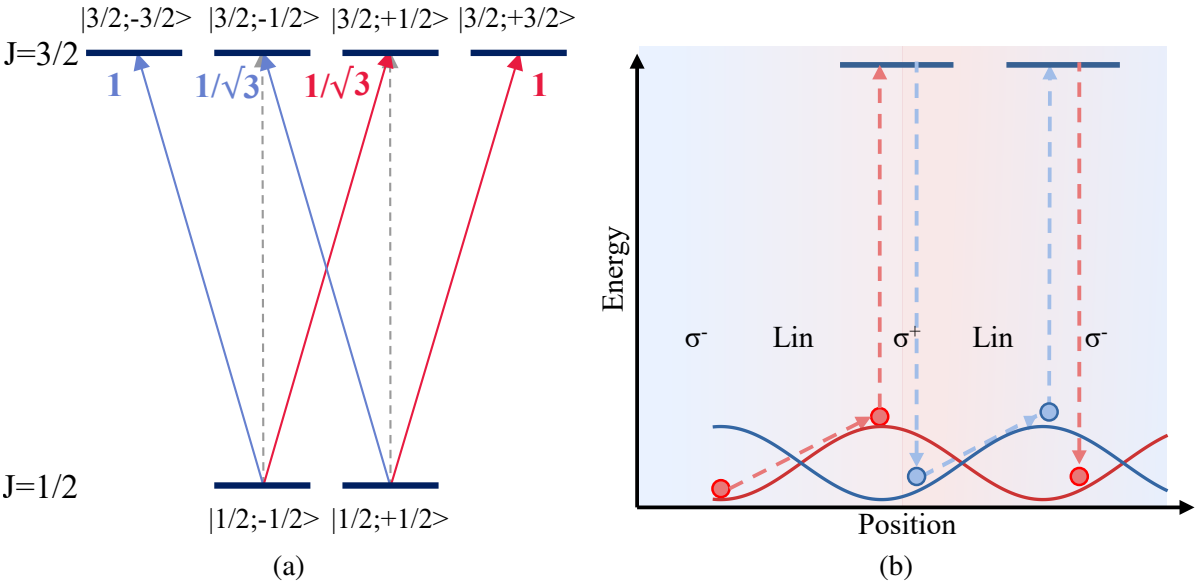

Fig. 2.9 **Principle of Sisyphus effect**. (a) Atomic level for a transition between the $|J = 1/2\rangle$ and $|J = 3/2\rangle$ levels. The Clebsh-Gordon coefficients for the $\sigma^{\pm}$ transition, which are different, are indicated. (b) Principle of Sisyphus cooling for a simple J=1/2 ground state. Due to the position dependency of the light polarization, the light shift intensity also varies with the position (because of the difference of the Clebsh-Gordon coefficients). Consequently, the energy of the two sublevels of the groundstate will have a modulation period of $\lambda_L/2$. Atoms with a velocity such that $v \cdot \gamma_p^{-1} \sim \lambda_L/4$ originally in the valley will climb the hill, reach the top, absorb and re-emit a photon, before being transferred to the valley of the other sublevel to climb another hill. Thus on average, atoms travel more uphill than downhill, which lead to the Sisyphus cooling.

2.8.1 Principle of sub-Doppler cooling

Sisyphus cooling relies on the fact that a pair of counter propagating waves, with a wavelength λ_L can give rise to a spatial modulation of the polarization, with a period of modulation $\lambda_L/2$ [8] [95]. For a multilevel atom, this polarization modulation can lead to a spatial modulation of the light shift of the groundstate (only for a Lin⊥Lin configuration : configuration in which the originally propagating beam and the retro-reflected one have orthogonal linear polarization), thanks to the different values of the Clebsch-Gordon coefficients for the various transitions between the ground- and the excited state (see fig. 2.9a). For a bright molasses, the pair of counter-propagated laser beams is red-detuned with respect to the addressed transition. In particular, if the optical pumping rate γ_p between the sublevels of the groundstate and the atoms' velocity v is close to the condition $v \cdot \gamma_p^{-1} \sim \lambda_L/4$, atoms reaching a loacal maximum

[8] Therefore, the two counter-propagating beams must initially have orthogonal linear polarization (Lin⊥Lin configuration) or opposite circular polarization (σ^--σ^+ configuration) [93, 94]

energy shift are most likely to be transfered to the other Zeeman sublevel, which present a local minimum of energy (see fig. 2.9b). Thus, on average, atoms will climb hills, created by the standing wave and once on top will be optically pumped to the potential's valley after absorbing and spontaneously re-emitting a photon, thus reducing their speed and their temperature until their kinetic energy cannot overcome the potential [95]. The figure 2.9b illustrates the principle of Sisyphus cooling for a 2 level groundstate and for $v \cdot \gamma_p^{-1} = \lambda_L/4$.

For the σ^--σ^+ laser configuration, the polarization remains always linear and rotates around the propagation axis of the counter-propagating beam. As a consequence, the light shift of each of the groundstate sublevels is translational invariant along the propagation axis and no Sisyphus cooling can occur [95]. Nevertheless sub-Doppler cooling mechanism still arrises from such initial polarization configuration, thanks to the radiation pressures of each couter-propagating beams being unbalanced for an atom moving along the pair of beams' propagation axis [9] [95]. It can be shown [93] that for vanishing intensities, the limit temperature is then given by the recoil temperature,

$$k_B T_{rec} = \frac{h^2}{2\lambda_L^2 m}$$

which is equal to 0.4 µK for ^{40}K.

Unfortunately due to the narrow splitting of the hyperfine level of the excited state of the D2 line with respect to the natural linewidth of 6 MHz, the ensuing sub-Doppler cooling is less efficient. Even in presence of an additional laser beam to return stray atoms into the cooling transition, non resonant coupling between the different sublevels can occur and lead to heavy losses despite reaching temperature as low as 15 µK [96, 97]. As a consequence, taking avantage of the well resolved (155.3 MHz) structure of the D1 transition's excited state, a gray molasses was implemented. While standard bright molasses relies on a $F \to F' = F+1$ transition, the D1 line corresponds to the $F \to F' = F$ and $F \to F' = F-1$ transitions [10].

It can be shown that, by using either of those two transitions as a cooling transition instead of the standard $F \to F' = F+1$ one, multiple dark states, linear combination of the Zeeman sublevels of the groundstate will emerge as eigenstates of the Hamiltonian [98, 99]. Those states of vanishing eigenenergies do not couple to the light field. The other eigenstates, on the other hand do couple to the light field and offer similar behaviour as the Zeeman state for the bright molasses. In particular, for a Lin⊥Lin configuration, those bright states' light shift are

[9] It should be emphasized that this imbalance of the two radiation pressures is not due to the Doppler effect as in standard Doppler cooling but arises from a non-adiabatic coupling between the different Zeeman sublevels (which experienced different light shifts) when the atom is not at rest.

[10] As a consequence, the D1 line does not have a cycling transition. In opposition to standard molasses, where the repumping transition is used, in a gray molasses the main beam (that we will call the cooling beam) and the less powerful one (called the repumping beam) form a so-called Λ-system

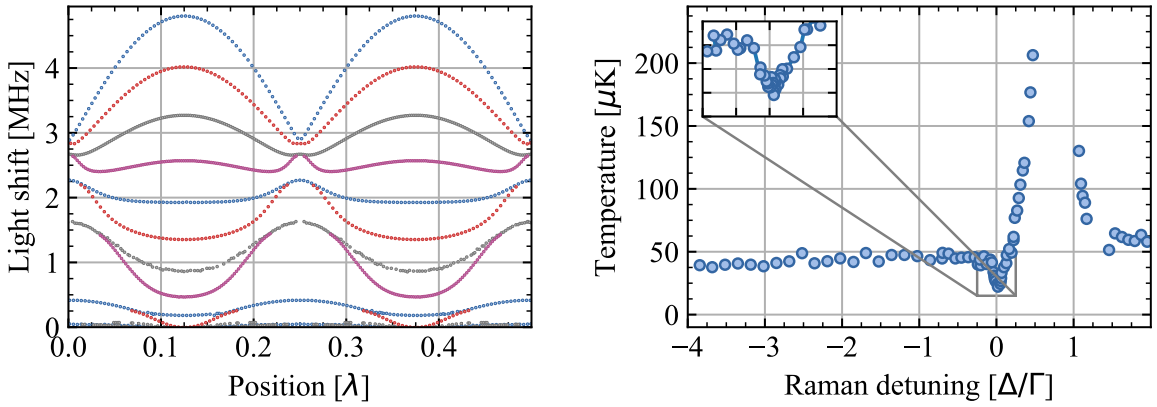

(a) (b)

Fig. 2.10 **Properties of the D1 gray molasses for the** ^{40}K. (a) Evolution of the eigeneneries as a function of the position (in unit of λ) for a Lin⊥Lin configuration as presented in [76]. (b) Evolution of the temperature as a function of the raman detuning. Data adapted from [71].

spatially modulated. The presence of dark states leads to two major differences with the bright molasses. First, the laser now needs to be blue detuned for the bright states, coupled to the light, to have higher energies than the uncoupled dark ones (as illustrated in fig.2.10 for ^{40}K). The second difference is that an atom pumped into a dark state will remain in this eigenstate until the motional coupling brings it back to a bright state. The probability of this passage increases for small energy differences between the bright state and the dark state and for atoms with high velocities. This implied cooling mechanism is called gray molasses cooling: atoms with elevated kinetic energy and initially in a dark states are transferred into a bright one. In order to minimize the difference of potential energy ensuing this non adiabatic passage, the transfer will most likely occur at the position of an energy minimum of the bright state (in the valley). Atoms will then proceed to climb the hill, losing kinetic energy in the process and be pumped into one of the dark state after reaching the climax of the hill. On the contrary, cold and slow atoms will accumulate in the dark states. This accumulation of atoms into the dark state decreases the amount of fluorescence light emitted, which can reduce the amount of light induced collisions and losses and increase the PSD (Phase-Space Density) compared to bright molasses [94] .

2.8.2 Experimental implementation of the gray D1 optical molasses

The principle of gray molasses was originally presented [100, 101] and realized experimentally for the first time [102, 103] on the D2 Line of Cesium. Λ−enhanced gray molasses on the D1 line was implemented for the first time on the Fermix experiment [76, 75]. Due to its great capacities in terms of capture efficiency and cooling power, it has, since then, been widely used

in numerous research groups [104–111]. Since the technical and experimental details have already been presented in great detail in previous PhD thesis [71, 77], we will only provide a brief summary of the key parameters of the D1 molasses, its cooling and trapping performance as well as its general role in the context of our experiment.

^{40}K offers two possible transitions for the gray molasses: the principal (or cooling) $|\,F = 9/2\rangle \rightarrow |\,F' = 7/2\rangle$ and the repumping $|\,F = 7/2\rangle \rightarrow |\,F' = 7/2\rangle$ (see Fig. 2.6b), both of which exhibit dark states. The optimal ratio cooling/repumping was found to be 12.5. The frequencies of both beams are overlapped and sent to the main table using a single-mode fiber. Once on the main table, the beam is first superimposed with the MOT beam thanks to a D-shape mirror, then enlarged and split on the way to the MOT chamber, facilitating its alignment on the atoms. As a consequence, our D1 gray molasses was implemented in a σ^--σ^+ configuration. Experimentally, three parameters, related to the capture velocity v_c and the reachable final equilibrium temperature T_{D1}, can be tuned to increase its performance: the detuning δ between the cooling beam wavelength and the cooling transition, the Raman detuning Δ between the two beams and the total intensity I. While v_c is proportional to I/δ^2, indicating that the capture range increases with the optical power available (contrary to Doppler cooling for example), T_{D1} scales as I/δ resulting in poor cooling efficiency for high intensity. An optimum was found by tuning the optical intensity during the D1 cooling. The total intensity is kept as its maximum (the total power at the fiber output being close to 200 mW) during 3 ms, to capture most of the atoms from the hot CMOT then linearly ramped down in 5 ms to low intensity values to reach cold temperatures. 3 compensations coils were also installed 80 cm from the MOT chamber to cancel any stray magnetic field, since the potential energy splitting of the various Zeeman states is solely due to the light shift as illustrated in fig. 2.9.

The lowest cooling temperature are reached for the Raman-condition, when the Raman detuning $\Delta = 0$ (see fig. 2.10). The influence of the detuning δ has been extensively studied in previous work and provided an optimum for $\delta = 2.3 \times \Gamma = 2\pi \times 13.7\,\text{MHz}$. Under those conditions, one can trap more than 1.4×10^9 atoms of ^{40}K and cool them down to 9 µK, offering much better results than with a bright molasses in terms of capture efficiency [96, 97] despite the final temperature being still far away from the recoil limit. At this time, it remains unclear why such a disrepancy between the D1 gray molasses final temperature and the recoil temperature exists.

Due to the large fine splitting between the D2 and the D1 lines, a separate setup was built for the D1 molasses. A main diode laser, is frequency stabilized on the D1 line crossover of ^{39}K then shifted thanks to an AOM to serve as a cooling beam. The repumping frequencies is generated by an EOM, set to the ground state hyperfine splitting of 1285.8 MHz. After amplification via a TA, the light is delivered to the polarization maintening single mode fiber and sent to the atoms as mentionned earlier. Additional description and details regarding the implementation of the

D1 setup can be found in [71, 72, 77]. Since the D1 molasses greatly reduces the temperature while conserving the spatial density acquired after the recompression step, the phase-space density increases from around 10^{-7} after the MOT loading to 10^{-4} after the D1 molasses.

2.8.3 Optical pumping into magnetically trappable states

Subsequent to the optical gray molasses, once the optical light is switched off, the atoms are distributed among all the Zeeman sublevels of both hyperfine ground states. Only few Zeeman sublevels of the groundstate manifold are low-field seekers (see sec. 2.9) and as such can be magnetically trapped. Moreover, the atomic cloud must be stable against spin-exchange collisions to prevent atoms from being transferred into a non-trappable Zeeman sublevel. Therefore, we optically pumped the atoms into low field seeker states before applying the magnetic confinement. Moreover, by transferring atoms solely into the two lowest Zeeman level one can create a mixture stable against spin relaxation.
A small magnetic vertical bias field of 1 G is applied during 400 µs to provide the symmetry axis. Once the symmetry axis set, a beam with a σ^+-polarization is sent along the quantization axis direction. The beam is applied during 70 µs to pump the atoms into the stretched state $|\,F = 9/2, m_F = 9/2\rangle$. The optical pumping light is provided by modifying the frequency composition of the 3D-MOT light and rerouting it to pass into a dedicated fiber connected to the main table (see fig. 2.4). The former 'cooling' frequency component is tuned to address the hyperfine manifold $F' = 11/2$ of the excited state and its optical power is greatly reduced to minimize the heating of the atomic cloud. Finally, the repumping frequency of the 3D-MOT is recycled to drive the $|\,F = 7/2\rangle \rightarrow |\,F' = 9/2\rangle$ transition. The optical pumping efficiency is close to 100% and the temperature of the cloud increases to 17 µK.

2.9 Magnetic trapping and transport to the science cell

Thanks to the optical gray molasses on the alkali D1 line, the PSD of ^{40}K after the D1 cooling is increased by 2 order of magnitude [77]. Nonetheless, it is still several order of magnitude away from degeneracy, mainly because of our atomic cloud being very dilute. In order to proceed to the later stages of evaporation, a magnetic transport transfers the atoms from the MOT chamber to the science cell.

2.9.1 Principle of magnetic confinement

Magnetic confinement was one of the first confining technique implemented to trap neutral atoms [29] and was realized thanks to a pair of coils in anti-Helmholtz configuration: the magnetic field is created by having the same current flowing into the two coils, coaxially

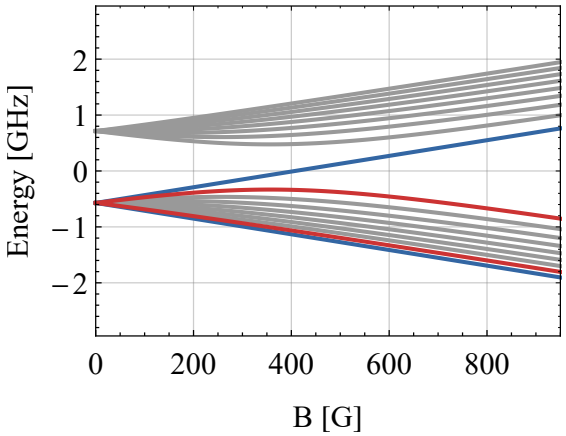

Fig. 2.11 **Evolution of the energy shift of the ground state manifold as a function of the magnetic field**. The blue line represents the streched states ($|\,9/2,+9/2\rangle$ and $|\,9/2,-9/2\rangle$) while the red line states represents the $|\,9/2,+7/2\rangle$ and the $|\,9/2,-7/2\rangle$ Zeeman sublevels. A mixture composed of the two low field seekers $|\,9/2,+7/2\rangle$ and $|\,9/2,+9/2\rangle$ Zeeman sublevels is stable against spin exchange collisions and thus can be magnetically trapped.

arranged, but in opposite directions. Moreover, Anti-Helmholtz configuration (also referred as a quadrupole trap) can be achieved when the distance between the two coils is equal to their radii. It can be shown that near the coils' center of symmetry, the magnetic field evolves as: $\mathbf{B}(\mathbf{r}) \simeq b\cdot(x,y,-2z)$, where $\mathbf{z}$ represents the axis of the coil pair. The parameter b characterizes the steepness of the trap and depends of the coils' parameters and the current circulating through them [11]. Atoms with a non-vanishing magnetic moment μ will interact via the magnetic dipole interaction with the magnetic field, resulting in a potential energy shift $\Delta E = -\mu\cdot\mathbf{B}$. For small value of the magnetic field ($B \ll \mathrm{a_{hf}}/\mu_\mathrm{B}$, $\mu_\mathrm{B} \approx 1.4\mathrm{MHz.G^{-1}}$ being the Bohr magneton and $\mathrm{a_{hf}}$ the hyperfine constant), the total atomic angular momentum basis $\{|\,\mathrm{F},\mathrm{m_F}\rangle\}$ constitutes a set of good quantum numbers and an atom in a Zeeman sublevel $\mathrm{m_F}$, confined in a quadrupole potential, will experience an energy shift ΔE as long as the atomic spin can adiabatically follows the local direction of the magnetic field, with

$$\Delta E = \mu_\mathrm{B} g_\mathrm{F} \mathrm{m_F} b \sqrt{x^2+y^2+4z^2}. \tag{2.1}$$

Here, g_F represents the Landé factor of the hyperfine Zeeman state $|\,\mathrm{F},\mathrm{m_F}\rangle$. Atom experiencing a positive energy shift will favor region of low magnetic field intensity to minimize their potential energy. Those states, called low-field seekers, can be confined in the center of the quadrupole trap and occupy a volume of typical dimension $r_0 = k_\mathrm{B}T/\mu_\mathrm{B}b$. On the other hand, high-field seekers cannot be trapped since static magnetic fields cannot have a local maximum according to Maxwell's equations. In the vicinity of the trap center, the magnetic field orientation is abruptly changed. Atoms accumulated in this region cannot adiabatically follow the local direction of the magnetic field. Consequently, in the frame of the local magnetic field, atoms appeared to have flip their spin. This can lead to atoms flipping from a low-field seeking

[11] In this convention, the gradient is defined by its value along the weak directions $\mathbf{x}$ and $\mathbf{y}$. Another convention is to simply defined it by its value along the strong axis $\mathbf{z}$.

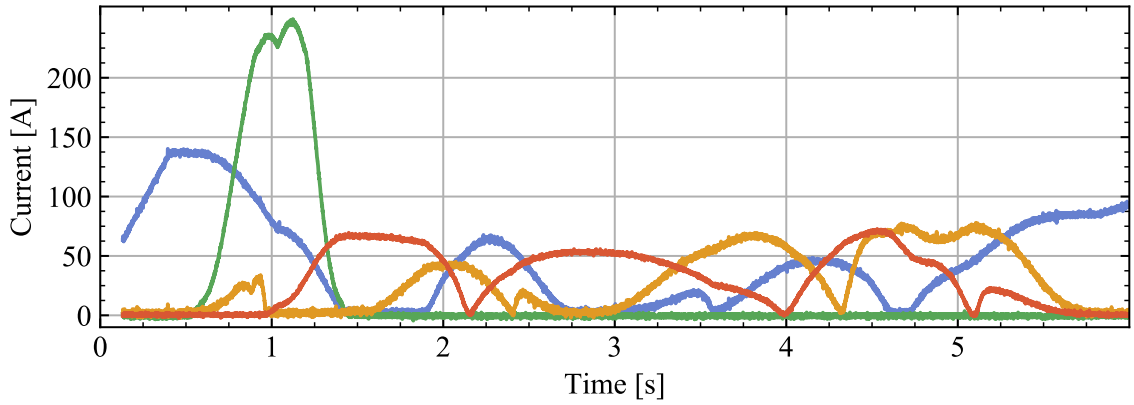

Fig. 2.12 **Magnetic transport currents**. The different colours correspond to the different power supplies.

Zeeman state to a high-field seeker one and be expelled from the trap. This phenomenon, called Majorana losses [112, 113], acts as an anti-evaporation process that ultimately leads to the heating of the cloud [114–116].

2.9.2 Magnetically trappable Zeeman levels of ^{40}K groundstate

The evolution of the Zeeman energy shift as a function of the magnetic field B is presented in fig. 2.11 for the ^{40}K $4^2S_{1/2}$ groundstate, which has several trappable low-field seeking states. In particular, $|\,9/2,9/2\rangle$ and $|\,9/2,7/2\rangle$ of the lowest manifold, which are the two states targeted by the optical pumping described in 2.8.3. While a mixture of $|\,9/2,9/2\rangle$ and $|\,9/2,7/2\rangle$ is stable against spin relaxation, the addition of the magnetically trappable $|\,9/2,5/2\rangle$ states can induce spin-exchange collisions and result in losses of the form [85]:

$$|\,9/2,7/2\rangle + |\,9/2,5/2\rangle \rightarrow |\,9/2,9/2\rangle + |\,9/2,3/2\rangle + E_{\mathrm{rel}}.$$

A detailed study of the spin composition of the atomic cloud in the magnetic trap can be found in [73]. After the optical pumping the loading into the quadrupole trap, the spin composition of the cloud is roughly 60 % of the total atom number in $m_F = 9/2$ and 35 % in $m_F = 7/2$.

2.9.3 Magnetic transport to the science cell

In order to increase the lifetime of our atomic sample (see fig. 2.2a) as well as the optical access to the atoms, the ^{40}K is transferred from the MOT chamber to the science cell. A possible solution to move the atoms over a long distance (the MOT chamber and the science cell are separated by 65 cm) is to slowly move a deep confining potential with respect to the characteristic timescale of the atomic motion within the trap. In addition, the speed of the trap

displacement also need to be fast enough (compare to the typical losses timescale) to minimize the losses. The cloud will then adiabatically follow the center of the trap, thereby reducing the induced heating. One standard technique is to optically confine the atomic cloud and to displace the waist of the dipole trap using highly precise movable [117] or deformable lenses [118]. Another possible solution is to magnetically trap the atomic cloud and move the center of the magnetic gradient, thanks to a motorized translation stage for example [119, 120]. Magnetic transport tends to be more robust with respect to slight misalignment and daily maintenance than their optical counterpart. Moreover, it facilitates the transport along angled paths. The magnetic transport implemented in FerMix consists in a series of 12 partially overlapping pairs of coils in anti-Helmholtz configuration, as represented in the figure 2.1.
After the optical molasses, a gradient of $150\,\mathrm{G.cm^{-1}}$ is ramped up within 500 ms and captures around 1.4×10^9 atoms with a final temperature of 135 µK. Following the loading of the magnetic trap, the atoms are transported in 5.3 s by varying the current circulating through the different anti-Helmholtz pairs over time (see fig 2.12). At any given time, three coils are activated in order to ensure a smooth displacement of the magnetic center and preserve the aspect ratio of the quadrupole potential. Details regarding the implementation and the optimization of the transport can be found in [77]. Two large water-cooled brass-made plates are connected to the top and bottom layer of the transport assembly to act as a heat sink and dissipate the accumulated heat generated by the high currents circulating through the coils during extensive period of time. Because of their proximity with the science cell, they can be the cause of long lived (up to 9 ms) Foucault's currents when strong magnetic fields are switched on in the science cell. Our magnetic transport has an overall efficiency of roughly 77% and heats up the atomic cloud by up to 60 µK. Once in the science cell, successive stages of evaporative cooling both in a magnetic trap and in an optical dipole trap, efficiently cool the atomic cloud to degeneracy.

2.10 Microwave evaporation in a quadrupole trap

Upon arrival in the science cell, the atoms are kept in a deep quadrupole trap. The steepness generated by the pair of coils [12] is $b \approx 250\,\mathrm{G.cm^{-1}}$. The total atom number arriving in the science cell is typically 10^9 and their temperature is around 200 µK. In order to make use of the numerous Feshbach of the ^{40}K [13], transfer into an optical dipole trap is necessary. To increase the mode matching between the quadrupole trap and the optical confinement and facilitate the transfer from one trap to the other, we first perform a MW (microwave) evaporation in the magnetic trap, reducing the cloud temperature well below 100 µK.

[12] called inner coils and creating a gradient of $2.50\,\mathrm{G.cm^{-1}.A^{-1}}$.
[13] To enhance the collision rate or study the properties of a degenerate Fermi gas close to unitarity for example.

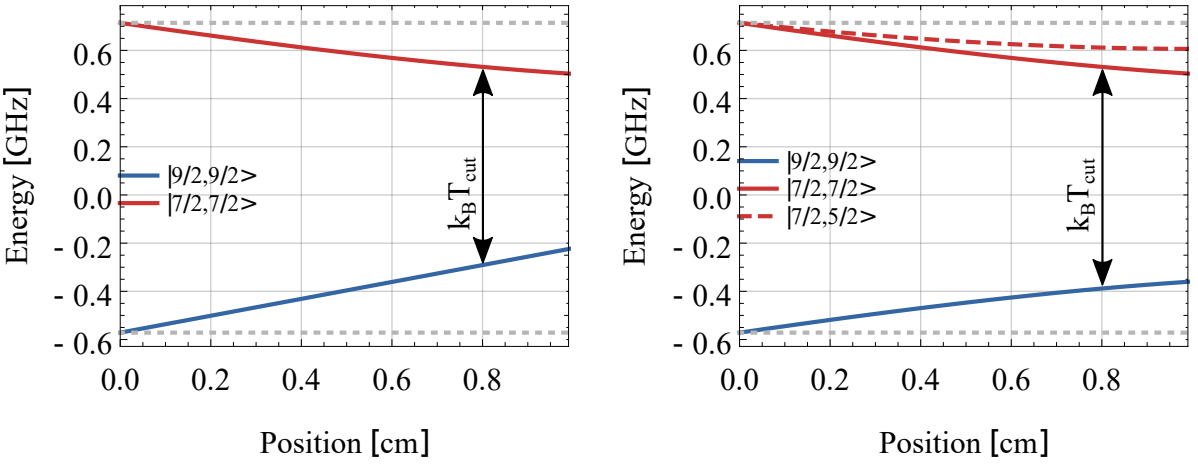

Fig. 2.13 **Evolution of the energy Zeeman states in the quadrupole trap as a function of the distance to the trap center**. (a) Evolution of the $|9/2,+9/2\rangle$ (blue line) Zeeman sublevel as well as the target state of our MW transition $|9/2,+7/2\rangle$ (red line) with respect to the position to the magnetic center in our quadrupole trap (with a gradient of $250\,\mathrm{G.cm^{-1}}$). (b) same as (a) for the $|9/2,+7/2\rangle$ (blue line) and the two Zeeman sublevels targeted by the MW transition $|7/2,+7/2\rangle$ (red line) and $|7/2,+5/2\rangle$ (red dashed line). By sweeping the frequency of the MW signal towards the higher frequencies, one can flip the Zeeman state of the atoms closer to the central region, thus expelling colder particle from the quadrupole trap

The principle of evaporative cooling consists of removing the most energetic particles from a trapping potential. In a confinement of finite depth, collisions between trapped particles redistribute the energy, which can lead to losses if one of the particles can gather enough kinetic energy to overcome the trap depth. Thereby, the most energetic atoms will tend to leave the trap. By removing the high energy tail of the thermal distribution, the distribution of the remaining ensemble will have less energy and therefore relaxes towards colder temperatures after rethermalization. As a consequence, contrary to Doppler cooling for example, evaporative cooling relies on the atom losses to reach colder temperature and attain the quantum degeneracy. The quantum degeneracy regime is reached when the central PSD (Phase-Space Density) [14] exceeds unity. While a complete quantitative treatment of this out-of-equilibrium process is very challenging, several quantitative models highlighting the key parameters have been successfully developed [121–123]. In order to characterize the evaporation efficiency, one can

[14] Defined as $\mathrm{PSD} = n_0 \lambda_{\mathrm{dB}}^3$, where $\lambda_{\mathrm{dB}} = \hbar\sqrt{2\pi/mk_{\mathrm{B}}T}$ is the De Broglie wavelength and represents the spatial extension of the particle wavepacket, while n_0 denotes the peak spatial density. For a classical gas, the spatial extension of the particles is much smaller than the typical interparticles distance while in the degenerate regime, the extension of the particle wavefunction becomes comparable to the interparticle distance.

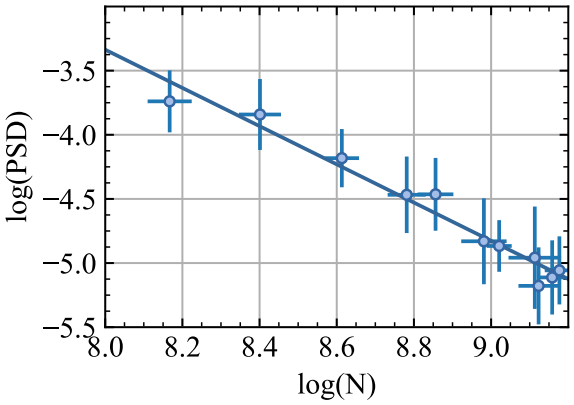

Fig. 2.14 **Efficiency of the MW evaporation**. After the magnetic transport, a mixture of $m_F = 9/2, 7/2, 5/2$ is confined in the quadrupole trap. The trap depth is then lowered from 1.15 GHz to 1.60 GHz in 5 s. The evaporation efficiency of $\alpha = 1.49$, despite being low is sufficient to efficiently load the optical dipole trap.

compute the parameter

$$\alpha = -\frac{d\log(\text{PSD})}{d\log(\text{N})}.$$

α estimates and represents how many atoms need to be sacrificed to increase the PSD by one order of magnitude thanks to evaporative cooling. The higher the α, the less atoms need to be expelled to reach the quantum degeneracy. Atoms with a kinetic energy close to the trap depth can escape from the trap. This process, called spilling occurs without any collisions and thus limit the evaporation efficiency. For a sufficiently low trap depth, close to the temperature of the atomic cloud, losses can be dominated by spilling, thus making the evaporation inefficient. On the other hand, for a trap too deep, the probability of atoms gathering enough kinetic energy to leave the trap will be too low, thus making background collisions losses prevalent. Consequently, trap depth must be careful tuned during any evaporative process to accompany the evaporation. In the case of a quadrupole trap, one can selectively flip the spin of the most energetic atoms to a high-field seeking state instead of lowering the magnetic trap depth, which, due to the reduced steepness, would decrease the spatial density. By doing so, the affected atoms will experience an anti-trapping potential and leave the trap. In case of ^{40}K, a MW signal drives the $F = 9/2 \rightarrow F = 7/2$ transitions (see fig. 2.13). The energy splitting of the transitions $|9/2, 9/2\rangle \rightarrow |7/2, 7/2\rangle$ and $|9/2, 7/2\rangle \rightarrow |7/2, 7/2\rangle$ increases as a function of the magnetic field up to 300 G (for the transition $|9/2, 7/2\rangle \rightarrow |7/2, 5/2\rangle$, it increases for magnetic fields up to 250 G). As a consequence, for small values of the MW knife, one will probe the wings of the atomic cloud and remove the most energetic atoms. Then, by increasing the frequency of the MW signal, one will expel atoms that are closer (and thus colder) to the trap center. In the Fermix experiment, the MW signal is generated by the SMB100A from Rohde&Schwarz and emitted by an antenna located close to the science cell (see fig. 3.1). The MW evaporation lasts 4 s, during which the MW frequency is decreased from 1.150 GHz to 1.270 GHz. Using the Breit-Rabi formula, one can convert the initial and final MW frequencies to determine the corresponding resonant magnetic field B_{cut} and by extension the equivalent

trap depth $k_B T_{cut} = \mu_B B_{cut}$:

$$h\nu_{cut} = E(|7/2,7/2\rangle, B_{cut}) - E(|9/2,9/2\rangle, B_{cut}).$$

Here, E denotes the energy of the corresponding Zeeman sublevel at the magnetic field B_{cut} and can be computed using the Breit-Rabi Formula. At the trap center, the magnetic field (and the temperature T_{cut}) is null and the energy splitting between $|7/2,7/2\rangle$ and $|9/2,9/2\rangle$ corresponds to the hyperfine splitting of $1,2858\,\mathrm{GHz}$. The initial (resp. final) MW frequency corresponds to an initial trap depth of $k_B \times 3.7\,\mathrm{mK}$ (resp. $k_B \times 430\,\mu\mathrm{K}$), reducing the atom number from around 8.0×10^8 to 4.5×10^7 and the temperature from around $200\,\mu\mathrm{K}$ to $70\,\mu\mathrm{K}$ (increasing the PSD to about 2.0×10^{-4}). For the early stage of the evaporation (up to $1260\,\mathrm{MHz}$), the efficiency is $\alpha = -1.49 \pm 0.05$ (see fig. 2.14). The evaporation's low efficiency is due to a low collision rate that cannot be enhanced by the use of Feshbach resonances [124] combined to the very high trap depth compared to the cloud temperature. Nonetheless, at the end of the MW evaporation, the conditions are met for an efficient transfer and the atomic cloud is moved into an optical dipole trap, offering the possibility to tune the interaction strength and the density of the cloud to reach the quantum degeneracy. Over the course of this thesis several upgraded and modifications had to be implemented around the science cell, such as the complete rebuild of the optical dipole traps, had to be performed in order to produce a deeply degenerate Fermi gas. As a consequence, those changes as well as the new procedure for the production of a deeply degenerate Fermi gas of ^{40}K will be the focus of the following chapter.

Chapter 3

Realization of a quantum degenerate Fermi gas of ^{40}K

Following the MW evaporation, we transfer our atomic cloud from the quadrupole trap to an optical dipole trap in which successive evaporative cooling stages will take place in order to reach quantum degeneracy. In this chapter, after highlighting the numerous modifications implemented to take advantage of the large optical access provided by our science cell, we will describe the different steps necessary to control, manipulate and produce a quantum degenerate Fermi gas of ^{40}K.

3.1 Experimental apparatus surrounding the science cell

Despite the large access provided by our science cell, numerous modifications needed to be carried out in order to implement the optics necessary for the realization of a strongly interacting 1D Fermi gas. To begin with, both optical dipole traps were upgraded, freeing up the optical access available while at the same time increasing their stability. Moreover, all imaging systems were rebuilt, improving their limit of resolution and making the visualization of the lattice tubes possible. Finally, additional hardware was added to generate the lattice tubes and to project

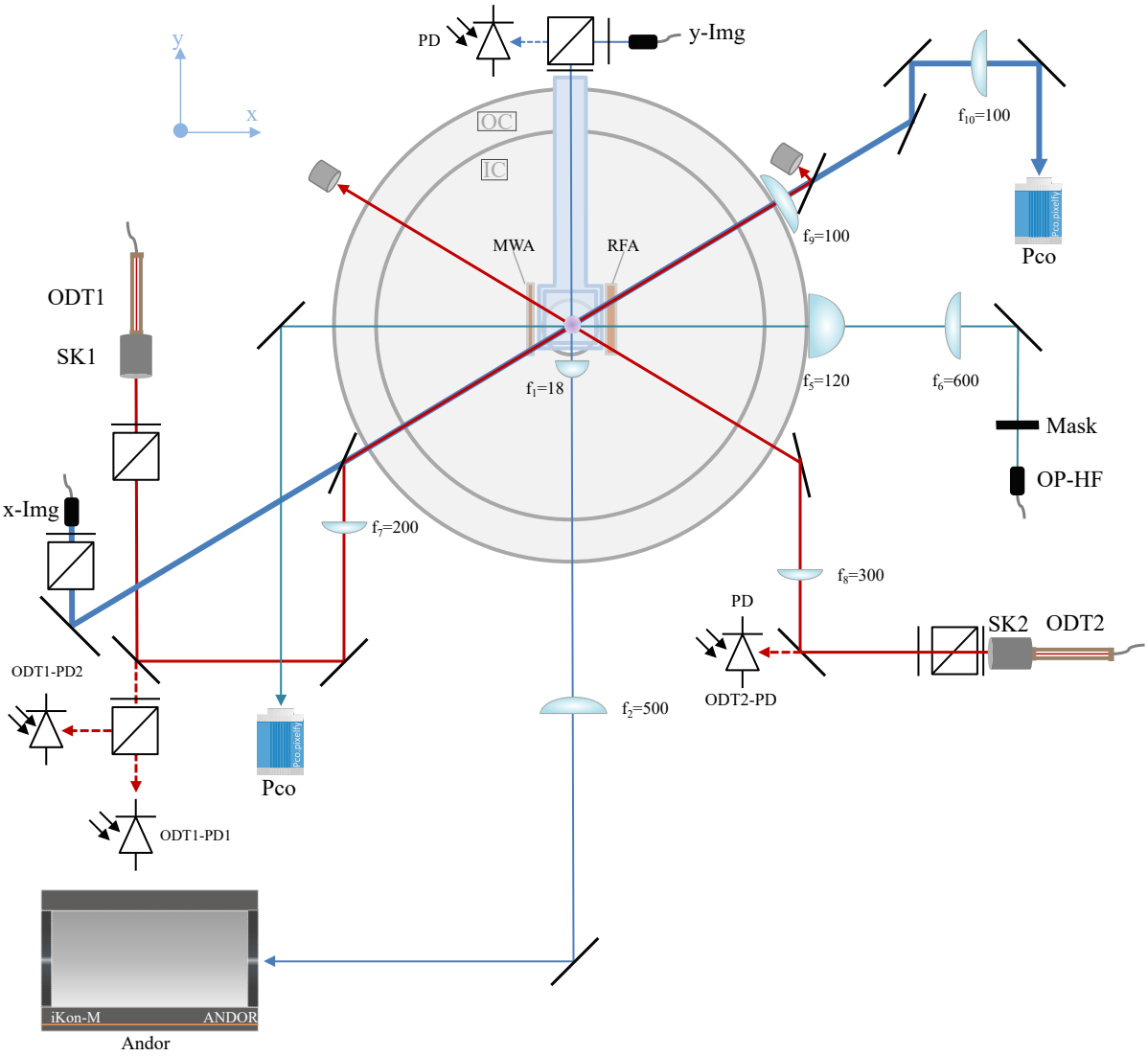

Fig. 3.1 **Schematics of the hardware surrounding the science cell**. The ODT1&2 are sent on the atoms under an angle of 69° with respect to the $y-$axis. The two antennae called MWA and RFA emit the microwave and radiofrequency pulses used to excite magnetic dipole transitions. Magnetic field are generated by the Inner (IC) and Outer (OC) pair of coils. Finally, an optical mask and light coming from the OP-HP outcoupler are used for the optical pumping at high field. **Principal optical elements**: ODT1/2: optical Fibers LMA-PM-10 from NKTPhotonics. SK1/2: fiber outcouplers model 60FC-SMA-0-M30-37 and 60FC-0-A11-03 from Schäfter-Kirchhoff.

custom potential onto the atoms. The figure 3.1 depicts our current optical and MW/RF signal apparatus surrounding the science cell:

Optical dipole traps. The optical confinement is ensured by two Optical Dipole Traps (ODTs): the main ODT (called ODT1) that is directly loaded from the quadrupole trap while the second

ODT (called ODT2) is used to provide an additional confinement to increase the density and the collision rate during the latter stage of the optical evaporative cooling. Both dipole traps are generated by the same source: a 16 W [1] laser with a wavelength of 1064 nm from the company Innolight (model Mephisto MOPA 25W). After the laser head, the optical beam is separated to generate the light for the ODTs 1&2. Once split, both beams are sent through separate AOMs (allowing the independent power regulation of each dipole trap), before being guided to the main table by means of a high-power-single-mode crystal fiber (detailed description of the apparatus is provided in sec. 3.2 and represented in fig. 3.4). In order to maximize the overlap between the trap volume of the quadrupole and the optical traps, a waist of less than 60 µm is necessary for the latter due to its limited available power (maximum 7 W). Moreover, because of the geometry of the coils installed around the science cell, propagating an optical beam on the atoms with a focusing lens whose focal length is below 150 mm is very challenging since the optics necessary for the propagation would greatly reduce the available optical access. Consequently, for the ODT1, the fiber output is attached to a Schäfter-Kirchhoff fiber collimator with an effective focal length of 30 mm (model 60FC-SMA-0-M30-37) which generate a collimated beam with a diameter of 4.6 mm. The optical beam is polarization cleaned before being shined on the atoms with a 200 mm focusing lens, creating a dipole trap with a 39 µm waist and a maximum trap depth of roughly $k_B \times 350\,\mu K$ when used at full power (7 W). Intensity control of the dipole trap is ensured by two fast photodiodes (one used when high power is required for the ODT1 while the second one is employed for the low power regime), picking up the laser light transmitted through a mirror and acting as a feedback signal to a PID controller (model SIM960 from Stanford Research Systems) connected to the corresponding AOM. In order to maximize the available optical access along the x-axis (orthogonal to the transport direction as represented in 3.1), the ODT1 is sent into the science cell under an angle of 69° with respect to the transport direction (that we will call y-axis). The pointing of the optical beam is stabilized and controlled by a piezoelectric actuated mirror mount from Newport. The ODTs 1&2 being built symmetrically with respect to the transport, the ODT2 is also shined on the atoms with an angle of 69° with the $y-$axis. A 300 mm lens focuses the beam on the atoms. The maximum power available is 3.0 W which, combined with the 110 µm of the waist, offers a maximum trap depth of 19 µK. As for the ODT1, a fast photodiode provides the feedback signal to regulate the power intensity of the dipole trap thanks to a SIM960 PID controller connected to the dedicated AOM and the pointing stability is ensured by a piezoelectric actuated mirror mount. Furthermore, to avoid interference between the two dipole traps, their respective polarization

[1] Due to aging of the laser over the years, the current maximum power output of the Mephisto is reduced to 65 % of its original capacity

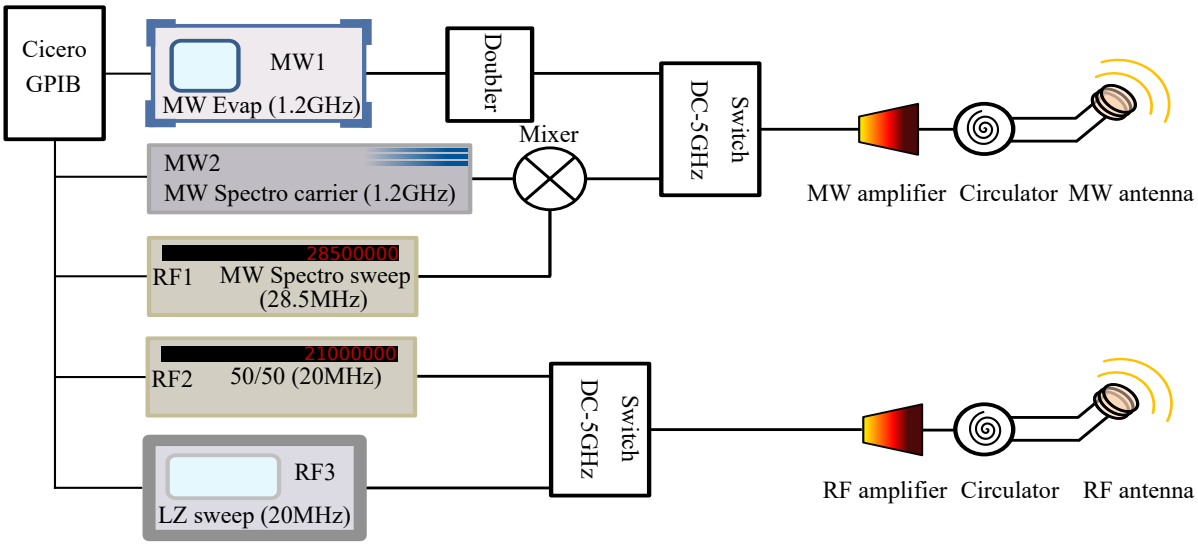

Fig. 3.2 **Overview of the MW/RF hardware**. All signal generators are controlled via GPIB during early stage of the sequence and triggered during the desired sequence step with TTL signals. **Signal Generators**: MW1: Rohde&Schwarz model SMB100A, MW2: Keysight Technologies model 33600A, RF1/2: Stanford Research Systems model DS345, RF3: Agilent Technologies model MXG ATE N5161A. **Switch**: model ZASW-2-50DR+ from Minicircuits

are kept orthogonal and opposite orders of diffraction were chosen for their AOMs.

Microwave and radio-frequency system. Two new antennae, whose dimensions match the dimension of the science cell, were installed in its vicinity (see fig. 3.1). They are used to manipulate the internal structure of the atoms thanks to magnetic dipole interactions when electric dipole transitions are forbidden due to the associated selection rules ($\Delta L = \pm 1$). The first antenna, located on the same side as the optics used to propagate the ODT1 (see figure 3.1) and called MWA, is optimized for MW signals and is used to directly transfer atoms from one of the hyperfine sublevel of the groundstate to the other (during the MW evaporation described in sec. 2.10 for example). As such, the MWA antenna is mostly used with MW signals with a frequency close to the ^{40}K groundstate hyperfine splitting of 1.2858 GHz. Contrary to the MWA antenna that has a single winding, the second antenna (called RFA antenna), is a multiple loop antenna used for modifying the internal state of an atom from one Zeeman sublevel to a targeted sublevel within the same hyperfine manifold. It is optimized for frequencies comprised between 5 MHz and 50 MHz (for manipulation of the relative spin population of $|9/2, -9/2\rangle$ and $|9/2, -7/2\rangle$ at any magnetic field up to 230 G for example). Several MW and RF sources are used to generate those AC signals. They are computer controlled via GPIB connection and are directed to high attenuation switches before being sent to power amplifiers and to their dedicated antenna. Finally, to protect the amplifiers from potential back reflections from the

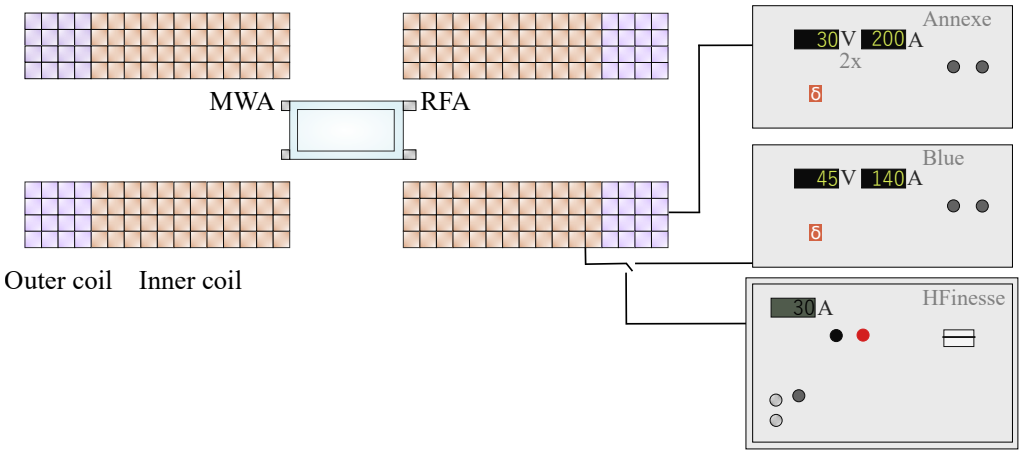

Fig. 3.3 **Schematics of the main coil arrangement**. The inner coils (in orange) can be used to create either a magnetic bias field of $8.0\,\mathrm{G.A^{-1}}$ or a gradient of $2.5\,\mathrm{G.A^{-1}.cm^{-1}}$ thanks to two power supplies: High Finesse USC 30/15 and Delta Electronica SM45-140. The outer coils (in purple) can be used to create either a magnetic bias field of $2.05\,\mathrm{G.A^{-1}}$ or a gradient of $0.24\,\mathrm{G.A^{-1}.cm^{-1}}$ thanks to two Delta Elektronika (model SM 30-200) power supplies in parallel. Each square represents the cross-section of the hollow copper wire of $4\times4\,\mathrm{mm^2}$. Figure style adapted from [77] and [74].

antennae, additional circulators are installed (see fig.3.2).

Magnetic Fields generators. A schematic view of the coil's arrangement near the science cell is provided in fig.3.3. It is composed of two principal pairs of coils (called inner and outer coils) aligned along the vertical direction (called z-axis) and used to create either a gradient or a bias field on the atoms [71, 72]. The inner pair of coils has a inner (resp. outer) diameter of 40 mm (resp.71.6 mm). The two coils are separated by 35 mm along the vertical direction. They generate either a gradient of $2.50\,\mathrm{G.cm^{-1}.A^{-1}}$ or a bias field of $8.05\,\mathrm{G.A^{-1}}$ (with a curvature of $0.31\,\mathrm{G.cm^{-2}.A^{-1}}$). The current circulating through the pair in either Helmholtz or anti-Helmholtz configuration is provided by a high power DC supply from Delta Electronica (model SM45-140) which can provide up to 140 A. By switching the configuration of the dedicated IGBTs, the inner coils can be connected to another power supply, the model UCS 30/15 from High Finesse, which despite being less powerful than the Delta Electronica power supply (the High Finesse can only deliver up to 30 A), is much more stable (the current stability is around 10^{-5} while the current stability of the Delta Electronica is around few 10^{-4}). As a consequence, by using the High Finesse, one can create a bias field of up to 240 G, which is enough to reach the s-wave Feshbach resonance between $|9/2,-9/2\rangle$ and $|9/2,-7/2\rangle$ at 201.2 G [125, 126]. Because of the positive curvature of $0.31\,\mathrm{G.cm^{-2}.A^{-1}}$, a weak repulsive harmonic confinement is located at the center of the coil arrangement in addition to the bias

field.

The outer coils are aligned along the z-axis and encircle the inner coils due to their inner and outer diameter of 72.5 mm and 89.7 mm. In Helmholtz configuration the outer coils generate a bias field of $2.05\,\mathrm{G.A^{-1}}$. In this situation, the pair of coils additionally create a negative curvature of $-0.026\,\mathrm{G.cm^{-2}.A^{-1}}$. Consequently, if necessary one can use the two pairs of coils at the same time in Helmholtz configuration. In this case, both bias field will add up. Moreover, due to the opposite sign of the two curvatures, one can completely cancel the resulting curvature by choosing the appropriate value for the current circulating through the two pairs ($I_{\mathrm{outer}} = 11.9\,I_{\mathrm{inner}}$). Finally, in anti-Helmholtz configuration the gradient created has a steepness of $0.24\,\mathrm{G.cm^{-1}.A^{-1}}$. Both pairs of coils are water cooled in order to dissipate the heat generated by the current circulated through them during extended period of time (up to several tens of seconds). In addition to those two principal pairs of coils, five additional coils are located next to the science cell to compensate all stray DC magnetic fields occurring in its vicinity. Originally, those compensation coils were large square coils located away from the cell. They were eventually replaced to allow the installation of both our new imaging systems and the breadboard dedicated to the lattice tube. Information regarding the design of those new compensation coils can be found in [74].

New imaging systems. In order to obtain the atomic cloud properties, we perform absorption imaging. To this end, three pictures are necessary: first, an absorption shot during which the atoms will absorb and scatter photons. Secondly, an exposure shot of only the resonant imaging light, which provides the imaging beam in the absence of any atoms. Finally, a dark shot is recorded in absence of any imaging light in order to isolate the ambient noise as well as the noise of the camera. The duration of the imaging pulse was reduced to 20 µs, instead of the original 80 µs and the intensity to $I \approx 0.1 \times I_{\mathrm{sat}}$[2]. A more detailed description of the working principle of absorption imaging can be found in appendix A.

Around the science cell, three different new imaging systems with different purposes and magnifications were installed. Apart from the system installed along the y-axis, all pictures are recorded thanks to a scientific CCD camera operating in double shutter mode from PCO (model Pixelfly QE 270XD). Its quantum efficiency for ^{40}K, whose imaging wavelength is at 767 nm, is 25 %. This sensitivity is sufficient for imaging systems with low enough magnification and with high enough signal to noise ratio. For our experiment, this is true until the latest stage of evaporation in the cross dipole trap when the atom number drops below few 10^5 per spin

[2] The original duration as well as the optical intensity of the imaging light were found to be too high. Due to the excessive intensity, all resonance imaging characterization were Doppler-broadened. Moreover, due to the ensued undue optical pumping, the recorded atom number for atoms in a atom in a Zeeman sublevel that offered no closed transition was severely inaccurate.

state. Since for the lattice, we expected to load around few 10^3 ^{40}K per tube and would need a magnification of 15 with the pixelfly to decently resolve the tubes, we decided to install a more sensitive camera along the transport direction (more details are provided in 5.3.2).

X-imaging. Our primary imaging system is aligned with the ODT1 and is called x-imaging. Two lenses with a focal length of 150 mm are installed in the so-called 4-*f* configuration providing a magnification of $M = 1$. This low magnification is particularly useful to image the cloud at the earlier stage of the experiment when it is still relatively hot (for example after the MW evaporation) and expands quickly during a time of flight experiment. As such, it is used as an important diagnostic tool to optimize the transport, the MW evaporation and the loading of the ODT1. When the atomic cloud is confined in the single ODT1, it also benefits from a very high signal to noise ratio, the atomic signal being integrated along the entire length of the single dipole trap. Due to the direction of propagation of the imaging beam being perpendicular to the vertical quantization axis of the atomic cloud, the light polarization cannot be purely σ^+ or σ^-. More precisely, considering the horizontal polarization of the light field, the resulting polarization along x-imaging is an equal superposition of both σ^+ and σ^-. As a consequence, using closed transition to image atoms in a stretched Zeeman states is only possible in presence of a high bias field and the value of the theoretical cross section $\sigma = \frac{3\lambda^2}{2\pi} = 2.81 \times 10^{-13}\,\mathrm{m}^2$ must be multiplied by a correcting factor. At high field, due to the superposition of polarization this correcting factor is simply equal to 0.5 while at low field it is equal to 0.4 (more details about absorption imaging can be found in Appendix A).

Y-imaging. The transport axis, called y-imaging, is the favored direction to image the density distribution of the atomic sample once loaded into the our new optical lattice. Given the large lattice spacing of 2.3 µm, optics with a moderately high Numerical Aperture (NA) needed to be implemented in order to image the individual tubes with a sufficient contrast. To this end, a commercial objective (model LMPLN10XIR from Olympus) with a NA of 0.3 (and an associated optical resolution of 1.6 µm [3]) was installed. This imaging system has a total magnification of $M = 33$ and a highly sensitive CMOS camera from Andor (model iKon-M 934 with a quantum efficiency of roughly 95 % at 767 nm) is used to record the weak atomic signal. Due to the direction of propagation of the imaging beam, using closed transitions for atoms in a stretched state are also only possible in presence of a strong bias field. Details about this new imaging are provided in 5.3.2.

Z-imaging. Aligned with the quantization axis of the atoms, the vertical imaging is the only direction that can produce pure σ^+ or σ^- light along the magnetic field direction. Therefore, it is the only imaging system allowing the optical pumping or imaging of atoms in a stretched state on a cycling transition even for low magnetic field. As such, this direction is mostly

[3] This theoretical resolution of 1.6 µm was also measured using a resolution target as explained in sec 5.3.2.

used for optical pumping at low and high magnetic field. Nonetheless, z-imaging can also be used to observe the lattice structure thanks to the high signal to noise ratio (the signal of the atoms inside the tubes will be integrated along the entire length of the tube, thus providing a better signal to noise ratio compared to the transport direction for example). Consequently, a homemade objective with a NA=0.23, which corresponds to a resolution of 2.0 µ, was installed as well as a high magnification $M = 15$ optical system. A demagnification stage was also installed to be able to image the cloud after the MW evaporation, facilitating the alignment of both dipole traps in the *xy*-plane. In order to image and manipulate both negative and positive Zeeman sublevels, the polarization of the optical beam can be tuned by rotating a quarter-waveplate to produce pure σ^+ or σ^- light (further details are provided in sec 5.3.1).

2D optical lattice. In order to study the behaviour of fermions in one dimension, a two dimensional lattice was set. The lattice is created by two pairs of far off-resonant optical beams. Those Gaussian beams have a wavelength of 1064 nm and intersect on the atoms with a full angle of 27°. Each individual beam has a waist of roughly 210 µm and a maximum trap depth of $k_B \times 14\,\mu K$ when used at full power (8 W). A single laser source is used to generate those four arms: a 50 W MOPA system from AzurLight. This main laser first produces two independent beams that will be propagated on the lattice breadboard via two high power fibers (x-and y-lattice). Once on the breadboard, each beams is split to generate the two pairs of lattice beams before being send downwards in pair of two towards the atoms, generating the 2D lattice. The 2D lattice is the main focus of the section 5.2.

High-field repumping. In order to observe the physics of the individual tubes along the y-direction, one has to isolate a single tube along the integrated direction of imaging. Thus, a repumping beam is shone onto the atoms perpendicularly to the y-imaging, transferring atoms into the upper groundstate hyperfine manifold, making them invisible when illuminated with resonant light during the high field imaging around 210 G. To isolate one layer of tubes, the repumping beam first illuminates a small rectangular mask, which is then imaged onto the atoms with a width smaller than the distance between two tubes. Moreover, an additional mask with rectangular mask of variable width can also be inserted. With a projected width on the atoms comprised between 2.4 µm and 12 µm, it can be used to image few layers of tube. Realized in a clean room, it is made of chromium and gold. The gold deposit (with a thickness of roughly 150 nm) is used to reflect the incoming light in order to not deteriorate the chromium deposit. Due to the small depth of field of the objective along the transport direction, one can only correctly imaged pattern with a 2.5 µm witdh on a distance of roughly 16 µm along the

y-imaging direction. After that blurriness of the periodic pattern starts to occur. Further details are available in sec. 6.4.

3.2 Transfer to the optical dipole trap

3.2.1 Optical trapping of neutral atoms

Ever since the first use of a laser light to confine atoms [28], optical trapping and cooling became one of the most standard techniques to cool down atoms and reach quantum degeneracy. One of its main advantages compared to magnetic trap, is the possibility to trap atoms in any Zeeman sublevel of the ground state. Moreover, one can take advantage of Feshbach resonances to tune freely the collision rate between particles.

In presence of an inhomogeneous light field, atoms will experience an induced dipole moment $\mathbf{d}$ oscillating at the driving frequency w_L of the incoming light [127]. It results in an electric dipole interaction between the induced atomic dipole moment and the electric field of the laser source $\mathbf{E}$. The intensity of the interaction depends of the complex polarizability $\alpha(w_L)$ (defined such as $\mathbf{d} = \alpha(w_L)\mathbf{E}$) of the atom and the light source intensity [91]:

$$U_{\text{dip}}(\mathbf{r}) = \frac{1}{2\varepsilon_0 c}\text{Re}\left[\alpha(w_L)\right] \times I_L(\mathbf{r}), \tag{3.1}$$

where $I_L(\mathbf{r})$ denotes the light intensity at the position $\mathbf{r}$. Using the semiclassical approach [127], one can determine the complex polarizability and obtain the following expression of U_{dip}:

$$U_{\text{dip}}(\mathbf{r}) = \frac{3\pi c^2}{2w_0^3}\left(\frac{\Gamma}{w_0 - w} + \frac{\Gamma}{w_0 + w}\right) \times I_L(\mathbf{r}) \simeq \frac{3\pi c^2}{2w_0^3}\frac{\Gamma}{\Delta} \times I_L(\mathbf{r}), \tag{3.2}$$

with $\Delta = w_0 - w$ being the detuning between the far-off resonance laser and the atomic transition w_0. Similarly, the scattering rate can also be determined, using the imaginary part of the complex polarizability and yields:

$$\Gamma_{\text{dip}}(\mathbf{r}) = \frac{3\pi c^2}{2\hbar w_0^3}\left(\frac{\Gamma}{\Delta}\right)^2 \times I_L(\mathbf{r}). \tag{3.3}$$

Due to the intensity of the light shift varying with the light intensity (see eq. 3.2), depending on the sign of the detuning Δ, one can create an attractive potential for neutral atoms by creating a position dependent light field intensity. More precisely, for red-detuned light, the atoms are attracted by an intensity maximum. Moreover, since the scattering rate scales as I/Δ^2 while the dipole potential only scales as I/Δ (see eq. 3.2 and 3.3), one can create deep optical potential while keeping the scattering rate to a minimum by simply using a high intensity laser beam with a large detuning. This model, valid for an atom represented as a 2-level system can be modified

to take into account the multi-level structure of atoms, such as alkali metals [127]. Still, for an alkali and a far-off resonant lasers with respect to the D-line doublet $^2S_{1/2} \rightarrow ^2P_{1/2}, ^2P_{3/2}$, the expressions 3.2 and 3.3 give an accurate approximation of the light shift U_{dip} and the scattering rate experienced by an atom in any Zeeman sublevel $|\mathrm{F}, \mathrm{m_F}\rangle$ of the hyperfine groundstate. In order to create a position dependent light gradient, one can use a focused Gaussian laser beam of waist ω_0 on the atoms. In this case, after the focusing lens, the intensity $I_{\mathrm{L}}(\mathbf{r} = (x, y, z))$ is given by:

$$I_{\mathrm{L}}(\mathbf{r}) = \frac{2P_{\mathrm{L}}}{\pi\omega^2(z)} \exp\left(\frac{-2r^2}{\omega^2(z)}\right). \tag{3.4}$$

Here, P_{L} represents the total power of the Gaussian beam while $\omega(z) = \omega_0\sqrt{(1+(z/z_{\mathrm{r}})^2)}$ denotes the value of the beam radius at the position z along the propagation axis $\mathbf{z}$ of the laser (with $z_{\mathrm{r}} = \pi\omega_0^2/\lambda_{\mathrm{L}}$ being the Rayleigh range of the beam). In the vicinity of the waist ω_0 ($r = \sqrt{x^2+y^2} \ll \omega_o$ and $z \ll z_{\mathrm{r}}$), one can realize a Taylor expansion of eq. 3.4 to the second leading order to obtain the following harmonic approximation for the trapping potential $U_{\mathrm{dip}}(\mathbf{r})$:

$$U_{\mathrm{dip}}(\mathbf{r}) = U_{\mathrm{dip}}(0) + \frac{1}{2}m\left(\omega_x^2x^2 + \omega_y^2y^2 + \omega_z^2z^2\right). \tag{3.5}$$

$U_{\mathrm{dip}}(0)$ is the trap depth of the optical potential. The transverse and axial trapping frequencies are respectively defined as $\omega_\perp = \omega_{x,y} = \sqrt{4U_0/m\omega_0^2}$ and $\omega_\parallel = \omega_z = \sqrt{2U_0/mz_{\mathrm{r}}^2}$. For the ODT1 and ODT2 of FerMix (represented in fig. 3.1), the trap depths at full power (7 W and 3 W) are $\mathrm{k_B} \times 350\,\mu\mathrm{K}$ and $\mathrm{k_B} \times 19\,\mu\mathrm{K}$ respectively and the corresponding transverse and axial trapping frequencies are $\omega_\perp = 2\pi \times 2.2\,\mathrm{kHz}$ (resp. $2\pi \times 180\,\mathrm{Hz}$ for the ODT2) and $\omega_\parallel = 2\pi \times 13\,\mathrm{Hz}$ (resp. $2\pi \times 0.40\,\mathrm{Hz}$). Details concerning the experimental measurement of the trapping frequencies can be found in Appendix A.

3.2.2 Laser setup of the two ODTs

The laser setup used to generate both optical dipole traps was briefly described in sec. 3.1. Originally, both dipole traps were generated using a common AOM: the diffracted order was directed into a high power fiber before being send onto the main table and the atoms while the non-diffracted, zero order beam was recycled and guided towards a second AOM before directly heading towards the science cell [72]. Consequently, due to the interconnection between both optical traps, one had to wait for the main ODT1 to be weak enough before ramping up the ODT2 to obtain enough additional confinement. Another technical limitation occurred from the use of a large aperture high-power AOM (model MCQ80-A2.5-L1064, from AA Opto-Electronic with a aperture of $2.5\,\mathrm{mm} \times 2.5\,\mathrm{mm}$). Because of its large aperture, the AOM needed 15 W of RF power to reach the maximum diffraction efficiency, which, due to the dissipated

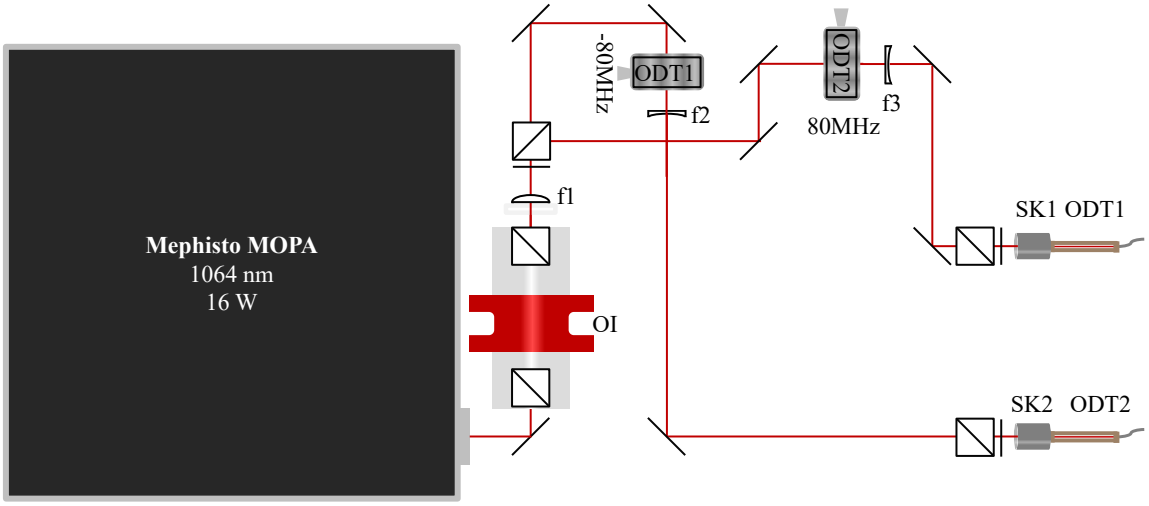

Fig. 3.4 **Schematics of the main dipole traps setup**. The Mephisto laser (16 W of maximum power) is splitted thanks a polarized beam splitter cube, after being directed to a convex lens f1 to recollimate the output beam, generating the ODT1 and the ODT2 laser beams. Each beam is then rerouted to an AOM before being sent to a dedicated high power fiber. To prevent any damage of the main laser due to back reflexion, an optical isolator is located right after the Mephisto output. **Optical elements**: OI (optical isolator) from EO Tech, ODT1 and ODT2 AOMs 80 MHz AOM from Gooch&Housego, model 3080-197, f1: 400 mm convex lens from Lambda Research Optics (LRO), model VAR2-R1064-PCX-25.4U-400, f2: -300 mm concave lens from LRO, model VAR2-PCC-25.4U-(FL-300)-1064, f3: -1000 mm concave lens from LRO, model VAR2-R1064-PCC-25.4U-500, SK1 and SK2: fiber collimator $f = 11$ mm from Schäfter-Kirchoff, model 60FC-SMA-T-4-A11-03, ODT1 and ODT2 fibers: large mode area high power fibers from NKT Photonics, model LMA-PM-10.

heat, caused permanent pointing drifts issues with the ODT1 but more importantly with the non-fibered ODT2. To avoid those issues, a new optical system was designed (see fig. 3.4). As briefly described earlier, the 16 W main laser source, coming from the Innolight Mephisto MOPA 25 W is (after a collimation lens) split thanks to a polarization beam splitter into the ODT1&2 path. A simple half waveplate allows the tuning of the ratio between the two intensities. The two splitted beams go through high powers AOMs (model 3080-197 from Gooch&Housego) that act as fast switches while regulating the optical power of the ODTs thanks to the control of their respective RF power. Finally, after some final beam shaping, the two diffracted beams are sent through high power fibers (model LMA-PM-10 from NKT-photonics). Both fibers are terminated with a 5° angle SMA connector (to avoid degradation of the laser induced by potential back reflection) and a copper heat sink to dissipate the non coupled light. In addition, the fiber is protected with a stainless steel tube in order to reduce power fluctuation caused by thermal drift as well as limiting potential damage due to mechanical stress. Finally, the laser system is contained in an aluminum enclosure, thus protecting it from

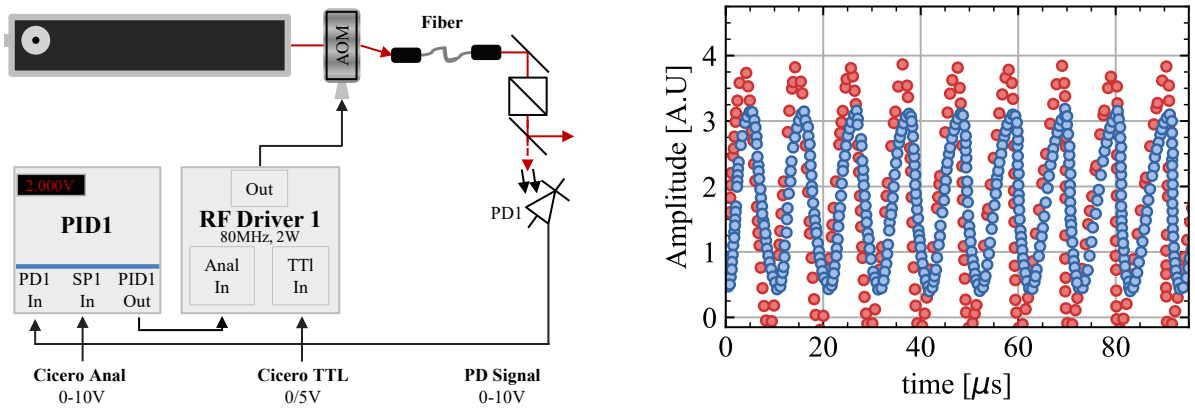

(a) (b)

Fig. 3.5 **Principle of our regulation system**. (a) A photodiode picks up a reduced fraction of the power of the optical beam. The photodiode signal is used as an input signal for a PID regulator, while the instruction signal is provided by Cicero. The output signal of the PID finally acts as a regulator for the RF driver of the AOM, thus regulating the diffraction efficiency of the AOM. (b) typical regulated signal (blue) of our dipole traps for a 100 kHz instruction signal (red).

turbulence and temperature fluctuation.

After the output of the two fibers both beam are sent towards the atoms and intersect under an angle of 138° as described in sec. 3.1. The intensity regulation of both beams is ensured by the PID controller SIM960 from Stanford Research Systems: an analog setpoint is first given by the analog channel of the NI card (as illustrated in fig. 3.5). A small fraction of the beam that is transmitted through a mirror serves as a picked up signal for a photodiode. The photodiode provides the necessary feedback for the active control of the optical power and is connected to the input of the PID. Finally the output, regulated by the PID, acts as the analog input of the RF driver (model MODA080 from AA Opto-Electronic) used as a RF source for the AOM. The bandwidth of the system is 100 kHz (see fig. 3.5). Due to the range of the ODT1 optical power explored during the evaporation stage (3 orders of magnitude), a simple linear photodiode was used for the feedback signal of the PID controller. Unfortunately, for the latest stage of evaporation, because of the finite resolution of the analog card [4], the evaporation ramp was becoming noticeably discrete for optical power below 100 mW, which caused massive atom losses (of up to 50 %) and prevented any efficient evaporation. To circumvent this problem, one could use a logarithm photodiode or install a voltage scaling converter to make use of the full range of the NI analog card (the analog setpoint required is comprised between 0 V and 10 V only). However, by implementing those approaches, we noticed that they increased the

[4] Our analog card (model NI PXI 6713) can produce a DC signal between −10 V and +10 V with a 12-bit (= 4.9 mV) resolution, which was equivalent to 2.5 mW of optical power for our ODT1.

electronic noise and didn't increase the evaporation efficiency for low optical power. We thus set a second PID and an additional photodiode in parallel. This parallel regulation system also has its own dedicated analog channel. The first PID and first photodiode, would be used for regulating and ramping the ODT1 for high power (down to roughly 500 mW, which is well above the resolution limit of the first photodiode) while the second photodiode (with a higher gain) and the additional PID would regulate the ODT1 for optical power below 500 mW. An analog IC switch handles the alternation between both PID controller.

3.2.3 Loading of the optical dipole trap

As described in sec. 2.10, after the MW evaporation, the atoms are transferred into an optical dipole trap. During this first step of evaporation in the quadrupole trap, the ODT1 is already switched on to full power [5] and the total potential is equal to $U_{\text{tot}}(\mathbf{r}) = U_{\text{mag}}(\mathbf{r}) + U_{\text{dip}}(\mathbf{r}) + mgz$, where $U_{\text{mag}}(\mathbf{r})$ and $U_{\text{dip}}(\mathbf{r})$ represent the quadrupole potential and the optical trap as defined in equation 2.1 and 3.5 while mgz denotes the gravitational potential. The center of the ODT1 is located approximately two waists ω_0 (80 µm) below the center of the quadrupole trap to avoid enhancing Majoranana losses during the MW evaporation by accumulating atoms in the central region (which would occur if the center of the two traps coincided). To this end, after reaching the end of the MW evaporation the steepness of the quadrupole confinement is adiabatically reduced from 250 G.cm^{-1} to 5.1 G.cm^{-1} in 800 ms. Two pairs (along x and z) and one single coil (along y) are used to prevent the center of the magnetic field to move during the quadrupole trap opening by compensating any ambient parasitic field. The levitation threshold of ^{40}K to compensate gravity being equal to 7.1 G.cm^{-1} (respectively 9.1 G.cm^{-1} and 12.8 G.cm^{-1}) for atoms in the $|9/2,9/2\rangle$ Zeeman sublevel (respectively $|9/2,7/2\rangle$ and $|9/2,5/2\rangle$), the atoms will progressively leave the magnetic quadrupole and accumulate into the ODT1. The efficiency of the loading into the dipole trap is an intricated problem that depends on a correct mode matching between the two traps volume and the collisions between particles. A detailed analysis of the loading is provided in both [128] and [77]. Experimentally, we managed to load around 25 % – 30 % of the atoms which corresponds to typically 10^7 atoms. After loading the ODT1, we wait 50 ms for the atoms to thermalize and to settle completely into the ODT1 before performing any optical evaporation. The equilibrium temperature of 30 µK gives us a high initial ratio trap depth over temperature $\eta = U_{\text{dip}}(0)/k_B T = 11.5$.

[5] While the atoms are too hot to notice the presence of the optical potential during the early stage of the MW evaporation, switching on the dipole as soon as possible during the sequence and not right after the end of the MW evaporation increases its power stability.

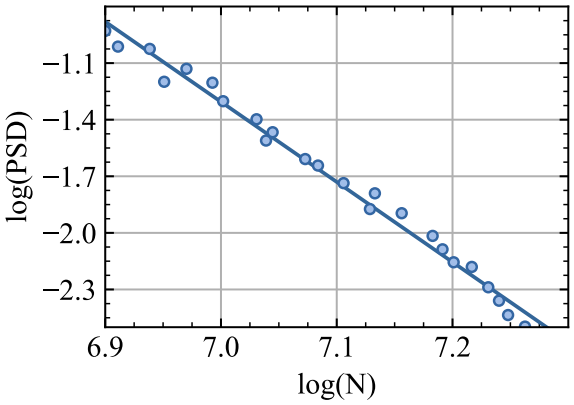

Fig. 3.6 **Efficiency of the optical evaporation**. After the loading of the main dipole trap, the trap depth is progressively lowered from $k_B \times 350\,\mu K$ to $k_B \times 45\,\mu K$ in 4 s to enhance the evaporation of the atomic mixture of $m_F = 9/2, 7/2, 5/2$. The efficiency of the first optical evaporation $\alpha = 3.67$ is much greater than the previous MW evaporation but is reduced at the end of evaporation due to the low collision rate (the atomic density being reduced during evaporation, the collision rate keeps decreasing as well). Data adapted from [79].

3.3 Optical evaporation in a single ODT

The first stage of optical evaporation is performed in the single ODT with a mixture of ^{40}K in the positive states ($|9/2,9/2\rangle$, $|9/2,7/2\rangle$ and $|9/2,5/2\rangle$) with a large majority ($\geq 80\,\%$) of the atoms in the two most energetic Zeeman sublevel. Prior to evaporation, the role of the inner and outer pairs of coils are flipped: the outer coils are used to create a magnetic gradient of $5.1\,\mathrm{G.cm^{-1}}$ while the inner coils, previously employed to generate the strong quadrupole field during the MW evaporation, now generate a bias field of 3.0 G. This allow us to make use of the high stability of High Finesse for the generation of our bias field. While such stability isn't necessary for low magnetic field, it is crucial at high magnetic field when one wants to explore properties of a Fermi gas at unitarity. This small bias field is sufficient to maintain the quantization axis and is small enough to avoid both the d-wave Feshbach resonance between $|9/2,9/2\rangle$ and $|9/2,7/2\rangle$ located around 8.0 G and the strong inelastic losses occurring from 15 G [6]. At this bias field, due to the absence of resonances between the various states, the interaction strength is set by the s-wave singlet and triplet scattering length: $a_s = 104.41 a_0$ and $a_t = 169.67 a_0$ [129] (more precisely, for a mixture of $|m_F = 9/2\rangle$ and $|m_F = 7/2\rangle$, collisions are completely dominated by the triplet channel [84]), where $a_0 \simeq 0.53\,\mathrm{nm}$ is the Bohr radius. To enhance the evaporation, the trap depth is exponentially lowered in 4 s from $k_B \times 350\mu K$ to $k_B \times 45\mu K$ (which corresponds to an optical power of 0.8 W on the atoms). Prior to evaporation, the magnetic gradient is also marginally increased to $6.2\,\mathrm{G.cm^{-1}}$, thus providing an additional confinement in the axial direction with an angular frequency $\omega_{mag} = \mu b / 4 m z_0$ (where μ denotes the magnetic moment of an atom in a given Zeeman sublevel and $z_0 = 80\,\mu\mathrm{m}$ represents the distance between the atom and the magnetic center). At the end of evaporation, one is

[6] Experimentally, we noticed losses of 25 % of our atomic sample after 4 s of waitime of 15 G while the lifetime in the dipole trap exceeds 180 s at 3 G.

left with typically 2.0×10^6 atoms at a temperature of $4.0\,\mu$K, increasing the PSD by nearly two order of magnitude over the course of the evaporation (in an harmonical trap, the PSD scales as NT^{-3}). At this stage of evaporation, the spin composition, obtained thanks to a Stern-Gerlach imaging, is $55\,\%\,|9/2,9/2\rangle$, $33\,\%\,|9/2,7/2\rangle$ and $12\,\%\,|9/2,5/2\rangle$ and our atoms in the $|9/2,9/2\rangle$ sublevel are degenerate with a temperature $T=0.7\,T_{\mathrm{F}}=4.0\,\mu$K. T_{F} denotes the Fermi temperature. For a sample of N_α atoms in a given spin state $|\alpha\rangle$, confined in an harmonic trap of mean trapping frequency $\overline{\omega}=(\omega_x\omega_y\omega_z)^{1/3}$, it is given by $\mathrm{k_B}T_{\mathrm{F}}=(6N_\alpha)^{1/3}\hbar\overline{\omega}$[7]. The figure 3.6 and [79] depict the efficiency of the optical evaporation in the ODT1, which is much greater than the efficiency in the quadrupole trap ($\alpha_{\mathrm{ODT}}=3.67>\alpha_{\mathrm{MW}}=1.49$). At this stage, the trap depth of ODT2 is enough to provide a meaningful additional confinement. As a consequence, we load a cross optical dipole trap, thus increasing the spatial density. Collision rate is further increased by transferring the atoms to the lowest Zeeman states to make use of the s-wave Feshbach resonance between the two lowest Zeeman states.

3.4 Landau-Zener transfer to the negative states

In order to enhance our optical evaporation efficiency, we would like to transfer the atoms into the negative Zeeman states of the $\mathrm{F}=9/2$ manifold. Due to the selection rules, one cannot easily use electric dipole transitions to transfer the atoms in a given manifold F to a targeted states inside the same manifold thanks to a laser light [8]. Nonetheless, one can use magnetic dipole transitions. The strength of magnetic dipole transitions are typically several orders of magnitude smaller than their electric counterparts (by a ratio $(2/\alpha)^2\simeq10^5$, with α being the fine structure constant) [130] and yield different selection rules. While electric dipole transition can only couple states of different parity ($\Delta L=\pm1$), magnetic dipole transitions only have a non-vanishing matrix element between two states of the same parity ($\Delta L=0$) and with the same principal quantum number n. Moreover, when considering the total electronic angular momentum, the selection rules follow: $\Delta\mathrm{J}=0,\pm1$ (except for a transition from $\mathrm{J}=0$ to $\mathrm{J}=0$) and $\Delta m_{\mathrm{J}}=0,\pm1$.

Transfer from a Zeeman state $|g\rangle$ to a neighboring state $|e\rangle$ using magnetic dipole transition can be achieved by applying a π-pulse: a resonant MW pulse(for targeted states in different

[7] However, evaporative cooling in the single ODT can still be carried on by further lowering the trap depth. Unfortunately, contrary to the MW evaporation, the collision rate is not constant during an optical evaporation due to the confinement being reduced alongside the trap depth ($\omega_{\perp,\parallel}\propto\sqrt{I_{\mathrm{L}}}$). The low density in the single ODT (resulting from the weak axial confinement) combined to the rather small scattering length prevent an efficient evaporation for temperature below $1.0\,\mu$K. Depending on the initial condition, one can at best reach in our single ODT 10^6 atoms at a temperature of $0.8\,\mu\mathrm{K}=0.5T_{\mathrm{F}}$.

[8] While this is true for one-photon transitions, one could think of implementing two lasers and drive raman transitions to circumvent this issue.

hyperfine manifolds, but with the same principal quantum number) or RF pulse (for targeted states inside the same manifold) radiated onto the atoms for a duration $t = \pi/\Omega$, with Ω being the Rabi frequency. π-pulses require a very stable magnetic field for the splitting between the two states to be constant both during the entire duration of the pulse and from an experimental sequence to the next. A possible way to circumvent potential issues arising from magnetic field fluctuations is to perform a so called Landau-Zener adiabatic passage between the two states [131–133].

Following the approach developed in [134], we represent an atom as a two level system $\{|g\rangle, |e\rangle\}$. In presence of a external field, the new eigenstates $|+\rangle$ and $|-\rangle$ of the coupled atom-field Hamiltonian are given by:

$$|+\rangle = \sin\theta|g\rangle + \cos\theta|e\rangle$$

and

$$|-\rangle = \cos\theta|g\rangle - \sin\theta|e\rangle$$

where θ represents the Stückelberg angle which, for a detuning Δ from the addressed transition, is defined as $\tan 2\theta = -\Omega/\Delta$. The adiabatic passage is made possible by the coupling to the field which causes an avoided crossing between the eigenergies of the coupled Hamiltonian [134]. If the chirp is started far below the resonance ($\Delta \ll -\Omega$), the phase angle $\theta \approx 0$ and $|-\rangle \approx |g\rangle$. As the detuning is slowly increased from $\Delta \ll -\Omega$ to $\Delta \gg \Omega$, the atom adiabatically follow and remains in $|-\rangle$. Once the sweep ends far above resonance, $\Delta \gg \Omega$, the phase angle increases to $\theta \approx \pi/2$ and thus, $|-\rangle \approx |e\rangle$. As a consequence, the coupling between the atoms and the electromagnetic radiation allows one to adiabatically exchange the entire population from the state $|g\rangle$ and $|e\rangle$. On the other hand, when the chirp is infinitely fast, the atoms will not tunnel through the avoided crossing and thus remain in their initial state. The Landau-Zener formula expresses the probability for an atom to follow the dressed state and successfully being transferred from a given state to another:

$$P_{\text{trans}} = 1 - \exp\left(-\frac{\pi\Omega^2}{2\,|\,\partial_t\Delta\,|}\right). \tag{3.6}$$

The advantage of Landau-Zener adiabatic passage lies in the possibility to start and end the sweep far away from resonance, thus making the chirp range much larger than any magnetic field fluctuation. Moreover, due to the very long lifetime of magnetic dipole transitions, one can safely neglect the spontaneous decay of the state $|e\rangle$ even for very long sweep. For the ^{40}K, due to the richer structure of the F = 9/2 hyperfine manifold, 10 Zeeman sublevels need to be considered and the derivation of the transition probability is more complex than for the

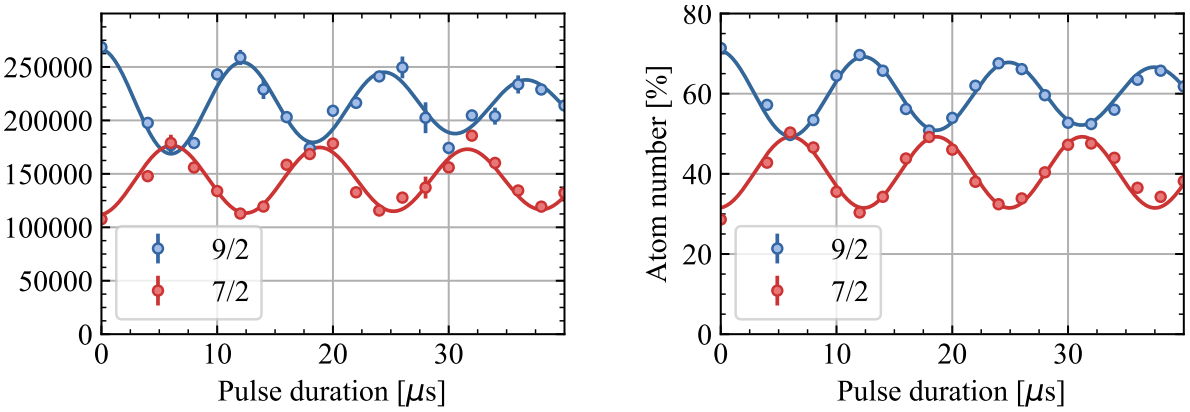

Fig. 3.7 **Rabi oscillations at 60.2 G**. Measurement of the Rabi frequency for the bare atom numbers (a) and the corresponding normalized population (b). The Rabi frequency can then be used to characterize the efficiency of the Landau-Zener adiabatic passage. The best fit is obtained for $\Omega_{\text{Rabi}} = 2\pi \times 79.7 \pm 0.5\,\text{kHz}$. The low contrast is due to the difference of detectivity of the two spin states.

two-level system. Still, in order to estimate the transfer efficiency, one can numerically solve the Hamiltonian H_{tot} describing the system [9] and compute its eigenstates to ensure that the targeted crossing are indeed avoided. Finally, one can also estimate the Rabi frequency of a transition thanks to the Landau-Zener formula [79].

Experimentally, we perform the Landau-Zener passage after 4 s of evaporative cooling in the ODT1. At the end of the evaporation, due to their reduced kinetic energy the atoms are naturally loaded into the cross dipole trap formed by the ODT1 and ODT2. Thanks to the additional confinement provided by the ODT2, the spatial density is sufficiently high to allow high evaporation rate. As a consequence, we switch off the gradient created by the outer coils as well as all magnetic fields apart from the bias field of 3 G generated by the inner coils. The current circulating through the inner coils is provided by the highly stable High Finesse. After increasing the magnetic bias field to 60.2 G we perform the Landau-Zener sweep using the antenna RFA (see sec. 3.1). The optimized response of the antenna for RF signal leads to a maximum Rabi frequency of 80 kHz (see fig. 3.7). In order to transfer the $|9/2, 9/2\rangle$ and $|9/2, 7/2\rangle$ to their negative counterpart $|9/2, -9/2\rangle$ and $|9/2, -7/2\rangle$, we need to cover all resonances transition from the $|9/2, 9/2\rangle$ to $|9/2, 7/2\rangle$ transition (with a transition resonance frequency of 21.2 MHz) all the way to the transfer of $|9/2, -7/2\rangle$ into $|9/2, -9/2\rangle$ (with a resonance frequency of 16.8 MHz). To that end, we generate a RF sweep from 22 MHz to

[9] The total Hamiltonian is composed of the Zeeman Hamiltonian, as represented in figure 2.11, the RF field energy shift which is equal to $-\hbar\omega_{\text{RF}} m_{\text{F}}$ for an atom in a given m_{F} Zeeman sublevels of the $F = 9/2$ manifold and the atom field coupling characterized by the Rabi frequency Ω.

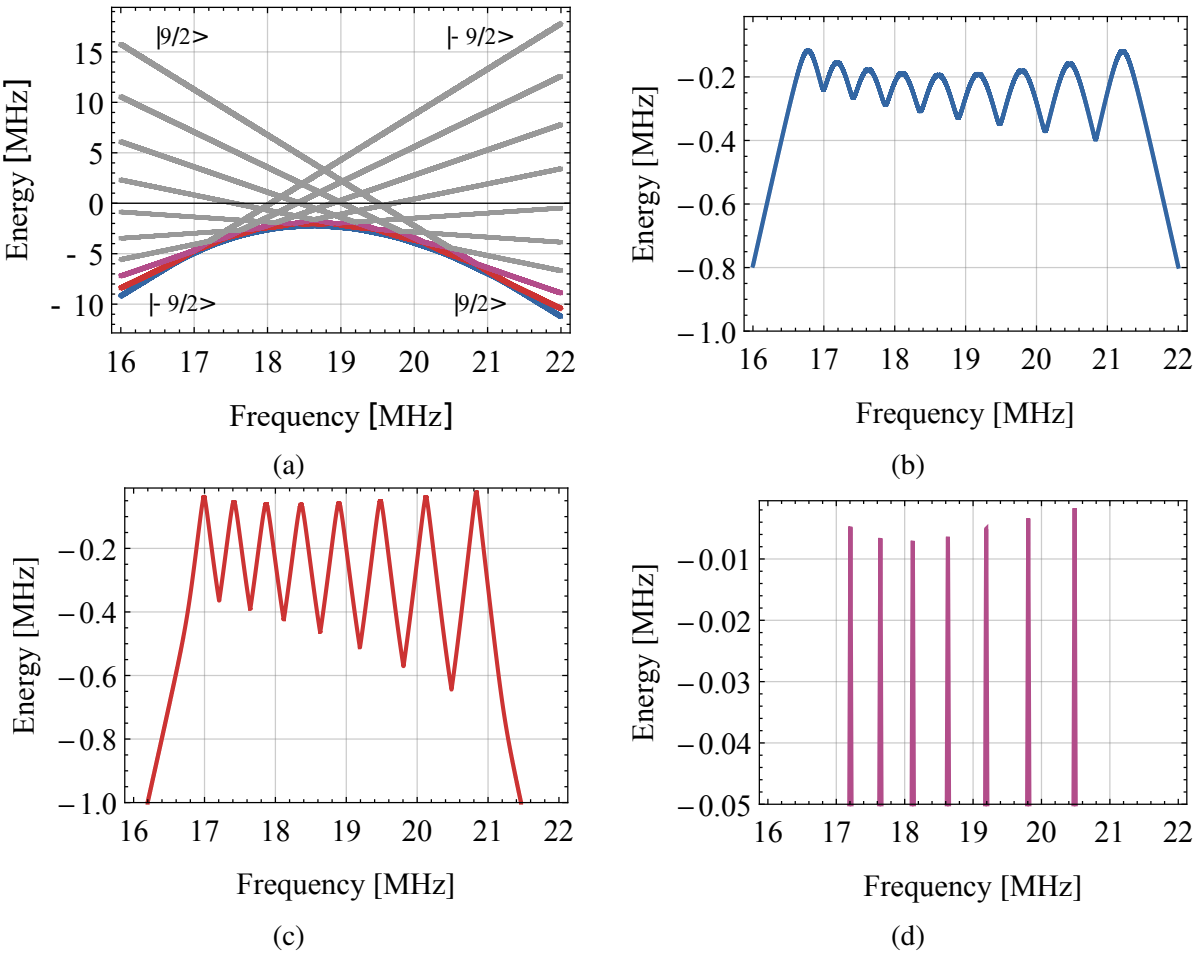

Fig. 3.8 **Landau Zener adiabatic passage to the negative states at** 60.2 **G**. (a) Eigenergies of the 10 RF-dressed states of the F= 9/2 manifold. (b), (c), (d) Evolution of the splitting between the eigenergies of the RF-dressed states adiabatically connected to $|9/2,9/2\rangle$ (and $|9/2,-9/2\rangle$) and $|9/2,7/2\rangle$ (b), $|9/2,7/2\rangle$ and $|9/2,5/2\rangle$ (c) and $|9/2,5/2\rangle$ and $|9/2,3/2\rangle$ (d). While the efficiency of one adiabatic passage is $P_{\text{trans}} \geq 99\,\%$ for both $m_{\text{F}} = 9/2$ and $m_{\text{F}} = 7/2$, it drops to typically 53 % for $m_{\text{F}} = 5/2$ because of the reduced splitting $\Omega_{5/2} \sim 5\,\text{kHz}$. Thus, only an insignificant fraction of $m_{\text{F}} = 5/2$ is transferred to its negative counterpart.

16 MHz in 20 ms.
Thanks to the magnetic field being sufficiently large, the difference between two successive resonant frequencies is larger than the Rabi frequency. The complete adiabatic passage from $|9/2,9/2\rangle$ to $|9/2,-9/2\rangle$ can thus be reduced to 9 independent passages $|9/2\rangle \rightarrow |7/2\rangle \rightarrow ... \rightarrow |-9/2\rangle$. Each transition can then be estimated using eq. 3.6. However, the typical splitting between two eigenenergies of the dressed states doesn't correspond to the Rabi frequency anymore and needs to be numerically computed. To this end, we diagonalized the Hamiltonian of the system H_{tot} and computed both its eigenenergies and eigenstates for our Rabi frequency of $2\pi \times 80\,\text{kHz}$ (see fig. 3.8a). By looking at the splitting between the two states adiabatically connected to $m_F = 9/2$ and $m_F = 7/2$ for an infinitely large positive detuning, one can see that the typical energy splitting $\Omega_{9/2} \simeq 2\pi \times 120\,\text{kHz}$ (as illustrated in fig. 3.8b). Using the eq. 3.6, this splitting leads to a transfer efficiency of more than 99 % after one passage. For $m_F = 7/2$, the typical splitting $\Omega_{7/2} \simeq 2\pi \times 40\,\text{kHz}$ (see fig. 3.8c) also allows a transfer of more than 99 % after one passage. On the other hand, for $m_F = 5/2$, due to the reduced splitting of $\Omega_{5/2} \simeq 2\pi \times 4\,\text{kHz}$, the transfer efficiency after one of our sweep drops to roughly 53 % (see fig. 3.8d). As a consequence, while the entire population of $m_F = 9/2$ and $m_F = 7/2$ gets transferred to their negative counterpart, atoms initially $m_F = 5/2$ gets diluted into most of the $F = 9/2$ manifold.
After the Landau-Zener transfer we perform an additional incomplete Landau-Zener (by shining a RF sweep from 16.3 MHz to 14.9 MHz in 1 ms) passage at the same bias field $B = 60.2\,\text{G}$ to create a 50:50 mixture of both spin state enhancing the evaporation (for temperature below 20 µK, p-wave interactions are deeply suppressed and only s-wave collisions between different spin states subsist [84]).

3.5 cODT and evaporation to degeneracy

Following the incomplete Landau-Zener passage we obtain a balanced gas of ^{40}K in the $|9/2,-9/2\rangle$ and $|9/2,-7/2\rangle$ Zeeman sublevels in a crossed dipole trap. As previously mentioned, the cross dipole trap is naturally populated during the evaporation in the ODT1 by keeping the ODT2 at full power during the optical evaporation (the atoms being initially too hot to significantly populate the cross region). By doing so, at the end of the first evaporation, we manage to transfer 50 % of the remaining atoms into the cODT, which corresponds to roughly 10^6 atoms at a temperature of 4 µK. The additional confinement is provided by the ODT2, a 110 µm waist dipole trap with a maximum trap depth of 19 µK (3.0 W) crossing the ODT1 under an angle of 138 °. As previously mentioned, the polarization of the ODT2 is orthogonal to the ODT1's and their respective wavelength detuned by 160 MHz to avoid interferences between the two dipole traps. Consequently, the resulting potential is simply the sum of the two separate

confinements $U_{\text{cross}}(\mathbf{r}) = U_{\text{ODT1}}(\mathbf{r}) + U_{\text{ODT2}}(\mathbf{r})$ while the corresponding measured trapping frequencies ($\omega_{x,y,z}$) along the three directions x, y, z of the experiment (see sec. 3.1) are thus given by:

$$\begin{aligned}
\omega_x^2 &= \sin^2\alpha\left(\omega_{\perp,1}^2 + \omega_{\perp,2}^2\right) + \cos^2\alpha\left(\omega_{\parallel,1}^2 + \omega_{\parallel,2}^2\right),\\
\omega_y^2 &= \cos^2\alpha\left(\omega_{\perp,1}^2 + \omega_{\perp,2}^2\right) + \sin^2\alpha\left(\omega_{\parallel,1}^2 + \omega_{\parallel,2}^2\right),\\
\omega_z^2 &= \omega_{\perp,1}^2 + \omega_{\perp,2}^2,
\end{aligned}$$

with $\alpha = (\pi - 138^\circ)/2 = 21^\circ$ being the angle between the x-axis and the ODT1 [10].
Prior to evaporating in the cODT, the magnetic field is raised in 100 ms from 60.2 G to 238 G in order to jump to the attractive side of the s-wave Feshbach resonance between the $m_F = -9/2$ and $m_F = -7/2$ located at 202.1 G while avoiding the p-wave Feshbach resonance between atoms in the $m_F = -7/2$ state located at 198.8 G [129]. This magnetic field corresponds to a scattering length of $+136\,a_0$. To increase the interaction, once on the positive side of the Feshbach resonance, the magnetic field is decreased to 205 G, generating attractive interactions between the two spin states with an interaction strength of $-294.0\,a_0$. The atomic cloud is then evaporated for 10 s by ramping down both ODTs to a trap depth of 3.6 µK (resp. 15 µK) for the ODT1 (resp. ODT2). At the end of evaporation, we obtain typically a cold sample of 1.5×10^5 atoms per spin state at a temperature of $T = 0.35 T_{\text{F,harm}} = 300$ nK. Finally, to reach the deeply degenerate regime, the scattering length is further enhanced to $-4834\,a_0$ by decreasing the bias field to 202.4 G. After 1 s of evaporation of this bias field we manage to get around 1.5×10^4 (from 1.0×10^4 up to 2.5×10^4) atoms per spin state at $0.14\,T/T_{\text{F,harm}}$. Imaging of the atomic cloud is then performed by ramping the magnetic field to the zero crossing (at 209.9 G) of the Feshbach-resonance to switch off any interaction between atoms and perform spin selective imaging. The successive steps to reach degeneracy are summarized and presented in figure 3.9 as well as [74].

3.6 Spin selective imaging at high magnetic field

In order to only detect the atoms in a given spin states several methods exist. At low field magnetic field, one can perform a Stern-Gerlach imaging or transfer the atoms in the targeted Zeeman sublevel into the other ground state manifold, thanks to a MW-pulse, and estimate the missing population. Both techniques present severe drawbacks [11]. Consequently, since the last

[10] Details concerning the measurement of the cODT trapping frequencies can be found in Appendix A and in [74].

[11] In a Stern-Gerlach imaging, one relies on the thermal expansion of the clouds to be smaller than the acceleration gained from the magnetic field gradient to spatially separate atoms in different Zeeman state. As a

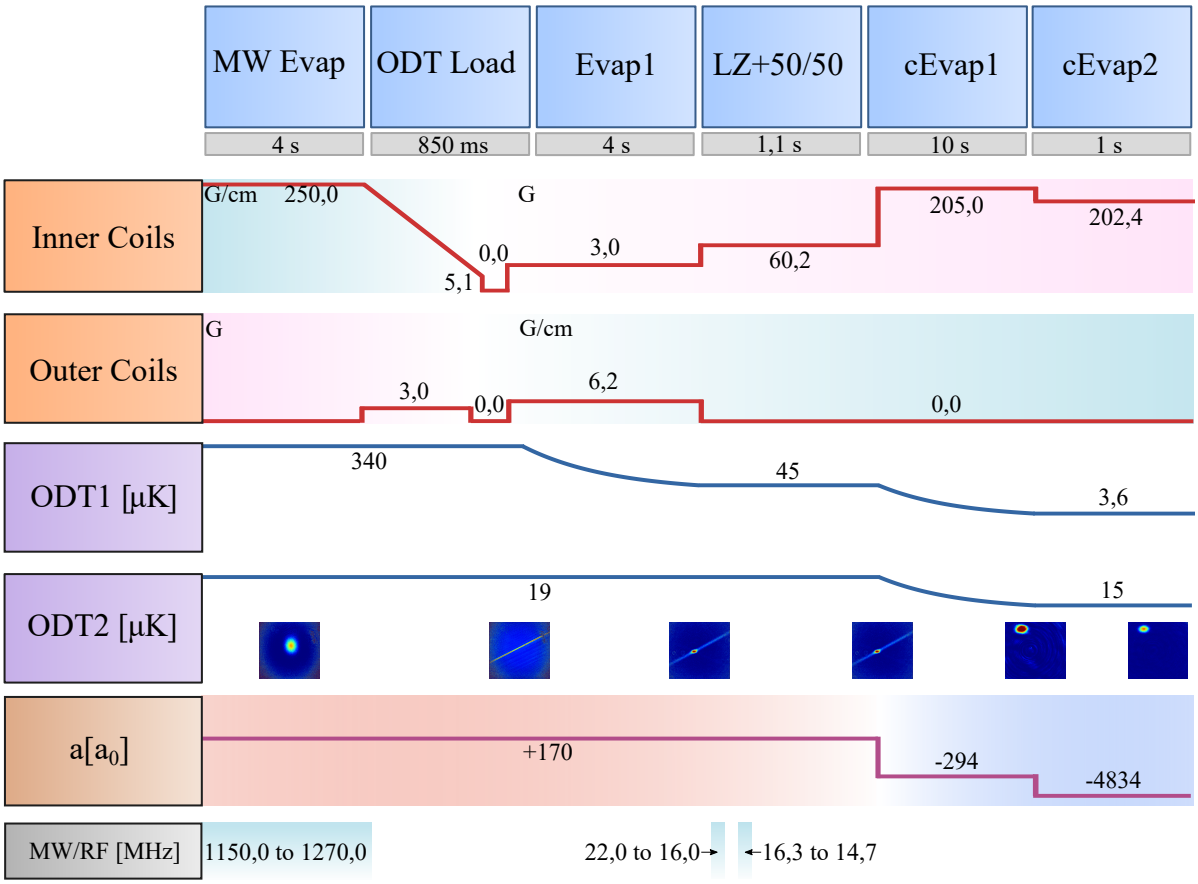

Fig. 3.9 **Summary of the key step of our sequence to generate a deeply degenerate atomic cloud**.

stage of evaporation 3.5 as well as the lattice loading 6.1 are performed at high magnetic field, we simply image the atomic cloud close to the Feshbach resonance, more precisely at the zero crossing (at 209.9 G) to cancel the interactions between the atoms.

At high magnetic field, the splitting between the different Zeeman sublevels is sufficiently large with respect to the natural linewidth of the D2- and D1-line to only resonantly image one spin state. In the limit case, called the Paschen-Back regime (when $B \gg a_{\mathrm{hf}}/\mu_{\mathrm{B}}$), the base $\{|\mathrm{F}, \mathrm{m_F}\rangle\}$ doesn't constitute the natural basis of the Hamiltonian and the good quantum numbers form the basis $\{|\mathrm{m_I}, \mathrm{m_J}\rangle\}$. The three lowest energy level of the ground states are then $|\mathrm{m_I} = -4, \mathrm{m_J} = -1/2\rangle = |1\rangle$, $|\mathrm{m_I} = -3, \mathrm{m_J} = -1/2\rangle = |2\rangle$ and $|\mathrm{m_I} = -2, \mathrm{m_J} = -1/2\rangle = |3\rangle$. Those three states are adiabatically connected to the lowest three Zeeman sublevels (respectively $|9/2, -9/2\rangle$,$|9/2, -7/2\rangle$ and $|9/2, -5/2\rangle$) of the natural basis for low magnetic fields (when

consequence, Stern-Gerlach can only be applied when the atoms are cold enough. Moreover, applying strong currents induces eddy currents that can last up to 10 ms. While MW-pulse imaging can work for any temperature, it requires precise calibration of the different transitions as well as an estimation of the duration of the transfer to not alter the spin composition of the cloud due to spin exchange collisions.

$B \ll a_{\mathrm{hf}}/\mu_{\mathrm{B}}$).

As mentioned earlier 3.1, imaging light polarization is purely $\sigma^{\pm}$ along the z-axis and an equal superposition of σ^{+} and σ^{-} along the $y-$axis. Using the D2-Line, as for low-field imaging, and the selection rules for electronic dipole transition [12] there is only one purely cycling transition at our disposal: $|1\rangle \rightarrow |1'\rangle$, with $|1'\rangle = |\mathrm{m_I} = -4, \mathrm{m_J} = -3/2\rangle$ which is adiabatically connected at low field to the Zeeman state $|\mathrm{F} = 11/2, \mathrm{m_F} = -11/2\rangle$ of the $^4\mathrm{P}_{3/2}$ excited state. This transition being possible using σ^{-} polarized light, the additional transitions for the levels $|2\rangle$ and $|3\rangle$ are $|2\rangle \rightarrow |2'\rangle$ and $|3\rangle \rightarrow |3'\rangle$, with $|2'\rangle = |\mathrm{m_I} = -3, \mathrm{m_J} = -3/2\rangle$ and $|3'\rangle = |\mathrm{m_I} = -2, \mathrm{m_J} = -3/2\rangle$.

In order to know if atoms will also be transferred into other states due to the σ^{+} component of the polarization light, one has to numerically diagonalize the hyperfine Hamiltonian (see appendix A for additional details) to look at both the eigenenergies between the level and its eigenvalues. Figure 3.10 and [74] depict our imaging process. In addition, the eigenvalues quantify how far in the Paschen-Bach regime the groundstate and the excited state are. At 209.9 G, despite the superposition of polarization along the transport direction, one will still only reach the desired targeted states ($|1'\rangle$, $|2'\rangle$ and $|3'\rangle$) thanks to the large energy splitting between the reachable state by using σ^{+} or σ^{-} light [13]. Moreover, by diagonalizing the hyperfine Hamiltonian at the zero crossing, one can decompose its eigenstates in the $\{|\mathrm{m_I}, \mathrm{m_J}\rangle\}$ basis. Looking at the lowest energy levels of both the ground state and the excited state one can find:

$$|1\rangle = |\mathrm{m_I} = -4, \mathrm{m_J} = -1/2\rangle, \tag{3.7}$$

$$|2\rangle = \sqrt{0.946}|\mathrm{m_I} = -3, \mathrm{m_J} = -1/2\rangle + \sqrt{0.054}|\mathrm{m_I} = -4, \mathrm{m_J} = +1/2\rangle, \tag{3.8}$$

$$|3\rangle = \sqrt{0.886}|\mathrm{m_I} = -2, \mathrm{m_J} = -1/2\rangle + \sqrt{0.114}|\mathrm{m_I} = -3, \mathrm{m_J} = +1/2\rangle \tag{3.9}$$

for the ground state and:

$$|1'\rangle = |\mathrm{m_I} = -4, \mathrm{m_J} = -3/2\rangle, \tag{3.10}$$

$$|2'\rangle = \sqrt{0.998}|\mathrm{m_I} = -3, \mathrm{m_J} = -3/2\rangle + \sqrt{0.002}|\mathrm{m_I} = -4, \mathrm{m_J} = -1/2\rangle, \tag{3.11}$$

$$|3'\rangle = \sqrt{0.996}|\mathrm{m_I} = -2, \mathrm{m_J} = -3/2\rangle + \sqrt{0.004}|\mathrm{m_I} = -3, \mathrm{m_J} = -1/2\rangle \tag{3.12}$$

for the excited one. Few remarks emerged from this spin decomposition. The first one is that the

[12] $\Delta J = 0, \pm 1$, $\Delta L = \pm 1$, $\Delta I = 0$, $\Delta \mathrm{m_J} = 0, \pm 1$ and $\Delta \mathrm{m_I} = 0$

[13] For example, for the state $|1\rangle$, one can reach $|1'\rangle$ (resp. $|19'\rangle$=$|\mathrm{m_I} = -4, \mathrm{m_J} = +1/2\rangle$) thanks to σ^{+} (resp. σ^{-}) polarization. At the zero crossing, the energy difference between the two states is $\Delta E = 813.606\,\mathrm{MHz} \gg \Gamma$. Consequently, while resonant with the $|1\rangle \rightarrow |1'\rangle$ transition, the transition $|1\rangle \rightarrow |19'\rangle$ will be energetically suppressed

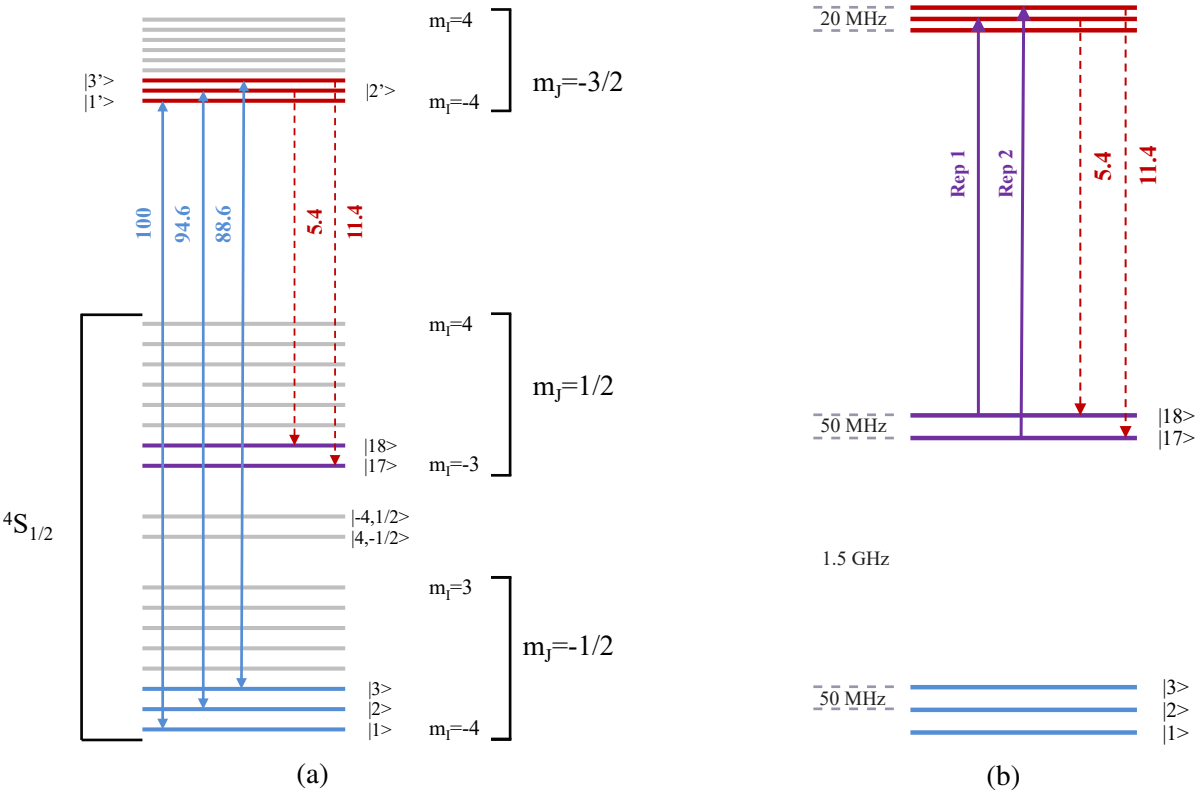

Fig. 3.10 **Principle of our high field imaging**. (a) Imaging transitions for imaging at the zero crossing (209.9 G) . (b) Repumping transitions at the same magnetic bias field to keep atoms into the imaging transition cycle.

excited states are much more in the Paschen-Back regime than the groundstate. Consequently, transitions forbidden in the Paschen-Back regime, such as $|1\rangle \rightarrow |2'\rangle$ and $|2\rangle \rightarrow |3'\rangle$ for instance, are still possible despite the small coupling between those states. Nonetheless, this could lead to incorrect estimation of the population in state $|2\rangle$ and $|3\rangle$ and thus should be avoided. This is made possible thanks to the imaging light polarization that is an equal superposition of σ^+ or σ^- along the $y-$imaging and purely σ^- when imaging along z. π-transitions $|1\rangle \rightarrow |2'\rangle$ and $|2\rangle \rightarrow |3'\rangle$ are consequently both forbidden despite being energetically close to their σcounterpart.

Nonetheless, because the transitions $|2\rangle \rightarrow |2'\rangle$ and $|3\rangle \rightarrow |3'\rangle$ are not closed, one has to look at the spontaneous decay of atoms, once transferred in the excited level. While atoms can obviously decay back to the $|2\rangle$ and $|3\rangle$ sublevel, looking at eq. 3.10 they can also decay to the

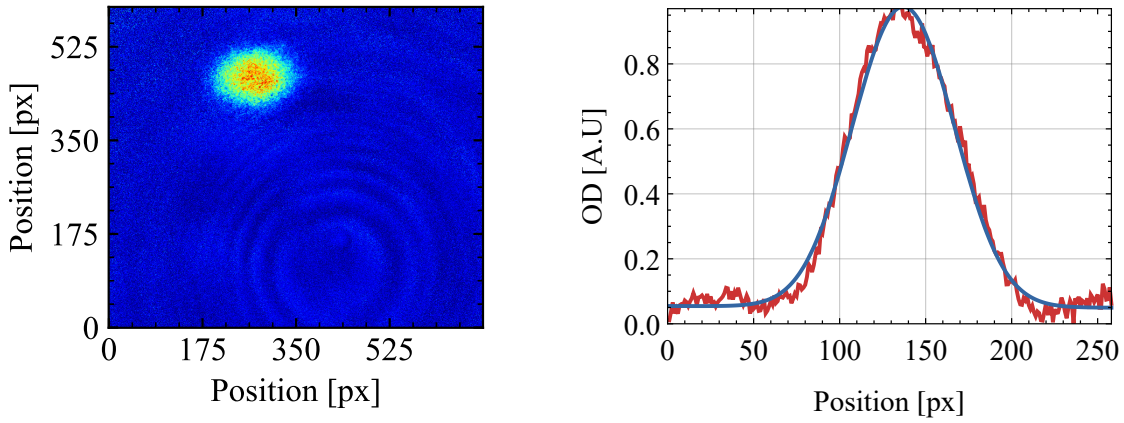

(a) (b)

Fig. 3.11 **integrated density profile of an atomic cloud deeply degenerate**. Typical integrated 2D (a) density profile obtained at the end of the successive evaporation. The cloud shape can be fitted using polylogarithmic function to extract the fugacity Z, directly related to T/T_F [135, 73]. (b) corresponding 1D integrated profile (red point) with the best fit of the 2D-profile (blue line). The best fit yields $T/T_F = 0.14 \pm 0.005$.

states $|18\rangle$ and $|17\rangle$, where:

$$|18\rangle = \sqrt{0.946}|m_I = -4, m_J = 1/2\rangle + \sqrt{0.054}|m_I = -3, m_J = -1/2\rangle, \tag{3.13}$$

$$|17\rangle = \sqrt{0.886}|m_I = -3, m_J = +1/2\rangle + \sqrt{0.114}|m_I = -2, m_J = -1/2\rangle \tag{3.14}$$

After 5 absorption-emission cycles, only 75 % (resp. 55 %) of the atoms initially in $|2\rangle$ (resp. $|3\rangle$) remains in the imaging transition cycle. Consequently, a repumper, transferring the atoms back to the main imaging transitions has to be implemented. The repumping beam, with pure σ^- polarization, is shone onto the atoms along the vertical direction. The concerned transitions are represented in 3.10b.

Using the σ^- transition $|1\rangle \rightarrow |1'\rangle$, we image, at the zero crossing the atomic cloud in the $|1\rangle = |9/2, -9/2\rangle$ states after the second evaporation in the cODT (see sec. 3.5). By sitting at the zero crossing during the ToF and the imaging step, one can suppress the interaction between particles and the atomic cloud can be considered as a ideal Fermi gas. In the degenaracy regime, the density profile can no longer be described using a classical Boltzmann distribution and is replaced by a Fermi-Dirac distribution. As a result, the value of the ratio T/T_F can be extracted from the shape of the atomic cloud. For a non interacting degenerate Fermi gas in 2D, its density profile $n_{2D}(x,y)$ is proportional to $\mathbf{Li_2}\left[-Z\exp\left(-\beta m/2(\omega_x^2 x^2 + \omega_y^2 y^2)\right)\right]$, where $\mathbf{Li_n}$ is the polylogarithmic function of order n. T/T_F is then simply obtained from the fugacity Z

through the relation:

$$T/T_F = [-6\mathbf{Li_3}(-Z)]^{-1/3}. \tag{3.15}$$

The resulting atomic cloud as well as the fitted profile are presented in figure 3.11. As stated before, we typically reach 1.5×10^4 atoms per spin states at a temperature of $T/T_F = 0.14 \pm 0.005$ (the error being induced by the fitting procedure) which is below the typical critical temperature for superfluidity in 3D [41]. As indicated in the following chapter, we are mostly interested in transport phenomena in both three and reduced dimensions in the normal phase. As such, being able to realize a deeply degenerate gas at temperature below the superfluidity critical temperature constitute an ideal starting point for the physics we desire to explore. The following chapters describe transport properties of fermionic mixture in both three and reduced dimensions as well as the implementation of the 2D lattice that we will use to create a deeply degenerate 1D Fermi gas.

Chapter 4

From Landau to Luttinger liquids

As described in chapter 1, strongly correlated Fermi gases are of wide interests and are at heart of many open problems of quantum many body systems. In this context, the Landau-liquid theory [17], model successfully describing the properties at low temperatures of many-body fermions in the normal state even in presence of strong interaction constituted a major breakthrough. However, by reducing the dimensionality of a many-body system, one can drastically modified its properties. For instance, contrary to three dimensional systems, long range order cannot exist in one and two dimensions [63]. In this regard, one dimensional systems represent a very exotic platform and exhibit unique properties compared to interacting particles in higher dimensions. Indeed in one dimension, owing to the predominant role of interactions, paradigms that were applicable for both the description of two and three dimensions systems cease to be valid. A striking example is the breakdown of the Landau liquid theory, which is not applicable in 1D due to a collectivization of the excitations [136] (as illustrated in figure 4.1). Those excitations can be understood and described using the so-called Tomonaga-Luttinger liquid model [136, 137]. While Luttinger liquid theory behaviour has been reported in several physical system such as organic conductors, quantitative comparisons with the theory remains

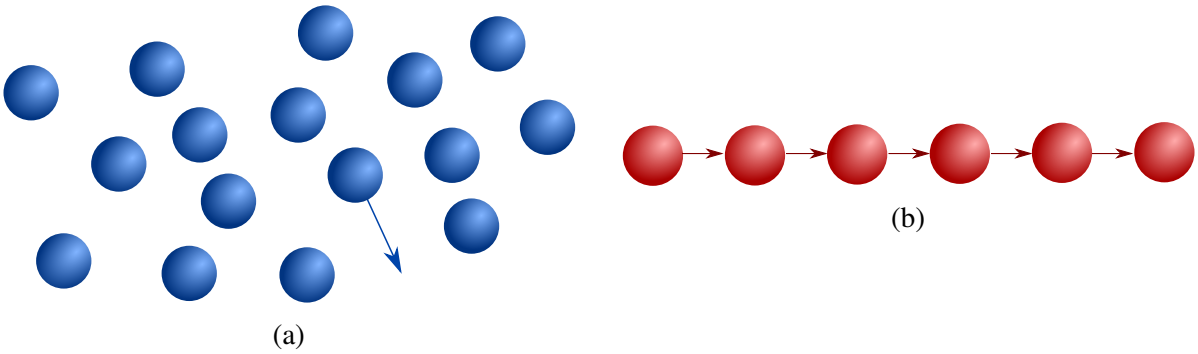

Fig. 4.1 **Difference between one-dimensional system and particles in higher dimensions**. In higher dimensions (a), particle can freely move without interacting with surrounding particles contrary to one dimension (b). Consequently, only collective excitations are possible in one dimension.

challenging due to the screening of the long-ranged Coulomb interactions [138]. Moreover, due to their very 3D nature, beyond Luttinger liquid behaviour, such as phase transition at high temperature are also present in those systems [138].
Cold atoms experiments thus represent an extremely powerful and versatile tool for quantum simulation. By tailoring the trapping potential confining the atoms, one can either study strongly interacting fermions in three dimensions, mimic lower dimension systems or even probe the intriguing dimensional crossover between 1D and 3D. In this chapter, after discussing the mean field phase diagram of an imbalanced Fermi gas as well as the range of application of the Fermi liquid theory in ultracold atoms, properties of Fermi- and Luttinger-Liquids will be summarized. Finally, the influence of dimensionality in spin transport phenomena will be discussed.

4.1 Phase diagram of an imbalanced Fermi gas

The mean-field diagram of a spin balanced Fermi mixture in three dimensions was presented in chapter 1. For temperatures above the critical temperature, the Fermi gas exists in the normal phase and can be described using the Landau liquid theory. For a two-component Fermi gas, by changing the relative population between the two spin states $|\uparrow\rangle$ and $|\downarrow\rangle$, the phase diagram becomes much richer and the normal phase occupies a larger portion of it (as detailed in [139–141]). The phase diagrams of an imbalanced Fermi mixture are represented in the figure 4.2, which is adapted from [139, 51]. For resonant interactions, represented in fig. 4.2b, depending on the temperature, the nature of the normal to superfluid phase transition is modified. For low temperatures and below the tricritical point, in addition to the superfluid and the normal phase, a phase separation region exists and the superfluid to normal phase transition occurs abruptly, which is a signature of a first order phase transition. In this phase separation, the

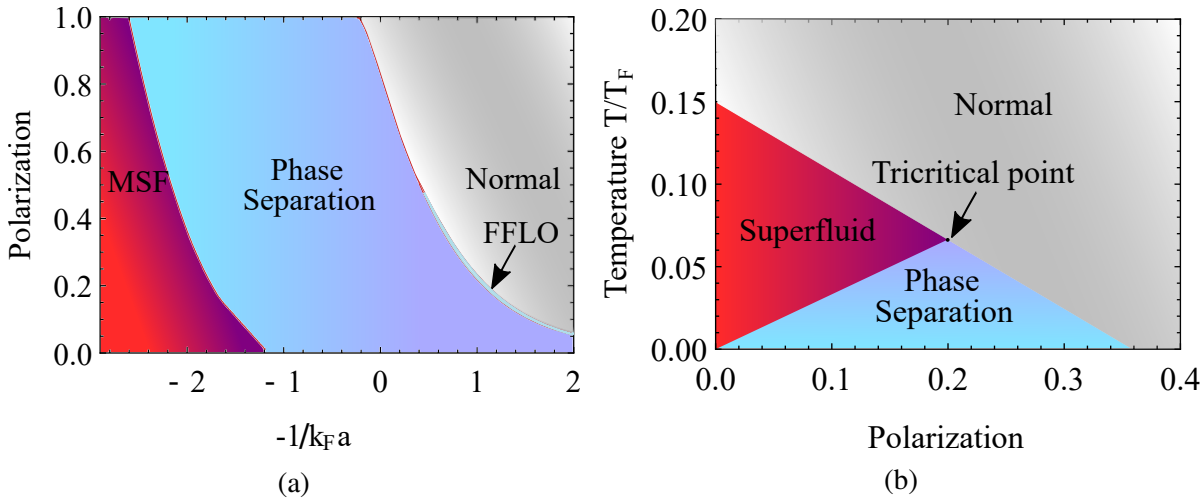

Fig. 4.2 **3D phase diagrams of an imbalanced Fermi gas**. (a) Phase diagram of the ground state of a Fermi mixture as a function of the interaction strength and the population imbalance. Four regime, including the elusive FFLO phase can be identified. Figure adapted from [139]. (b) Phase diagram of a Fermi mixture as a function of the population imbalance and the temperature for resonant interactions. It depicts three different phases including the normal state which can be described using the Landau liquid theory. Figure adapted from [51].

system is unstable which leads to the phase separation between the superfluid pairs and the normal unpaired fermions [51]. At high temperatures, the superfluid to normal phase transition is smooth and of second order. This transition always depends on the polarization $p = \frac{N_\uparrow - N_\downarrow}{N_\uparrow + N_\downarrow}$ and the critical limit is called the Chandrasekhar-Clogston limit [142, 143]. In the BCS limit, it is reached when the pairing gap $\Delta \simeq \sqrt{2}h$, with $2h = \mu_\uparrow - \mu_\downarrow$ being the imbalance between the chemical potentials of the two spin components. Above the CC-limit, the system is in the normal phase and the minority of spins $|\downarrow\rangle$ is immersed in a non interacting gas of spins $|\uparrow\rangle$. The extreme case of a single impurity in the spin state $|\downarrow\rangle$ immersed in the Fermi sea of the spin state $|\uparrow\rangle$ is referred to as the Fermi polaron [45]. Experimentally, even though preparing fermionic mixtures with unequal spin populations is comparatively challenging in condensed matter [1], realization of an imbalanced mixture of fermions is rather straightforward for ultracold atoms. Superfluidity was witnessed below the critical imbalance while above the CC-limit, imbalanced Fermi gas have been reported to behave as a normal Fermi liquid. [144, 51, 145–148].

[1] For example, in superconductors, spin imbalanced can only be induced by applying a external magnetic field. However, due to the Meissner effect, external magnetic fields are expelled from any superconductor in a superconducting state.

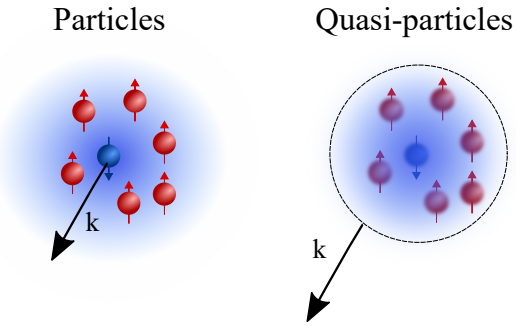

Fig. 4.3 **Fermi liquid description of interacting particles**. After switching on the interactions, an impurity becomes dressed by its interaction with the majority component.The ensemble can be considered as a quasi-particle with a lifetime τ and an effective mass m^*.

4.2 Landau-Fermi liquid theory

Landau's Fermi liquid theory [17–19] describes the properties of a large class of unordered fermionic system at low temperatures (compared to their Fermi temperature) and in the normal state. As such, it can be applied to a large variety of situations such as most normal metals, liquid helium 3 above the superfluid transition or quantum gases. The basic idea of the Fermi liquid theory is that the low-lying states of a non-interacting system can be adiabatically linked to the interacting ones. These interactions conserve the statistics, the spin and the momentum of the non interacting particles as well as their total number. In the non-interacting case, the groundstate of the atomic ensemble is a Fermi sea. This ideal gas is defined by its momentum distribution and all energy states are occupied up to the Fermi energy $E_F = p_F^2/2m$, with $p_F = \hbar k_F$ being the Fermi momentum and m the mass of the fermions. Since all states with a momentum $\mid p \mid \leq p_F$ are occupied, a particle with a momentum p and a spin σ can only be added into one of the excited states of the Fermi sea with a momentum $p > p_F$. However, a particle with a momentum $p \leq p_F$ can be removed from the groundstate, thus creating a hole in the distribution.

After adiabatically increasing the interaction strength, the low-lying excitations with energies close to the Fermi energy [2], can be mapped to the excited states of the non-interacting system. The excited states thus correspond to either quasi-particles with a momentum $p > p_F$ and a spin σ or quasi-holes with a momentum $-p$ and a spin $-\sigma$ if $p \leq p_F$. These quasi-excitations do not correspond to a true eigenstate of the interacting Hamiltonian and thus have a finite lifetime τ. Loosely speaking, the quasi-particles can be seen as a ensemble composed of a particle that is "dressed" by the interaction with the surrounding particles (see figure 4.3). Their lifetime can be estimated using Fermi Golden Rule and is proportional to $1/(p-p_F)^2$. Consequently, the quasi-excitations rapidly decay into a superposition of the eigenstates of the interacting Hamiltonian as soon as they are located away from the Fermi surface but can have a very long lifetime when their energy approaches the Fermi level owing to the Pauli blocking.

[2] The Fermi momentum and the volume of the Fermi surface are not affected by interaction

Furthermore, one can show that for low temperatures, when $k_B T \ll E_F$, $\tau \propto 1/T^2$ [149]. Quasi-excitations can also be characterized by a change of the occupation number $\delta n_{\mathbf{p},\sigma}$, which is equal to +1 for quasi-particles and -1 for quasi-holes. The presence of the quasi-excitations modifies the initial groundstate momentum distribution $n_0(\mathbf{k})$ [3] such that the new distribution is given by $n(\mathbf{k}) = n_0(\mathbf{k}) + \delta n(\mathbf{k})$ in case of a single quasi-excitation. In the limit of few excitations, the change of energy due to the quasi-excitations can be expressed as a power expansion of $\delta n(\mathbf{k})$ [149]:

$$\delta E = \sum_{\mathbf{k}} \varepsilon^0_{\mathbf{k}} \delta n(\mathbf{k}) + \frac{1}{2} \sum_{\mathbf{k},\mathbf{k}'} f(k,k') \delta n(\mathbf{k}) \delta n(\mathbf{k}') + \mathscr{O}(\delta n^3(\mathbf{k})) \tag{4.1}$$

Here the first term represents the energy of a single quasi-excitation and the second term denotes the interaction between two of them. Assuming that their energy are in the vicinity of the Fermi level, one can take the lowest order of the expansion of $\varepsilon^0_{\mathbf{k}}$ in terms of $(k - k_F)$ and obtain [149]:

$$\varepsilon^0_{\mathbf{k}} = \frac{k_F}{m^*}(k - k_F) + \mathscr{O}\left((k - k_F)^2\right) \tag{4.2}$$

where the effect of interactions leads to a renormalized effective mass m^*. The function $f(k,k') = f(\mathbf{k}\sigma, \mathbf{k}'\sigma')$, which represents the interaction between the quasi-excitations is characterized through a set of the so-called Landau parameters $F_L^{s,a}$ [4]. All macroscopic properties of a normal Fermi liquid can be expressed in terms of the Landau parameters. Therefore, both the thermodynamics quantities, such as the compressibility and the spin susceptibility as well as the non-equilibrium properties (the quasi-excitations lifetime and the diffusion constant for instance) of a Landau liquid can be obtained from the Landau parameters. For instance, the spin susceptibility χ is proportional to $k_F m^*/F_0^a$. The effective mass is also related to the Landau parameters through the relation $m^*/m = 1 + F_1^s/3$. Fermi liquid behaviour has been reported in cold atoms experiments and the understanding of its properties still constitutes an on-going topic of research. To that end several techniques, such as measuring the spectral function via momentum-resolved RF spectroscopy [150], can be employed to witness the Fermi liquid behavior of an ultracold Fermi gas. The spectral function $A(k,\omega)$ is related to the single particle Green's function $G(k,\omega)$. For an interacting system, it is defined as:

$$G(k,\omega) = \frac{1}{i\omega - \varepsilon_k^{00} - \Sigma(k,\omega)}.$$

[3] Which for a degenerate Fermi gas corresponds to the Fermi dirac distribution.

[4] F_L^s is related to spin symmetric part of the function $f(\mathbf{k}\sigma, \mathbf{k}'\sigma')$ and F_L^a to the anti-symmetric one.

Here, $\varepsilon_k^{00} = \hbar k^2/2m - \mu$ represents the bare particle energy while $\Sigma(k,\omega)$ is the self-energy correction. For a non-interacting system $\Sigma(k,\omega)$ is equal to zero. The single-particle excitation energy of the system is given by the poles of the Green function [151]. The imaginary part of the Green function is connected to the spectral function through the relation $A(k,\omega) = -1/\pi Im[G(k,\omega)]$. For a non-interacting system, it reduces to $A(k,\omega) = \delta(\omega - \varepsilon_k^{00})$ and the excited state appears as a Dirac peak. For the interacting case, the spectral function takes on the form [149]:

$$A(k,\omega) = -\frac{1}{\pi}\frac{Im[\Sigma(k,\omega)]}{\left(\omega - \varepsilon_k^{00} - Re[\Sigma(k,\omega)]\right)^2 + Im[\Sigma(k,\omega)]^2}.$$

The delta function expected for non-interacting particles is thus replaced by a Lorentzian centered around $\omega = \varepsilon_k^{00} + Re[\Sigma(k,\omega)]$. The imaginary part of $\Sigma(k,\omega)$ can then be associated to the quasi-particle lifetime τ through the relation $Im[\Sigma(k,\omega)] = -1/2\tau$. It confers a finite width and height to $A(k,\omega)$. While well above the Fermi sea, particles can freely scatter, close to it, the available phase space is greatly reduced due to Pauli blocking. Thus close to the Fermi surface, one can have long-lived quasi-excitations.
$Re[\Sigma(k,\omega)]$ alters the dispersion relation of the single particle excitations as per $E(k) = \varepsilon_k^{00} + Re[\Sigma(k,\omega)]$. Moreover, it also defines the spectral weight z_k of the quasi-particle [149]. The spectral function of a Fermi liquid can thus be ultimately written as [149]:

$$A(k,\omega) = \frac{z_k}{\pi}\frac{1/2\tau}{\left(\omega - \varepsilon_k^{00} - Re[\Sigma(k,\omega)]\right)^2 + (1/2\tau)^2} + A_{\text{inc}}(k,\omega). \tag{4.3}$$

$A_{\text{inc}}(k,\omega)$ denotes the incoherent part of the spectral function. It corresponds to a broad featureless spectrum that contains excitations that do not resemble free particle excitations and has a weight $(1 - z_k)$ [149]. The spectral weight z_k therefore indicates the portion of the Fermi liquid that can be considered as free particles despite the presence of interactions. A representation of the spectral function of an ideal Fermi gas and a Fermi liquid is available in figure 4.4.

4.3 Fermi gases in one dimension

By reducing the dimensionality of a system, one can drastically alter its properties due to the increased impact of fluctuations (both quantum and thermal) and correlation between particles [152]. As mentionned earlier, in one dimension only collective excitations exist. The elementary excitations of a Fermi liquid being single particles excitations, quantum gases in one

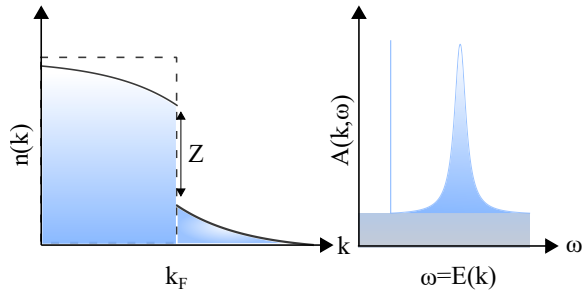

Fig. 4.4 **Momentum distribution and spectral response of an ideal Fermi gas (dashed line on the left figure and Dirac peak on the right one) and a Landau liquid**. The spectral function of a Fermi liquid consists of an incoherent background with a weight $1-z_k$ and the quasi-particle peak with a weightz_k. The width of the peak is proportional to $1/\tau$, with τ being the lifetime of the quasi-particles.

dimension cannot be described using the Landau liquid theory. Thus, one dimensional systems exhibit very unique properties. Extensive theoretical research on 1D systems exist [137, 153–156]. A stricking feature of several one dimensional models, such as the Hubbard or the Lieb-Liniger Hamiltonians is their integrability as oppose to many three-dimensions quantum-field theories that require the use of pertubative methods based on expansions of the coupling constant [5]. As a result,such 1D systems can be solved exactly to obtain quantities such as the groundstate or the energy spectrum. Despite the fact that the experimental realization of a true 1D system is impossible in our 3D world, by confining particles in a highly anisotropic potential one can freeze out motional excitations along two directions and realize an effective quasi-1D confinement. Quasi 1D systems have for example been realized in organic conductors [157], quantum wires [158] as well as spin ladder [159]. In cold atoms, one can produce a 1D gas by confining the atomic cloud in a very elongated trap, in which the transverse trapping frequencies ($\omega_\perp$) vastly exceed the longitudinal one ($\omega_\parallel$) [160, 161]. More precisely, for a degenerate Fermi gas at a temperature $T \ll T_F$, this condition can be translated into the following relation: $k_B T, \mu \ll \hbar\omega_\perp$. In the limit $T = 0$, one then obtains $k_B T_F = N_{|\uparrow\rangle}\hbar\omega_\parallel \ll \hbar\omega_\perp$, with $N_{|\uparrow\rangle}$ denoting the atom number of the majority component of the Fermi gas [162].

4.3.1 Groundstate of a Fermi gas in one dimension

Despite the 1D-like behavior of the system, the physical parameters characterizing the physics can be derived from their 3D-counterparts. Among these, the interparticle interaction strength is of the upmost importance. Assuming a 3D contact interaction, one can describe the low-energy two body scattering in 1D by using an effective interaction potential $V_{1D}(z) = g_{1D}\delta(z)$. The renormalized coupling constant g_{1D} can be expressed as a function of the 3D scattering length a_{3D}:

$$g_{1D} = \frac{2\hbar^2 a_{3D}}{m a_\perp^2} \frac{1}{1 - A a_{3D}/a_\perp}. \tag{4.4}$$

[5] Quantum electrodynamics and quantum chromodynamics being two prominent exampls

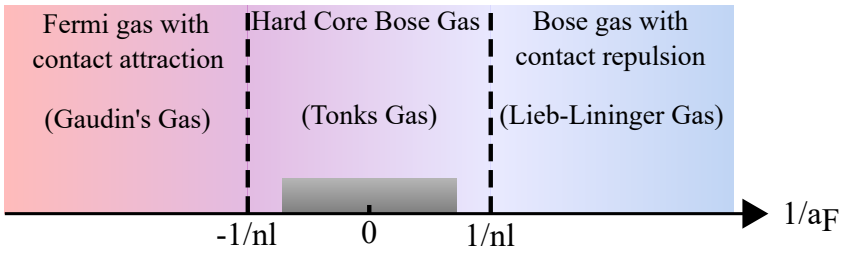

Fig. 4.5 **Phase diagram of a 1D Fermi mixture**. (a) Ground state of a balanced Fermi mixture as a function of the interaction strength. Figure adapted from [173].

Here $a_\perp = \sqrt{\hbar/m\omega_\perp}$ denotes the transverse oscillator length of the highly anisotropic trap and $A = 1.0326$ is a constant. Alternatively, g_{1D} can also be represented as a function of an effective 1D scattering length a_{1D} ($g_{1D} = -2\hbar^2/ma_{1D}$), with

$$a_{1D} = -a_\perp \left(\frac{a_\perp}{a_{3D}} - A \right). \tag{4.5}$$

These results were derived by Olshanii [163] by considering particles in a highly elongated trap and it successfully describes the interaction of two particles in 1D irregardless of their statistics (bosonic of fermionic). For bosons, by tuning the 3D scattering length by means of a Feshbach resonance for instance, one can realize either a quasi-BEC [6] or a Tonks-Girardeau gas when g_{1D} diverges and interactions tower over the kinetic energy [154, 164]. In this strongly interacting regime, bosons act as spinless fermions [165, 166] and mimic the Pauli exclusion principle, causing them to exhibit fermionic properties [167, 168].
For fermions, one can freely tune across the BEC-BCS crossover in 1D for a two component Fermi gas [169–171]. Contrary to the 3D BEC-BCS crossover, in quasi 1D, the underlying 3D physics of the system in addition to the tight transverse confinement allow for the existence of a bound state even when the scattering length is tuned to the negative side of the Feshbach resonance. This peculiar behaviour, known as confinement induced resonances, was observed and characterized near the standard Feshbach resonance of ^{40}K located at 202.1 G [172]. Finally, a natural question arising from the fermionization of bosons concerns the existence of a similar feature for fermions. In one dimension, spin-$\frac{1}{2}$ fermions are described by the Gaudin-Yang model [174, 175], an extension of the Lieb-Liniger Hamiltonian:

$$H_{GY} = \sum_{\sigma=\uparrow,\downarrow} \int_x \Psi^\dagger_\sigma(x) \left(-\frac{\hbar^2}{2m}\partial_x^2 + \mu_\sigma \right) \Psi_\sigma(x) + g_{1D} \int_x \Psi^\dagger_\uparrow(x)\Psi^\dagger_\downarrow(x)\Psi_\downarrow(x)\Psi_\uparrow(x), \tag{4.6}$$

where $\Psi^\dagger_\sigma(x)$ and $\Psi_\sigma(x)$ represent the creation and the annihilation operator of a fermion at the position x and with a spin σ. The chemical potential of each spin state is referred to as μ_σ while

[6] When the kinetic energy dominates the interaction between particles.

g_{1D} characterizes the interaction, which can be either attractive ($g_{1D} < 0$) or repulsive ($g_{1D} > 0$). The model is integrable and solvable for arbitrary population imbalance and interaction strength using the so-called Bethe Ansatz [176, 177].
At zero temperature, the groundstate can be computed and its phase diagram derived [178–180]. A striking feature shown in the figure 4.5 (adapted from [173]), is the existence in 1D of two distinct crossovers instead of the single crossover presents in the three-dimensional case. On the right hand side of the phase diagram, for small repulsive interactions ($1/a_{3D} \ll 1$), the two component Fermi gas forms small size molecules made of atoms with opposite spins, the Fermi mixture thus behaves as a weakly interacting Bose gas and can be described using the Lieb-Liniger Hamiltonian. As the repulsive interaction strength increases, the bosonic molecules undergo a crossover and form a Tonks-Girardeau Gas. While changing the interaction from strongly interacting to strongly attractive, the mixture experiences a crossover similar to the BEC-BCS crossover in 3D, with the Fermi gas forming strongly overlapping pairs on the entire left side of the phase diagram. Moreover, the universal regime, achieved at unitarity for a 3D Fermi mixture, extends on a much broader region of the 1D phase diagram (represented as a shaded region in fig. 4.5).
Similarly to the 3D case, the phase diagram can be enriched by considering a spin imbalanced mixture. Using the Gaudin-Yang Hamiltonian for both zero and finite temperature, the phase diagram can still be exactly computed [181].

4.3.2 Tomonaga Luttinger Liquids

Despite being exact and powerful, the Bethe ansatz approach still cannot be used to describe several physical quantities such as the dynamical correlation functions. One can then resort to the Tomonaga-Luttinger approach that describes the low-energy properties of a gapless one dimensional quantum gas. In the following, we will briefly summarized this approach, which is sometimes called *bosonization* of fermions and described in much more detail in [156, 182].
Another way to represent eq. 4.6 is to use the momentum representation $\Psi_\sigma(x) = 1/\sqrt{N}$ $\sum_k c_k \exp[ikx]$ instead of the field operator one. In this representation, considering a box of size L, the Gaudin-Yang Hamiltonian becomes:

$$H_{GY} = \sum_{k,\sigma} \varepsilon_k c^\dagger_{k,\sigma} c_{k,\sigma} + \frac{g_{1D}}{L} \sum_{k_1,k_2,q} c^\dagger_{k1,\uparrow} c_{k1-q,\uparrow} c^\dagger_{k2,\downarrow} c_{k2+q,\downarrow}, \tag{4.7}$$

where, $\varepsilon_k = \hbar^2 k^2/2m - \mu$ and $\mu = (\mu_\uparrow + \mu_\downarrow)/2$. Contrary to systems in higher dimensions, in 1D the Fermi surface is discrete and solely composed of two points at $\pm\hbar k_F$. Near the Fermi points, one can separate the fermions into left movers with a momentum $\hbar k \approx -\hbar k_F$ and right movers with a momentum $\hbar k \approx +\hbar k_F$. The quadratic dependence of the energy can then be

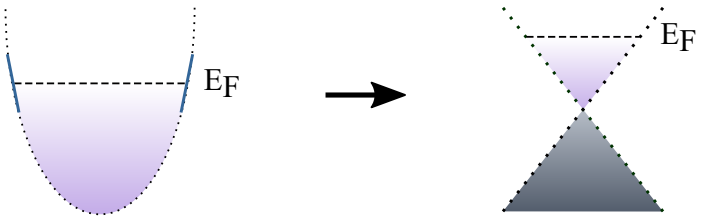

Fig. 4.6 **Single particle energy spectrum**. For fermions confined in an optical potential, the energy spectrum can be derived using the harmonic oscillator approximation and fermions populate energy states up to the Fermi energy. In a region close to the Fermi energy, the quadratic dispersion relation of the particles with an energy between $E_F - \Lambda$ and $E_F + \Lambda$ (Λ being an energy cut-off) can be approximated by a linear one, leading to the energy spectrum of the Tomonaga-Luttinger model(right). In this model, the cut-off is extended to infinity, leading to the addition of an infinite number of negative energy states (grey area) on top of the occupied ones (purple area). To circumvent this issue, all estimated quantities (such as the number of particles) describing the excited states must be normally ordered.

linearized by performing a Taylor expansion up to the first order around $k = \pm k_F$ as represented in fig. 4.6. As a result, the dispersion relation becomes $\varepsilon_{R,k} = v_F \hbar k$ for right movers and $\varepsilon_{L,k} = -v_F \hbar k$ for left movers, with $v_F = \hbar k_F / m$. At zero temperature, all states between those two wavevectors are occupied and one has two branches of particles. By introducing left and right creation and annihilation operators $c^{(\dagger)}_{r,\sigma}(k)$ as well as their respective density operators [7] $\rho_{r,\sigma}(k) = \sum_q c^\dagger_{r,\sigma}(q+k) c_{r,\sigma}(q)$ [8], one can express the Hamiltonian as a function of the density operators. In that representation, the interaction part of the Gaudin-Yang Hamiltonian can be separated into three different sectors. The first sector concerns collisions between fermions on the same side of the Fermi surface and with momentum $k \approx \pm k_F$. The collision can be described as $(k,\sigma;k,-\sigma) \longrightarrow (k,\sigma;k,-\sigma)$ and its renormalized coupling constant is conventionnaly called g_4. The second one, with a coupling constant g_2, concerns fermions on opposite sides of the Fermi surface $(k,\sigma;-k,-\sigma) \longrightarrow (k,\sigma;-k,-\sigma)$. Finally, the backward scattering process corresponds to an exchange of a momentum $\Delta k \approx 2k_F$ $(k,\sigma;-k,-\sigma) \longrightarrow (-k,\sigma;k,-\sigma)$ and its renormalized coupling constant is called g_1 [182].
In the long-wavelength limit, one can introduce the four bosonic fields ϕ_ν and Π_ν [9] ($\nu = s,c$) such that:

$$\rho_{r,\sigma}(x) = \frac{1}{\sqrt{8\pi}} \left[\partial_x \phi_c - a_r \Pi_c + \sigma (\partial_x \phi_s - a_r \Pi_s) \right]. \tag{4.8}$$

Here, $a_{R(L)} = +1(-1)$ and s and c are used for the spin and the charge (i.e the density of fermions) respectively. The four bosonic fields are related to the charge and the spin densities

[7] The density operators additionally follow the bosonic commutation relations [151].
[8] With $r = R, L$ indicating the direction of motion of the fermions.
[9] The fields ϕ_ν and Π_ν are conjugate and satisfy the bosonic commutation relations $[\phi_\nu(x_1), \phi_{\nu'}(x_2)] = [\Pi_\nu(x_1), \Pi_{\nu'}(x_2)] = 0$ and $[\phi_\nu(x_1), \Pi_{\nu'}(x_2)] = \imath \delta_{\nu,\nu'} \delta(x_1 - x_2)$.

$\rho_c = \partial_x\phi_c/\sqrt{\pi}$ and $\rho_s = \partial_x\phi_s/\sqrt{\pi}$ as well as the charge and the spin currents $j_c = -\Pi_c/\sqrt{\pi}$ and $j_s = -\Pi_s/\sqrt{\pi}$. Using the expression of the density 4.8 with the Hamiltonian 4.7, one obtains the bosonized Hamiltonian [182]:

$$H_{LT} = \sum_{\nu=c,s} \frac{u_\nu}{2} \int_x \left(K_\nu \Pi_\nu^2 + \frac{1}{K_\nu} (\partial_x \phi_\nu)^2 \right) + 2g \int_x \cos(\sqrt{8\pi}\phi_s), \tag{4.9}$$

where g is related to the coupling constant g_1 [182]. The coefficients K_ν and u_ν, are called the Luttinger parameters and characterize completely the low energy properties such as the specific heat, the compressibility or the momentum state distribution of a 1D gas. In that regard, they are the equivalent of the Landau parameters of Fermi liquid theory. They are a function of the fermi velocity and the renormalized coupling constants characterizing the various scattering processes [182]:

$$u_\nu = \sqrt{\left(v_F + \frac{g_{4,\nu}}{\pi}\right)^2 - \left(\frac{g_\nu}{2\pi}\right)^2} \quad \text{and} \quad K_\nu = \sqrt{\frac{2\pi v_F + 2g_{4,\nu} + g_\nu}{2\pi v_F + 2g_{4,\nu} - g_\nu}}. \tag{4.10}$$

Here $g_c = g_1 - 2g_2$, $g_s = g_1$, $g_{4,c} = g_4$ and $g_{4,s} = 0$. The u_ν represent the effective propagation speed of the spin or charge wave and the parameters K_ν are connected to the long distance decay of the correlation functions. In the absence of backscattering ($g_1 = 0$) the Hamiltonian 4.9 shows that there is a complete separation between the spin and charge degrees of freedom. Consequently, the eigenmodes are reduced to the pure charge and spin excitations. It prevents any kind of single particle excitation carrying both spin and charge and implies that, contrary to higher dimensions, the only low energy excitations of a 1D quantum gas are collectives. The Luttinger liquid model is therefore a non-interacting field theory and contrary to the Landau liquid model does not describe elementary single particles excitations.

Furthermore, in case of a non-interacting system, both spin and charge velocities are equal ($u_\nu = v_F$) and $K = 1$. As interactions increase, the two velocities differ and the spin-charge separation appears [183–185]. The Tomonaga-Luttinger Hamiltonian can be modified to take into account partial polarization. Imbalance spin population acts as an effective magnetic field, which can be translated into an additional term for the Hamiltonian of the form $H_{mag} = \mathbf{h}/2 \int_x \nabla\phi_s$ that breaks spin-charge separation [182]. Luttinger liquids are sometimes considered as the 1D equivalent of Landau Fermi liquids since it succesfully describes a broad range of one-dimensional systems such as spins, bosons and fermions [186, 187, 69, 188, 189]. In particular, for the BEC-BCS crossover in 1D represented in fig 4.5, Luttinger liquid theory successfully describes the behaviour of both the Gaudin's Gas and the Lieb-Liniger gas. For a Tonks-Girardeau gas, due to the strong interaction, the charge excitation dominates over the spin one. In this regime, one can excite several states of the spin degree of freedom while remaining

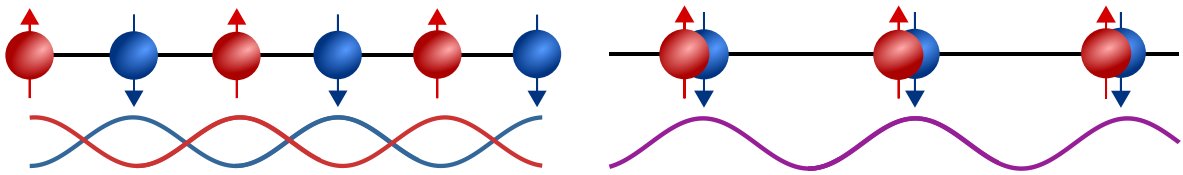

Fig. 4.7 **Collective excitations of a 1D system**. (Left) For a spin density wave (SDW), one has two waves for the spin up and the spin down component. The two waves are shifted with respect to one another and while the spin modulation is maximum the density is uniform. For a charge wave density (CDW), the two waves are synchronized leading to zero modulation of the spin but a modulation of the density.

in the ground state of the charge degree of freedom. Consequently, the Tonks-Girardeau gas is an example of a spin-incoherent Luttinger liquid, whose properties are rather distinct from Luttinger liquids. Nonetheless, properties of a spin-incoherent Luttinger liquid are also a function of the Luttinger parameters [190, 191].

4.4 Transport and spin diffusion in ultracold Fermi gases

The very nature of the normal phase of a Fermi gas in one and three dimensions is very different. In three dimensions, one has single particle excitations and the interaction between particles leads to the formation of polarons, quasi-particles with a finite lifetime and an effective mass. By contrast, in one dimension only collective excitations exist in the form of density and spin-wave. While extensive theoretical study of both limits exist, few experimental results regarding 1D Fermi gas were obtained and the dimensional crossover between these two quantum liquids remains vastly unexplored. So far, investigation of the dimensional crossover was realized by studying the phase separation for a trapped spin-imbalanced Fermi gas in both one and three dimensions [192]. Similarly to the study of the 1D to 3D crossover for bosons [193], the dimensionality was tuned by varying the tunneling between adjacent sites of a 2D optical lattice. Alternatively, one could also invastigate the dimensional crossover by probing the spectral function of the Fermi gas. In 3D, the spectral function of the Fermi liquid presents a well define sharp peak as represented in fig. 4.4. In 1D, a Tomonaga-Luttinger liquid is expected to have a continuum with singularities [151]. In the following, we will describe another method to study the 1D-3D dimensional crossover which is the study of the transport properties of the quantum liquid and more specifically the spin transport.

4.4.1 Towards the perfect fluid

Quantum dynamics of strongly interacting fermions [194–197] is at heart of many field of physics such as the electronic transport in most of modern technology, spintronics and the quark-gluon plasma. The quantitative theoretical description of such systems can be very challenging due to the absence of small parameters. For instance, in 3D at unitarity, it remains uncertain if a deeply degenerate Fermi gas above the critical temperature can be described using Landau-liquid theory. As such, the study of transport properties of ultracold Fermi gases can be used to shed a new light on the non-equilibrium properties of strongly correlated fermions. Kinetic arguments predict an interesting behaviour of several transport properties such as the shear viscosity [10], the diffusivity and the conductivity as these quantities are expected to present a minimum.

More precisely, while bulk viscosity can take any positive value and even reach zero for an ideal monoatomic gas or for a Fermi gas at unitarity [198, 199], shear viscosity seems to be bounded. The constant $\hbar/4\pi k_B$ is assumed to constitute a lower limit for the ratio of shear viscosity and entropy η/s [200]. Discovery of this limit triggered numerous research of a *perfect* fluid that would reach this theoretical value. The quark-gluon plasma is currently the closest to a perfect fluid, with an estimated ratio η/s around $0.4\hbar/k_B$ [201]. For ultracold Fermi gases near Feshbach resonances, a ratio η/s equals to $0.6\hbar/k_B$, close to the quark-gluon plasma was reported [201].

4.4.2 Spin diffusion in a fermionic mixture in 3D

A quantity closely related to the shear viscosity is the diffusion constant D_η. They are linked by the Einstein relation $\eta = \rho D_\eta$, where ρ represents the mass density of the fluid. Diffusion processes (shear, charge diffusion and spin diffusion) in an ultracold atoms were therefore the subject of many experimental research. Similarly to the shear viscosity, the diffusion coefficients are expected to exhibit a quantum limit, bounding their lowest possible value. At unitarity, and in the degenerate regime, the scattering cross section σ is proportional to the Fermi wavevector $\sigma \sim 1/k_F^2$. This implies that the mean free path l_σ evolves like $l_\sigma \sim 1/n\sigma \sim 1/k_F$ with n being the atomic density. Consequently, the diffusion constant $D \sim v l_\sigma$, where v represents the average atomic speed, is bounded by a universal quantum limit of the order of $D \approx \hbar/m$. A less handwaving argument, based on the minimum value $\eta = 0.5\hbar n$ of the shear viscosity in the normal state just above the superfluid transition, provides a quantum limit of the shear diffusion constant of $D_s = 0.5\hbar/m$ [42].

[10] Viscosity is usually separated into two types: the shear viscosity η (related to the Newton's law of viscosity $\tau = \eta \frac{\partial u}{\partial z}$, where τ represents the stress tensor, u the velocity and $\frac{\partial u}{\partial z}$ the shear) and the bulk viscosity κ, that is related to the relaxation dynamics of a fluid after being subjected to a small shearless compression or dilation

Spin transport features several unique properties setting it aside from charge transport. For example, accumulation of spins, contrary to the accumulation of charge does not lead to the induction of a counteracting force [61]. Moreover, while considering fermions, due to collisions between particles with opposite spin, spin current, as opposed to charge current, are supposed to be damped due to the possible non-conservation of the relative momentum. This phenomenon known as spin drag [202] is expected to be enhanced for low dimensions systems [203]. An additional effect arising from collisions between particles of opposite spins is spin diffusion, which can lead to the minimization of the magnetization $\mathbf{M} = M\mathbf{e}$ [11] and the relaxation of the system towards a steady state after being brought out-of-equilibrium. The spin diffusion constant D_s is consequently related to the spin conductivity σ_s through the relation $D_s = \sigma_s/\chi_s$ with χ_s being the equilibrium spin-susceptibility. More precisely, the gradient of the non equilibrium magnetization $\overrightarrow{\nabla}\mathbf{M}$ drives two distinct spin currents. The gradient of magnitude $\mathbf{e}\overrightarrow{\nabla}M$ drives the longitudinal spin current $\overrightarrow{\mathbf{J}}_{\parallel}$ while the gradient along the direction $M\overrightarrow{\nabla}\mathbf{e}$ drives the transverse current $\overrightarrow{\mathbf{J}}_{\perp}$. The longitudinal and transverse spin diffusion coefficients are then related to their respective spin currents by the diffusion equations:

$$\overrightarrow{\mathbf{J}}_{\parallel} = -D_s^{\parallel}\mathbf{e}\overrightarrow{\nabla}M \quad \text{and} \quad \overrightarrow{\mathbf{J}}_{\perp} = -D_s^{\perp}M\overrightarrow{\nabla}\mathbf{e}. \tag{4.11}$$

The loss of magnetization is then given by the spin currents via the relation:

$$\frac{\partial \mathbf{M}}{\partial t} = -\overrightarrow{\nabla}\cdot\overrightarrow{\mathbf{J}_{\text{tot}}} = -\overrightarrow{\nabla}\cdot(\overrightarrow{\mathbf{J}}_{\parallel} + \overrightarrow{\mathbf{J}}_{\perp}). \tag{4.12}$$

Several remarks arise from these relations. First, the longitudinal and the transverse spin diffusion coefficients can differ from one another. In practice, that difference is noticeable for a strongly interacting Fermi system below an specific temperature, called the anisotropy temperature, when Pauli blocking prevents efficient longitudinal diffusion [205]. For a three dimensional Fermi gas at unitarity, the anisotropy temperature T_{ani} is predicted to be $T_{\text{ani}} \sim 0.14\,T_F$ [206]. Second, an additional mode of spin transport caused by the precession of the spin current around the local magnetization was neglected so far. This effect, called the Leggett-Rice effect [207, 208] is of the form $-\mu_{\text{LR}}\overrightarrow{\mathbf{J}}\times\mathbf{M}$, where μ_{LR} is the Leggett-Rice parameter, adds to the total spin current which is then equal to:

$$\overrightarrow{\mathbf{J}_{\text{tot}}} = \overrightarrow{\mathbf{J}}_{\parallel} + \overrightarrow{\mathbf{J}}_{\perp} - \mu_{\text{LR}}\overrightarrow{\mathbf{J}}\times\mathbf{M}.$$

[11] Here and in the following, following convention used in [204], arrows are used to denote spatial vectors while bold fonts represent vectors in spin space.

Consequently, using eq. 4.12, one can determine the value of the diffusion constants from the evolution of the magnetization with respect to time. Experimentally, several groups investigated the evolution of the diffusion coefficient in both two and three dimensions. In three dimensions, the lowest observed longitudinal spin diffusion constant was equal to $D_s^{\parallel} = 6.3\hbar/m$ [12] [60] and an even lower transverse spin diffusion constant $D^{\perp} = 1.1\hbar/m$ [209] was reported, confirming the difference between the two constants in the low temperature regime. A striking similarity between those two components was that not only the minimum of both constants was observed for a similar temperature range ($T/T_F \simeq 0.3-0.4$) but also that their evolution with respect to T/T_F was similar. Several theoretical models were developped to explain the evolution of the spin diffusion constants with respect to temperature such as presented in [206, 210, 211]. In the high temperature regime ($T/T_F \gg 1$) one can consider fermions as standard particles and use the Boltzmann kinetic theory to predict the behavior of both the longitudinal and transverse spin diffusion constant [210, 212]:

$$D_s \propto \left(\frac{T}{T_F}\right)^{d/2}$$

where d is equal to the dimensions of the system. For low temperatures ($T/T_F \ll 1$), fermions cannot be considered as well defined particles and the Boltzmann kinetic theory of the classical gas ceases to be applicable. Consequently, more advanced models such as the Luttinger-Ward theory [211] or the use of Fermi liquid theory to solve the Landau-Boltzmann equation [210]. The diffusion constants can then be expressed as a function of the Landau parameters defined in sec. 4.2. Due to Pauli blocking, the longitudinal spin diffusion diverges as one approaches $T = 0\,\mathrm{K}$. The behavior of the transverse counterpart depends on the polarization of the gas. For a non polarized gas the longitudinal and transverse spin diffusion constant behaviors are identical. However, for a polarized gas, the transverse constant saturates at a finite value, that decreases with increasing polarization [206]. Nevertheless, for a balanced Fermi gas and for $T/T_F \ll 1$, the spin diffusion constants evolve as:

$$D_s \propto \left(\frac{T}{T_F}\right)^{-2}$$

in three dimensions. Experimentally, $D_s^{\parallel}$ and $D_s^{\perp}$ were measured at unitarity for an effective temperature T/T_F respectively between $0.15 < T/T_F < 10$ and $0.15 < T/T_F < 1$ and are in remarkable agreement with predictions from the Luttinger-Ward model [211]. In a similar fashion, the spin drag coefficient [60] as well as the shear viscosity [213] were also measured.

[12] This value was not corrected to take into account the influence of the trapping potential

4.4.3 Spin diffusion of a Fermi gas in reduced dimensions

In two dimensions the evolution of both spin diffusion constants with respect to temperature is to some extend analogous to the results observed in three dimensions. At high temperature, the two constants are similar and evolve like in the 3D case:

$$D_s \propto \left(\frac{T}{T_F}\right).$$

In the low temperature limit and for a balanced Fermi gas, the two spin diffusion coefficients are still functions of the Landau parameters and their scaling is identical to the 3D case [206]:

$$D_s \propto \left(\frac{T}{T_F}\right)^{-2}.$$

In two dimensions the effect of polarization is more pronounced, and one can thus achieve lower transverse diffusion coefficients than in 3D by increasing the polarization [206]. Experimentally, two different groups have measured the transverse diffusion constant so far [61, 214]. Surprisingly, a strong violation of the quantum limit was observed in [61] with a transverse diffusion coefficient $D_s^{\perp} = 6.3 \times 10^{-3}\,\hbar/m$ being reported. This striking result still remains unexplained by theoretical means [206, 215]. Looking at other results, no quantum violation was witnessed in the second experiment where a transverse diffusion coefficient $D_s^{\perp} = 1.7\,\hbar/m$ was observed [214]. Other transport properties such as the bulk viscosity do not display such behavior either as reported in [59] for example. Consequently, it is not sure whether one is actually constraint by the quantum limit in two dimensions remains a open topic. Nevertheless, both experiments witnessed a minimum of the diffusion constant for $\ln(k_F a_{2D}) = 0$, with a_{2D} being the 2D scattering length.

In 1D, transport properties are even more intriguing. To begin with, the notion of shear diffusion does not apply anymore and consequently shear viscosity is absent in one dimension. Moreover, while the bulk viscosity vanishes in three dimensions in the low temperature regime since $\kappa \propto (T/T_F)^2$, the situation differs in one dimension. The theoretical expression of κ in 1D, which is valid for both bosons and fermions has been derived using Luttinger liquid theory and depends on the Luttinger parameters u_ν and K_ν [216]. In the low temperature regime, the bulk viscosity evolves as $\kappa \propto (T/T_F)^{1/2}$ before reaching a minimum non vanishing value at $T = 0$. Contrary to 2D and 3D systems, longitudinal and transverse spin diffusion constants still remain to be measured. For the high temperature regime ($T/T_F \geq 1$), one expects the diffusion coefficients to scale as $D_s \propto (T/T_F)^{1/2}$. In the deeply degenerate regime, when the behavior strongly deviates from a Landau Fermi liquid, the evolution of the diffusion constants remains unknown. Typically, the temperature dependency of transport quantities

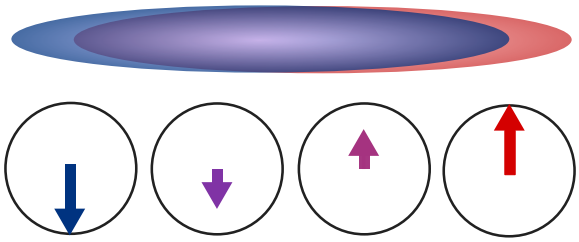

Fig. 4.8 **Experimental measurement technique of the longitudinal magnetization**. Owing to selective spin imaging the longitudinal magnetization can be easily measured.

such as the conductivity are functions of the Luttinger parameters. However, diffusion process are not described by the Luttinger liquid theory. Usually, relaxation processes are mediated by interaction. The Luttinger liquid Hamiltonian being a non interacting field theory do not predict any relaxation and equilibrium mechanics [217]. As a consequence, contrary to the 2D and 3D cases, building a kinetic theory of 1D liquids still remains an open question [217].
Experimentally, using a 2D lattice, we would like to investigate the evolution of the diffusion coefficients in one dimension across the BEC-BCS crossover for a deeply degenerate gas. Once probed, the temperature dependency of the longitudinal and transverse diffusion constant will be looked into. The study of spin diffusion will then be extend to the dimensional crossover between 1D and 3D. Contrary to previous experiments, the crossover will not be achieved by increasing the tunneling energy. Instead, the crossover will be realized by tuning the dimensionality of each lattice site by increasing the potential depth. The tunneling energy will always be suppressed such that the 2D lattice will form an array of independent microtraps. To this end, a 2D optical lattice with a large spacing will be realized. It allows us to freely tune the dimensionality of the system from an array of independent 3D elongated micro traps to 1D tubes when one increases the optical power and thus the confinement. Measurements of the longitudinal diffusion coefficient will be simply achieved by means of spin state selective imaging at the zero crossing of the Feshbach resonance and is represented in figure 4.8, while the transverse diffusion constant will be measured using the spin-echo technique [209]. In the following chapters, the implementation of the optical lattice will be presented in details as well as the description of our new high resolution imaging systems. The loading of the lattice, the measurement of the spacing and the trapping frequencies will also be discussed as well as the progress towards the realization of a deeply degenerate Fermi gas in one dimension.

Chapter 5

Experimental implementation of a 2D lattice

5.1 Neutral atoms in periodic potential

5.1.1 Optical lattices with tunable spacing

As previously discussed, dipole force created by a spatially inhomogeneous light source can be used to confine atoms in the vicinity of its intensity maximum [1]. A first application was introduced in sec 3.2 with the use of Gaussian beams to trap and evaporate to degeneracy our atomic sample of ^{40}K. Additionally, one can also create a periodic optical potential by interfering two beams. A standard way to create such optical lattices, is to retro-reflect a

[1] Or minimum depending on the sign of the detuning.

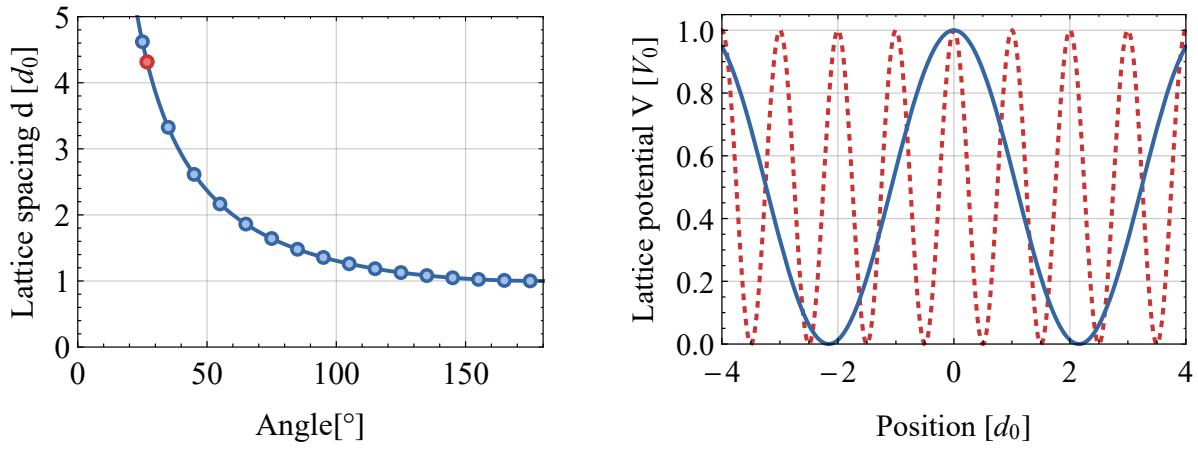

(a) (b)

Fig. 5.1 (a) Evolution of the lattice spacing in unit of $d_0 = 0.532\,\mu$m of as a function of the total crossing angle of the two lattice beams. Our lattice spacing $d_\alpha = 4.32 \times d_0$, for a total angle $\alpha = 26.8^\circ$ is represented in red. (b) Evolution of the normalized lattice potential as a function of the position (in unit of d_0) for a retro-reflected lattice (red dashed line) and for a total angle of $\alpha = 26.8^\circ$ (blue line).

Gaussian beam. The corresponding periodic potential $V_{\text{Latt,1D}}(x,y,z)$ can then be written as:

$$\begin{aligned} V_{\text{Latt,1D}}(x,y,z) &= V_0 \exp\left(-2r^2/\omega^2\right) \sin^2\left(k_\lambda x\right) \\ &= V_0 \left(1 - 2r^2/\omega^2\right) \sin^2(k_\lambda x) \end{aligned}$$

with x being the direction of propagation of both the initial beam and the retro-reflected one, ω denotes their waist, $k_\lambda = 2\pi/\lambda$ the wavenumber associated with the laser wavelength λ and $V_0 = V(0)$ the maximum trap depth of the optical lattice. In case of a retro-reflected beam with an initial trap depth $U_{\text{dip}}(0)$, $V_0 = 4U_{\text{dip}}(0)$, owing to the constructive interference [65]. In this configuration, the lattice spacing is equal to $d_0 = \lambda/2$. Consequently, the spacing cannot be adjusted and will be solely set by the wavelength of the laser. To bypass this issue, let's consider a lattice formed by two beams, defined by their respective wavevector $\mathbf{k_1}$ and $\mathbf{k_2}$, interfering under a total angle $\alpha \leq \pi$:

$$\begin{aligned} \mathbf{k_1} &= k_\lambda \left(\mathbf{e_x} \sin\frac{\alpha}{2} + \mathbf{e_y} \cos\frac{\alpha}{2}\right) \\ \mathbf{k_2} &= k_\lambda \left(-\mathbf{e_x} \sin\frac{\alpha}{2} + \mathbf{e_y} \cos\frac{\alpha}{2}\right). \end{aligned}$$

(a) (b)

Fig. 5.2 **Creation of an optical lattice**. Two counter-propagation beams interfere two create a 1D optical lattice (left). When two pair of beams are used a cubic 2D optical lattice can emerge to create an array of elongated micro traps (right). The lattice spacing in both cases is $d_0 = \lambda/2$, where λ corresponds to the wavelength of the beams.

In the basis $\{\mathbf{x},\mathbf{y},\mathbf{z}\}$, interference will only occur along the x-axis, unique direction where the two projected wavevectors are counter-propagating. The intensity of the two interfering beams along x is thus given by:

$$\begin{aligned} I_\alpha(x) &= 2I_0 |\exp[-i\mathbf{k_1}\cdot\mathbf{r}] + \exp[-i\mathbf{k_2}\cdot\mathbf{r}]|^2 \\ &= 2I_0\,(1+\cos[\Delta\mathbf{k}\cdot\mathbf{r}]) \end{aligned}$$

with $\Delta\mathbf{k}\cdot\mathbf{r} = (\mathbf{k_1}-\mathbf{k_2})\cdot\mathbf{r} = 2k_\lambda \sin\frac{\alpha}{2}x$. The lattice spacing d_α can then easily be obtained from the condition: $\forall x, I_\alpha(x+d_\alpha) = I_\alpha(x)$ as well as the potential $V_\alpha(x)$ that can be derived from $I_\alpha(x)$ as described in sec. 3.2. Using the aforementioned condition, one can find the lattice spacing:

$$d_\alpha = \frac{\pi}{k_\lambda \sin\frac{\alpha}{2}} = d_0 \sin^{-1}\left(\frac{\alpha}{2}\right), \tag{5.1}$$

where d_0 represents the lattice spacing for the retro-reflected lattice ($\alpha = \pi$). For a 1064 nm laser, $d_0 = 0.532\,\mu$m. The evolution of the lattice spacing for different values of α is presented in fig 5.1. By reducing the total angle between the two lattices beams, one can increase significantly the lattice spacing. Experimentally, we chose an angle $\alpha = 26.8°$, yielding a spacing $d_\alpha = 4.32 \times d_0 = 2.30\,\mu$m (see sec. 6.2 for additional details).

5.1.2 Adjusting the dimensionality

Depending on the detuning of the laser with respect to the atomic transition, one can trap the atoms in the minima or maxima of intensity. For a red-detuned laser beam, atoms can be

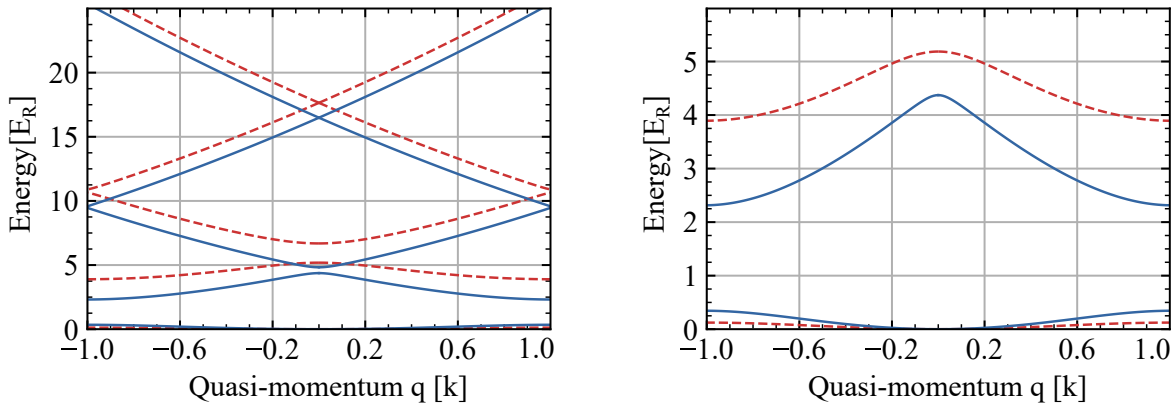

Fig. 5.3 **Bandstructure of an atom in a 1D optical lattice**. (a) Eigenenergies of the first 5 bands as a function of the reduced quasi-momentum q/k for a lattice depth $V(0) = 4.0\,E_R$ (blue line) and $V(0) = 8.0\,E_R$ (red dashed line). (b) Zoom on the first two bands of the plot presented in (a). For low lattice depth, the band gap between the first two bands (n=1 and n=2) is close to $V(0)/2$.

confined at the anti-nodes of the standing wave and their radial profile will have a pancake-like structure (see fig. 5.2a). The trapping frequencies characterizing the confinement can be calculated by computing the Taylor expansion up to the second order of $V_{\mathrm{Latt,1D}}(x,y,z)$ around one of the nodes of the potential. One thus obtains:

$$\hbar\omega_{\alpha,r} = h\sqrt{\frac{2U_{\mathrm{dip}}(0)}{m}}\frac{1}{d_\alpha} = \frac{h^2}{md_0}\sqrt{\frac{U_{\mathrm{dip}}(0)}{E_R}}\frac{1}{d_\alpha} \tag{5.2}$$

for the transverse trapping frequency and

$$\hbar\omega_{\mathrm{Latt},z} = 2\frac{\lambda}{\pi\omega}\sqrt{s}E_R \tag{5.3}$$

along the longitudinal direction. Here, we introduced the recoil energy $E_R = \hbar^2 k_\lambda^2/2m$ and expressed the lattice trap depth in terms of E_R: $V_0 = sE_R$. For ^{40}K and a 1064 nm laser, $E_R = \mathrm{k_B} \times 0.2\,\mu\mathrm{K}$.

Moreover, in presence of the lattice, forbidden energy regions emerge. Those regions give rise to the so called band structure of the energy spectrum. In one dimension, this structure can be derived by using the Bloch's theorem to solve the Matthieu's equation and obtain the eigenstates and the eigenergies of the system [218]. The dispersion relation and the evolution of the energy gap for different lattice depths are given in fig. 5.3. One fundamental energy scale

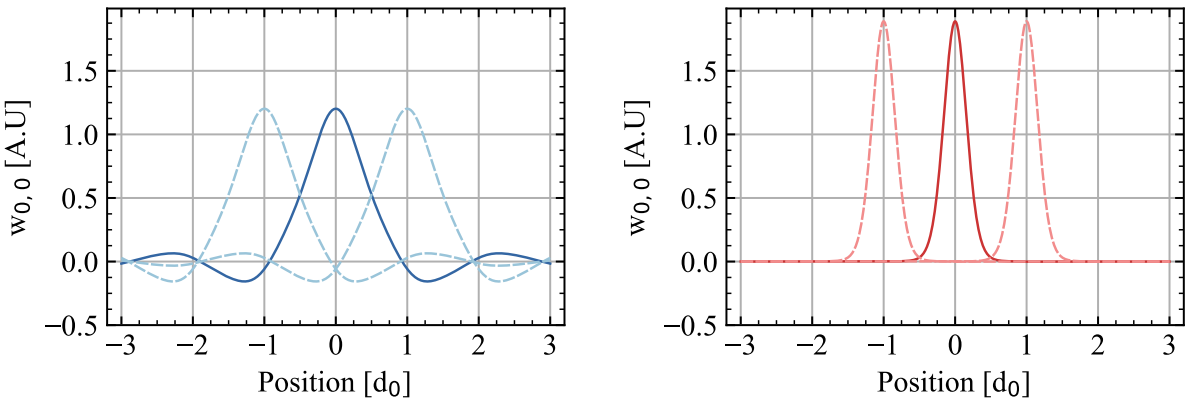

Fig. 5.4 **Representation of the Wannier function for the lowest band and a quasi-momentum** $\hbar q = 0$. (a) Representation of the Wannier function $\omega_{0,0}(x)$ as a function of x/d_0 (blue) as well as $\omega_{0,\pm1}(x)$ (dashed blue) for $V_0 = E_R$. The overlap between the Wannier functions is important. (b) Same as (a) for $V_0 = 20E_R$. The overlap is greatly reduced. When $V_0 \geq 4.0E_R$, the wannier function can be approximated by the wavefunction of an harmonic oscillator with a precision greater than 97 % [220].

emerges from the band structure, the tunneling energy J. It represents the kinetic energy gained by an atom from tunneling between adjacent sites. For a given band n, the amplitude $J_n(j'-j)$ to hop from the node located at the position $d \times j$ to the node $d \times j'$ of the lattice is defined as [219]:

$$J_n(j'-j) = \int \omega^*_{n,j'}(x)\widehat{H}\omega_{n,j}(x)\mathrm{d}x$$

with $\widehat{H} = \frac{\widehat{p}^2}{2m} + \widehat{V}(x)$ being the Hamiltonian of the system. The functions $\omega_{n,j}$ are the so-called Wannier function, a set of orthonormal functions localized around the local minima of the lattice. In the absence of any periodic potential, the Wannier function is proportional to a Sinc function while for deep lattice, $V_0 \gg E_R$ [2]and each lattice site can be seen as an individual harmonic trap. In this configuration, the Wannier functions can be thus approximated by the Hermite polynoms [220] and the function $\omega_{0,0}(x) \propto \exp(-x^2/2\sigma^2)$. As an illustration, the Wannier functions $\omega_{0,0}(x)$ for few lattice depths are represented in figure 5.4. Each amplitude $J_n(j'-j)$ can as well be calculated in terms of the eigenergies of the Hamiltonian $E_n(q)$ [220]:

$$J_n(j'-j) = \frac{d}{2\pi}\int_{-\pi/d}^{+\pi/d} \mathrm{d}q e^{i|j'-j|dq} E_n(q).$$

[2]In practice, when considering the lowest band, the deep lattice approximation is better than 10 % as of $V_0 \geq 15E_R$.

This relation can be inverted to express the eigenergies $E_n(q)$ in a band n and for a given quasi-momentum $\hbar q$ as a sum of the various amplitude $J_n(j'-j)$:

$$E_n(q) = \sum_{|j'-j|\in\mathbb{Z}} J_n(j'-j)e^{-\imath|j'-j|dq} = 2\sum_{|j'-j|=0}^{+\infty} J_n(j'-j)\cos\left(|j'-j|dq\right) \tag{5.4}$$

In the tight binding limit (when only the tunneling between nearest neighbor is allowed), we can truncate the equation 5.4 to $|j'-j| \leq 1$. For the first band $n=1$, the amplitude (or tunneling energy) $|J_1(1)| = J$ is consequently directly related to the width of the lowest band by:

$$J = \frac{1}{4}\left[E_1(q=+\pi/d) - E_1(q=0)\right]. \tag{5.5}$$

In addition, still in the tight binding regime, J can also be analytically calculated [221] and one can find:

$$J \propto \exp\left(-2s^{1/2}\right). \tag{5.6}$$

For large values of J, the overlap between the various Wannier function is important. As a consequence, the atoms are delocalized and can tunnel through several lattice sites. On the other hand, when J is small, tunneling is marginal and the dynamics of the atomic cloud is ruled by the on-site interaction and its total kinetic energy.

Higher lattice geometry can be obtained by superimposing at least two lattices. When the frequencies of each 1D lattices are different, the lattice potentials will simply add up independently to form a 2D or a 3D lattice. In particular, when both lattices cross each other under a right angle, atoms will be confined in an array of elongated traps (see fig. 5.2b). For identical trap depth and waist in both directions the radial and axial trapping frequencies are once again given by: $\hbar\omega_{\mathrm{Latt},r} = 2\sqrt{s}E_{\mathrm{R}}$ and $\hbar\omega_{\mathrm{Latt},z} = \sqrt{2}\frac{\lambda}{\pi\omega}\sqrt{s}E_{\mathrm{R}}$. Similarly, the tunneling energy is still proportional to $J \propto \exp\left(-2s^{1/2}\right)$ in the very deep lattice limit.

As such, optical lattices constitute an unique platform to tune the dimensionality of a cold atomic gas. For a 2D lattice, by increasing the trap depth, one can reduce the tunneling energy J (see eq. 5.6), creating an array of independent elongated microtraps. Furthermore, the dimensionality inside each individual tube is set by the transverse energy $\hbar\omega_{\mathrm{Latt},r}$: for an ideal Fermi gas inside a tube, the $\mathrm{N}_{|\uparrow\rangle}$ atoms in the spin state $|\uparrow\rangle$ will populate all the vibrational level up to the Fermi energy $E_{F,|\uparrow\rangle}$. If the first energy level in the transverse direction exceeds the Fermi energy ($E_{F,|\uparrow\rangle} < \hbar\omega_{\mathrm{Latt},r}$), the $\mathrm{N}_{|\uparrow\rangle}$ atoms will then fill the first $\mathrm{N}_{|\uparrow\rangle}$ energy level of the harmonic oscillator in the axial direction while only populating the lowest level in the transverse directions. In that configuration the atoms are effectively confined in a one dimensional trap and will have a Fermi energy $E_{F,|\uparrow\rangle} = \mathrm{N}_{|\uparrow\rangle}\hbar\omega_{\mathrm{Latt},z} < \hbar\omega_{\mathrm{Latt},r}$. By reducing the power, one

can tune the dimensionality inside each single tube from 1D to 3D (by reducing the trapping frequency until reaching a condition where $E_F \sim \hbar\omega_{\text{Latt},r}$ for example). However, owing to the exponential dependency of the tunneling rate with respect to the optical power, by doing so, one will also exponentially increase the tunneling energy. This will eventually lead to interconnection between tubes. In order to be able to treat the microtraps independently, one has to make sure that the tunneling energy is small even when the lattice depth is reduced. This can be achieved by increasing the lattice spacing. In the following, we will calculate the tunneling energy as a function of the total crossing angle α. To this end, we thus consider the 1-D Hamiltonian of the system to determine the band structure:

$$\widehat{H} = \frac{\widehat{p}^2}{2m} + \widehat{V}_\alpha(x)$$

and the associated Schrodinger equation: $\widehat{H}\phi_n(x) = E_{\alpha,n}\phi_n(x)$. As discussed earlier, due to the periodicity of the system ($V(x) = V(x+d_\alpha)$), the eigenfunctions $\phi_n(x)$ must satisfy the Bloch's theorem and can be written as [218]:

$$\phi_n(x) = u_n^q(x)e^{iqx}$$

where, $\hbar q$ is the so-called quasi-momentum (within the first Brillouin zone comprised between $-\hbar k$ and $+\hbar k$ with $k = \pi/d_\alpha$) and the functions $u_n^q(x)$ are d_α-periodic. For a given quasi-momentum $\hbar q$, several solutions, characterized by their band index n exist. One energy band n is thus composed of all the eigenenergies $E_{\alpha,n}(q)$ with the same band index n. The modified Schrodinger equation is obtained by taking into account the form of the eigenfunctions $\phi_n^q(x)$:

$$H_q u_n^q(x) = E_{\alpha,n}(q)u_n^q(x) \quad \text{with} \quad H_q = \frac{\hbar^2}{2m}\left(-\imath\frac{\partial}{\partial x} + q\right)^2 + V_\alpha(x) \tag{5.7}$$

Given the d_α-periodicity of both $u_n^q(x)$ and $V_\alpha(x)$, we can perform a Fourier expansion of both terms:

$$u_n^q(x) = \sum_{\ell\in\mathbb{Z}} a_{l,n}(q)e^{2\imath\pi\ell x/d_\alpha} \quad \text{and} \quad V_\alpha(x) = \sum_{\ell\in\mathbb{Z}} \tilde{V}_l e^{2\imath\pi\ell x/d_\alpha} \tag{5.8}$$

Furthermore, since $V_\alpha(x) = 2U_{\text{dip}}(0)\,[1+\cos(2\pi x/d_\alpha)]$, the only contributing terms of the Fourier expansion of $V_\alpha(x)$ are $\tilde{V}_0 = 2U_{\text{dip}}(0)$ and $\tilde{V}_1 = \tilde{V}_{-1} = U_{\text{dip}}(0)$. The final expression for the system can be ultimately be obtained by injecting the relation 5.8 into the modified Schrodinger equation 5.7:

$$\sum_{i\in\mathbb{Z}} a_{i,n}(q)H_{q,ij} = E_{\alpha,n}(q)a_{j,n}(q) \tag{5.9}$$

with:

$$H_{q,ij} = \begin{cases} 2U_\alpha(0) + \frac{\hbar^2}{2m}\left(\frac{2\imath\pi}{d_\alpha} + q\right)^2 & \text{for} \quad i = j \\ U_\alpha(0) & \text{for} \quad |i-j| = 1 \\ 0 & \text{for} \quad |i-j| > 1. \end{cases}$$

For a given quasi-momentum $\hbar q$, the value of the various $E_{\alpha,n}(q)$ represents the eigenenergies for the band of index n. They (as well as the eigenvectors $a_{i,n}(q)$) can be computed by diagonalizing the Hamiltonian $H_{q,ij}$[3]. The tunneling energy J_α is then obtained from the energy of the lowest band $E_{\alpha,1}(q)$ through the relation:

$$J_\alpha = 1/4\,(E_{\alpha,1}(q = \pm k) - E_{\alpha,1}(q = 0)) \tag{5.10}$$

In order to consider each micro traps as independent, the tunneling energy, which set the dynamics between the microtraps has to be small compared to the kinetic energy of the atoms ($J \ll k_B T$). In the deep lattice limit ($V_0/E_R \gg 1$), the analytical expression of the tunneling is equal to [222] [4]:

$$J = \frac{4}{\pi}(V_0/E_L)^{3/4} E_L \exp\left(-2(V_0/E_L)^{1/2}\right). \tag{5.11}$$

with $E_L = \frac{\hbar^2 k^2}{2m} = \frac{\hbar^2\pi^2}{2md_\alpha^2} = E_R\frac{d_0^2}{d_\alpha^2}$. Consequently one can finally obtain the expression of the tunneling,

$$J = E_R \frac{4}{\pi}\left(\frac{d_0}{d_\alpha}\right)^{1/2}\left(\frac{V_0}{E_R}\right)^{3/4} \exp\left[-2\left(\frac{d_\alpha}{d_0}\right)\left(\frac{V_0}{E_R}\right)^{1/2}\right]. \tag{5.12}$$

Characterizing the tunneling of atoms confined in a periodic potential with the tunneling energy must be done carefully since it has to be compared to the cloud temperature. Another quantity, can also be used to evaluate the tunneling: the effective mass m^*. The effective mass is related to the curvature of the different bands n through the relation:

$$\frac{1}{m^*} = \frac{1}{\hbar^2}\frac{d^2E_n(q)}{dq^2} \tag{5.13}$$

and can either be positive or negative. When the standing wave is switched off the atoms are in free space and, using the dispersion relation $E = \hbar q^2/2m$, one finds that $m^* = m$. In presence of the lattice potential, the lattice energies are defined by eq. 5.4. For the lowest band $n = 1$, in the tight-binding regime, $E_1(q) = 2J\cos(d_\alpha q)$, up to a constant independent of q. By increasing

[3] In practice, to numerically compute the diagonalization, one has to truncate the sum in eq 5.9 for large values of $|i|$. For lattice up to $V_0 = 50E_R$, a precision of the order of 10^{-6} for the lowest band can be obtained by summing on all $|i| \leq 20$ [220].

[4] For large trap depth $V_0/E_R \geq 15$,the accuracy of equation 5.11 [222] is better than 10 %

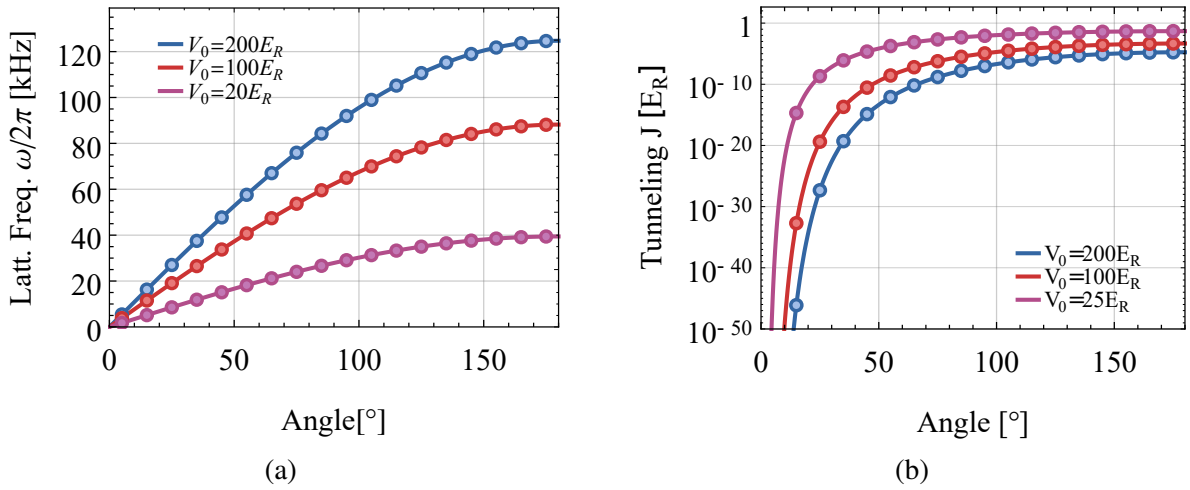

Fig. 5.5 **Evolution of the transverse trapping frequencies and the tunneling energy with respect to the total angle α for various lattice depth**. While frequencies vary slowly with the angle (a), changing the angle from the retro-reflected lattice to 65° reduces the tunneling energy by 5 orders of magnitude. The tunneling energy was calculated using eq. 5.6.

the lattice depth, the dispersion relation will evolve from a free space parabola into a cosine function as can be seen in fig. 5.3. The curvature of the energy band (resp. the effective mass) will consequently becomes flatter (increases) for increasing lattice depth up to 0 (resp. ∞) for infinite depth. In the tight-binding limit, due to the cosine dispersion relation,

$$\frac{1}{m^*} = \frac{1}{\hbar^2}\frac{d^2E_1(q)}{dq^2} = \frac{1}{\hbar^2}\frac{d^2 2J\cos(d_\alpha q)}{dq^2}.$$

Thus, the ratio $|\,m^*\,|\,/m$ can be analytically calculated and for a quasi-momentum $q/\hbar = 0$ or $\pm k$ is equal to:

$$\frac{|\,m^*\,|}{m} = \frac{1}{m}\frac{\hbar^2}{2Jd_\alpha^2}. \tag{5.14}$$

Consequently, one can simply use the tunneling energy or the effective mass to characterize the independence of the different lattice sites.

The evolution of the tunneling rate and the trapping frequencies for various lattice spacing are presented in figure 5.5 and 5.6 as well as in [74]. While for a given value of $s = V_0/E_R$, the dimensionnality inside a tube (governed by the trapping frequencies) scaled as $\propto 1/d_\alpha$ (see eq. 5.2), the tunneling between tubes scaled as $\propto \sqrt{1/d_\alpha}\exp[-2d_\alpha]$ (see eq. 5.12). Due to the two different scalings, one can find an optimal value of α for which in the 1D regime, the trapping frequencies are very high while in the 3D, the tunneling energy will be sufficiently low to have independent tubes. More precisely, for very wide angle ($\alpha \geq 150°$), reaching a regime

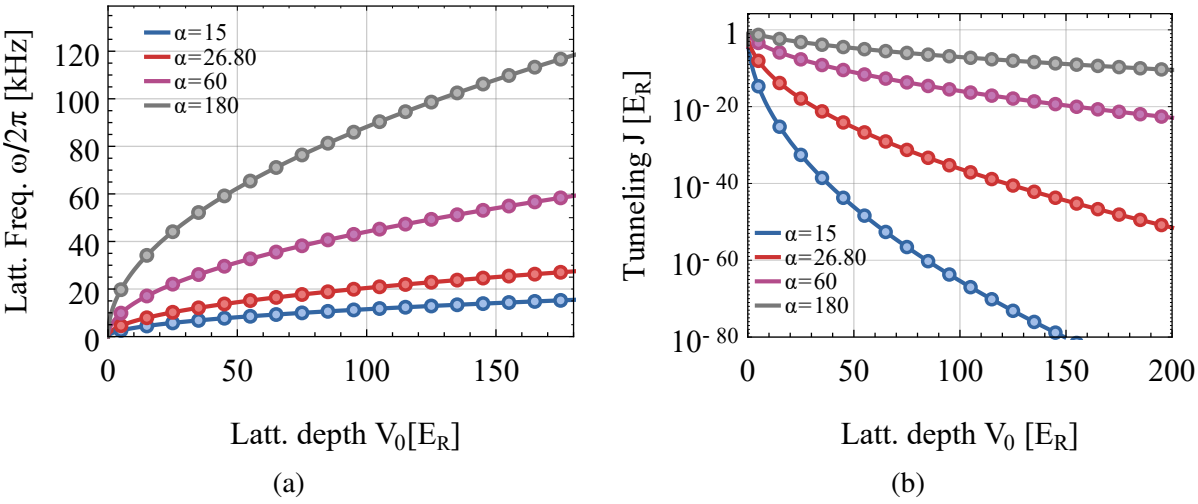

Fig. 5.6 **Evolution of the trapping frequencies and the tunneling energy as a function of the lattice depth in unit of the recoil energy for various crossing angle** α.(a) The tranverse trapping frequencies is reduced by only a factor 4.32 by reducing the angle from $\alpha = \pi$ (retro-reflected lattice in gray line) to $\alpha = 26.8^\circ$ (our experimental total crossing angle in red line). (b) for identical parameter the tunneling energy is decreased by more than 20 orders of magnitude for a lattice depth $V_0 = 50 E_R$. The tunneling energy was calculated using eq. 5.12.

where the micro-traps are always independent can be very challenging since the tunneling energy is of the order of $10^{-2} E_R$ when V_0 drops to few E_R). On the other hand, for small angle $\alpha \leq 20^\circ$, even for very deep lattices $V_0 \sim 150 E_R$, the transverse trapping frequency is only of the order of 15 kHz, which is too marginal to confine atoms in 1D (see sec. 6.6). As a result, we determined that the best condition would be to cross the two lattices beams under a total angle $20^\circ \leq \alpha \leq 30^\circ$.

Experimentally, our final choice for the total crossing angle was 26.8°. In order to be able to study fermions in one dimension, one has to generate a 2D lattice instead of the 1D lattice explored so far. Fortunately, if the polarization of each pairs are orthogonal, this development of a 1D lattice can be easily generalized for a 2D lattice and the resulting potential is the sum of two superimposed 1D lattices. Moreover, even for non orthogonal polarization, as long as the frequency difference of each pair of beam are higher than the laser bandwidth, the cross interference between different pair of lattice beams averages out due to the time phase rotating rapidly [65]. Thanks to our low value of α, we effectively reduced the tunneling rate by typically more than 8 order of magnitude with respect to the retro-reflected case (where $\alpha = \pi$) while only reducing the trapping frequencies by a factor 4.32 (see fig. 5.6). The experimental considerations used to generate the lattice beams are described in the next section.

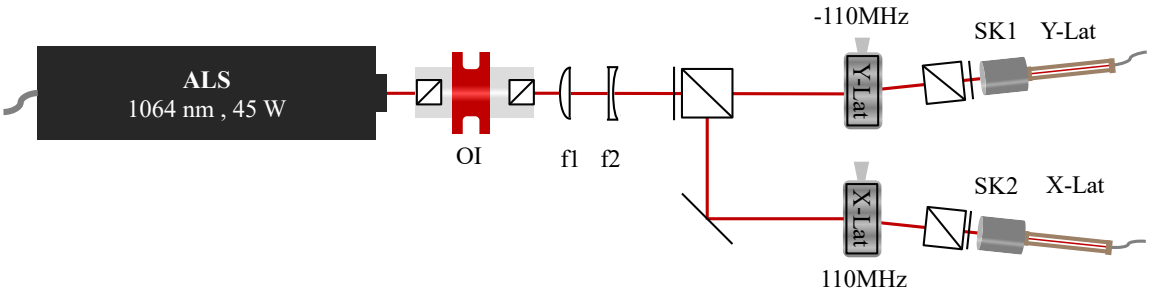

Fig. 5.7 **schematics of the main 2D lattice setup**. The main ALS laser (45 W) is equally splitted using a polarized beam splitter cube after being directed through a telescope used to beam shape the laser beam diameter to maximize the two AOMs diffraction efficiency. After the two AOMs, opposite diffraction orders are used to inject the X- and the Y-lattice optical fibers while their respective zero orders are sent into beam dumps. To prevent any damage due to back reflection, an optical isolator is located right after the laser head. **Optical elements**: Laser: ALS 1064nm fiber laser 45 W output power, O I (Optical isolator): EOT Tech, X-Lat and Y-Lat AOM: 110 MHz, model 3110-197 from Gooch & Housego , SK1/2 (fiber collimator): effective focal length $f = 11$ mm, model 60FC-SMA-T-23-A11-03 from Schäfter-Kirchoff, X-Lat and Y-Lat fibers: large mode area high power fibers, model LMA-PM-15 NKT Photonics.

5.2 Experimental realization of a large spacing optical lattice

In the previous section, we expressed the important physical quantities to characterize the dimensionality of our systems. In the following, we describe the experimental system used to create the tube lattice as well as the imaging apparatus used to observe the 2D lattice.

5.2.1 Laser setup of the 2D optical lattice

The description of the behavior of neutral atoms in an optical lattice developed in sec. 5.1 relies under the assumption that the spatial curvature of the lattice due to the Gaussian's envelope of its two beams can be neglected. The additional potential provided by the curvature is neglected and each micro-trap are identical. Experimentally, this approximation is valid as long as the atomic cloud size is small with respect to the lattice beams waist. Given that the standing wave is loaded from a cross dipole traps created by two beams with a respective waist of 40 µm and 110 µm, we opted for a lattice with a large waist of roughly 210 µm. As a result, high optical power is required to obtain a trap depth around $k_B \times 10\,\mu K$. The figure 5.7 and [74] depict the optical setup used to generate the lattice beams.

The main laser source is a 45 W ultra low noise fiber laser from the company ALS (**A**zur**L**ight **S**ystems) emitting at a wavelength of 1064 nm. After the laser head output, as simple 1:2 telescope is used to both re-collimate and de-magnify the laser beam in order to increase the mode matching with the two following AOMs. Each of the two AOMs (model 3110-197 from

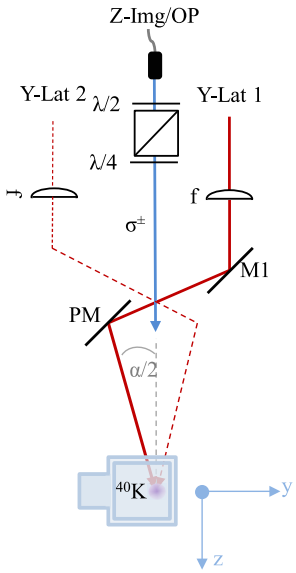

Fig. 5.8 **Schematic of the lattice beam propagation in the vertical direction.**. After the focusing lens, the lattice beams are sent towards the atoms under an angle $\alpha/2$ with respect to the vertical direction thanks to the piezoelectric actuator mirror mount PM. The lattice breadboard is also used to direct the imaging beam as well as the optical pumping at both high and low magnetic field along the vertical direction. Thanks to the last quarter waveplate the polarization of the beam is purely $\sigma^{\pm}$. **Optical elements**: f: focusing lens with a focal length $f = 400\,\text{mm}$ model: VAR2-R1064-PCX-25.4U-400 from Lambda Research Optics, z-img/OP fiber collimator: effective focal length $f = 4.5\,\text{mm}$ from Thorlabs.

Gooch&Housego) are used to generate a different pair of lattice beams (called x-lattice and y-lattice). In order to suppress cross interference between the two standing waves, different orders of diffraction were selected for the two AOMs, providing a 220 MHz detuning. Finally, both diffracted beams are guided towards two large mode area high power fibers (model LMA-PM-15 from NKT-photonics) while the zero orders are directed into two beam dumps. The maximum power at each fiber output is equal to $\sim 16\,\text{W}$. As explained in section 3.2.2, both fibers are terminated with an 5° angle SMA connector, a copper heat sink and are protected by a stainless steel tube. Finally, the output power regulation of both fibers is identical to the one described in fig. 3.5a.

5.2.2 Realization of a 2D optical lattice

Four beams have to be generated to realize a 2D lattice. To this end, the two lasers coming out of the x- and y-lattice fibers are split to create the x- and the y-lattice pair of beams which will be ultimately sent on the atoms. The schematics of the optical setup is presented in figure 5.9 and 5.8 as well as in [74]. Each of the two laser beams are first split in two owing to a high power 50 : 50 beam splitter, thus creating the x- and y-lattice pairs. The two arms of the same lattice have the same power, therefore offering a maximum contrast and trap depth for the lattice potential [5]. Each of these four beams are directed towards a $f = 400\,\text{mm}$ focusing lens, focusing each beams to a waist of roughly $210\,\mu\text{m}$ on the atoms. To route the two pairs of beam on the atoms, the optical setup is mounted on a custom breadboard with an cross-shaped

[5] In a retro-reflected configuration, due to reflections from the glass windows, the retro-reflected beam is weaker than the main beam. In our setup, the 4 % reflection per surface of the science cell would lead to a loss of 15 % of optical power

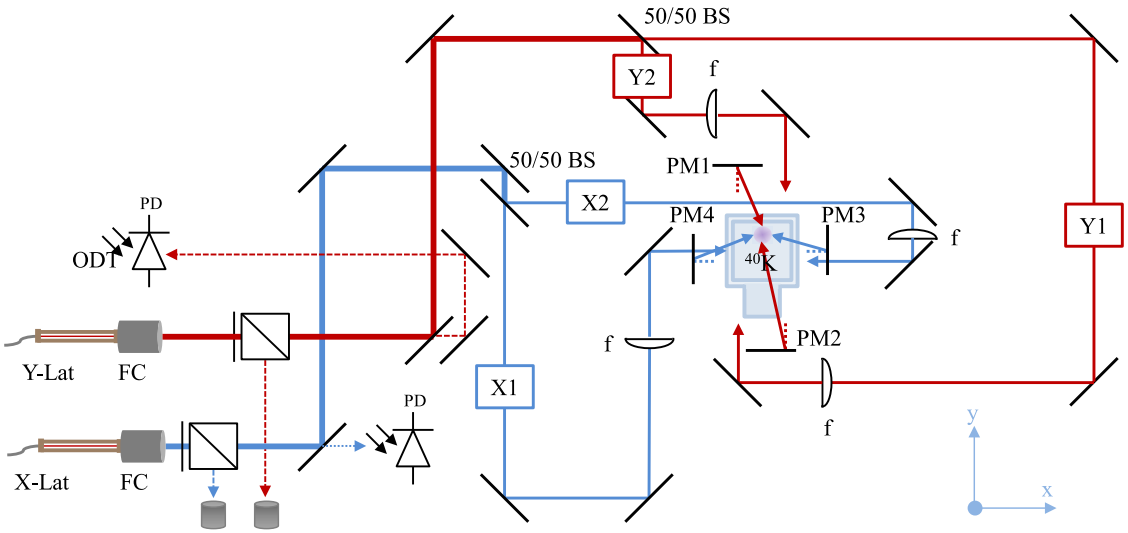

Fig. 5.9 **Top view of the lattice breadboard used to project the 2D lattice onto the atoms**. After the two fibers (X- and Y-Lattice), each beams is split into two thanks to a beam splitter, generating the two pairs of beams necessary to create the 2D optical lattice. Each beams get directed to the focusing lens before being sent downwards on the atoms through a cross-like shape opening. The angle of propagation ($\alpha/2$ with respect to the vertical axis) is tuned thanks to four piezoelectric mirror mounts. **Optical elements** : FC: fiber collimators effective focal length $f = 7.5\,\text{mm}$, model 60FC-SMA-T-23-A7.5-03 from Schäfter-Kirchoff, f: focusing lens with a focal length $f = 400\,\text{mm}$ model VAR2-R1064-PCX-25.4U-400 from Lambda Research Optics, PM1-4: motorized mounts, model: 8816-6 from Newport.

opening at its center and located above the science cell. This opening is used to allow the passage of the four beams from four piezoelectric actuated mirror mounts [6], located after each focusing lens, to the atoms. Each beam having a waist of roughly $210\,\mu\text{m}$ and a maximum power of $8\,\text{W}$ has a maximum individual trap depth of $k_\text{B} \times 14\,\mu\text{K}$. As a result, the maximum depth of each lattice will be equal to $V_0 = k_\text{B} \times 56\,\mu\text{K}$, which is equal to $267\,E_\text{R}$. The angle between two lattice arms is set firstly by the vertical distance between the atoms and the custom breadboard as well as the size of cross-shaped opening [7] and is then tuned by the piezoelectric actuators.

The optimization of the lattice beams position in the $x-y$ plane was made possible using the z-imaging. While a dichroic mirror is used to separate the imaging and the lattice beams, one can still use the remaining transmitted $1064\,\text{nm}$ light to monitor on the pixelfly CCD camera the position of all beams. Ideally, one could rely on the fact that the lattice and the imaging beams should intersect in the imaging focal plane. However, due to the achromatic shift of our

[6] To tune the direction and the angle of each beam.
[7] Which set the minimum horizontal distance between the atoms and the last mirror

homemade objective, the imaging plane for 767 nm and 1064 nm light are shifted and in the imaging plane, the lattice arms do not intersect. Nonetheless the z-imaging camera can still be used to monitor the position of the lattice rays since they are symmetrically distributed with respect both the atoms and the imaging beam once in the imaging plane. The optimization of the lattice position is more precisely described in the following sec. 5.3.

5.3 Visualization of the lattice structure using single site imaging

Owing to the weak tunneling energy of the lattice (see sec. 5.1.2) each microtraps constitute an independent system. As a consequence, in order to observe and measure the evolution of thermodynamics quantities inside each tubes and not probe averaged quantities, site resolved imaging is necessary. In the following section, we will describe the two site resolved imaging systems implemented along the vertical direction (z-axis) and the transport direction (x-axis).

5.3.1 High resolution imaging along the vertical direction

To ensure a weak tunneling energy even for reduced lattice depth, we implemented a 2D lattice with a large spacing $d_\alpha \sim 2.5\,\mu$m characterized by the total angle α between the two beams creating the confining potential. To resolve each tube separately, one has to design an optical system with a sufficient optical resolution. The resolution R of the system is ultimately limited by aberration and diffraction. It can be estimated using the Rayleigh criterion[8] [223] and is related to its angular aperture as well as its numerical aperture $NA = n\sin\theta/2$, with n being the refracted index of the medium between the lens and the object imaged and $\theta = 1.220 * f/D$ the angular resolution of the imaging lens. D denotes its diameter and f its focal length. More precisely, $R = \frac{0.61\lambda}{NA}$, λ representing the wavelength of the imaging beam. As such, a $NA \geq 0.19$ is required to resolve each tube separately with our imaging light of $\lambda = 767\,$nm.
Along the vertical direction, the atoms are located 9.0 mm above the external face of the glass cell. Moreover, due to the 6.5 mm distance between the atoms and the inner side of the glass along the $y-$direction [9], the best achievable resolution along the vertical direction is $R = 0.68\,\mu$m and the corresponding $NA = 0.68$. Therefore, the large spacing also constitutes an important technical advantage. While standard optics with a numerical aperture as high as 0.20 can be easily found, given our technical limitation, we will not be able to resolve a retro-reflected lattice, that requires a $NA \geq 0.88$. Originally, we used a standard aspheric

[8] The Rayleigh criterion considers the resolution of an optical system as the minimal distance R between two point sources of equal intensity I to be able to obtain an intensity dip of at least 26.5 % between them. This criterion is related to the first zero of the Airy pattern, pattern obtain when a point-like source gets transmitted through an optical lens.

[9] which is the shortest distance between the atoms and the inner side of the science cell in the $x-y$ plane

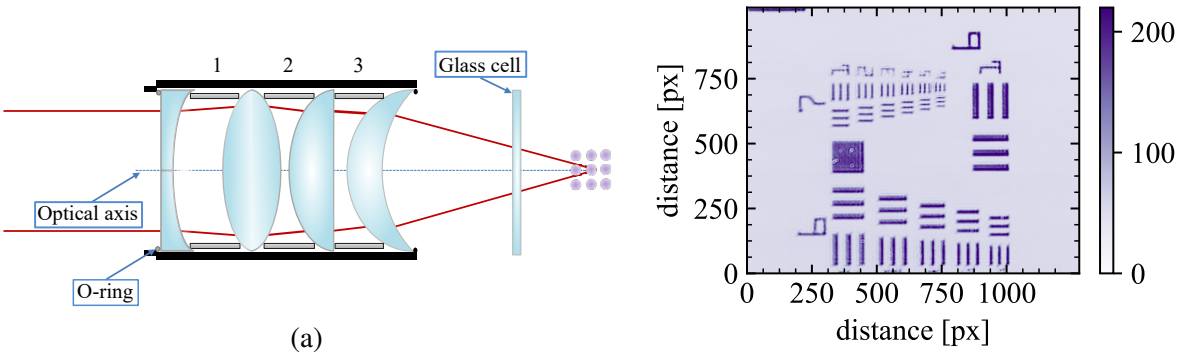

(a) (b)

Fig. 5.10 **Homemade one inch long working distance objective**. (a) Representation of the homemade objective. Spacer rings: 1) 11.00 mm 2) 2.75 mm 3) 2.75 mm. All spacers have a 22.00 mm diameter from Thorlabs and Edmund Optics. **Optical elements** (from left to right): LC4513-B from thorlabs, 100 mm with a VIS-NIR coating from Edmund Optics, LA4725-B and LE4173 from Thorlabs. (b) Using a USAF 1951 resolution target and the Rayleigh criterion we could determine our resolution to be better than the smallest element of the target $R < 2.19\,\mu m$.

lens, a lens of high precision designed to correct the spherical aberrations. With a $NA = 0.39$ and a working distance $WD = 25.67\,mm$, its theoretical resolution was enough to image the tubes while being sufficiently far away from the atoms to not get in contact with the glass cell. Moreover its one inch diameter was small enough to fit inside the bottom coil of the inner coil pair, located 17.5 mm below the atoms (see fig. 3.3). Unfortunately, the alignment of the asphere with respect to the glass cell turned out to be very challenging. A small angle between the asphere and the science cell was enough to deteriorate the resolution signal and we could not achieve satisfactory results.

As a consequence, we decided to build a homemade long working distance objective. While several long working distance homemade objective are available [224–226], most of them are based on an original design from 2002 [227]. Following the design from Wolfgang Alt, we developed a one inch objective (see fig. 5.10) using the software OSLO. It is composed of three standard lenses and a meniscus lens. Using multiple lenses allows us to correct the aberration from one lens with the aberration of the others. The objective is corrected to take into account the astigmatism induced by the 4 mm Vycor glass cell, has a working distance of $WD = 42.1\,mm$, a $NA = 0.24$ and an effective focal length $EFL = 39.6\,mm$. Its diffraction limited spot size is 1.95 µm and its effective depth of field[10] 16 µm. The objective field of view

Surface	Curvature (mm)	Thickness (mm)	Material
1	0	3.50	FS
2	34.50	12.13	Air
3	91.09	3.78	FS
4	-91.09	0.28	Air
5	34.50	4.40	FS
6	0.00	1.73	Air
7	31.00	4.00	FS
8	91.20	33.12	Air
9	0.00	4.00	Vycor
10	0.00	0.00	Air
11	0.00	5.00	

Table 5.1 **One inch long working distance objective prescription**. Lenses from left to right: 1) plano-concave lens $f = -75.0\,\text{mm}$ in fused silica, model LC4513-B from Thorlabs; 2) double convex lens: $f = 100.0\,\text{mm}$ in fused silica, model Fl: 100 mm with a VIS-NIR coating from Edmund Optics; 3) plano-convex lens: $f = 75.0\,\text{mm}$ in fused silica, model LA4725-B from Thorlabs; meniscus lens: $f = 100.0\,\text{mm}$ in fused silica, model LE4173 from Thorlabs. All optical elements are available off-the-shelf.

is $FOV = \pm 200\,\mu\text{m}$[11]. All elements are available off-the-shelf from standard constructors and are detailed in table. 5.1. Each optical element is made of fused silica to limit thermal effects induced by the high power beams of the lattice. Furthermore, except for the meniscus lens, they are also AR coated for both the imaging beam wavelength of 767 nm and the lattice wavelength of 1064 nm. As a result, the uncoated meniscus lens induces a reflection of 4 % of all the beams directed towards the objective. While those reflections can be safely overlooked for the imaging beam, we took a special care to make sure the reflections of the lattice beams, with a power of up to 300 mW were properly dumped.

Once assembled, the objective was tested using a standard 1951 USAF resolution test target (see fig 5.10b). Using the Rayleigh criterion, we determine the resolution to be better than 2.19 µm, which is the width of the last element of the resolution target (group 7 element 6). To be more precise, we also calculated the Modulation Transfer Function (MTF), which is the evolution of the contrast with respect to the spacing between two lines of the resolution target. The figure fig 5.11b presents the MTF of the objective which is in good agreement with the

[10] We define the effective depth of field as the distance along the imaging propagation over which we can resolve two objects separated by our lattice spacing d_α.

[11] We define the field of view as the distance from the optical axis to which the Root Mean Square (RMS) error, which quantifies the smoothness of the average wavefront, is below 0.06285. This corresponds to a Strehl ratio greater than 0.85 while the standard commercial convention for the FoV is a Strehl ratio greater than 0.8.

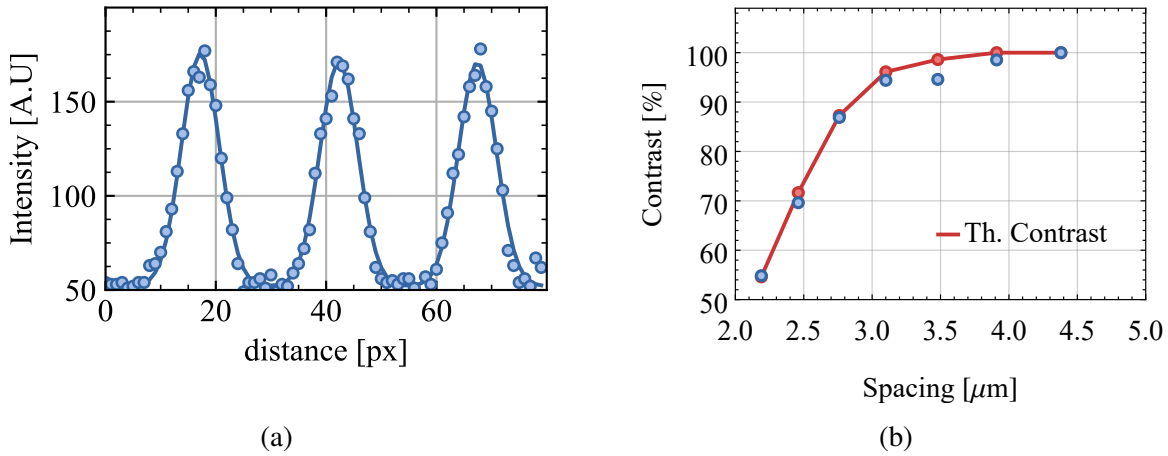

(a) (b)

Fig. 5.11 **Resolution test of our long working distance homemade objective**.(a) 1D profile of the group 7 element 2 of the USAF 1951. The three lines were fitted assuming three infinitely long lines of equal width imaged by an optical object of limited resolution R. The fitted resolution was found to be: $R = 1.89 \pm 0.04\,\mu$m and the estimated spacing $L = 3.45 \pm 0.03\,\mu$m which shall be compared to the theoretical resolution of $R = 1.95\,\mu$m and spacing of $L = 3.48\,\mu$m. (b) A more accurate evaluation of the resolution is to compute the MFT of the $z-$obj: evolution of the measured (blue dot) contrast as a function of the line spacing of the resolution target element. The red dots indicate the theoretical contrast of the objective assuming a resolution of $R = 1.95\,\mu$m imaging three infinitely long lines with a thickness equal to the spacing of the resolution target element. Both are in very good agreement.

theoretical one. This objective, called $z-$obj, is used as the first element of our lens system along the vertical direction, which is represented in fig. 5.12. The object lens is mounted on a standard one inch tube. The lens tube outer diameter is also milled to offer wider angle to properly align the object lens with respect to the glass once inside the inner coil. The precise alignment of both the vertical position of the object lens and its angle of inclination with respect to the science cell are controlled by a vertical position translation stage [12] and a 5-axis tilt stage [13]. The $z-$obj is used in combination with a $f = 600\,$mm two inch diameter diffraction limited achromatic lens, which focuses the atomic signal on a standard scientific CCD camera from Pixelfly. The high optical system magnification of $M \sim 15.0$ results in a effective lattice spacing of $34.5\,\mu$m $\simeq 5\,$px on the Pixefly sensor. Thanks to the propagation axis of the imaging beam coinciding with the lattice orientation, the atomic signal is integrated along the entire length of the tubes conferring a decent signal to noise ratio despite the high magnification and the low quantum efficiency of the camera. Finally, a dichroic mirror located between the two

[12] Model M-MVN50 from Newport with a travel range of 8 mm.
[13] Model 9081-M from Newport with a travel range of 3 mm and angular range of $\pm 4^\circ$.

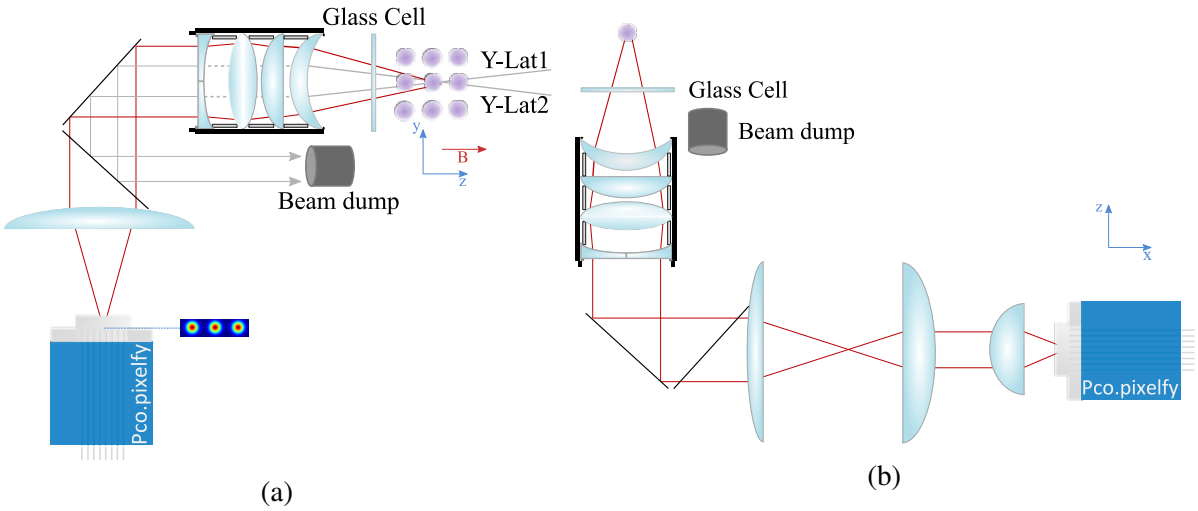

Fig. 5.12 **Imaging system along the vertical direction**. (a) The atomic signal being integrated along the entire tube length offers a high SNR for the imaging. A dichroic is placed between the object lens and the focusing lens to reroute the four lattice beams into a beam dump. **Optical elements**: homemade long working distance objective, two inches plano convexe lens, model: 600 mm achromatic lens from Edmund Optics (EO), dichroic lens and a pixelfly camera from PCO placed on a magnetic stage. (b) By moving the camera position, one can use the demagnification stage to image the hot cloud after the MW evaporation and check the ODTs alignement in the $xy-$plane. The demagnification stage is made of two lenses: a 160 mm achromatic lens from EO and a 50 mm aspheric lens from Asphericon (model ALL25-50).

lenses, reroutes the high power beams, to a beam dump while transmitting the imaging light. While this imaging axis cannot be used to quantitatively measure the atom number, it is particularly useful to align the lattice beams in the $xy-$plane. In the focal plane, the four lattice beams are symmetrically distributed around the imaging beam. Further tuning of each lattice beam position was done by using the main dipole trap ODT1 (described in sec. 3.3): after loading the atoms into the single ODT1, we ramp one of the lattice arms to full power, thus creating a cross dipole trap. The final position of each lattice arm is then tuned such that the central position of the cloud in the cODT coincide with its position in ODT1. Once the lattice beam position fixed, we used the $y-$imaging to confirm the lattice does not move the atoms along the vertical direction.

5.3.2 High resolution imaging along the transport direction

The transport direction is our primary imaging axis to observe the lattice. The atoms are located 10.5 mm from the outer part of the glass cell along the transport axis called $y-$axis. As discussed in the previous section 5.3.1, the vertical distance between the atoms and the

inner side of the glass cell is 5 mm, leading to a maximum resolution of $R = 0.92\,\mu m$ and a maximum achievable $NA = 0.51$. Due to the technical limitations of the asphere exposed in sec. 5.3.1, we installed a commercial objective from Olympus [14], which combines a long working distance of 18 mm with a high enough numerical aperture $NA = 0.30$ [15] to resolve the tubes. Its depth of field is $DOF = \pm 4.3\,\mu m$ and its field of view $FOV = 2.2\,mm$. Prior to mounting the objective, its resolution was also confirmed using 1951 USAF resolution test target. The complete imaging system along the $y-$axis is depicted in fig. 5.13. It is made up of a telescope, in 4-f configuration. It has a theoretical magnification of $M_y = 28$ and consists of the Olympus objective, with an $EFL = 18\,mm$ and a 2 inch (to be able to collect all the light from the diverging imaging beam) achromatic lens of 500 mm focal length [16]. Similarly to the z-imaging, the objective is mounted close to the science cell in a one inch tube milled on the sides and mounted on a tilt stage for precise alignment. The lens tube aperture is also large enough to not clip the imaging beam. The transport direction being orthogonal to the lattice tubes direction, the signal to noise ratio is extremely low once the atoms are loaded into the standing wave confinement. Because of the low atom number and the high magnification, which leads to a small photon count per pixel, we use an iKon-M 934 from Andor, a camera with a quantum efficiency at 767 nm exceeding 95 %. Additionally, an optical filter was installed to reduce parasitic light from reaching the CCD sensor of the camera.

Moreover, due to the low intensity of the imaging beam, our sensitivity to intensity and position fluctuations increased. Because of the low atom number, we observed that the intensity fluctuations between the absorption and the reference pictures sometimes exceeded the atomic signal. While this issue can easily be solved by implementing a corrective factor equal to the intensity fluctuation in a region without atoms, another issue arises from the use of the long working distance objective. Due to its transmission efficiency (around 90 %), interference between the different lenses of the object lens creates circular fringes that get embedded into the imaging beam after the objective. The fast position fluctuations of the imaging shift the position of the fringes between the absorption and the reference picture destroying the atomic signal. To reconstruct it, an algorithm was implemented in our imaging program to remove the fringes by creating a database made of several fringed pictures [17]. Finally, the frame transfer mode of the Andor was used in order to shorter the delay between two consecutive pictures, thus preventing extreme intensity fluctuation.

[14] Model LMPLN10XIR.
[15] Equivalent to a resolution of $R = 1.56\,\mu m$
[16] Model 50x500 VIS-MIR from Edmund Optics, reference EO49388
[17] Technical details regarding the algorithm and its implementation will be described in future thesis

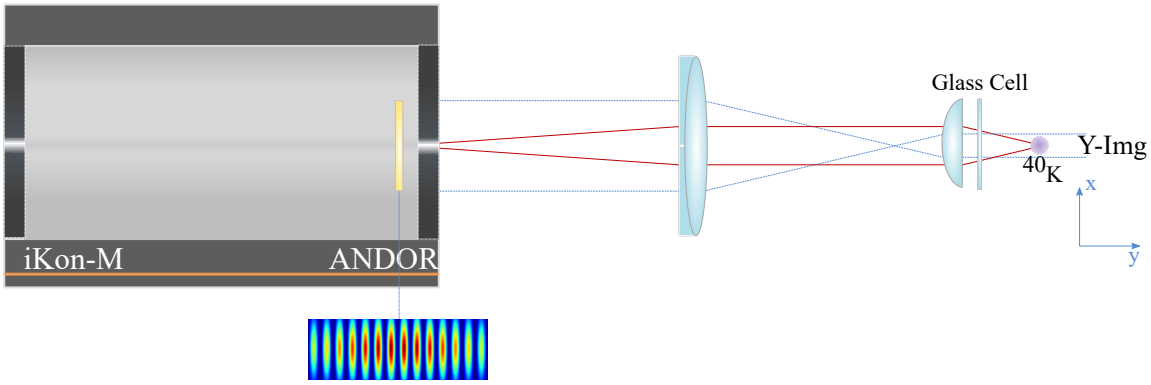

Fig. 5.13 **Imaging system along the transport direction**. A telescope in 4-f configuration offer a high magnification of $M_{\text{meas}} = 33$. Due to the reduced atomic signal, a high quantum efficiency camera was used to image the lattice tubes. An optical mask can also be placed in front of the camera to use the frame transfer mode of the Andor. **Optical elements**: objective: EFL: 18 mm model LMPLN10XIR from Olympus, achromatic doublets of 500 mm focal length model 50x500 VIS-MIR from Edmund Optics. Camera: model iKon-M 934 from Andor.

Chapter 6

Towards a one dimensional Fermi gas of ^{40}K

In this section, we will discuss the loading procedure of the optical lattice, its full characterization as well as the final steady state properties of the atomic cloud. In this context, we will also present the high magnetic field depumping implemented to isolate a single row of tubes along the y imaging, facilitating the study of the thermodynamic properties of each independent tube.

6.1 Adiabatic loading of the optical lattice

In order to be able to reach the one-dimensional (1D) regime in the optical lattice, the cloud temperature $k_B T$ and its Fermi energy E_F must be small compared to the transverse oscillation frequency $\hbar\omega_\perp$. A first approach to load the lattice and reach the 1D regime, would be to ramp up the lattice arms early during the sequence in order to transfer as many atoms as possible into the micro-traps. Enhanced evaporative cooling could then be simply performed in each micro-tubes by reducing the optical power of the various beams. Unfortunately, this initial approach presents several issues. By reducing the lattice trap depth, one also reduces $\omega_\perp$ potentially

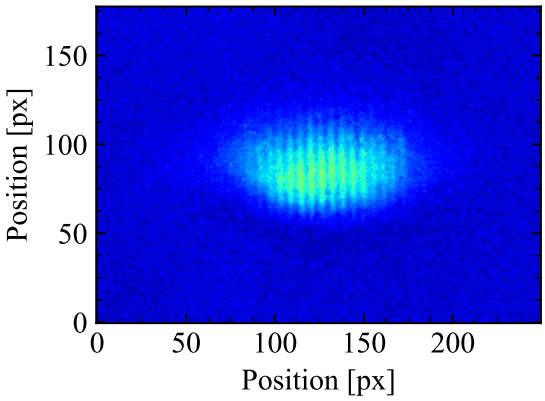

Fig. 6.1 **Average signal of the optical lattice**. Nine consecutive shots of the atomic cloud after the adiabatic loading of both 1D-lattices were averaged. Thanks to single site resolve imaging, one can clearly see the lattice structure.

making it more difficult to realize a 1D Fermi gas. Furthermore, evaporating in the tubes is highly inefficient. Due to the large waist of the lattice beams, the horizontal confinement is rather weak, thus potentially limiting the spatial density and the collision rate in comparison to the tight confinement provided by the cODT. Furthermore, the evaporation efficiency is related to the fraction of atoms with a kinetic energy comparable to the trap depth ($\Gamma_{\text{evap}} \propto \mathrm{e}^{-\eta}$, where $\eta = U_{\text{dip}}(0)/\mathrm{k_B}T$). While typically $\eta \leq 10$ for a standard dipole trap, in an optical lattice, population of the band n is given by $\mathrm{e}^{-E_n/\mathrm{k_B}T}$. For a gas mostly occupying the lowest band, the population of the bands $n > 1$ is minimal and thus only a very small fraction of the atomic cloud has a kinetic energy comparable to the lattice depth. Thus, the evaporation is highly suppressed as soon as the lattice depth exceeds few E_{R} (see fig.5.3b). More importantly, upon reaching the 1D regime, it is possible that evaporative cooling ceases completely to be efficient due to the cloud potentially not being able to thermalize anymore (more discussion about the thermodynamics in 1D can be found in sec. 6.6 and sec. 7). Consequently, we decided to first prepare a deeply degenerate Fermi gas in the cODT before loading the lattice by gradually ramping up the lattice depth.

Experimentally, following evaporative cooling of the atomic cloud to $0.15\,T/T_{\text{F}}$ with 1.5×10^4 atoms per spin state, the scattering length is reduced to $-294.0\,a_0$ by ramping the magnetic field from 202.4 G to 205 G, thus reducing the interaction strength and limiting the collision rate. The reduced collision rate is still enough for the atoms to thermalize while allowing us to slowly ramping up the lattice while avoiding losses [1]. Moreover, the optical confinement being close to the spilling limit, we also adiabatically ramp back the trap depth of the ODT1 and ODT2 in 1 s from respectively 3.6 µK and 15.0 µK to 5.4 µK and 17.0 µK. Once in this recompressed crossed dipole trap, we gradually increase either one or the two 1D lattices power depending on the physical situation we want to realize. A picture obtained by averaging nine in situ shots

[1] We also tried to load the lattice with a positive scattering length of $136\,a_0$ (which corresponds to a magnetic field of 238 G). Since both methods lead to similar loading efficiency we decided to load at the closer magnetic field at 205 G, which allows us to ramp it faster.

of the atoms after being loaded into the optical lattice is presented in figure 6.1. In order to minimize the perturbation of the system due to the additional potential, one wants to allow the atomic cloud to adiabatically evolve as it is transferred into the optical lattice. Considering shallow lattices (with $V_0 \sim E_R$), the adiabaticity criterion can be derived by estimating the typical timescale for inter-band transitions and yields [220] :

$$t_{\text{ramp}} \gg \frac{\hbar V_0}{32\sqrt{2}E_R^2}. \tag{6.1}$$

Research on adiabtic following have been performed for lattice depth V_0 up to $14\,E_R$ [228]. For a Fermi gas close to degeneracy, the underlying assumption of eq. 6.1 is that both the cloud temperature and its Fermi energy are smaller than the bandwidth of the lowest band of the lattice. Moreover, the Fermi energy being small with respect to the bandwidth, the momentum distribution will be narrow enough to not explore the band edge [2].

However, this approximation breaks down for $V_0 \gg E_R$, since the lattice potential can no longer be treated as a perturbation of the initial Hamiltonian. In this case, a standard and more restrictive approach consist in ramping the lattice slower than any timescale of the experiment, which can still lead to heating despite the adiabatic following of the atomic cloud during the entire loading [229]. The three relevant timescales are related to the atomic movement $t_{\text{atom}} \propto 1/\overline{\omega}$ (with $\overline{\omega} \sim 2\pi \times 100\,\text{Hz}$ being the smallest trapping frequency of the cODT), $t_{\text{adia}} = \hbar V_0/32\sqrt{2}E_R^2$ and the average tunneling time $t_{\text{tunnel}} = \hbar/J$. The tunneling time represents the timescale over which hopping between lattice sites can occur, thus allowing thermalization of the entire cloud after its loading into the different tubes. Since the tunneling time increases exponentially with the lattice depth (see eq. 5.12), it ultimately dominates any adiabaticity condition. For a lattice depth of $V_0 = 40\,E_R$ and our lattice spacing of $2.3\,\mu\text{m}$, $t_{\text{tunnel}} = 5 \times 10^6\,\text{s}$. As such, tunneling will be completely suppressed no matter the duration of the lattice ramp. Consequently, the micro-traps will always remain independent and cross thermalization (as well as hopping) between adjacent sites will not occur. As a consequence, we decided to exponentially ramp the lattice up to $V_0 = 40\,E_R$ in $t_{\text{ramp}} = 2\,\text{s}$, with the exponential time constant being equal to $\tau = 1\,\text{s}$. The loading duration vastly exceeds both $t_{\text{adia}} = 30\,\mu\text{s}$ and $t_{\text{atom}} \sim 10\,\text{ms}$.

With our 2 s exponential ramp to $V_0 = 40\,E_R$, the total heating was found to be around $0.1\,T_F$ [3], which is consistent with other experiments working with ^{40}K at $T/T_F \simeq 0.2$ that measured a total heating induced by the lattice around $0.15\,T_F$ for a depth up to $12\,E_R$ despite the adiabaticity

[2] This statement is not valid during the initial loading of the lattice, during which the trapping potential is small enough for the energy gap between the first two bands to vanish, thus preventing any adiabatic loading

[3] The heating was obtained by measuring the ratio T/T_F prior to the lattice loading and after switching on and then off the lattice with our 2 s exponential ramp.

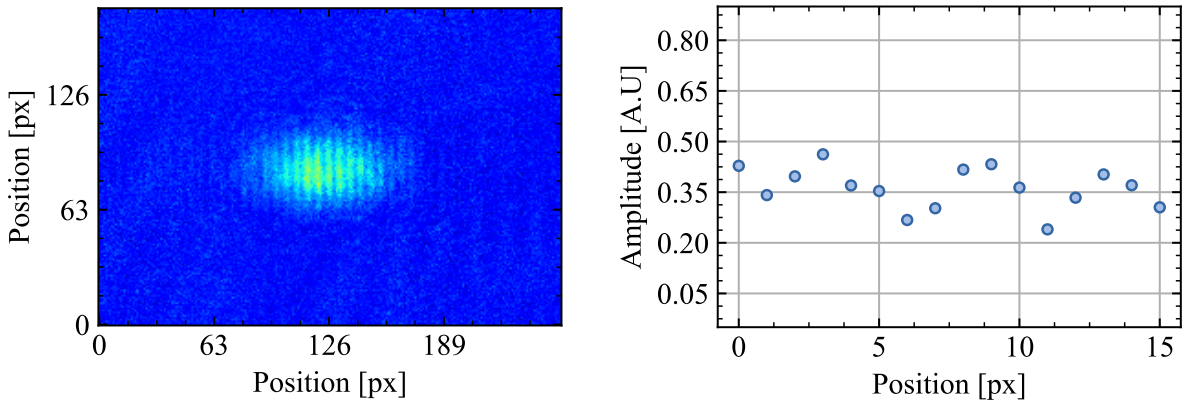

(a) (b)

Fig. 6.2 **Determination of the lattice spacing**. (a) typical in situ picture of the atomic cloud after the loading of the x-lattice. (b) 1D profile of the central region of the cloud. 3 lattice pancakes can be seen. Using the magnification and the pixelsize of the andor camera, the lattice spacing can be estimated to $d_\alpha = 2.26 \pm 0.06$µm.

of the loading (see [230–232]).

6.2 Determination of the lattice spacing

Since each 1D optical lattice is generated by two running waves intersecting under a total angle $\alpha \leq \pi$, we need to measure the lattice spacing $d_\alpha \geq d_0$. In this section, we will present a direct method based on in-situ imaging and used in our experiment. As more precisely detailed in the following section, one can use matter-wave diffraction to calibrate the lattice spacing. However, this indirect method requires an overly precise control of the interaction time and the lattice power. A straightforward way to measure the lattice spacing is to take advantage of the high resolution imaging along the $y-$direction in order to directly detect the in situ density profile of the various traps after the loading into the lattice. A careful calibration of the magnification is then sufficient to determine the lattice spacing from the distance between several maxima (or minima).

A standard picture of the periodic potential created by the x-Lattice, imaged along the $y-$axis as well as a the density profile centered around few maximums are presented in figure 6.2. Using the magnification $M_y = 33.0$ along the $y-$img, we estimate a lattice spacing of $d_\alpha = 2.26 \pm 0.06\,\mu$m. The two main limitations to determine more accurately the spacing are the optical resolution of our imaging system, which reduces the contrast between the node and the anti-node of the standing wave and the magnification which limits the number of pixels per tube to ~ 5. Another possible method to determine the lattice spacing more precisely is to perform

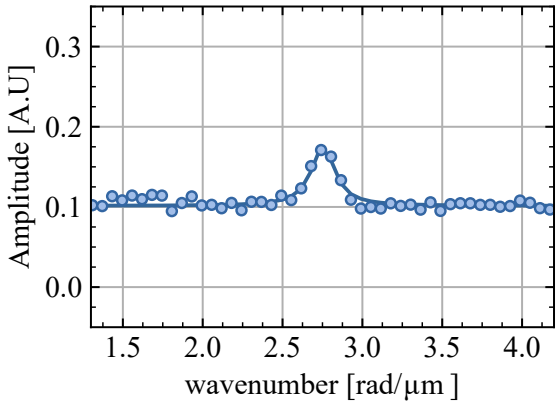

Fig. 6.3 **Fourier transform of the density profile of atoms in the 1D x-lattice**. Using the $y-$imaging picture (see fig. 6.2a), we perform the Fourier transform of the atomic signal. The peak corresponding to the lattice structure is clearly visible. The wavenumber k is obtained from a Lorentz fit. The corresponding spacing is equal to $d_\alpha = 2\pi/k = 2.29 \pm 0.01\mu$m.

the Fourier transform of the atomic signal in the lattice. The Fourier transform of the figure 6.2 is presented in figure 6.3. A Lorentz fit provides a wavenumber of $2.74 \pm 0.01\,\text{rad.}\mu\text{m}^{-1}$ and a corresponding lattice spacing of $2.29 \pm 0.01\,\mu$m. To characterize the spacing of the $y-$lattice, we rely on both the Kapitza-Dirac pulse and the lattice depth calibration (see sec. 6.3). For identical trap depth and pulse duration, the same number of diffracted orders will be populated. The distance between the two most extreme diffraction orders of figure 6.6 being identical for both 1D-lattices, the lattice spacing must also be similar for the $x-$ and $y-$lattice, assuming that the lattice depth of the two 1D lattice are identical.

6.3 Lattice depth calibration

As explained in section 5.1, precise calibration of the transverse trapping frequency is crucial to estimate the dimensionality of the system for any experiment performed in presence of the standing wave. In this section, we will first estimate the maximum lattice depth achievable using matter-wave diffraction before precisely calibrating the lattice depth by measuring the transverse trapping frequencies.

6.3.1 Matter wave diffraction

One of the most common methods to measure the lattice depth consists in using matter-wave diffraction. If the atoms are subjected to the lattice for a duration $t_{\text{int}} \ll t_{\text{adia}}$, atoms cannot follow adiabatically the raising periodical potential. Consequently, the lattice will then simply diffract the atoms [234]. For a standing wave with a wave number k_L, two adjacents diffraction orders will be separated by $2\hbar k_L$ in momentum space. Assuming a momentum distribution centered around $\hbar k = 0$, for a given lattice spacing, the diffracted pattern will solely depend on two parameters: the duration of the lattice pulse (sometimes called the interaction time) t_{int} and its strength, characterized by the lattice depth V_0. The number of diffraction orders that

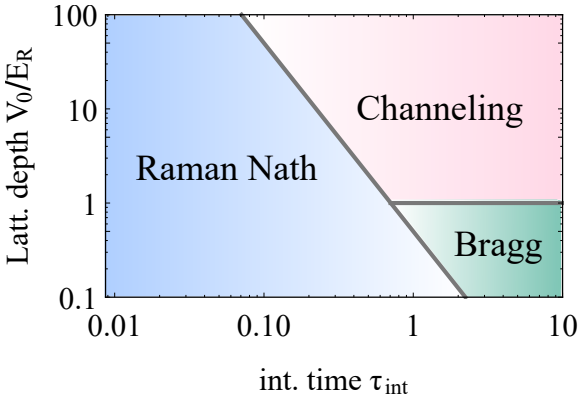

Fig. 6.4 **Matter-wave diffraction spectrum.** Depending on the interaction time and the optical power, three distinct regimes will describe the diffraction pattern: Raman Nath, Bragg and the channeling regime. When conditions are set for Bragg scattering, only one diffraction order will be populated. In the Raman Nath regime, all orders between the diffraction orders $-n$ and $+n$ will be populated. The last populated order $\pm n$ is proportional to both the light intensity and the interaction duration. Finally for long interaction time and strong lattice power, the diffraction will be described by the channeling regime, in which the population of the different diffracted orders cannot be easily determined anymore. Figure adapted from [233].

will be populated using matter-wave diffraction depends on the value of those two parameters and three different regimes can be identified: the first one corresponds to short interaction time and is called the Raman-Nath (also called Kapitza-Dirac) regime. For long interaction time, depending on the strentgh of the pulse, two regimes can be identified: the Bragg regime, which requires weak lattice depth and the channeling regime which necessitates strong interactions. The figure 6.4, adapted from [233], represents the parameter range for those three regimes.
For shallow lattices ($V_0 \leq 4E_R$) and long pulse time, atoms can be subjected to Bragg diffraction [235, 236] and acquire a momentum $2n\hbar k_L$, where n is an integer. Consequently, only one diffracted order, namely the n-th one will be predominantly populated. Determination of the value of n can be done analytically as detailed in [233].
For strong interaction and short pulses, Kapitza-Dirac diffraction can be observed [237]. In order to stay in the Kapitza-Dirac regime and not crossover to the channeling regime, precise control of the pulse duration is critical. The maximum allowed duration of the lattice pulse to stay in the Raman-Nath regime is directly related to the lattice depth. One can safely stay in the Kapitza-Dirac regime for an interaction time $t_{int} < \hbar/E_R\sqrt{2s}$, with $s = V_0/E_R$. In this regime, one can analytically solve the Schrödinger equation describing the diffraction process and thus estimate the population of each diffracted order. The population of each diffracted order p is equal to $|J_p(n)|^2$ with $n = V_0/2\hbar \times t_{int}$ [4] and J_p the $p-$th order Bessel function [233]. Thus, as represented in figure 6.5, the most populated diffracted orders are around $\pm n$, the population

[4] Since n has to be an integer for all the following calculations, the value of n is approximated to the nearest integer.

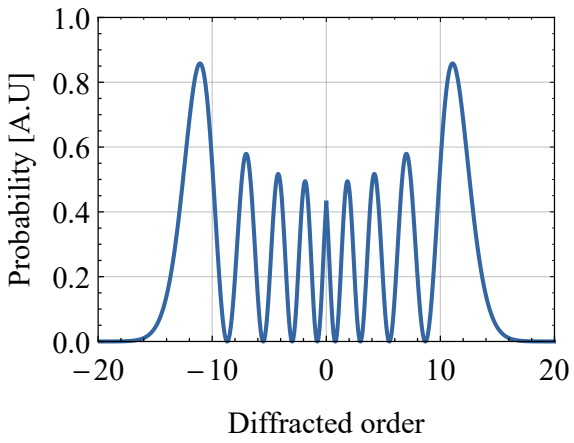

Fig. 6.5 **Evolution of the population of the different diffracted order in the Kapitza-Dirac regime**. In this regime, the population of each diffracted order p is equal to $|J_p(n)|^2$. Here, we chose $n = 13$, which corresponds to the estimated experimental value.

of higher orders vanishing exponentially. To predominantly populate the first orders (± 1), the interaction time t_{int} must be equal to:

$$t_{\text{int}} = \frac{2\hbar}{V_0} = \sqrt{\frac{8E_{\text{R}}}{V_0}} \times t_{\text{lim}} \tag{6.2}$$

and $V_0 \geq 8E_{\text{R}}$. Here, $t_{\text{lim}} = \hbar/E_{\text{R}}\sqrt{2s}$. Finally, with strong interaction and long pulses, one will reach the channeling regime in which the population of the different diffraction orders cannot be easily determined since atoms have enough time to channel between the potential valleys. Consequently, matter-wave diffraction could be used to indirectly determine the lattice spacing, since it only requires precise measurement and control over the two pulse parameters (its duration and the lattice depth) [5]. However, since we were able to precisely measure the lattice spacing of the x-lattice, matter-wave diffraction can be employed to indirectly estimate the lattice depth. As an illustration, a picture of the diffraction pattern obtained with a lattice pulse in the Kapitza-Dirac regime after is presented in figure 6.6. We can see the two most populated orders $\pm n$ as well as several orders being populated in between. After a given time of flight τ, the distance L between the two orders is equal to $L = 2n\hbar k_L \tau/m$. n and V_0 can thus be estimated. Here, given the interaction time of $t_{\text{int}} = 6\,\mu\text{s}$, we found $n = 13$ and $V_0 = 135\,E_{\text{R}}$ which is much lower than the expected lattice depth of $V_0 = 267\,E_{\text{R}}$, with $E_{\text{R}} = \text{k}_{\text{B}} \times 0.21\,\mu\text{K}$ being the recoil energy for a retro-reflected lattice. This discrepancy is an initial potential indication that due to the polarization of the lattice beams, the highest achievable lattice depth is lower than the

[5] The necessary control over the lattice depth would be experimentally challenging since the actual lattice depth can greatly differ from the theoretically expected $4U_{\text{dip}}(0)$ due to polarization misalignment. Moreover, the momentum distribution of the atomic cloud prior to the lattice pulse must be small with respect to the lattice wavenumber in order to resolve each diffraction order, which in our case is only achievable with deeply degenerate cloud, which leads to small signal to noise ratio and.

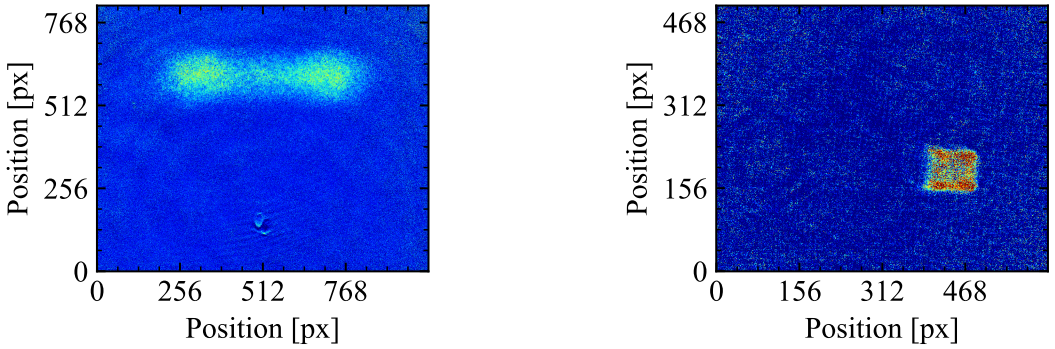

(a) (b)

Fig. 6.6 **Raman-Nath (Kapitza-Dirac) diffraction of the atomic cloud**. By shining the lattice at $V_0 \sim 140\,E_R$ during $t_{int} = 6\,\mu s$, one can populate all the order between $\pm n$ where $n = V_0 t_{int}/2\hbar$. (a) Kapitza-Dirac realized with the x-lattice. (b) Kapitza-Dirac realized with both 1D lattice. For similar interaction time and lattice power, the last populated orders $\pm n$ are identical.

Fig. 6.7 **Band structure of a 1D optical lattice**. The first three bands are indicated by their respective color area. The harmonic approximation for each band is represented in gray. For low lattice depth, the discrepancy between the harmonic approximation and the exact calculation of the band structure is important due to the large width of the band and the reduced gap. This discrepancy increases with the band number.

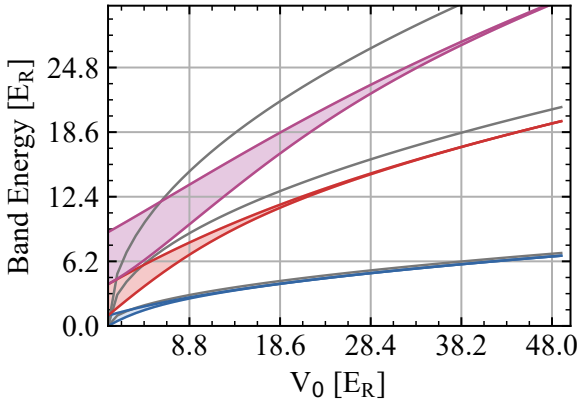

theoretical one. In the following section, a more precise calibration of the lattice depth based on the measurement of the transverse trapping frequencies will be presented.

6.3.2 Calibration of the lattice depth by measuring the transverse trapping frequencies

For a 1D lattice, the trapping frequencies illustrate the maximum splitting between two consecutive bands. Considering the lowest band, the transverse trapping frequency $\omega_\perp$ is defined as $\hbar\omega_\perp = E_{\alpha,2}(q=0) - E_{\alpha,1}(q=0)$ [6]. Figure 6.7 represents the evolution of the band structure as a function of the lattice depth for the first three bands as well as the evolution of the approximated one dimensional harmonic oscillator (of frequency $\omega_\perp$). For low lattice depth, the

[6] Here, for a given quasi-momentum $\hbar q$ and an angle α, $E_{\alpha,n}(q)$ represents the eigenenergy of the band of index n

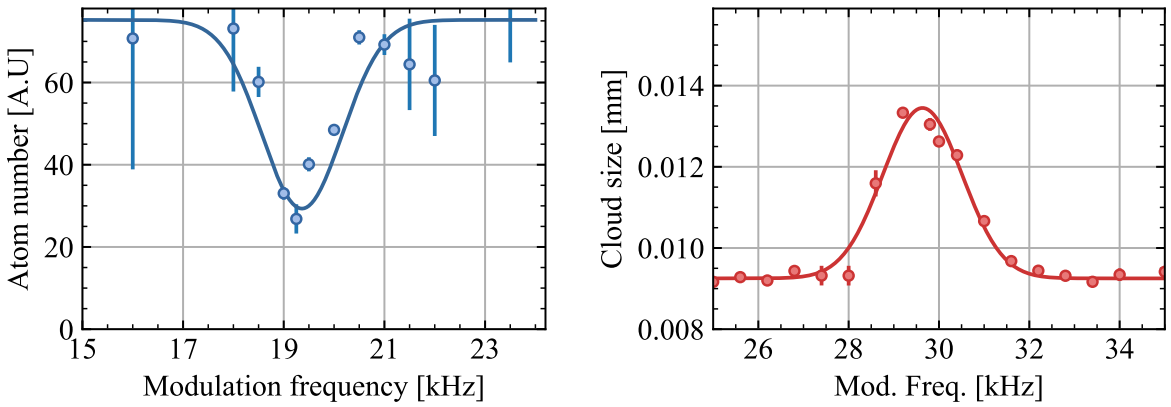

(a) (b)

Fig. 6.8 **Measurement of the transverse trapping frequencies**. Using parametric heating, one can excite the atomic cloud at twice the trapping frequencies. (a) For strong induced heating, atoms can gather enough kinetic energy to leave the lattice confinement. (b) For moderate heating, atoms remains in the trap and the transverse frequency can be measured by looking at the cloud size directly.

harmonic approximation ceases to be valid due to the large width of the band and the resulting reduced gap. For a lattice depth of $12\,E_R$ for example, the discrepancy between the numerical calculations and the harmonic approximation is equal to 25 %.

Measurements of the 2D lattice transverse trapping frequencies were performed using what is sometimes colloquially referred to as shaking spectroscopy, which is the modulation of the lattice light intensity to induce parametric heating [238]. Since parametric heating couples motional states of the harmonic oscillator with identical parity, the measured frequency is equal to twice the frequency of the harmonic oscillator (more details concerning regarding parametric heating can be found in annexe A.3). Experimentally, the calibration was performed by first loading one of the two 1D lattices by ramping it in two seconds to an arbitrary depth V_{cal} instead of the standard $V_0 = 40\,E_R$. Following the loading of the periodic trapping potential, we modulate its intensity and the lattice depth 200 times by roughly ± 5 % of V_{cal} at a given frequency ω_{mod}. The duration of the step is set to 20 ms such that after 200 cycles, the lattice intensity will stay constant during the remaining duration of the step. After the modulation, the lattice power is ramped down to 0 in 200 ms. The magnetic field is then ramped to the zero crossing in 100 ms and the atomic cloud imaged after a few ms ToF to record the remaining atom number and the cloud size. For low-level of induced heating, the atom number remains constant and the cloud temperature increases as one approaches the resonance frequency. For stronger heating, the energy of the atoms increases sufficiently and atoms can leave the trap. The figures 6.8a and 6.8b represent the typical evolution of the atom number and the cloud size

as a function of the modulated frequency.
This calibration of the transverse frequencies via parametric heating can be used to extract the lattice depth. As explained in sec. 5.1.2, the transverse trapping frequencies are solely function of the lattice depth and its spacing. The figure 6.9 represents the evolution of the transverse frequency of both 1D lattices as a function of their respective depth. Using the measurement of the x-lattice spacing, one can estimate the maximum trap depth in terms of E_R. For our maximum analog setpoint of 2 V, we expect a corresponding transverse trapping frequency $2\pi \times 24.1$ kHz. Given the spacing of the x-lattice, this corresponds into a maximum depth of $147\,E_R$ which is much lower than originally expected. This contradiction, which was already hinted by matter-wave diffraction experiment is most likely due to the polarization of the two arms of the x-lattice.
Calibration of both transverse frequencies can also be used to determine the lattice spacing of the $y-$lattice. Trap depth is a function of the optical power and the waist. Measurement of the waist using a beam profiler estimated the waist of the $x-$lattice $\omega_{\mathrm{Latt,x}} = 222\,\mu$m (resp. $\omega_{\mathrm{Latt,y}} = 190\,\mu$m). Consequently, for identical power and spacing, the $y-$lattice will be 36 % deeper than the $x-$lattice, which would alter the trapping frequencies by 16 %. Experimentally, for identical lattice power, the measured discrepancy between the trapping frequency is $\omega_{\mathrm{Latt,y}} = 1.05\,\omega_{\mathrm{Latt,x}}$ (instead of the expected ratio of 1.16. Two reasons can explain this difference: the respective polarization between the two y-lattice arms or the spacing of the $y-$lattice. Assuming, that this difference is solely due to the lattice spacing, we found a spacing $d_{\alpha,\mathrm{y}} = 1.1\,d_{\alpha,\mathrm{x}} = 2.5\,\mu$m, which is still close to $x-$lattice spacing and in good agreement with our predictions. Finally, when loading the lattice, the confinement is provided by both the 1D lattice and the cODT. While the trapping potential in the transverse direction of the lattice is dominated by the standing wave since $\omega_\perp \gg \omega_{\mathrm{cross}} \sim 100$ Hz, the longitudinal confinement is provided by the cODT due to $\omega_\parallel \ll \omega_{\mathrm{cross}}$. Thus, the longitudinal trapping frequency is extracted from the calibration of the cODT (see sec 3.5) and is equal to $\omega_\parallel = 2\pi \times 305$ Hz.

6.4 Isolation of a single row of tubes

Owing to the very high tunneling time, each micro-trap of the 2D-lattice is independent from its neighbors. Moreover, the evolution of the various thermodynamics quantities of interest might evolve differently in each tube. For example, the Fermi energy in the central region of the lattice will be higher than in the wings [7]. As a result, assuming an atomic cloud in thermal equilibrium, the system might be confined in 1D in the wings, but the central region might

[7] This phenomenon arises from the fact that the central region of the cODT is denser than the wings

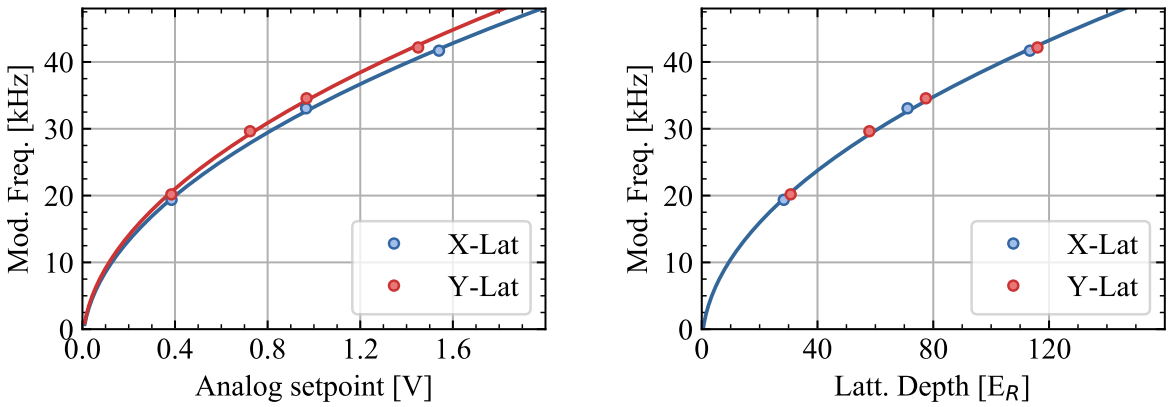

(a) (b)

Fig. 6.9 **x- and y-lattice calibration**. (a) Measured trapping frequencies as a function of the analog setpoint of the optical lattice for both 1D lattice. (b) Evolution of the trapping frequencies as a function of the lattice depth using the harmonic approximation of the band structure.

very well be in 3D due to the greater number of atoms per tube. While single site resolution allows us to see each tube independently along $y-$imaging, an additional issue arises along this direction. Even though, one can easily see independently each lattice pancake created by the x-lattice, we still have to integrate the atomic signal from all the particles confined in each micro-trap created by the $y-$lattice. Furthermore, a technical drawback must be added to this fundamental issue. Due to the single site resolution, the depth of field along both $y-$ and $z-$axis is rather small. Along the $y-$imaging, the depth of field of the Olympus objective is $\pm 4.3\,\mu$m. As a result, $4.3\,\mu$m away from the focus, which corresponds to only 3 lattice sites, the sharpness of the reconstructed atomic signal will drastically decrease.

To circumvent these issues, one can isolate a single lattice row perpendicularly to the $y-$imaging. A possible way to do so would be to create a magnetic gradient B' in order to make all lattice rows except the one of interest transparent to the imaging light. For light to be solely resonant with a single row, the energy shift between two adjacent sites must be greater than the imaging transition linewidth $\Gamma \sim 2\pi \times 6\,$MHz, which given the lattice spacing of $2.30\,\mu$m, leads to a gradient $B' \geq 1.9 \times 10^4\,\mathrm{G.cm^{-1}}$ (resp. $B' \geq 2.2 \times 10^4\,\mathrm{G.cm^{-1}}$) for atoms in the $|9/2,-9/2\rangle$ Zeeman sublevel (resp. $|9/2,-7/2\rangle$) [8]. Generating such a large magnetic gradient not being technically feasible, we decided to hide the different lattice rows by means of a optical depumper.

Prior to imaging the atomic cloud, one could shine in resonant light to optically pump the

[8] One could also use microwave transition to transfer atoms into the $F = 7/2$ manifold but as detailed in the appendix A.4, the efficiency of the transfer is limited to less than 75%

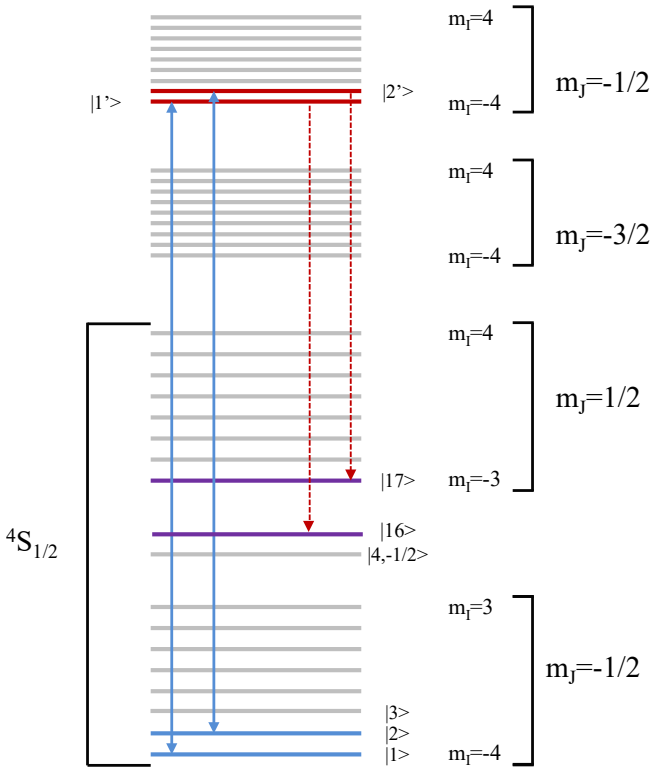

Fig. 6.10 **Transition scheme for optical pumping at the zero crossing at** 209.9 **G** .

atoms into a dark state with respect to the imaging light. Several transitions can be used for this optical pumping scheme depending on the light polarization. In order to make use of the already existing hardware, we used π-transitions to transfer the atoms in the states [9] $|1\rangle$ and $|2\rangle$ to the $m_j = -1/2$ manifold of the $^4P_{3/2}$ excited state (see figure 6.10). Once in the excited state, atoms can decay back to the states $|1\rangle$ and $|2\rangle$ or to the dark states $|16\rangle$ and $|17\rangle$. Once in $|16\rangle$ and $|17\rangle$, atoms will not be resonant with respect to the de-pumping light nor the imaging light. A description of the optical pumping at high field can also be found in [74]. In order to image one lattice row, one has to spatially modulate the de-pumping light by means of an optical mask before directing it to the atoms, thus shining it to all but one lattice rows.

The optical setup of the high field depumping is presented in fig. 6.11. It consists of an optical mask and a relay telescope. The optical mask is a 20 µm wire. It is mounted on a 3-axis translation stage with micrometer screws to be able to align it precisely on the atoms and to place it at the exact focal plane of the relay telescope. This first lens is a 500 mm achromatic lens [10] while the second one is a two inch homemade objective. Developped by Pritchard et al. [225], this TRAP objective has a theoretical $NA = 0.172$ and a corresponding resolution

[9] Using the notations introduced in sec. 3.6

[10] A 2 inch diameter from Edmund Optics with a VIS-NIR coating to prevent reflection.

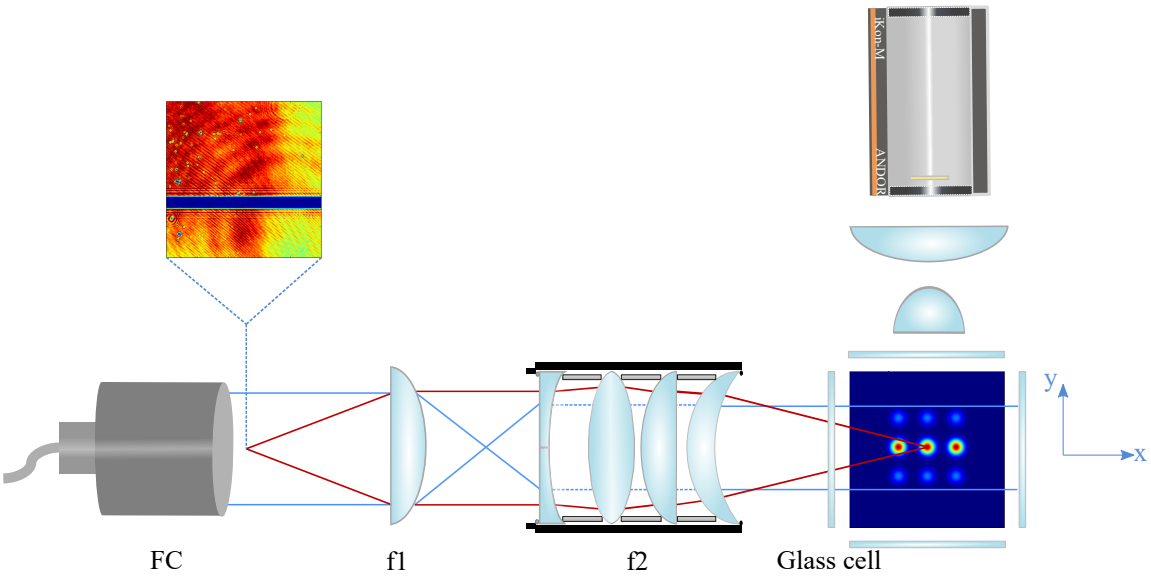

Fig. 6.11 **Optical setup for the high field optical pumping**. An optical mask, located at the focal plane of a telescope is imaged on to the atoms. The size of the mask on the atoms is comprised between one and few lattice spacing. A picture of the optical mask is depicted in the top left corner. Thanks to the mask, by shining the optical pumping light only one row is still resonant with the imaging light, allowing the image of a single lattice row along the $y-$axis. **Optical parts**: f1: 2 inch diameter 500 mm focal length achromatic lens from Edmund Optics, f2: 2 inch homemade objective built according to [225]. Lenses used for the objective from left to right: Newport KPC067, Thorlabs LB1199, LA1256 and LE1985.

$R = 2.85\,\mu$m. Its resolution was tested using a resolution target after being assembled and was estimated to be $2.79 \pm 0.15\,\mu$m even in presence of a 4 mm thick glass window. Thanks to its long working distance of 119.5 mm, the objective can be mounted outside of the coils mount, thus not obstructing the path of ODT1&2 while provinding a sufficiently high resolution to preserve a single row of tubes from the optical depumping. Given its $EFL \simeq 120$ mm, the relay demagnification is $M_{\mathrm{OP}} = 0.24$. Consequently, the theoretical effective size of the mask on the atoms is equal to $4.8\,\mu$m, which can theoretically allow us to cast the shadow on a single layer of tubes. The precise alignment of the TRAP objective's position along the propagation direction as well as its angle of inclination are controlled by a translation stage from Newport and a mirror mount. To confirm the beam alignment, the optical system was first used to shine imaging light and image the cODT, which allowed us to center the mask position. The optical depumping was then tested at high field by first transferring part of the main ODT into a dark state (fig. 6.12a) and then the cODT. The final duration of the pumping pulse was set to $2\,\mu$s, which was enough to transfer atoms illuminated by the light into a dark state while not transferring atoms shadowed by the mask as well (see fig. 6.12b and 6.12c). In presence of the optical pumping, the diameter of the cloud along the transverse direction was reduced to

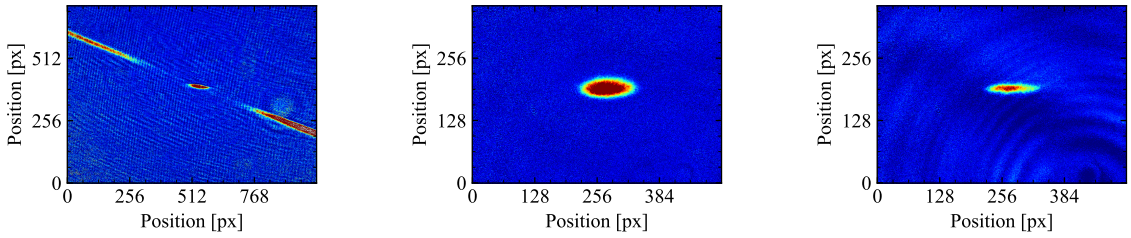

(a) (b) (c)

Fig. 6.12 **High field optical pumping implementation**. (a) By shining depumping light at high magnetic field, one can transfer part of the atomic cloud into a dark states. By additionally imprinting an optical mask on the atoms, one can preserve part of the cloud from being transferred. Image of the atomic cloud when confined in the cODT with (c) and without (b) 2 µs of optical pumping. The estimated size of the sliced cloud is 4.1 µm.

4.1 µm. The peak OD was also reduced by 25 %. The results of the optical pumping on the lattice are provided in fig. 6.13, which presents pictures of the lattice with and without optical pumping. In presence of the optical pumping, the central OD dropped by roughly 15 % and the contrast also slightly deteriorated from around 40 % to 32 %. The reason why the contrast gets altered still remains to be explained.

6.5 Experimental realization of a deeply degenerate 2D Fermi gas of ^{40}K

Following the lattice characterization, we tried to load the 2D lattice and estimate to which degree the cloud purely evolves in one dimension. However, loading both 1D lattices at the same was proven to be quite inefficient and induced severe losses. Consequently, we chose to ramp the two 1D lattice one after another, thus first loading a degenerate 2D Fermi gas before ramping the second standing wave to confine the atomic cloud in 1D. By exponentially raising the x-lattice trap depth up to $V_0 = 40 E_R$ in two seconds, we manage to macroscopically populate around 20 pancakes. In the central region of the standing wave, we typically transfer 250 atoms per pancake. Assuming that the gas is indeed confined in two dimensions, one can fit the 1D density profile to obtain the fugacity Z. For a Fermi gas confined in two dimensions, its 1D density profile $n(z) \propto \mathbf{Li}_{3/2}(-Z\exp(-\beta m/2\omega_z^2 z^2)$. The ratio T/T_F is then obtained from the fugacity using the relation $T/T_F = [-2\mathbf{Li}_2(-Z)]^{-1/2}$. Using this relation we estimate that in the central region of the x-lattice the temperature of the confined atoms was around$T \simeq 0.34\, T_F$. In order to estimate the 2Dness of the atomic cloud, we first assume that $E_F \ll \hbar\omega_\perp$. As a consequence, each pancakes can be considered as a 2D harmonical oscillator characterized by the longitudinal frequency $\omega_\parallel$. The N atoms will thus occupy the first n levels of the harmonic oscillator. The $n-$level of a 2D harmonic oscillator having a $n+1$

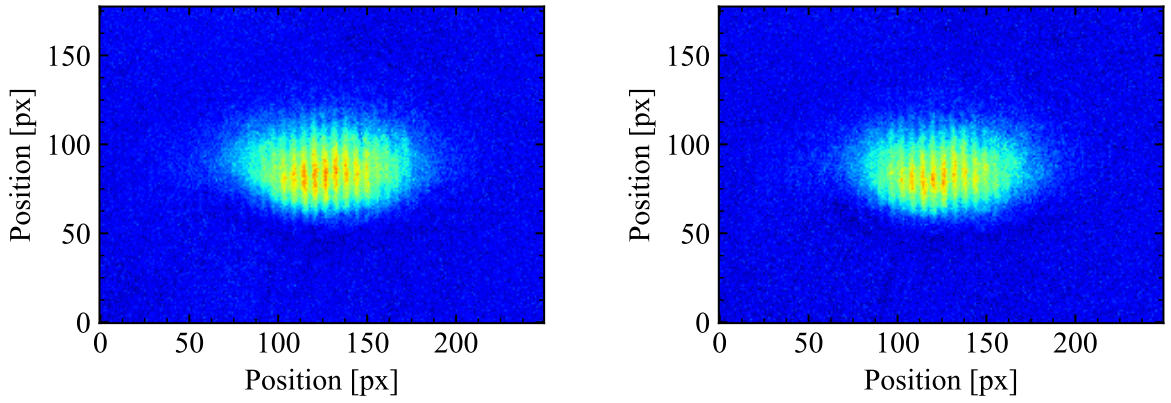

Fig. 6.13 **x-lattice in absence or presence of optical pumping**. In presence of optical pumping, the peak OD dropped to roughly 0.7 indicating that a small part of the depumping light passes through the optical mask.

degeneracy, we can conclude that the 250 atoms will occupy the first 21 levels of the oscillator. Using the calibration of our cODT (see Appendix A), we estimated that our axial frequency of $2\pi \times 300\,\mathrm{Hz}$. This imply that upon adiabatically loading the atomic cloud into the pancakes the Fermi energy in the central region will be equal to $E_F = 0.66\hbar\omega_\perp$. Finally, using a Fermi-Dirac distribution with $T = 0.34\,T_F$, we can estimate that statistically, only 6 % of the total atom number aren't occupying the fundamental level in the transverse direction. The creation of this deeply degenerate 2D Fermi gas, in addition to the long lifetime (above 4 s) in the pancakes, both constitute an important milestone towards the realization of a strongly interacting 1D Fermi gas and an good initial condition to ramp the y-lattice.

6.6 Towards one dimensional Fermi gases of ^{40}K

After the loading of the one-dimensional x-Lattice, we exponentially ramp in two seconds the y-lattice to $V_0 = 40\,E_\mathrm{R}$. In order to estimate the 1Dness of the system, similarly to sec. 6.5, one needs to estimate the following three standard parameters: the atom number per tube, their temperature and the Fermi energy. However, the capacity of a system to redistribute energy and thermalize while being confined in one dimension is not a trivial problem. Classical thermalization is related to the notion of integrability and phase space trajectories [239]. Chaotic systems, once brought out of equilibrium will explore the entire phase space and relax towards equilibrium while integrable systems only execute closed orbits and fail to thermalize [239].Even for near-integrable systems, the timescale to reach thermal equilibrium might greatly exceed the typical experimental cycle. Research on near-integrable systems and

thermalization in general is still an on-going topic of research in both 3 as well as in reduced dimensions [240, 241].

Thus, a problem naturally arises from the realization of 1D Fermi gas. As explained in chapter 4, one of the main interest of 1D systems is the integrability of several models such as the Lieb-Liniger Hamiltonian. Consequently, one of the first goals before trying to estimate the temperature and the Fermi energy of the system is to verify the breakdown of integrability of our quasi-one-dimensional Fermi gas, which was already verified and investigated for bosons [240, 242]. Chapter 7 will present experimental methods to explore the thermalization properties of fermions confined in one dimension. For the moment, we will assume that our atomic cloud is indeed in thermal equilibrium. Under this assumption, using a polylogarithmic fit (see sec 6.5) one can estimate the fugacity and the ratio T/T_F from the shape of the integrated atomic profile. Pictures of the 2D lattice in presence of the optical pumping still remains to be taken at the time of writing this thesis so we will extrapolate results from the unsliced cloud and the 1D lattice to estimate the atomic cloud parameters inside a single tube. By ramping the x-lattice, we managed to load around 250 atoms per spin states into the central region of the lattice at a temperature $T/T_F = 0.34$ from an initial cloud of 1.5×10^4 per spin state at a temperature $T/T_F = 0.15$. By loading the second 1D lattice (y-lattice), and in the absence of slicer, one can load in the tubes around 70 % of the atom number confined in the pancakes. It is not clear at the moment if the reduced loading efficiency is due to the 2D lattice loading procedure or some more fundamental issue. Nonetheless, under those circumstances, we manage to transfer around 180 atoms inside the tubes. Given the size of the pancakes in the horizontal directions (12 µm diameter), one can expect to load in the central region up to $N_{|\uparrow\rangle} = 50$ atoms per tube since the central region of the cloud contains more atoms that the wings. Estimating the ratio T/T_F in those conditions being quite challenging we will safely assumes that it also increased significantly upon loading the 2D lattice.

By raising the lattice depth to its maximum value after the loading one would have $\omega_\perp \simeq 25$ kHz while the longitudinal frequency $\omega_\parallel = 300$ Hz is given by the cODT. This lead to a 1D gas with $k_B T_F = N_{|\uparrow\rangle}\hbar\omega_\parallel = 0.6\hbar\omega_\perp$. Using a Fermi-Dirac distribution with a reasonably safe $T = 0.7\,T_F$, such conditions would result in 80 % of the atomic population in the lowest energy state along the transverse direction, providing an interesting starding point to explore 1D physics phenomena.

Chapter 7

Summary and outlook

In this manuscript, we reported on our progress towards the experimental study of the dimensional crossover between strongly interacting fermions in 1D and 3D. In 3D, a deeply degenerate Fermi gas in the normal phase can be understood using the so-called Landau-Fermi liquid theory. However, in 1D, only collective excitations remain and a degenerate Fermi gas in the normal phase is described by the Tomonaga-Luttinger liquid theory. While extensive research on these regimes has been carried-out, the interpolating transition in-between remains mostly unexplored. Our aim is thus to study this dimensional crossover using a strongly interacting Fermi gas of ^{40}K.

To this end, we first realized a deeply degenerate Fermi gas of ^{40}K at a temperature $T/T_F = 0.14$, just below the critical temperature for superfluidity. The chapter 3 of this work detailed the key steps that were necessary to achieve this initial milestone, from the loading of the optical dipole trap to the ensuing phases of evaporative cooling to finally reach degeneracy. After a brief description of both the Landau-Fermi liquid theory and the Tomonaga-Luttinger liquid model in chapter 4, the chapters 5 and 6 summarized the experimental progresses regarding the implementation of the 2D optical lattice that will be used to confine the ^{40}K in 1D. We laid out in chapter 5 the experimental considerations regarding the tunability of the dimensionality of our system as well as the apparatus used to generate the 2D lattice with large spacing. Such spacing is a necessary means to guarantee a very long tunneling time and thus obtain independent tubes, even in the regime where the confinement is too weak to create a quasi-1D gas. Finally, the two-single site imaging systems were presented. Owing to their high resolution, they make it possible to resolve each tube. Chapter 6 is dedicated to the realization of a degenerate Fermi gas in reduced dimensions. The strategy employed to adiabatically transfer atoms into a single 1D lattice before loading them in the 2D standing wave was discussed. Using the high resolution imaging along the y-direction, the lattice spacing of 2.29 µm was obtained from the in-situ density profile of the microtraps. Additionally, the depth of both 1D lattices was calibrated using matter-wave diffraction and measurement of their transverse frequencies presented. The

2D lattice was also loaded and an optical repumper installed. By transferring all but a single row of tubes into dark states, single tube imaging along the $y-$direction was achieved. Finally, the realization of degenerate Fermi gases in two dimmensions composed of 250 atoms per spin state at a temperature of $T/T_F = 0.34$ was reported.

Outlook

The next milestone will be the realization of a deeply degenerate 1D Fermi gas. A possible strategy would be to recompress the x-lattice before ramping up the y-lattice. Once in the 2D-lattice, the optical power of the ODTs will be reduced in order to decrease the trapping frequency along the longitudinal direction of the standing wave. Owing to the optical pumping into the dark states, the estimation of T/T_F and $T_F/\hbar\omega_\perp$ in the 1D and 3D regimes will be possible via in situ imaging of the density profiles. Following the realization of a 1D Fermi gas, our experimental platform would allow us to address numerous physical phenomena in addition to the dimensional crossover. A first possible experiment will be the exploration of thermalization in 1D. As developed in sec. 6.6, thermalization of fermions confined in one dimension still remains to be proven given the integrability of the Hamiltonians describing quantum gases in 1D. The breakdown of integrability can be investigated by probing the evolution of the spin diffusion coefficient with respect to the magnetic field. After subjecting the two component Fermi gas to a magnetic gradient, the centers of mass of each component will be spatially separated due to the 10 % difference in magnetic moment. Once brought out-of-equilibrium, the gradient can be switched off and we will probe the relaxation dynamics of the Fermi gas for various interaction strengths, the main signature of relaxation being the relaxation time, which should depart from the value obtained for a non interacting gas.
Results on integrability would also be an initial step to study the validity of the Luttinger theory. Being a free field theory, the Tomonaga-Luttinger liquid model does not contain any mechanism of relaxation or equilibration [217]. Moreover, deviations from this theory are expected when the interaction between particles increases and becomes comparable to the kinetic energy [217]. More importantly, strongly interacting system can also be used to observe deviations to purely one-dimensional models due to the possibility of virtual transitions to the transverse excited states of the confining potential.
Finally, based on a proposition from [243], a two-component Fermi gas of ^{40}K confined in 1D might be a very promising system for the observation of itinerant ferromagnetism. In the ferromagnetic phase, all atoms are in the same superposition of the two spins and one thus has a system of identical fermions. The paramagnetic phase is defined as a statistical mixture of the two spin components and thus requires less energy than the ferromagnetic configuration.

In three dimensions, according to the Stoner criterion [244], the ground state of the system is the paramagnetic state unless the repulsive interactions between the components are strong enough to compensate the energy difference between the two phases. Using ultracold atoms, one could increase the repulsive interaction above the Stoner criterion by ramping the magnetic field close to an s-wave Feshbach resonance. However, due to the increased inelastic losses due to the formation of dimers, the ferromagnetic state could not be stabilized [245–247]. In reduced dimensions, the energy difference between the two phases is larger than in 3D. However, this can be overcome by sitting between the s-wave Feshbach resonance between the $m_F = -9/2$ and the $m_F = -7/2$ states located at 202 G (even wave in 1D) and the p-wave resonance for the $m_F = -7/2$ state at 198.8 G (odd wave in 1D). One can thus have both strong repulsive interactions above the Stoner criterion as well as a momentum-dependent odd wave interaction among one of the spin components, with the latter resulting in the groundstate to be ferromagnetic [243] . While already observed in 2D semiconducting Van der Walls crystals [248], ^{40}K appears as a promising system for the observation of itinerant ferromagnetism in 1D using ultracold atoms.

Chapter 8

Acknowledgements

By reading this manuscript, one can learn about the results achieved using the FerMix apparatus since I joined the Ultracold Fermi Gases group in late 2015. However, one fundamental aspect that deserves to be emphasized is that those milestones and achievements have only been possible thanks to the countless efforts of various personalities working together to accomplish a common goal. Over the next few pages, I would like to personally thank all of the people that took part in and helped me during the amazing journey that was my PhD.

First of all, I would like to express my gratitude to Roberta Citro, Robin Kaiser, Giacomo Roati and Jook Walraven for being part of my jury and for the evaluation of my work.

Second, I would like to thank the permanent members of the Ultracold Fermi Gases group: Frédéric Chevy, Christophe Salomon and Tarik Yefsah. Christophe and Frédéric gave me the opportunity to join the group for my master internship and then my PhD. As they give a lot of autonomy and trust to PhDs in the lab, I was able to grow as a physicist but also to discover various aspects of project managing. I was also impressed by Frédéric deep understanding of virtually every physical phenomena and his insatiable curiosity. Tarik joined the group as a permanent member in early 2016 and used his limitless energy to instigate right away profound changes to not only improve the machine but also the group dynamics. He is also a man of many, many stories and I am truly grateful for our conversations about physics as well as more profound and personal ones.

Third, I would like to thank Julian Struck. Julian joined in 2018 as a JRC researcher with the objective of implementing his project regarding the study of the 3D-1D dimensional crossover in ultracold Fermi gases. His deep knowledge about cold atom experiments combined with his unwavering dedication in the lab resulted in the achievement of great milestones as well as improvements of nearly every single aspect of the FerMix apparatus. Julian was always willing to share his vast knowledge about both experimental and theoretical aspects of cold atoms experiments. I was thus able to grow a lot as an experimentalist and a physicist during the time we worked together in the lab.

This work also represents the collective efforts of several generations of PhD students and I would like to thank a few of them for the time we shared in the lab: Daniel Suchet, Mihail Rabinovic, Thomas Reimann, Markus Bohlen, Clément De Daniloff and Marin Tharrault. Daniel started writing when I joined the group for my internship. Despite that, he still took the time to teach me about the machine and let me know some of the quirks of FerMix. We also shared a similar interest in giving scientific conferences for a wider audience and he helped me out several times with both his advice and contacts. Mihail was the senior PhD when I started mine and I was able to develop my experimental skills in electronics thanks to his great experience and knowledge in those topics. I was also able to polish (sometimes against my will) my knowledge of both classical music and Rihanna thanks to him. I never realized how deep "B**** better have my money" and "Umbrella" were before working in FerMix and I am particularly grateful for that.

Moreover, I would like to give a special thank to Thomas Reimann. First, because he strongly suggested several times that he wants one and second, because he truly deserves it. What started as a master-padawan relationship became a fantastic friendship over the years. As soon as I joined the lab, Thomas offered to show and teach me how the machine was working. At the time, he probably didn't realize that this would lead him to completely waste his week-ends for the next few weeks by having to show up at 8 o'clock in the morning so that I could discover the machine at my own pace without slowing down the entire team. This time was also a good occasion to discover our many similarities and similar tastes. Thanks to his joyful personality, peculiar sense of humor and eclectic taste of music, working in the lab was always fun. However, to some extend, Thomas' biggest impact on my PhD was outside the lab. I truly cherished the countless evenings and nights we spent "working" in P9 and the mezzanine as well as all the time we spent outside of LKB.

Markus, joined a year after I started my PhD and he quickly participated in the great lab atmosphere. Even though he left the lab before we could complete our latest projects described in this manuscript, I am sure that he and the rest of the Hamburg team will accomplish great things during the remaining years of his PhD. The next generation is composed of Clément and Marin. And even though I only overlapped for 8 months with Clément, I was already impressed by his dedication in the lab, his willingness to always learn new things and his quick thinking. I was also impressed by his mastery of many video games and some other hidden talents that would truly emerge outside the lab. Even though I resent him for besting me so easily at guitar hero III, I am certain the experiment will produce many amazing results under his and Marin's care.

I am also extremely grateful to the several interns, PhDs and postdocs from the Lithium team for the fruitful discussions, help and fun during those years: Marion Delehaye, Sébastien

Laurent, Shuwei Jin, Matthieu Pierce, Gentle Dash, Ragheed Alhyder, Kunlun Dai, Joanna Lis, Darby Bates and Bruno Peaudecerf.
Similarly, I would like to thank the fellow PhDs and postdocs of LKB and in particular Chayma Bouazza, Raphaël Saint-Jalm, Torben Pöpplau, Mohamed Baghdad and Lucas Béguin.
I would also like to thank Thomas Reimann, Julian Struck, Clément De Daniloff, Marin Tharrault and Karine Enesa for the proof reading of this manuscript and their helpful tips.
I would also like to express my gratitude to all the members of the workshops and the administration for their invaluable helps. In particular, I would like to thank Mathieu Sardin, Allan Hourdry, Didier Courtiade, Célia Ruschinzik, Catherine Gripe and Théo Charpentier for their constant help with the experiment as well as with personal side projects such as homemade Bluetooth speakers.
For their lectures, advice and/or help when I needed it during my master and my PhD, I would like to give my special thanks to Baptiste Allard, Lucile Julien, Alice Sinatra, Michel Talon, Matthieu Tessier and Philipp Treutlein.
Additionally, over the last four years and even long before, I had the chance to benefit from the support of many friends. Unfortunately I will not be able to thank each of them as much as I would like to. Nevertheless, I would like to express my deep gratitude to:

- All of the first (Oliv, Pitch, Enac, Vanish...) and second generation (Louise, Eléna, Margaux) members of *Les Pécores* for all the awesome moments, such as vacations in Croatia and annual visits to the "Percée du Vin Jaune".

- Ophé, Vigor, Audrey, Hortense and my other *Meuh-Meuh* friends. A special thanks to my dear "fillotte" Marine for her constant support, even when I had to stay in the lab on Christmas' eve because our AC had decided to stop working.

- My various roommates (Milica, Lauriane, Danijela, Marylou, Elena, Matthieu...) for all the fun times, stimulating discussions and the support during the tough times.

- My fellow physicist friends, which I made along the way (Andrea, Guillaume, Johannes...).

- All the amazing friends and special relationships in my life (Bichon, Céline, Ti Bouchon, Marie...).

Finally, I need to express my deepest gratitude to my family, particularly to Laure, Brigitte, Vigea, Didier, Folly, Karine and my precious Nora. I have been truly blessed to have such a fantastic family.

Appendix

Appendix A

Supplementary theoretical and experimental material

A.1 Absorption imaging and thermometry of ^{40}K

In the FerMix experiment, all atomic properties of ^{40}K are obtained using absorption imaging, standard technique to measure the density and momentum distribution of an atomic ensemble. Resonant light is sent towards the atoms and then observed using a CCD camera. The light being absorbed by the atoms, the atomic cloud casts a shadow on the recorded beam profile. In the limit of weak light intensities I_0 with respect to the saturation intensity I_{sat}, the transmitted intensity of the beam profile $I_{trans}(x,y)$ after its propagation through the cloud can be obtained using the Beer-Lambert Law:

$$I_{\text{trans}}(x,y) = I_0(x,y)e^{-OD(x,y)}. \tag{A.1}$$

I_0 represents the initial beam intensity while $OD(x,y)$ denotes the optical density. The latter can be approximated as:

$$OD(x,y) = \sigma n(x,y), \tag{A.2}$$

with $n(x,y) = \int_z n(x,y,z)$ being the integrated column density along the propagation axis z of the imaging beam and σ the scattering cross-section. Close to the atomic resonance frequency, the scattering cross-section can be written as [249]:

$$\sigma = \sigma_0 \frac{C^2}{1 + 4\Delta^2/\Gamma^2 + I_0/I_{\text{sat}}}. \tag{A.3}$$

Here $\Delta = \omega_{\text{Light}} - \omega_0$ is the detuning between the frequency of the imaging laser and the resonance frequency of the atoms and Γ refers to the linewidth of the addressed atomic transition. In this formula, the coefficient C denotes the Clebsch-Gordon coefficient of the atomic transition. For a closed transition, such as the transition between the levels $|1\rangle$ and $|1'\rangle$ at high magnetic field described in sec. 3.6, $C^2 = 1$ while in the absence of magnetic field and quantization axis, for the D2-line of ^{40}K, $C^2 = 0.4$ due to the averaging over all the possible

transitions [70]. Finally, $\sigma_0 = \frac{3\lambda_L^2}{2\pi} = 2.81 \times 10^{-13}\,\mathrm{m}^2$ is the theoretical resonant cross-section. The expression of the transmitted intensity along with the one for the theoretical cross-section are only valid in the regime $I_0 \ll I_{\mathrm{sat}}$ and for dilute gases. For very dense atomic cloud, the imaging beam cannot illuminate the entire cloud, causing part of the atoms to not be detected. As a consequence, the optical density is always kept below 1 during absorption imaging.
Theoretically, by using equation A.1, two pictures of the imaging beam (with and without the atoms) would be sufficient to reconstruct the optical depth and the integrated column density $n(x,y)$. However, experimentally, a CCD camera detects any neighboring source of light on top of the imaging beam. This parasitic light source has to be subtracted from the imaging beam in order to reconstruct the optical density from the pictures of the CCD camera. This yields the following formula for the optical density:

$$OD(x,y) = -ln\left(\frac{I_{\mathrm{trans}}(x,y) - I_{\mathrm{bg}}(x,y)}{I_0(x,y) - I_{\mathrm{bg}}(x,y)}\right). \tag{A.4}$$

$I_{\mathrm{bg}}(x,y)$ is obtained by taking a picture in absence of any imaging light while $I_{\mathrm{trans}}(x,y)$ and $I_0(x,y)$ respectively denote the absorption picture and a picture of the imaging light in absence of atoms. The total atom number N is then simply obtained from the column density:

$$N = \int_{x,y} n(x,y) = \frac{1}{\sigma}\int_{x,y} OD(x,y). \tag{A.5}$$

In order to obtain $I_{\mathrm{trans}}(x,y)$, one can either take an in-situ picture of the atoms while they are still confined by the trapping potential [1] or after switching off the confinement prior to imaging, leaving the atomic cloud to freely expend during few ms. This time-of-flight (TOF) technique also provide the momentum distribution of the cloud as well as its temperature, assuming that the particles are weakly interacting and thus conserve their initial momentum during the ballistic expansion.

Free ballistic expansion from an harmonic potential

For a non-interacting gas, released at $t = 0$ from an harmonic potential, the momentum $p_i(t)$ and the position $x_i(t)$ of each particle after a time t (where $i = (x,y,z)$) of ballistic expansion can be obtained from its momentum and position at a previous time. More precisely, in absence of any potential, the momentum of each particle is conserved during the expansion and the

[1] The advantage of in-situ imaging relies on the fact that it provides the density of the cloud as they are trapped in the confinement. However, it also does not give any reliable information regarding the temperature of the cloud. Moreover, most of the times, the spatial density is usually too high to accurately count the total atom number.

position $x_i(t)$ of each particles evolves as:

$$x_i(t) = x_i(0) + \frac{p_i(0)}{m}t. \tag{A.6}$$

In this situation, the cloud size and the spatial density distribution can provide a direct indication of the temperature of the atomic ensemble. Considering a phase-space distribution $f(\mathbf{r},\mathbf{p})$, the density distribution can be obtained by integrating the phase-space distribution function over the entire momentum space. For a 3D gas, one obtains:

$$n(\mathbf{r},\mathbf{p}) = \frac{1}{(2\pi\hbar)^3}\int_{\mathbf{p}} f(\mathbf{r},\mathbf{p}). \tag{A.7}$$

For a classical gas, the distribution $f(\mathbf{r},\mathbf{p})$ is given by the Boltzmann distribution while for a degenerate Fermi gas it corresponds to the Fermi-Dirac distribution:

$$f(\mathbf{r},\mathbf{p}) = f_B(\mathbf{r},\mathbf{p}) = Ze^{-\beta H(\mathbf{r},\mathbf{p})} \tag{A.8}$$

for $T \geq T_F$ and

$$f(\mathbf{r},\mathbf{p}) = f_{FD}(\mathbf{r},\mathbf{p}) = \frac{1}{\frac{1}{Z}e^{\beta H(\mathbf{r},\mathbf{p})}+1} \tag{A.9}$$

for $T \leq T_F$. Here, $\beta = 1/\mathrm{k_B}T$, $Z = e^{\beta\mu}$, with μ being the chemical potential and $H(\mathbf{r},\mathbf{p})$ denotes the Hamiltonian of the system. At $t = 0$, $H(\mathbf{r},\mathbf{p},t=0)$ is simply equal to:

$$H(\mathbf{r},\mathbf{p},t=0) = \frac{p^2}{2m} + \frac{m}{2}\sum_i \omega_i^2 x_i^2 \tag{A.10}$$

with ω_i representing the trapping frequencies of the harmonic oscillator along the i direction. After a time t, using the equation A.6 and the expression of the Hamiltonian, one can calculate the density distribution from equation A.7 in both classical and the degenerate regime [73]. In the classical case, one can find:

$$n(\mathbf{r},t) = \frac{1}{2\pi^2\hbar^3}\sqrt{\frac{\pi}{2}}\frac{1}{Z}\left(\frac{\beta}{m}\right)^{-3/2}\prod_i \frac{exp(-\beta m\omega_i^2 x_i^2/2(1+\omega_i^2 t^2))}{\sqrt{1+\omega_i^2 t^2}}.$$

The 2D and 1D density profile can then simply be obtained by integrated along 1 or 2 direction $n(\mathbf{r},t)$. For example the 1D-density evolves as:

$$n_{1D}(x,t) = \int_{y,z} n(\mathbf{r},(t) = \frac{1}{\sqrt{2\pi}\hbar^3}\frac{1}{Z}\frac{m^{1/2}}{\beta^{5/2}\omega_y\omega_z}\frac{1}{\sqrt{1+\omega_x^2 t^2}} exp\left(-\beta\frac{1}{1+\omega_x^2 t^2}\frac{m\omega_x^2 x^2}{2}\right). \tag{A.11}$$

The evolution of the density with respect to time being Gaussian one can extract the evolution of the width of the atomic cloud:

$$\sigma_i^2(t) = \sigma_i^2(0)(1+\omega_i^2 t^2), \tag{A.12}$$

with $\sigma_i^2(0) = 1/\beta m\omega_i^2$. Consequently, one can obtain the temperature of the atomic cloud T by taking successive absorption images for various time-of-flight duration t and fitting the measured cloud radii using the eq. A.12. Additionally, by knowing the trapping frequencies, one could also extract the cloud temperature from a single picture taking after a given time-of-flight. While being exact for a classical gas, this method is only a good approximation for a degenerate gas for temperature $T/T_F \geq 0.3$ (see [73] for a complete analysis).
Using the Fermi-Dirac distribution in equation A.7, one can find for the expression of the 2D and the 1D density profiles:

$$n_{2D}(x,y,t) = \int_z n(\mathbf{r},t) = -\frac{m}{2\pi}\frac{(\mathrm{k_B}T)^2}{\hbar^3\omega_z}\prod_{i=x,y}\frac{1}{\sqrt{1+\omega_i^2 t^2}}\mathbf{Li_2}\left[-Zexp\left(-\beta\frac{m}{2}\sum_{i=x,y}\frac{\omega_i^2 x_i^2}{1+\omega_i^2 t^2}\right)\right]. \tag{A.13}$$

$$n_{1D}(x,t) = -\sqrt{\frac{m}{2\pi}}\frac{(\mathrm{k_B}T)^{5/2}}{\hbar^3\omega_y\omega_z}\frac{1}{\sqrt{1+\omega_x^2 t^2}}\mathbf{Li_{5/2}}\left[-Zexp\left(-\beta\frac{m}{2}\frac{\omega_x^2 x^2}{1+\omega_x^2 t^2}\right)\right]. \tag{A.14}$$

The width and the amplitude of the cloud being related, the density profiles only depend on two parameters, presuming that the trapping frequencies are known. This allows to simultaneously determine the atom number and the cloud temperature. Moreover, as discussed in sec 3.6, one can also use the expression of the density profile to extract the ratio T/T_F from the shape of the cloud.

A.2 Calibration of an imaging system magnification

Propagation of the imaging beam and the shadow casted by the atoms is rendered possible by the use of an optical system. A first lens (or objective) with a focal length f_1 is placed such that its focal plane coincides with the position of the atoms and a second lens of focal length f_2 is placed at a distance f_1+f_2 from the first one. Finally, the CCD camera is placed in the

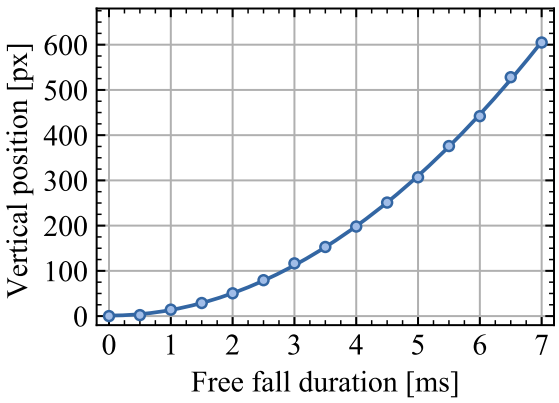

Fig. A.1 **Example of the calibration of an imaging system using a free fall experiment**. Atoms are only subjected to the gravitational potential and thus experience a free fall. The CoM position along the gravity axis is recorded to obtain the magnification from the fitted parabola. Our measured magnification for the $y-$imaging system is $M = 32.7 \pm 0.1$.

focal plane of the second lens [2]. While the theoretical magnification is given by the ratio of the two focal lengths $M = f_2/f_1$, it still needs to be verified experimentally. This can be achieved by letting the atoms fall freely and recording their center-of-mass position. In the absence of any external force (such as a magnetic gradient or a trapping potential), the atoms will only be subjected to gravity. Thus, the center of mass position along the gravity axis will simply evolve as $z(t) = z_0 + 1/2gt^2$, with g being the gravitational acceleration. Due to the magnification of the optical system, on the camera, the projected distance travelled during a free fall will be modified such that:

$$\bar{z}(t) = \frac{1}{M\alpha}(\bar{z}_0 + 1/2gt^2), \tag{A.15}$$

with α is the pixel size of the camera and $\bar{z}$ the position in unit of α. The pixel size being known, the magnification is the only free parameter of this equation. To illustrate this method, the figure A.1 represents the calibration of the imaging system along the $y-$axis using a free fall experiment.

A.3 Measurement of trapping frequencies

Extracting quantities such as the density or the temperature of an atomic ensemble requires the knowledge of the trapping frequencies of the harmonic confinement (see eq. A.12). For optical dipole traps created by Gaussian beams, one can measure them by exciting center-of-mass oscillations or breathing modes. The underlying assumption is that the Gaussian beam can be approximated by an harmonic oscillator. This is true under the condition that the temperature of the cloud is low enough with respect to the trap depth for the atoms to not explore the anharmonicity of the confinement [3].

Excitations of those collective oscillations can be achieved by rapidly modifying the optical

[2] Eventually, in order to achieve high magnification, one can also use a relay telescope between the two lenses such as described in sec. 5.3.1 for example.

[3] In practice, this condition can be met when $\eta = u_0/\mathrm{K_B}T \geq 8$

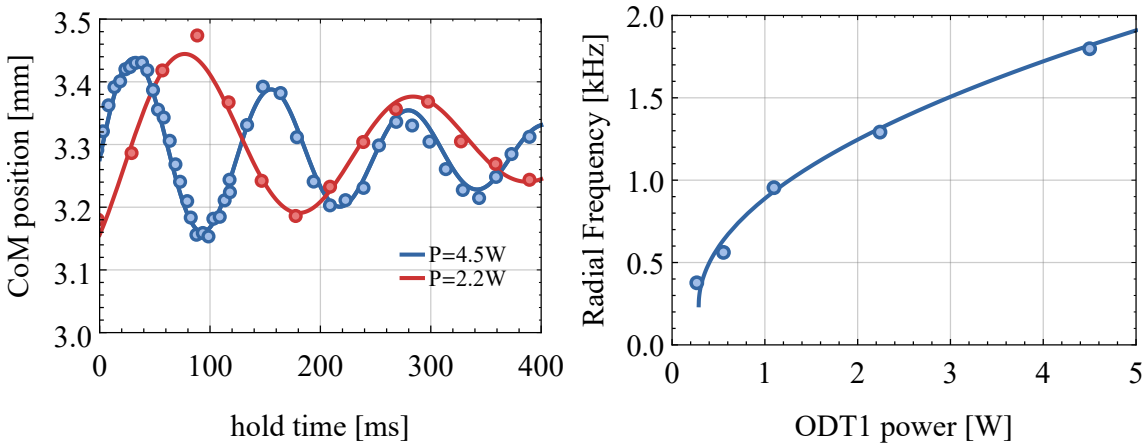

Fig. A.2 **measurement of harmonic trapping frequencies**. (a) Axial center of mass oscillations for different power. The oscillation frequency decreases with the optical power. (b) Evolution of the radial trapping frequencies with respect to the optical power. The waist $\omega = 39.8$ can be obtained as a fit parameter.

confinement, thus abruptly transferring them energy while keeping them trapped. This can be achieved by either switching off completely the optical confinement for a very short time (typically during less than 100 µs) and then switching it up back to its initial value or by using a magnetic gradient to accelerate the atoms. The atoms are then held in the original optical confinement for a given amount of time t_{hold} before proceeding to standard absorption imaging. By varying t_{hold}, one can reveal the oscillatory behaviour of the atomic cloud. Figure A.2a shows the center-of-mass oscillations along the horizontal direction for various power of the ODT1. Trapping frequencies being a function of only two parameters of the optical dipole trap (its waist and the optical power shined on the atoms), one can use the trapping frequencies to measure the waist of an optical dipole trap. More precisely, the radial and axial trapping frequencies evolve as:

$$\nu_\perp = \frac{1}{2\pi}\sqrt{\frac{4U_0}{m\omega_0^2}} \qquad \text{and} \qquad \nu_\parallel = \frac{1}{2\pi}\sqrt{\frac{2U_0}{mz_R^2}}, \tag{A.16}$$

with $U_0 \propto P$ being the depth of the optical potential. Estimation of the waist of the ODT1, using the radial trapping frequencies is available in fig. A.2b. Additionnally, another method consists in inducing parametric heating. To this end, one needs to modulate the laser intensity at twice the trapping frequency in order to cause transition between states of even parity (for a 1D harmonic oscillator it corresponds to transition between the states $|n\rangle$ and $|n \pm 2\rangle$) of the

harmonic oscillator [238]. Experimentally, the induced heating can be measured by recording both the atom number and the size of the atomic cloud. For small heating, the atoms remained trapped and one can see their temperature increasing when the modulation gets closer to twice the trapping frequency. For stronger heating, atoms have enough kinetic energy and can leave the trap. Parametric heating was used to measure the radial trapping frequencies of both $x-$ and $y-$lattice. An illustration of this method is presented in figure 6.8. It represents the typical evolution of both the atoms number and the cloud size with respect to the modulation frequencies.

A.4 Spin-selective imaging at low magnetic field

At low magnetic field, the Zeeman shift between the different Zeeman states is too small to allow spin-selective imaging. In order to still probe the spin composition of an atomic ensemble kept in an optical dipole trap [4], two methods can be used: a Stern-Gerlach experiment or the use of microwave transitions.

Stern-Gerlach imaging

Stern-Gerlach experiment is one of the most well-known methods to probe the composition of an atomic cloud. It can be achieved by keeping a magnetic gradient on during a time of flight experiment. As a consequence, atoms in different spin states will propagate at a different speed due to the difference between the magnetic moment. Thus after few ms of ToF, one can separate the CoM of atoms in different spin states. Mpre precisely, the acceleration experienced by atoms in a given zeeman states $|\alpha\rangle = |F, m_F\rangle$ is given by:

$$\mathbf{a}_\alpha = -g + \frac{1}{m}\nabla(\mu_\alpha \cdot \mathbf{B}). \tag{A.17}$$

The magnetic moment $\mu_\alpha = \frac{\partial E_\alpha}{\partial B}\Big|_{B=B(r,t)}$ is obtained by taking the derivative of the energy E_α of the Zeeman state α with respect to the value of the magnetic field (see appendix A.5 for details). The distance covered by each atoms along gravity can then be obtained by numerically integrated twice the equation giving the evolution of the position. When the distance between two different spin states is larger than the spread of the cloud $2\sigma(t) = 2\sqrt{\sigma_0^2 + \mathrm{k_B}T/m \times t_{\mathrm{ToF}}^2}$, the population of each spin states can be resolve. Consequently, for high temperature, the atoms will expand quickly and thus both strong magnetic gradients and high difference between the various magnetic moments are necessary to resolve the different spin states. Theoretical

[4] In a magnetic trap, one can probe the spin composition of an atomic assemble by reducing the magnetic gradient until the confinement becomes weaker than the gravitational field as explained in sec 3.2.

simulations of our Stern-Gerlach procedure are available in [74]. Experimentally, we perform our Stern-Gerlach by first precharging the capacitors of the Blue power supply connected to one of the inner coils (see fig. 3.3) while keeping its corresponding IGBTs open. During this step, atoms are kept in the optical dipole trap and a small bias field (of up to 20 G) generated by the outer coils is providing the quantization axis. Precharging the capacitors allow us to generate strong currents of up to 100 A in typically 2 ms [5]. Just after switching off the optical confinement, the IGBTs connecting to Blue get closed, creating a strong current pulse. The peak current is equal to 60 A, which corresponds to a magnetic gradient of 150 G.cm^{-1} and is reached after 2 ms. After this short pulse, the IGBTs are opened and the atoms accelerated by the magnetic gradient fly against gravity. After up to 10 ms of ToF (depending on the temperature of the atomic cloud), standard absorption imaging is performed.
Two drawbacks arise from our Stern-Gerlach experiment. First, because of the strong currents necessary to spatially separate the different spin states, strong parasitic Foucault currents are induced and persist for up to 12 ms. This causes a strong spatial inhomogeneity of the magnetic field during the imaging process and thus the different spin states do not share either the same resonance frequency nor the same detectivity. To circumvent this issue, optical repumping during ToF was introduce in order to transfer the atoms into the Zeeman states $m_F = \pm 9/2$ after the SG pulse and just prior to imaging. Nonetheless, SG technique can only be employed for cold sample due to the thermal expansion of the cloud. On our experiment, Stern-Gerlach experiment can only be used for temperature up to 10 µK. For hotter temperatures, the thermal expansion is too big to reliably separate the different spin components with a magnetic gradient and thus MW spectroscopy has to be used.

Optical repumping after Stern-Gerlach

In order to reliably determine the spin composition of the atomic cloud after a Stern-Gerlach, the detectivity of atoms in different spin states must be identical. This can be made possible by imaging each spin states using closed transitions. To this end, after separating atoms in different spin states using the Stern-Gerlach technique, we transfer them into the stretched states $m_F = \pm 9/2$ prior to imaging. Consequently, after Stern-Gerlach and prior to imaging, pure $\sigma^{\pm}$ polarized light is shined along the quantization axis . Experimentally, we optimized the polarization of the pulse (via tuning the angle of the $\lambda/4$ waveplate of the optical pumping represented in figure 5.8), its duration and its frequency by looking at the relative detectivity of the different spin states after a SG experiment as presented in fig. A.3. The optimal duration was found to be 10 µs. For longer pulse, the atoms heat up a lot due to the many absorption cycle while for shorter one, the detectivity of the $m_F = 7/2$ and $m_F = 5/2$ was not optimal.

[5] Without any precharging, our standard power supplies typically take 5 ms to reach such current.

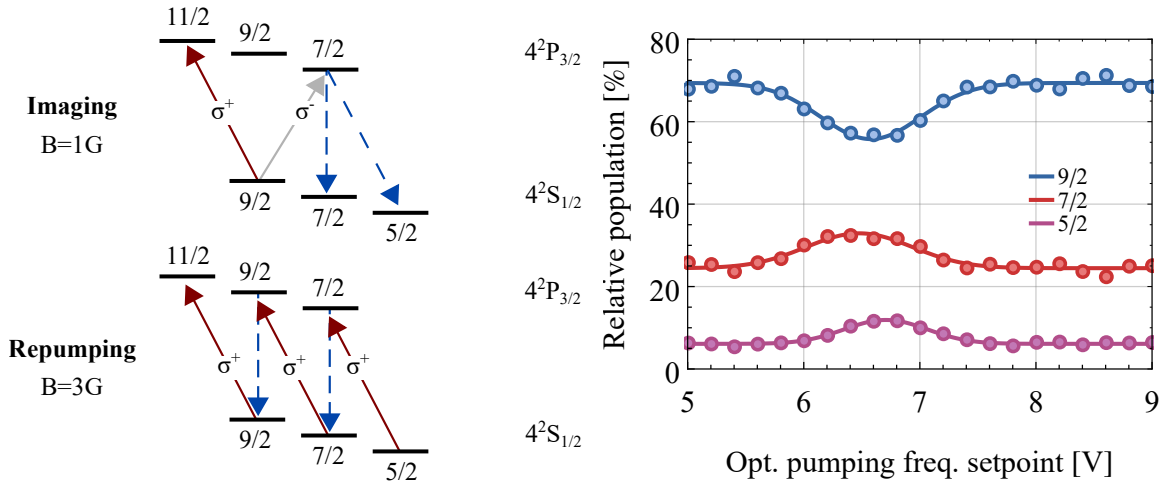

Fig. A.3 **Optical pumping and imaging transition at low magnetic fields**. (a) Imaging principle along the $x-$axis with horizontal polarization with respect to the quantization axis and optical repumping transitions into the $m_F = 9/2$ stretched state prior to absorption imaging. (b) Scan of the repumping frequency prior absorption imaging.

The fig. A.3 shows the evolution of the relative detectivity of each spin states with respect to the frequency of the optical pumping beam. By tuning the frequency to resonance, owing to their transfer into the $m_F = 9/2$ zeeman state, the detectivity of atoms in $m_F = 7/2$ and $m_F = 5/2$ increased. Consequently, the relative population of those spins states in comparison to atoms in $m_F = 9/2$ increased. In absence of any optical repumping the imaging resonance scan of atoms in $m_F = 9/2$, $m_F = 7/2$ and $m_F = 5/2$ greatly differ from one another because of the strong spatially dependent parasitic gradient induced by the SG procedure detailed in appendix A.4. In presence of the optical pumping, the imaging resonance scan of all the spin states coincide with the one of atoms in $m_F = 9/2$ (as depicted in fig. A.4). Finally, a picture of atoms using Stern-Gerlach with and without any optical pumping is depicted in figure. A.5.

Spin selective imaging using MW spectroscopy

Magnetic dipoles transitions can be used to connect the lower hyperfine groundstate manifold $F = 9/2$ and the upper one $F = 7/2$as explained in sec. 3.4. By using them, atoms in given spin state $|F = 9/2, m_F\rangle$ of the $F = 9/2$ groundstate manifold can be transferred to the upper manifold. Due to the large energy splitting of $\sim 1.2858\,\mathrm{GHz}$, atoms in the upper manifold will be transparent to the imaging light during absorption imaging. Consequently, by recording the atoms number with and without the transfer to the $F = 7/2$ manifold, one can infer the initial

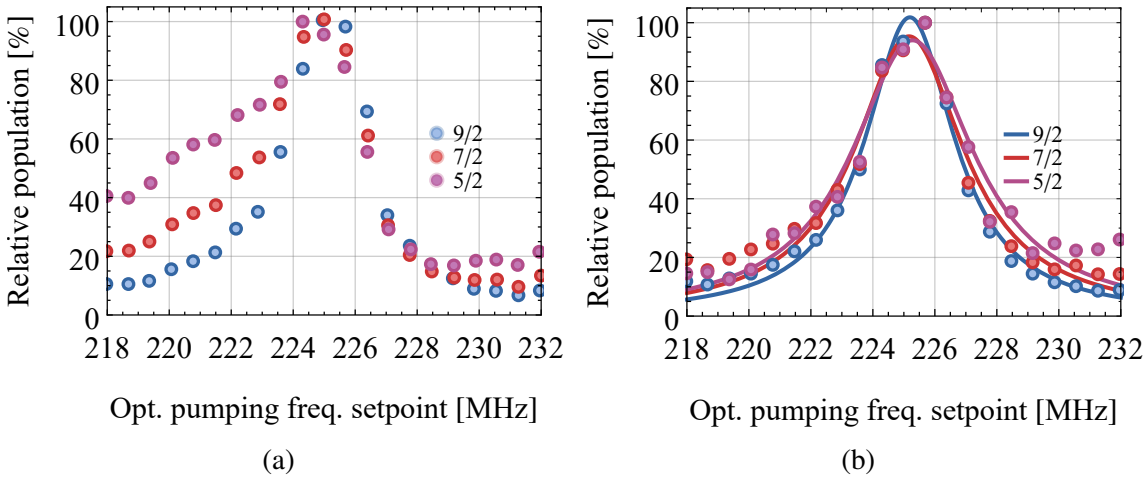

Fig. A.4 **Scan of the resonance imaging frequency after a SG**. (a) Without optical pumping, due to the remaining parasitic current, the resonance profile of atoms in $m_F = 9/2, 7/2$ and $m_F = 5/2$ are completely different. (b) By pumping the atoms prior to imaging, we transfer them into the $m_F = 9/2$ zeeman state. The resonance profile of atoms originally in the $m_F = 5/2$ and $m_F = 7/2$ zeeman states coincide with the $m_F = 9/2$ profile and the Lorentian fit for all three states are similar.

atom number in a given spin state from the apparent atomic loss [6]. The transfer of atoms to the $F = 7/2$ manifold is done via Landau-Zener sweep (see sec. 3.4 for a description of the Landau-Zener adiabatic transfer). For the positive Zeeman states of interests $m_F = 9/2, 7/2$ and $5/2$ [7], the possible hyperfine transitions are:

$$|F = 9/2, m_F = 9/2\rangle \rightarrow |F = 7/2, m_F = 7/2\rangle, \quad (\sigma^-) \tag{A.18}$$
$$|F = 9/2, m_F = 7/2\rangle \rightarrow |F = 7/2, m_F = 7/2\rangle, \quad (\pi) \tag{A.19}$$
$$|F = 9/2, m_F = 7/2\rangle \rightarrow |F = 7/2, m_F = 5/2\rangle, \quad (\sigma^-) \tag{A.20}$$
$$|F = 9/2, m_F = 5/2\rangle \rightarrow |F = 7/2, m_F = 7/2\rangle, \quad (\sigma^+) \tag{A.21}$$
$$|F = 9/2, m_F = 5/2\rangle \rightarrow |F = 7/2, m_F = 5/2\rangle, \quad (\pi) \tag{A.22}$$
$$|F = 9/2, m_F = 5/2\rangle \rightarrow |F = 7/2, m_F = 3/2\rangle, \quad (\sigma^-), \tag{A.23}$$

and are represented in figure A.6. Experimentally, the MW transfer is done at 3 G. At this magnetic field, the Zeeman splitting between the various Zeeman states, which can be calculated using the Breit-Rabi formula (see appendix A.5), is sufficiently large to be able to perform

[6] Under the assumption that the transfer efficiency is well known

[7] When atoms are transfer to the negative states, one can ramp the magnetic field to the zero crossing to perform selective imaging at high field.

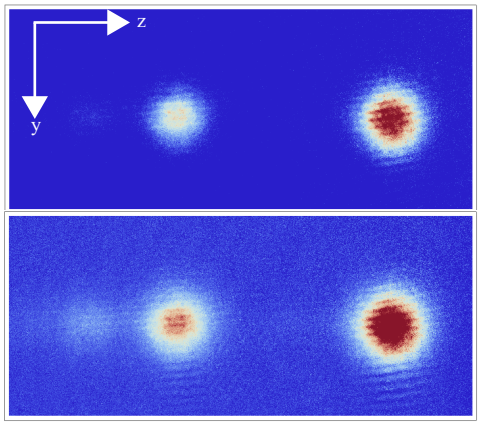

Fig. A.5 **SG picture taken along the x-imaging**. (Top) In absence of repumping the population in $m_F = 5/2$ is barely visible. (Bottom) Owing to the optical pumping, the spin states ($m_F = 5/2$ and $m_F = 7/2$) detectivity increased and one can see the signal of $m_F = 5/2$ (Left) and $m_F = 7/2$ (middle) greatly improved while not deteriorating the signal of $m_F = 9/2$ (right).

Landau-Zener sweeps with a bandwidth large enough to cover magnetic field fluctuations. The sweep duration is equal to 10 ms and its span equals to ± 0.25 MHz around the central frequency $\omega_{\text{trans}} \sim 1.2858$ GHz.

To characterize the microwave transfer efficiency, we record the evolution of the atoms number in all three Zeeman states $m_F = 9/2, 7/2$ and $5/2$ with respect to the microwave center frequency ω_{trans}. The atoms number is obtained using our Stern-Gerlach to spatially separate the different spin components and the optical pumping to reliably detect each spin population. The evolution of those three spin population with respect to the frequency of the microwave sweep is presented in figure A.7. Unfortunately the two transitions $|9/2,7/2\rangle \rightarrow |7/2,5/2\rangle$ and $|9/2,5/2\rangle \rightarrow |7/2,7/2\rangle$ coincide and thus, in absence of Stern-Gerlach cannot be used to determine the spin population in either $7/2$ or $5/2$ [8]. Once the efficiency of each transitions characterizes, one can probe the spin composition of the atomic cloud in absence of Stern-Gerlach, and thus perform spin-selective imaging even for atomic cloud hotter than 10 µK. The total atom number in $m_F = 9/2$ will be equal to $\frac{1}{f_{9/2}}(N_i - N_f)$, where N_i represents the total atom number recorded in absence of any resonant microwave sweep, N_f denotes the total atom number remaining after the σ^- microwave sweep addressing the $|9/2,9/2\rangle \rightarrow |7/2,7/2\rangle$ transition and $f_{9/2}$ the efficiency of the transfer, comprised between 0 and 1. Similarly, the population in $m_F = 7/2$ and $m_F = 5/2$ can be determined using the transitions $|9/2,7/2\rangle \rightarrow |7/2,7/2\rangle$ and $|9/2,5/2\rangle \rightarrow |7/2,3/2\rangle$. Finally, after the MW sweeps, a substantial amount of atoms can be the transferred into the upper hyperfine manifold. Collisions between atoms in different hyperfine manifold of the ground state can create inelastic collisions, thus both altering the spin composition of the atomic cloud and potentially leading to inelastic losses. Experimentally, we observed strong inelastic losses after 50 ms. As a consequence, absorption imaging must be perform as fast as possible after the microwave sweep.

[8] For optical transition, due to the difference of polarization between those two transitions, one could polarize the light to address only one of them. For microwave transition, our antennae emit all three types of polarizations.

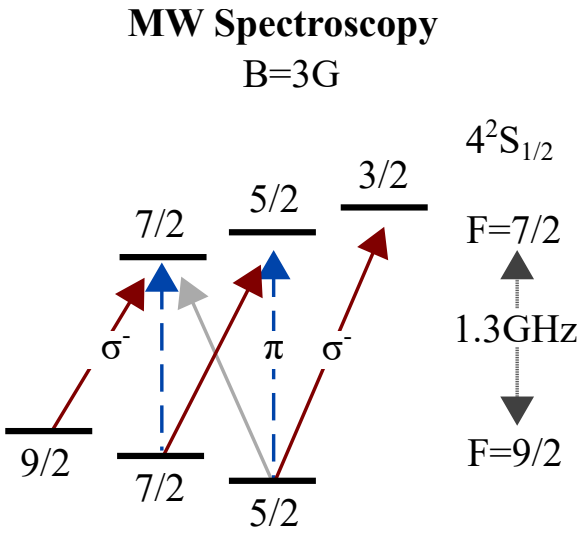

Fig. A.6 **Microwave transitions for the positive states of** ^{40}K. MW transitions between the three spin states $m_F = 9/2, 7/2$ and $m_F = 5/2$ of the $F = 9/2$ groundstate manifold and the $F = 7/2$ upper manifold of the groundstate.

A.5 Alkali atoms in magnetic fields

When subjected to a static magnetic field, non interacting alkali can be described by the following Hamiltonian [130]:

$$H = \frac{\widehat{p}^2}{2m} + \widehat{H}_0 + \widehat{H}_{SO} + \widehat{H}_{HF} + \widehat{H}_Z. \tag{A.24}$$

Here, the first term describes the kinetic energy of the center of mass. $\widehat{H}_0$ describes a single spinless valence electron evolving in a electrostatic field created by the nucleus and the closed electron shell. Similarly to the Hydrogen atom, for Alkali, the energy level of the valence electron depends on the principal quantum number n. However, in case of Alkali, it also depends on the angular momentum $\mathbf{L}$. The modified eigenergies take the form: $E_0(n,L) = -Ry/(n-\delta_{n,L})^2$. Here Ry denotes the Rydberg constant while $\delta_{n,L}$ is the quantum defect. It gives rise to the ground and the first excited state. Using the spectroscopic notation, they are respectively represented by nS and nP and the transition between them goes by the appellation Alkali D-line.

The term $\widehat{H}_{SO}$ corresponds to the coupling between the electronic spin $\mathbf{S}$ and the orbital angular momentum $\mathbf{L}$ and takes the form $\widehat{H}_{SO} = a_{fs}\mathbf{S}\cdot\mathbf{L}$. This interaction lifts the degeneracy of the $\mathbf{J} = \mathbf{L}+\mathbf{S}$ levels. For the groundstate, since $L = 0$, the total electronic spin $J = S = 1/2$. For the excited states, the fine structure interaction separates the first excited states nP into $nP_{1/2}$ and $nP_{3/2}$. The energy splitting between the two excited states is equal to:

$$\widehat{H}_{SO} = a_{fs}(J(J+1) - L(L+1) - S(S+1)). \tag{A.25}$$

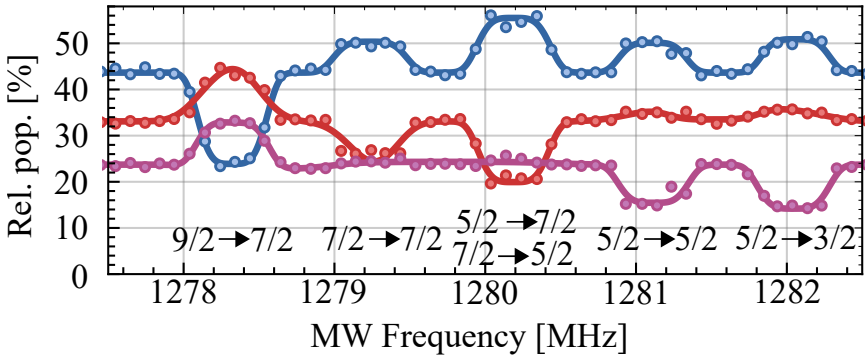

Fig. A.7 **Microwave transitions for the positive Zeeman states**. After a 10 ms sweep the atoms are subjected to the 2 µs SG pulse and then imaged via absorption imaging. Prior to imaging atoms were transferred in the $m_F = 9/2$ Zeeman states with 10 µs of optical pumping. By transferring atoms in a zeeman states to the upper manifold its relative population decreases while the other two spins states relative population increases. Solid lines are super-Gaussian fits and act as a guide to the eye.

The term $\widehat{H}_{HF}$ incorporates the interaction between the total electronic spin $\mathbf{J}$ and the nuclear spin $\mathbf{I}$. This hyperfine interaction lift the degeneracy of the of the $\mathbf{F} = \mathbf{J} + \mathbf{I}$ levels and takes the form:

$$\widehat{H}_{HF} = \frac{a_{hf}}{\hbar^2}\mathbf{I}\cdot\mathbf{J} + \frac{b_{hf}}{\hbar^2}\frac{3(\mathbf{I}\cdot\mathbf{J})^2 + 3/2(\mathbf{I}\cdot\mathbf{J}) - I^2J^2}{2I(2I-1)J(2J-1)}. \tag{A.26}$$

Here a_{hf} and b_{hf} are respectively the magnetic dipole and the electric quadrupole constants. Finally, $\widehat{H}_Z$ represents the interaction between the external magnetic field $\mathbf{B}$ and the various magnetic moments [9]

$$\widehat{H}_Z = -(\widehat{\mu}_I + \widehat{\mu}_L + \widehat{\mu}_S)\cdot\mathbf{B}. \tag{A.27}$$

Asymptotic behaviours

Low magnetic field

For low magnetic field, when the Zeeman energy shift is much smaller than the hyperfine splitting, one can treat the Zeeman effect as a perturbation. As a consequence, in this limit, the eigenstates of the Hamiltonian in absence of magnetic field still constitutes a good set of quantum number. As such, the basis $\{|F, m_F\rangle\}$ can still be used and up to first order in

[9] The magnetic moment $\widehat{\mu}_L$ is related to the orbital angular momentum through the relation $\widehat{\mu}_L = -\mu_B g_L \mathbf{L}$ with $g_L = 1$ and μ_B being the Bohr magneton. Similar relations connect the spin magnetic moment and the nuclear spin magnetic moments, with $g_S \simeq 2$. The value g_I is not universal. For ^{40}K $g_I \simeq 1.4 \times 10^{-4}$.

perturbation, the energy shift from the Zeeman effect is equal to:

$$\Delta E(B) - E_{HF} = \langle F, m_F | \widehat{H}_Z | F, m_F \rangle = \mu_B g_F m_F |B|. \tag{A.28}$$

g_F is the Landé factor of the hyperfine manifold and is equal to:

$$g_F = g_J \frac{F(F+1)+J(J+1)-I(I+1)}{2F(F+1)} + g_I \frac{F(F+1)+I(I+1)-J(J+1)}{2F(F+1)}.$$

Finally, $E_{HF} = a_{hf}(F(F+1)-I(I+1)-J(J+1)$ represents the hyperfine splitting in absence of magnetic field (and in case of $b_{HF} = 0$). For ^{40}K, this low asymptotic regime is only valid for magnetic field up to few Gausses.

High magnetic field

For high magnetic field, when the Zeeman energy shift far exceeds the hyperfine splitting, the basis $\{|F, m_F\rangle\}$ does not constitute a good basis anymore. In this regime, called the Paschen-Back regime, the correct set of eigenstates is given by the basis $\{|I, m_I; J, m_J\rangle\}$, eigenstates of the Hamiltonian $\widehat{H}_0 + \widehat{H}_{SO} + \widehat{H}_Z$. The hyperfine splitting can then be treated as a perturbation and the energy shift is given by:

$$\begin{aligned}\Delta E(B) - E_Z &= \langle I, m_I; J, m_J | \widehat{H}_{HF} | I, m_I; J, m_J \rangle \\ &= a_{hf} m_I m_J + b_{hf} \frac{9m_I^2 m_J^2 - 3I(I+1)m_J^2 - 3J(J+1)m_I^2 + IJ(I+1)(J+1)}{4IJ(2I+1)(2J+1)}\end{aligned}$$

Finally, $E_Z = \mu_B(g_I m_I + g_J m_J)B$ represents the energy shift for the Hamiltonian $\widehat{H}_0 + \widehat{H}_{SO} + \widehat{H}_Z$ compared to $B = 0$G.

The case L=0

For S orbitals, such as the groundstate nS of Alkali, $L = 0$. In this particular case, one can calculate analytically the Zeeman energy shift $\Delta E(B)$ for any magnetic field. This analytic solution is called the Breit-Rabi formula [250] and for the stretched states ($m_F = \pm(I + 1/2)$) it is equal to:

$$\frac{a_{hf}}{2\hbar^2} I \pm \frac{\mu_B}{\hbar}(1/2 g_J + g_I I)B.$$

And for the excited states ($|m_F| < (I + 1/2)$):

$$-\frac{a_{hf}}{4\hbar^2} + \mu_B g_I m_F B \pm \frac{a_h f(I+1/2)}{2} \sqrt{1 + \frac{2\mu_B(g_I - g_J)m_F)}{a_{hf}(I+1/2)^2} B + \frac{\mu_B^2(g_I - g_J)^2)}{a_{hf}^2(I+1/2)^2} B^2}.$$

The figure 2.11 represents the evolution of the energy shift of the ground state manifolds as a function of the magnetic field.

Appendix B

Characterization of a new ^{40}K Feshbach resonance

In this appendix we will report on the characterization of a novel Feshbach resonance in ^{40}K via the measurement of the inelastic loss rate constants. Characterization of this new Feshbach resonance was also reported in a previous thesis from the group [74]. In the following a brief description of Feshbach resonances in ultracold atoms will be provided before describing this novel resonance and its characterization.

B.1 Interaction in ultracold atoms

In Appendix A.5, we described the behavior of non-interacting particles. In low-energy physics, such as cold atoms, collisions between two particles is often described using the partial waves method. We Consider two particles interacting via the potential $V(\mathbf{R})$ and with a relative momentum $\hbar\mathbf{k}$. $\mathbf{R}$ represents the distance between the two particles. At large distance $\mathbf{R}$, $V(\widehat{\mathbf{R}}) \to 0$ [1]. The two particles can then be described as two incident plane waves. These plane waves can be decomposed in the basis of the spherical harmonic functions $Y_{lm_l}(\mathbf{R})$. l is the relative angular momentum between the two particles and m_l its projection along a given axis. This decomposition is called the partial wave expansion [46]. For a symmetrical potential, the angular momentum is conserved and thus only the radial component $\phi_l(R)$ of the wavefunction will be modified by the interaction. The Schrodinger equation associated to $\psi(R) = \phi_l(R)/R$ is equal to [46]:

$$-\frac{\hbar^2}{2\mu}\partial_{R^2}^2\psi_l(R) + V_l(R)\psi_l(R) = E_l\psi_l(R). \tag{B.1}$$

Here μ denotes the reduced mass of the two particles and the modified potential $V_l(R) = V(R) + \hbar^2 l(l+1)/2\mu R^2$ incorporates the centrifugal barrier, which vanishes for s-wave scattering ($l = 0$). For $E > 0$, the Schrodinger equation has a continuous spectrum of solutions while for $E < 0$ the eigenenergies E_{nl} are discrete and there is a finite number of bound state solutions. As $R \to +\infty$, the solutions of the scattering problem are the sum of the incident plane wave

[1] $\widehat{\mathbf{R}} = \mathbf{R}/R$.

with a momentum $\hbar k$ and a scattered wave decomposed in partial waves. The effect of the interacting potential $V(R)$ on the collision events is entirely contained in a single parameter $\eta_l(E)$ called the scattering phase shift [46]. In the particular case of s-wave scattering, one can define the scattering length a and the associated scattering cross section:

$$a = -\lim_{k\to 0} \frac{\tan \eta_0(k)}{k} \quad \text{and} \quad \sigma = \frac{4\pi a^2}{1+k^2a^2}. \tag{B.2}$$

The scattering length a can take any value from $-\infty$ to $+\infty$. Interaction between particles will be attractive for $a < 0$ and repulsive when $a > 0$. The most common technique to tune the value of a is by using Feshbach resonances.

B.2 Feshbach resonances in ultracold atoms

Initially discovered in nuclear physics [251], Feshbach resonances are a convenient way to tune the interactions strength between atoms to be strongly repulsive, strongly attractive, vanishing and anything in between. The existence of Feshbach resonances is related to the presence of bound states. Even though two atoms cannot form a bound states while colliding elastically, the presence of such states still alter the scattering properties of interacting cold atoms. Feshbach resonances occur when the energy of the two colliding atoms equals the energy of one of the bound states of the molecule composed of the two atoms. If the magnetic moment of the molecule differs from the magnetic moment of the two free atoms the energy difference can be tuned by changing the value of the magnetic field. In the vicinity of the resonance, the s wave scattering length takes the form [252]:

$$a(B) = a_0 \left(1 - \frac{\Delta}{B - B_0}\right), \tag{B.3}$$

where B denotes the applied magnetic field and B_0 the magnetic field for which the energy of both states coincide. Δ represents the width of the resonance and fixes the zero crossing of the scattering length at the magnetic field $B = B_0 + \Delta$. On the repulsive side of the Feshbach resonance, the energy of the bound states (referred to as the closed channel) are lower than the energy of the free atoms (referred to as the entrance channel). Owing to inelastic collisions [2], atoms can be adiabatically transferred to this bound state to form a Feshbach molecule by sweeping the magnetic field across the resonance starting from a small negative scattering

[2] Inelastic collisions are collisions that don't preserve the momentum nor the kinetic energy of the system.

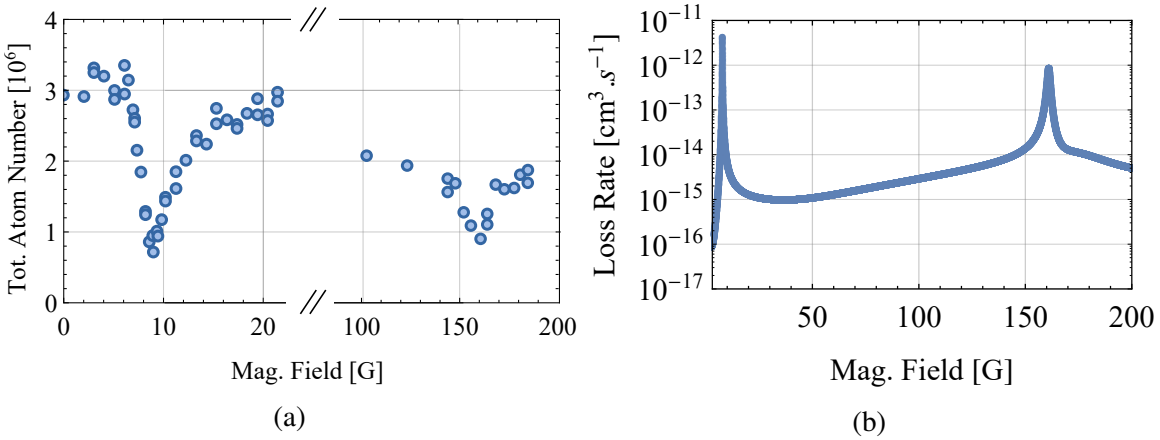

Fig. B.1 **Initial detection of two unreported Feshbach resonances**.(a) The evolution of the total atom number after 5 s of hold time with respect to the magnetic field reveals the presence of two resonances around 10 G and 150 G. Figure adapted from [73]. (b) Numerical simulation by E.Tiesinga of the two-body inelastic scattering rate between atoms in $m_F = 9/2$ and $m_F = 7/2$. Their collision energy was set to 60 nK.

length [125]. The energy of the Feshbach molecule is given by:

$$E_b = \frac{\hbar^2}{2\mu a}. \tag{B.4}$$

Kinetic energy not being conserved during an inelastic collision process, they can lead to inelastic losses and hinder the evaporative cooling. However, they can be an important tool to detect new Feshbach resonances or form bosonic molecules composed of fermions.

B.3 Initial detection of a new Feshbach resonance

A previous experimental study regarding the evaporation efficiency of ^{40}K in a single dipole trap revealed two unreported loss resonances at $B = 9$ G and $B = 150$ G. After the MW evaporation described in sec. 2.10, atoms were transferred into a single ODT and held for 5 s. At this stage of the sequence, the atomic cloud was composed of mostly atoms in the $m_F = 9/2$ and $m_F = 7/2$ Zeeman sublevel with a minority in the $m_F = 5/2$ state. The evolution of the total atom number with respect to the magnetic field was recorded after the 5 s of hold times. The figure B.1, adapted from [73] shows the corresponding losses diagram.
A more detailed analysis of the first loss feature located around 9 G revealed three losses feature as shown in the figure B.2. In this measurement, the atomic cloud was first evaporated during 4 s at a bias field of 18 G. The magnetic field was then quickly ramped to its target value before

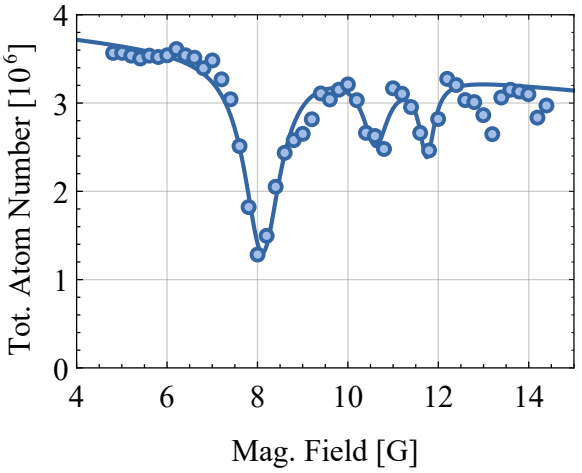

Fig. B.2 **Detailed analysis of the first loss dip**.(a) The evolution of the total atom number after 4 s of hold time with respect to the magnetic field reveals the presence of three losses feature around 10 G.

holding the cloud in the ODT for 4 s. The remaining fraction of atoms was then detected using standard absorption imaging. Among the three losses feature the one located at 8.1 G is the more pronounced. As the presence of these two additional features still remains to be explained, this appendix will be devoted to the understanding and the characterization of the initial feature located around $B = 8.1$ G. Due to the relatively low trap depth, one cannot easily extract the inelastic loss rate from the remaining atom number as evaporative cooling might still contribute to the losses. Consequently, the focus of the following section will concern the extraction of the loss rate.
In order to characterize this novel Feshbach resonance, several questions must be answered and will be addressed in the following section:

1. Which spin states are involved in the open channel?
2. In which partial wave do the atoms collide in the entrance and exit channel?
3. What is the value of the resonant magnetic field B_0?
4. What is the width Δ of the resonance?
5. What is the loss mechanism?

B.4 Characterization of the resonance via inelastic losses

As explained earlier, inelastic collisions do not conserve the angular momentum of the system nor the total kinetic energy. When the kinetic energy released after the collision exceeds the trap depth, atoms can be expelled from the confining potential. Two principal inelastic losses mechanisms can be identified: two and three body losses. For two body inelastic losses, the two

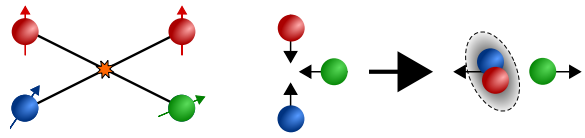

Fig. B.3 **Schematic description of two and three body inelastic collisions**. For two body inelastic collisions, the two atoms in the entrance channel will collide and flip their spin in the process. During three body collisions, two partners form a molecule and a third partner gather the excess of energy.

atoms in the entrance channel can flip their spin and after the collision will end up in a lower internal states. For three body inelastic losses, three partners collide, two of them will end up in a bound state and form a molecule while the third one will gather the excess of energy. As a consequence, for two body process, in the outgoing channel, the excess of kinetic energy will be on the order of the Zeeman shift while it will be of the order of the bound state energy for three body process. Figure B.3 depicts those two processes.
Characterization of a Feshbach resonance can be achieved from the study of the two- and three-body inelastic loss rates. These rates can be extracted from the measurement of the lifetime of the atomic cloud. In the following, we will described the theoretical framework associated to these loss mechanisms.

Loss rate equations for the shallow trap limit

For a single component gas, the evolution of the atom number with respect to time is given [46]:

$$\frac{\mathrm{d}N(t)}{\mathrm{d}t} = -L^{(1)}N(t) - \int_{\mathbf{r}} (L^{(2)}n^2(\mathbf{r},t) + L^{(3)}n^3(\mathbf{r},t)). \tag{B.5}$$

Here, $L^{(1)} = 1/\tau$ is the inverse of the lifetime of the cloud. It is set by the rate of background collisions. $L^{(2)}$ and $L^{(3)}$ denote the loss coefficients due to two-and three-body collisions. Finally $n(\mathbf{r},t)$ represents the spatial density of the trapped gas. Here, we neglected higher order terms (such as four body losses), since the probability of such events is extremely low, especially for fermions [3].

One-body losses

The background gases being in thermal equilibrium with the exterior of the vacuum chamber, each collision between a trapped atom and a background particle will lead to the atom escaping from the trap no matter the trap depth. Those collisions involving only one atoms from the confined sample, they are referred to as one body processes. The contribution of such collisions

[3] Due to Pauli blocking, two fermions in the same internal state cannot be at the same position

to the evolution of the total atom number is given by the relation:

$$\dot{N}(t) = -L^{(1)}N(t) = -\sum_{i=1}^{N} L^{(1)}N_i(t) \tag{B.6}$$

Where $N_i(t)$ denotes the atom number in a given Zeeman states i and the sum is done over all the different spin components present in the atomic mixture. Experimentally, the lifetime was measured by first recompressing the trap to suppress any evaporative cooling. The magnetic field was then set to 18 G which is sufficiently far away from the resonances for all the losses mechanisms to be strongly dominated by the background collisions. The evolution of the total trapped atom number with respect to time was finally recorded via absorption imaging and the lifetime $\tau = 47$ s obtained [4].

Two-body losses

Evaporative cooling

Two body losses can be due to elastic or inelastic collisions. Elastic collision is the main mechanism at hand during evaporative cooling. In an harmonic trap, the evolution of the atom number due to elastic collisions is given by the relation [122]:

$$\dot{N}(t) = -\Gamma_{\text{ev}}N(t). \tag{B.7}$$

Here Γ_{ev} represents the evaporation rate and encapsulate the evaporation dynamics. It is proportional to $n\sigma\exp(-\eta)$ with n being the atomic density, σ the elastic s-wave cross section and $\eta = U_0/k_B T$ the ratio between the trap depth and the temperature of the cloud. As such, one can suppress the evaporation rate by increasing the value of η. Experimentally, in order to correctly extract the inelastic loss rate from the lifetime measurement of the atomic cloud, we recompressed our ODT up to $\eta > 8$, which was enough for the two body losses to be completely dominated by inelastic collisions [5]. Consequently, in the following, elastic collisions will be neglected.

Two body inelastic collisions

In order to model the two body inelastic losses, one need to be able to know the composition of the entrance channel. Since all three spin states $m_F = 9/2, 7/2$ and $5/2$ are present in the ODT, each of them could potentially contribute. Howerver, given the magnitude of the losses in

[4] The lifetime is shorter than the lifetime obtained just after transferring the atoms into the ODT in presence of a small bias field $B = 4$ G.

[5] In practice, in the vicinity of the resonance, for $\eta = 8$ the two body elastic collisions rate was more than an order of magnitude lower than the lowest inelastic collision rate that we measured.

picture B.2, one could think that $5/2$ is absent from the loss process since it only represents 12 % of the total atom number. A preliminary numerical simulation, kindly provided by E.Tiesinga in a private communication was able to confirm the existence of both the resonance around 8 G and 160 G. In this private communication, he also identified those two resonances as d-wave in nature and that in the open channel the two states $m_F = 9/2$ and $m_F = 7/2$ were present. Following this indication, two body inelastic losses can be modeled. Assuming that the trap depth is sufficiently shallow for both atoms to leave the trap after an inelastic collision [6], the evolution of the population in the $m_F = 9/2$ and in the $m_F = 7/2$ spin states will be given by [253]:

$$\dot{N}_{9/2}(t) = -L^{(2)}\langle n_{7/2}\rangle(t) N_{9/2}(t) \tag{B.8}$$

$$\dot{N}_{7/2}(t) = -L^{(2)}\langle n_{9/2}\rangle(t) N_{7/2}(t). \tag{B.9}$$

Here, $\langle n_i\rangle$ denotes the number density of the spin states i and is equal to $\langle n_i\rangle = 1/N_i \int_{\mathbf{r}} n_i^2(\mathbf{r})$. Assuming that the cloud is in constant thermal equilibrium, $n_i(\mathbf{r})$ can be written as $n_i(\mathbf{r}) = n_{i,0} \mathrm{e}^{-\beta U(\mathbf{r})}$ with $n_{i,0} = N_i/V_e$ being the peak density. Using the harmonic approximation for the trap $U(r)$, one can obtain the expression of the number density [254]:

$$\langle n_i\rangle = \frac{N_i}{2\sqrt{2}V_e} \quad \text{with} \quad V_e = \sqrt{\frac{2\pi \mathrm{k_B} T}{m\overline{\omega}^2}}^3, \tag{B.10}$$

with $\overline{\omega}$ being the mean trapping frequency. Therefore, the two body losses can be written as:

$$\dot{N}_{9/2}(t) = -L^{(2)} \frac{N_{7/2}(t)}{2\sqrt{2}V_e} N_{9/2}(t) \tag{B.11}$$

$$\dot{N}_{7/2}(t) = -L^{(2)} \frac{N_{9/2}(t)}{2\sqrt{2}V_e} N_{7/2}(t). \tag{B.12}$$

Three body losses

Three boy collisions can be understood as a two steps process. At first two atoms collide and couple to a virtual bound state. While in the virtual state, collision could occur with a third atom causing the molecule to decay into one of the lower lying vibrational level. The excess energy resulting from that decay will be carried out by the third partner. While three body collisions could occur and dominate loss rate measurement, it was found that the effective two-body loss rate $L^{()3}N$ was an order of magnitude lower than the two body counterpart [74]. Three-body losses will therefore be ignored in the following.

[6] This condition can be met if $U_0 \ll E_z$, with E_z the released Zeeman energy after an inelastic collision.

B.5 Evolution of the total atom number

Using the relations presented in the previous section, we can derive the rate equation for the total atom number $N(t) = N_{9/2}(t) + N_{7/2}(t) + N_{5/2}(t)$:

$$\dot{N}(t) = -L^{(1)}N(t) - L^{(2)}\frac{N_{7/2}(t)N_{9/2}(t)}{\sqrt{2}V_e}. \tag{B.13}$$

We Introduce the population imbalance $\Delta N_{97}(t) = N_{9/2}(t) - N_{7/2}(t)$ between the states $m_F = 9/2$ and $m_F = 7/2$. The rate equation of $\Delta N_{97}(t)$ being given by $\Delta\dot{N}_{97}(t) = -L^{(1)}\Delta N_{97}(t)$, the evolution of the population imbalance with respect to time is given by: $\Delta N_{97}(t) = \Delta N_{97}(0)\mathrm{e}^{-L^{(1)}t}$. Similarly, the population in $m_F = 5/2$ does not undergo any two body process and the evolution of $N_{5/2}$ is thus given by $N_{5/2}(t) = N_{5/2}(0)\mathrm{e}^{-L^{(1)}t}$.
At this point, it is useful to introduce the notations $f_{5/2}, f_{7/2}, f_{9/2}$ and $f_{97} = f_{9/2} - f_{7/2}$ to represent the initial population in a given Zeeman state. Thus, $f_i = N_i(0)/N_0(0)$ denotes the initial fraction of atoms in the Zeeman state i. Finally, using the fact that $N_{9/2}(t) = N(t) - [N_{5/2}(t) + \Delta N_{97}(t)]$ and $N_{7/2}(t) = N(t) - [N_{5/2}(t) - \Delta N_{97}(t)]$, one can derive the rate equation for $N_{9/2}(t)$ and $N_{7/2}(t)$:

$$N_{9/2}(t) = N - [f_{5/2} + f_{97}]N(0)\mathrm{e}^{-L^{(1)}t} \tag{B.14}$$

$$N_{7/2}(t) = N - [f_{5/2} - f_{97}]N(0)\mathrm{e}^{-L^{(1)}t}. \tag{B.15}$$

The final rate equation for the total atom number can then be obtained by inserting the above equations into eq. B.13:

$$\dot{N}(t) = -L^{(1)}N(t) - \frac{L^{(2)}}{2\sqrt{2}V_e}\left[N^2(t) + (f_{5/2}^2 - f_{97}^2)N^2(0)\mathrm{e}^{-2L^{(1)}t} - f_{5/2}N(0)N(t)\mathrm{e}^{-L^{(1)}t}\right]. \tag{B.16}$$

Thus, the evolution of the atom number also depends on the temperature as $V_e \propto T^{-3/2}$. Moreover, the two body inelastic collisions act an anti-evaporation mechanism that leads to heating of the cloud. The heating rate is equal to [255]:

$$\dot{T} = \frac{T}{4}\left(\frac{\dot{N}(t) - \dot{N}_{5/2}(t)}{N(t) - N_{5/2}(t)}\right). \tag{B.17}$$

The population in $m_F = 5/2$ not experiencing any two body collisions, it has to be removed from the rate equation since background collisions do not contribute to heating of the atomic cloud. The rate equation of the temperature and the total atom number can then be fitted to extract

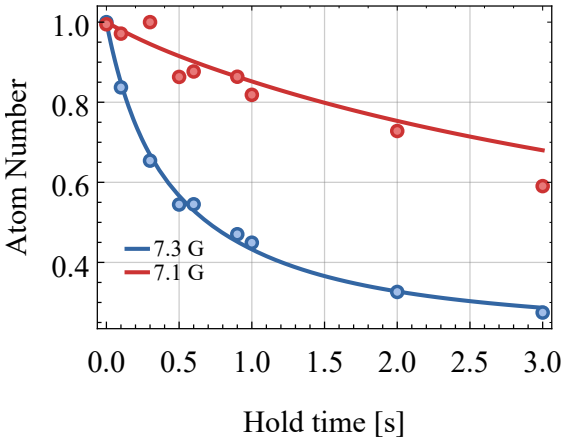

Fig. B.4 **Inelastic losses for different magnetic field**. Evolution of the total atom number as a function of the wait time for a magnetic field $B = 7.1\,\mathrm{G}$ and $B = 7.3\,\mathrm{G}$. The initial atom number and temperature were 1.2×10^6 and $2.8\,\mu\mathrm{K}$ respectively. In order to prevent evaporative cooling the dipole trap was recompressed to a final trap depth $U_0/k_B = 8.4T$. Lines are obtained by simultaneously fitting the differential equations B.16 and B.17.

the two body inelastic loss rate given that no additional loss process occurs. The underlying assumption is that evaporative cooling is suppressed while any two body inelastic collision results in a loss of the two partners. Those conditions can be met as long as $k_B T \ll \eta \ll E_Z$.

B.6 Evolution of the loss rate

In order to characterize the loss rate, the value of the two body inelastic loss rate $L^{(2)}$ as a function of the magnetic field has to be known. Furthermore, additional information regarding the nature of the resonance can be extracted from the temperature dependence of $L^{(2)}$. While for *s*-wave open channel, the inelastic loss rate is supposed to be temperature independent, for *d*-wave open channel, due to presence of the centrifugal barrier, both the witdh and the height of the resonance peak are supposed to increase with temperature [256].
As indicated by equation B.16, the loss rate can be extracted from the lifetime of the trapped atoms. Experimentally, we first evaporate in the single ODT the atomic cloud by reducing the trap depth up to an intermediate depth around $k_B \times 10\,\mu\mathrm{K}$. Following the evaporation, we recompress the trap to its final value $U_0 = k_B \times 24\,\mu\mathrm{K}$. The final value is set such that the ratio $\eta \geq 8$ and that as a consequence the losses are completely dominated by the inelastic collisions. The magnetic field is then ramped to a desired value B_{set} and the atoms kept in the ODT for a duration t_{hold}. The atoms number and the cloud temperature are recorded after various t_{hold}. As example of such experiment is shown in figure B.4 for two different value of B_{set}. One can see that close to resonance the inelastic losses are strongly enhanced. The heating causes the ratio η to decrease as the hold time t_{hold} increases, which could ultimately lead to evaporative cooling despite the initial suppression of this process owing to the starting value of $\eta \geq 8$. However, this is not an issue as the loss rate can still be extracted from the initial atom number decay. The loss rate is obtained by numerically and parametrically fitting both the total atom number and the temperature evolution at the same time using the two rate equations B.16

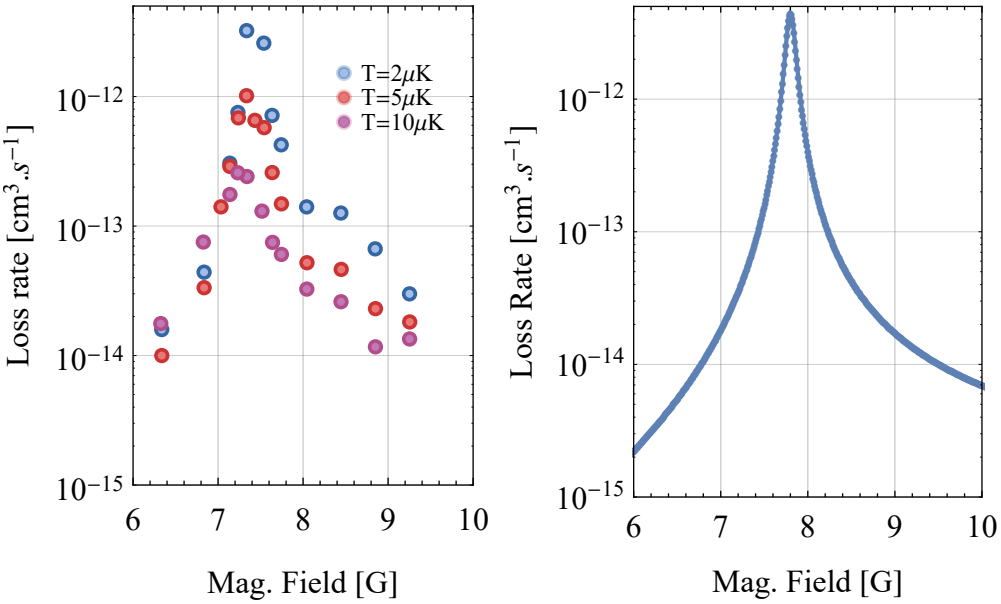

Fig. B.5 **Evolution of the two-body inelastic loss rate as a function of the magnetic field**.(a) Experimental measurement of the two-body inelastic scattering rate as a function of the magnetic field. The three sets correspond to three different average kinetic energies as given by their initial temperatures T_0. For $T_0 = 5\,\mu$K and $T_0 = 10\,\mu$K, the corresponding trap depths of $k_B \times 48\,\mu$K and $k_B \times 108\,\mu$K exceeded the Zeeman energy splitting causing the partial recapture of atoms after the collisions. This led to a reduction of the detected loss rate and an increase of the heating. (b) Numerical simulation by E.Tiesinga of the two-body inelastic scattering rate between atoms in $m_F = 9/2$ and $m_F = 7/2$. Their collision energy was set to 60 nK.

and B.17. Three fit parameters emerge from the rate equations: the initial imbalance f_{97}, the initial fraction of atoms in the $m_F = 5/2$ sublevel $f_{5/2}$ and the loss rate $L^{(2)}$. Both f_{97} and $L^{(2)}$ are obtained from the fitting routine under the constraint that the initial fitting total atom number is equal to its experimental value while the initial fraction $f_{5/2} = 0.12$ is fixed from the spin composition analysis of the cloud after its transfer into the science cell (see sec. 3.3 for additional information). On top of the resonance, we find $L^{(2)}_{\text{fit}} = 3.25 \times 10^{-12}\,\text{cm}^3.\text{s}^{-1}$ and an initial imbalance $f_{97,\text{fit}} = 0.26$ which is in excellent agreement with the expected initial spin population (see sec. 3.3).

B.7 Nature of the resonance

Once extracted, the evolution of the loss rate as a function of the magnetic field was recorded for various temperature by adjusting the intermediate trap depth as well as the final one in

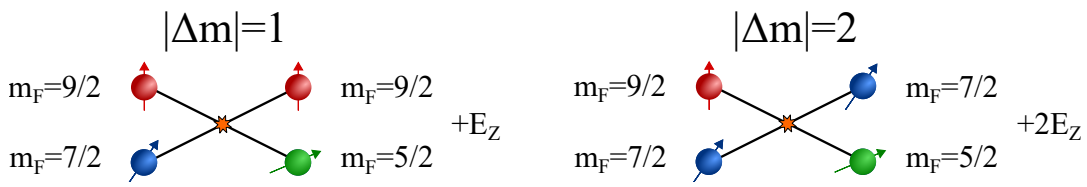

Fig. B.6 **Inelastic collisions channels due to the Feshbach resonance**. (Left) First possible collision channel. After the initial collision between atoms in the $m_F = 9/2$ and $m_F = 7/2$ states, only the atoms in the $m_F = 7/2$ state undergoes a spin flip to the lower lying $m_F = 5/2$ state. $|\,\Delta m_L\,| = 1$ and the energy released thus corresponds to the Zeeman splitting between the two states. (Right) Second possible channel: the two spin states changes their spin, $|\,\Delta m_L\,| = 2$ and the energy released correspond to twice the Zeeman splitting.

order to always stay in the regime $\eta \geq 8$ and is represented in fig. B.5a. For increasing trap depth, the magnitude of the loss peak decreases as well as its width. Moreover, its position seems to slightly shift towards higher magnetic field. The decrease of the peak magnitude can be explained by the recapture of atoms after undergoing a spin-exchange collision. For magnetic field around the resonance, the Zeeman splitting is roughly equal to $k_B \times 110\,\mu K$ [7]. The mean released kinetic energy per atoms is therefore around $k_B \times 55\,\mu K$. When the trap depth becomes comparable to the average released kinetic energy, atoms can remain trapped after an inelastic collision, thus reducing the measured loss rate. This recapturing process also leads to stronger heating of the cloud. Experimentally, the loss rate was measured for several trap depth: $U_0/k_B = 23,48\,\mu K$ and $,108\,\mu K$. Thus, for the last two set of measurements, the detected loss rate decreased because of the enhanced likelihood of recapture.

Additionally, the temperature dependency of the Loss rate provides information regarding the nature of the open channel. For p-wave collisions, the resonance position and the width of $L^{(2)}$ increases with T, but the height of the peak remains unchanged [257]. On the other hand, for d-wave collisions, the height also increases with temperature [256, 258]. Given that our resonance does not follow these patters, our entrance channel is in s-wave. This was confirmed by numerical simulations of E.Tiesinga, which predicted that the contribution of d-wave in the entrance channel was more than 5 orders of magnitude smaller than the s-wave contribution [74]. The numerical simulation provided by E.Tiesinga is provided in fig. B.5b and is in excellent agreement with the experimental data. In particular, the predicted peak of the loss rate was $4.05 \times 10^{-12}\,cm^{-3}.s^{-1}$ which agrees within 20 % with the measured value of $3.25 \times 10^{-12}\,cm^{-3}.s^{-1}$. The resonance position offset of 0.4 G is within the uncertainty of the numerical predictions of ± 0.5. To conclude this appendix, the two-body inelastic collision mechanism is presented in figure. B.6.

[7] This splitting corresponds to the Zeeman splitting at a magnetic field of $B = 7.4\,G$.

Appendix C

Quasi-thermalization of collisionless fermions

Quasi-thermalization of collisionless particles in quadrupole potentials. *J. Lau, O. Goulko,T. Reimann, D. Suchet,, C. Enesa, F. Chevy and C. Lobo.* Submitted to Phys. Rev. A
We analyze several puzzling features of a recent experiment with a noninteracting gas of atoms in a quadrupole trap. After an initial momentum kick, the system reaches a stationary, quasi-thermal state even without collisions, due to the dephasing of individual particle trajectories. Surprisingly, the momentum distribution remains anisotropic at long times, characterized by different "temperatures" along the different directions. In particular, there is no transfer of the kick energy between the axial and radial trap directions. To understand these effects we discuss and solve two closely related models: a spherically symmetric trap $V(r) \simeq r^{\alpha}$ and a strongly confined gas along one direction (a "pancake" trap). We find that in the isotropic trap, the gas unexpectedly also preserves the anisotropy of the kick at long times, which we are able to explain using the conservation of angular momentum and the virial theorem. Depending on the value of a we find that the kick can cool or heat the orthogonal directions. The pancake trap case is quantitatively similar to the quadrupole one. We show that for the former, the temperature anisotropy and memory of the kick direction are due to the change in the 2D effective potential resulting from the kick, thereby also explaining the quadrupole experimental results.

Quasi-thermalization of collisionless particles in quadrupole potentials

Johnathan Lau †,[1] Olga Goulko,[2] Thomas Reimann,[3] Daniel Suchet,[3,4] Cédric Enesa,[3] Frédéric Chevy,[3] and Carlos Lobo[1]

[1]*Mathematical Sciences, University of Southampton, Highfield, Southampton, SO17 1BJ, United Kingdom*
[2]*Department of Physics, Boise State University, Boise, ID 83725, USA*
[3]*Laboratoire Kastler Brossel, ENS-Université PSL, CNRS, Sorbonne Université, Collège de France, 24 rue Lhomond, 75005 Paris, France*
[4]*Institut du Photovoltaïque d'Île de France (IPVF), UMR 9006, École polytechnique, IP Paris, Palaiseau, France*

(Dated: October 31, 2019)

We analyze several puzzling features of a recent experiment with a noninteracting gas of atoms in a quadrupole trap. After an initial momentum kick, the system reaches a stationary, quasi-thermal state even without collisions, due to the dephasing of individual particle trajectories. Surprisingly, the momentum distribution remains anisotropic at long times, characterized by different "temperatures" along the different directions. In particular, there is no transfer of the kick energy between the axial and radial trap directions. To understand these effects we discuss and solve two closely related models: a spherically symmetric trap $V(r) \simeq r^{\alpha}$ and a strongly confined gas along one direction (a "pancake" trap). We find that in the isotropic trap, the gas unexpectedly also preserves the anisotropy of the kick at long times, which we are able to explain using the conservation of angular momentum and the virial theorem. Depending on the value of α we find that the kick can cool or heat the orthogonal directions. The pancake trap case is quantitatively similar to the quadrupole one. We show that for the former, the temperature anisotropy and memory of the kick direction are due to the change in the 2D effective potential resulting from the kick, thereby also explaining the quadrupole experimental results.

PACS numbers: 03.65.Vf, 37.10.Jk, 67.85.-d

I. INTRODUCTION

A major part of the theoretical study of classical Hamiltonian dynamics [1] concerns the ability of purely conservative systems to reach thermal equilibrium. This line of inquiry took its origin from Boltzmann's demonstration of the celebrated H-theorem, which provided for the first time a microscopic explanation of the second law of thermodynamics. This pioneering work quickly gave rise to many paradoxes due to the fact that the entropy of a Hamiltonian system $\mathscr{S}$ is conserved. Even 150 years after Boltzmann's work, problems like Loschmidt's paradox [2], Poincaré's recurrence theorem [3] or the Fermi-Pasta-Ulam-Tsingou [4, 5] problem remain largely unresolved [6]. A possible approach towards their resolution lies in the notion that any small sub-ensemble $\mathscr{S}_1$ can be described as an open system interacting with the rest of $\mathscr{S}$. The latter therefore plays the role of a bath allowing the thermalization of $\mathscr{S}_1$. In the quantum world, this picture is known as the Eigenstate Thermalization Hypothesis [7–9], which also applies to classical systems [10]. In this context, an intriguing question concerns the minimal system size required for thermalization. Despite the fact that the thermodynamic limit is usually associated with large-size systems, small objects such as nanoparticles [11], nuclei [12] or atoms trapped in optical lattices [13] are nevertheless known to relax towards thermal equilibrium.

With decreasing system size, a natural question to consider is to which degree a single particle is able to reach thermal equilibrium. This extreme limit can be studied experimentally using cold fermions by taking advantage of the Pauli exclusion principle. The associated suppression of interactions at low temperature gives rise to a unique experimental platform facilitating the study of purely Hamiltonian systems.

In this work, we consider an ensemble of non-interacting particles confined in non-separable power law potentials. The question of thermalization in this class of potentials was already raised in the context of collisionless atoms in quadrupole traps [14, 15]. This problem was recently revived in the context of quantum simulation of high-energy physics, where the behavior of (harmonically confined) massless Weyl fermions was studied experimentally using cold atoms in a quadrupole trap [16]. In this latter work, it was shown that after a rapid quench of the trap position, the center of mass motion is damped after a few oscillations and the system reaches a steady state characterized by partial thermalization of its momentum degrees of freedom. The corresponding distribution of the atomic ensemble closely resembles a thermal distribution, $np_{i=x,y,z} \propto \exp(-p_i^2/2mk_BT_i)$, but with anisotropic temperatures.

In this paper, we present a detailed theoretical analysis of these relaxation dynamics. Furthermore, we provide analytical calculations of the steady state properties in an isotropic as well as in a pancake geometry. These results are compared to numerical solutions of the corresponding dynamical equations. Our work clarifies the memory effect leading to the anisotropy of the momentum distribution and predicts a singular behavior for spherical potentials.

[1] †Deceased 21 May 2016

II. RELAXATION DYNAMICS IN QUADRUPOLE TRAPS

Motivated by recent experiments with non-degenerate spin-polarized fermions [16], we consider an ensemble of classical noninteracting particles confined by a quadrupole trapping potential

$$V(\mathbf{r}) = \mu_B b\sqrt{x^2+y^2+4z^2}. \tag{1}$$

where μ_B is the Bohr magneton and b is the magnetic field gradient, a positive quantity.

This potential is *non-integrable* since it has three degrees of freedom but only two constants of the motion (total energy E and angular momentum L_z). As a consequence its dynamics exhibits chaotic behaviour in some regimes. In contrast, the more usual potential of standard atomic traps is a sum of harmonic terms of the form $V_1(x)+V_2(y)+V_3(z)$ allowing us to define three conserved energies, leading to an integrable problem. Note that, since the quadrupole potential cannot be written as the sum of potentials as in the harmonic case, the motion along one direction depends on the other two so that momentum and energy are constantly being exchanged between the three directions as the atom moves along the orbit.

We will study the *relaxation dynamics* in this potential i.e., what happens to the gas after it is slightly perturbed from equilibrium. At $t = 0$ with the gas in thermal equilibrium, the atoms receive a "momentum kick" q that shifts every atom's momentum $\mathbf{p} \to \mathbf{p}+q$ and increases its energy by $\mathbf{p}\cdot q/m + q^2/2m$. Since the original (thermal) distribution before the kick is an even function of each component of $\mathbf{p}$, the first term drops out when averaged over that distribution, so that the average energy change ΔE per atom is:

$$\Delta E = q^2/2m. \tag{2}$$

We are interested in the subsequent evolution: how the gas relaxes to steady state and how the energy ΔE of the kick is redistributed along the different directions of motion. Normally, as is usually assumed, collisions would be responsible for this redistribution leading to a return to thermal equilibrium. However, in our case, there are no collisions nor mean-field interactions, so any relaxation process is due purely to the nonintegrability of the potential.

The state of the gas can be described by the Boltzmann distribution $f(\mathbf{r},\mathbf{p},t)$ which we normalize to unity:

$$\int d^3\mathbf{r}\int d^3\mathbf{p}\, f(\mathbf{r},\mathbf{p},t) = 1. \tag{3}$$

All extensive quantities are to be taken as ensemble averages over this distribution. For example, the final measured momentum distribution np_z is given by

$$np_z = \int d^3\mathbf{r}\int dp_x\, dp_y\, f(\mathbf{r},\mathbf{p},t\to\infty). \tag{4}$$

To simulate this distribution we perform molecular dynamics simulations of the gas [17, 18] where the trajectory of each atom is calculated following the classical equations of motion, without suffering any collision. This method gives us full access to all observables, including the Boltzmann distribution

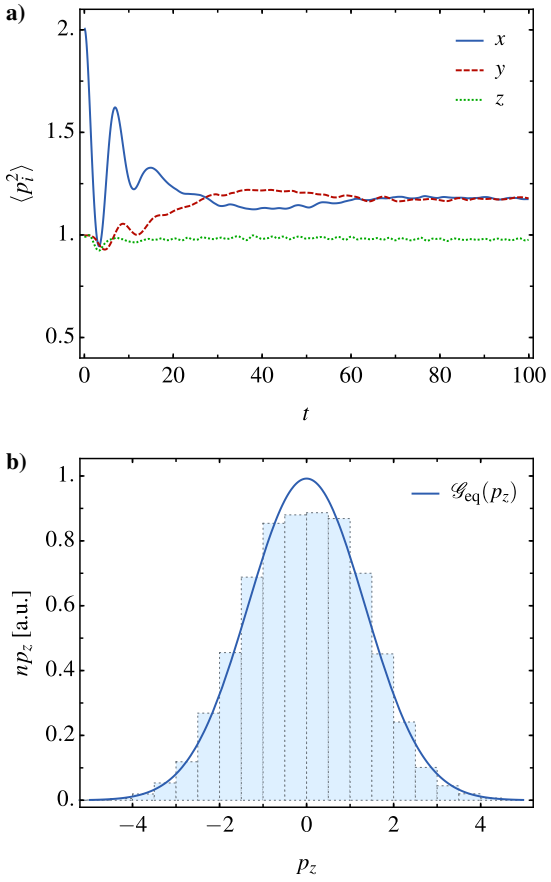

Figure 1. Numerical simulation of the relaxation dynamics in a quadrupole trap. a) Kinetic energy per atom along different directions as a function of time after a kick $q = 1$ along x at $t = 0$. The energies seem to reach a stationary state for $t \geq 80$. Along z the average kinetic energy is almost unchanged from its initial value ~ 1, but along x and y the corresponding values increase by the same amount to a final value of ~ 1.2. b) Momentum distribution np_z of the steady state. The solid line $\mathscr{G}_{\rm eq}$ is a Gaussian distribution with the same variance.

itself. For example, we can measure the phase-space average $\langle p_i^2 \rangle$ for $i = x,y,z$ over the entire system as a function of time by averaging over the trajectories of individual atoms:

$$\langle p_i^2 \rangle_t \equiv \int d^3\mathbf{r}\int d^3\mathbf{p}\, p_i^2 f(\mathbf{r},\mathbf{p},t) \simeq \frac{1}{N}\sum_{\text{all } N \text{ atoms}} p_i^2(t), \tag{5}$$

We start with a gas of $N = 10^5$ atoms sampled from the initial Boltzmann distribution at temperature $k_B T_0 = 1$ with a momentum kick of q along x:

$$f \propto \exp\left(-\frac{(p_x-q_x)^2+p_y^2+p_z^2}{2} - V(x,y,z)\right) \tag{6}$$

(analogously for a kick q_z along z etc.) and let each individual atom evolve according to the classical trajectory. From now on we set $m = k_B T_0 = \mu_B b = 1$, which is equivalent to choosing m as the mass unit, $l_0 = k_B T_0/\mu_B b$ as the unit of length and

$t_0 = \sqrt{mk_BT_0}/\mu_B b$ as the unit of time. The time evolution is calculated using the velocity Verlet algorithm [19, 20]. We use a time step $\Delta t = 0.001 t_0$, which provides sufficient accuracy, as the error of the algorithm is of the order $\mathcal{O}(\Delta t^2)$.

This very simple setup gives rise to some surprises which have also been confirmed experimentally [16]:

1. *Stationary "thermal" distribution*: In Fig. 1 a) we plot $\langle p_i^2 \rangle_t$. We see that, at long times, it has reached an apparently stationary distribution. In Fig. 1 b) we plot the long time doubly integrated momentum distribution np_z (4) and we see that it fits closely to a Gaussian (thermal) distribution $np_z \propto \exp(-p_z^2/2mk_BT_z)$ where we define an effective temperature analogously to the experiment [16]:
$$T_i \equiv \langle p_i^2 \rangle_{t\to\infty}, \; i = x,y,z \tag{7}$$
so that
$$\Delta T_i \equiv \langle p_i^2 \rangle_{t\to\infty} - \langle p_i^2 \rangle_{t=0}. \tag{8}$$

2. *Anisotropic temperatures*: From Fig. 1 a) we see that, even though the doubly integrated distributions np_i along the different directions i are Gaussian, their widths are different: generally we find $T_x \sim T_y \neq T_z$. We also see that $T_z \sim T_0 < T_{x,y}$ which we find to be true whenever the kick is in the xy plane, the opposite being true if the kick is along the z direction. This is unexpected because the quadrupole potential is non-separable, continuously transfering energy and momentum between all directions for each atom, so we might expect naïvely that on average $T_x \sim T_y \sim T_z$, i.e. there would be a certain degree of ergodicity.

3. *Apparent separability of the z and $x-y$ distributions*: for a kick along z, the width of the momentum distribution along x and y seems to be unchanged (i.e. $T_{x,y} \simeq 1$) whereas T_z increases. The energy increase ΔE due to the kick is mainly concentrated into the z direction so that $\Delta E \simeq 3/2\, \Delta T_z$. Likewise, if the kick is along x, the increase in kinetic energy along the z is negligible ($T_z \simeq 1$) but *both* T_x and T_y increase by the same amount ($T_x = T_y$) so that $\Delta E \simeq 3\Delta T_x$. In fact we will see below that this separation is not exact; there is a slight increase of energy in directions transverse to the kick. Nevertheless this behaviour is consistent with a strong separation of the dynamics into z and xy plane components even though the potential is non-separable.

The naïve, straightforward conclusion from these observations is that *the gas seems to have thermalized in the absence of collisions (since the doubly-integrated momentum distributions (4) become Gaussian-like, a hallmark of thermalization) but with some effective "decoupling" of the motion along z and xy directions leading to different temperatures T_z and T_{xy}.*

A. Apparent Thermalization

In point 1. above we noted that the gas becomes stationary after some time. This stationary state of the gas is not due to collisions but to the fact that, in the quadrupole trap, the orbits of different atoms will have different, incommensurate periods leading to the relative dephasing of individual trajectories. This dephasing, when averaged over the whole gas, leads to a stationary distribution. Note that the appearance of a stationary distribution would not happen in the standard harmonic trap since a momentum kick would lead to undamped oscillations of the center of mass. Note also that that irreversibility has not set in by this stage since there are no collisions.

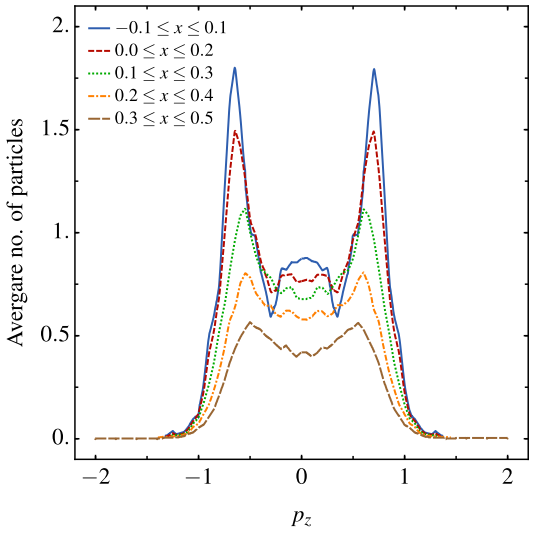

Figure 2. The long time Boltzmann distribution f after a kick along z plotted as a function of p_z keeping all other variables x, y, z, p_x, p_y fixed and for different values of x. To obtain a nonzero number of atoms in the six dimensional volume we considered a narrow region in phase space given by the coordinates in the figure and divided it into bins. We plot the number of atoms in each bin averaged over time. It can be seen that f does not resemble a Gaussian thermal function and that the three peaks feature becomes more prominent for x closer to the center. Similar results are found plotting along all other coordinates.

We also mentioned above that the gas seemed to have thermalized in the absence of interactions since the doubly-integrated momentum distributions (4) become Gaussian after the kick.

Of course, since the effective temperatures deduced from the width of the Gaussians are different ($T_z \neq T_{x,y}$) the state cannot be a true thermal state. Indeed, collisions are necessary to redistribute the kick energy ΔE among all accessible phase space regions of energy $E + \Delta E$ so that the entropy increases $S(E) \to S(E + \Delta E)$ whereas in this experiment, $E \to E + \Delta E$ but entropy is unchanged. Nevertheless, as can be seen from the simulations, several "thermal" properties *can* be achieved, e.g. stationarity and equilibration of temperatures along the x and y directions.

We can ask to what extent the final state of the gas is close to a thermal state. For example, could it be e.g. a product of three different Gaussians (with different temperatures) of the

type

$$f \sim e^{-p_x^2/2T_x} e^{-p_y^2/2T_y} e^{-p_z^2/2T_z} \times e^{-V/T} \quad ? \tag{9}$$

It is easy to see that this is not possible since it does not satisfy the time independent collisionless Boltzmann equation. In fact we can plot a "slice" of f as a function of one of its six coordinates keeping all others fixed as in Fig. 2 which shows a markedly non bell-shaped curve.

In fact, the Gaussian character is only restored upon integration of the other five coordinates of the Boltzmann distribution e.g.:

$$np_x = \int d^3\mathbf{r} \int dp_y dp_z f(\mathbf{r},\mathbf{p},t\to\infty) \propto \mathrm{e}^{-p_x^2/2mk_BT_x} \tag{10}$$

which raises the question of why averages over complex distributions such as those of Fig. 2 lead to a Gaussian profile. We will not consider this question further here, leaving it for further study.

B. Symmetries and sum rule of the distribution

We can be more quantitative regarding the ΔT_i. We first notice that the quadrupole potential (1) is homogeneous of order one, (a potential homogeneous of order α has the property that $V(\lambda\mathbf{r}) = \lambda^\alpha V(\mathbf{r})$). So we can apply the virial theorem which leads to the following relation [21]:

$$\Delta E = \frac{3}{2}(\Delta T_x + \Delta T_y + \Delta T_z). \tag{11}$$

Furthermore, for small kicks we can derive some symmetry considerations and a sum rule. Defining the matrix Θ_{ij} as

$$\Delta T_i \equiv \sum_j \Theta_{ij} \frac{q_j^2}{2} \tag{12}$$

where $i,j = x,y,z$, and q_i is the momentum kick along the ith direction, it is possible to show that this matrix is symmetric so that, for small kick momentum, we have $\Theta_{ij} = \Theta_{ji}$.

More generally it is straightforward to show using (2) and (11) that, if the potential is homogeneous of order α, the Θ_{ij} satisfy the constraint

$$\sum_j \Theta_{ij} = \frac{2\alpha}{2+\alpha}. \tag{13}$$

For potentials with axial symmetry around the z axis, which is the case of the quadrupole trap, the fact that the matrix is symmetric and that in any kick $\Delta T_x = \Delta T_y$ imply that the matrix can be written using only three distinct elements $\theta_{1,2,3}$ as

$$\Theta = \begin{pmatrix} \theta_1 & \theta_1 & \theta_2 \\ \theta_1 & \theta_1 & \theta_2 \\ \theta_2 & \theta_2 & \theta_3 \end{pmatrix}. \tag{14}$$

Using the sum rule we find $\theta_2 + 2\theta_1 = \theta_3 + 2\theta_2 = 2/3$ which leaves us with a single unknown parameter. The experimentally measured value $\Delta T_z/q_z^2/2 = 2/3$ (see point 3. above) implies $\theta_3 = 2/3$, $\theta_2 = 0$ and $\theta_1 = 1/3$, the latter also being in agreement with the measured value.

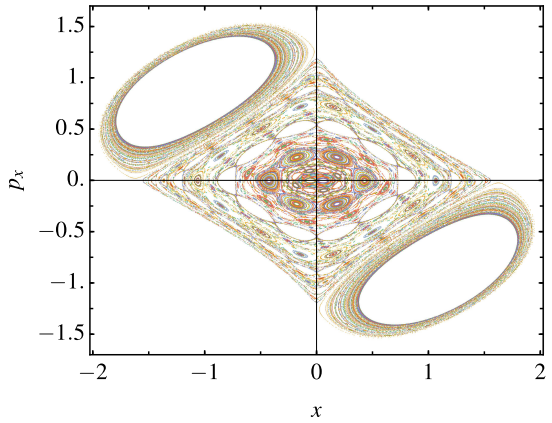

Figure 3. Poincaré map of the quadrupole potential. We study trajectories with the same energy but different initial phase-space coordinates. The values of x and p_x are recorded whenever $z = 0$ and $p_z > 0$. We see the appearance of small islands denoting invariant torii close to which quasi-integrable trajectories evolve, separated by contiguous regions of chaotic dynamics.

The quadrupole simulations confirm the experimental observations (1-3) (see Fig. 1) even though there is a small correction to the experimental values: a slight cooling of the directions transverse to the kick so that $\Theta_{xx} = 0.36$ (instead of 1/3) and $\Theta_{xz} = -0.05$. So the observation of point 3., the apparent separability of the z and $x-y$ distributions, seems not to be perfect but rather an excellent approximation. [2]

We can study the gas dynamics by analyzing individual atomic trajectories and then averaging over initial conditions. However the trajectories can be quite difficult to find due to the nonintegrability of the potential. To show this we constructed a Poincaré map: in Fig. 3, we see that there are both chaotic and quasi-integrable regions. A study of the gas starting from its individual trajectories would be quite complex analytically. For this reason, it is easier to study not the potential (1) but cases which might contain the same physics but in which all or nearly all trajectories are integrable or quasi-integrable. For example let us consider the family of potentials

$$V_\varepsilon(x,y,z) = \sqrt{x^2 + y^2 + (1+\varepsilon)z^2}. \tag{15}$$

When $\varepsilon = 3$ we get the quadrupole potential (1). But if we take $\varepsilon = 0$ the potential becomes spherically symmetric and therefore integrable. Alternatively, if $\varepsilon \gg 1$ then we are left with a highly confined potential along the z direction (a "pancake') so that the motion simplifies again and an effective motion in the $x-y$ plane can be studied.

We will begin with the study of the spherical potential in Sec. III which, surprisingly, exhibits many of the phenomena

[2] We also investigated anisotropic potentials, finding very similar behavior.

of the quadrupole potential, including the anisotropy of the momentum distribution. After this we will analyze the pancake case in Sec. IV, comparing both of these limits with the quadrupole potential.

III. SPHERICAL LIMIT

The simulations in the quadrupole potential suggest that after perturbing an equilibrium gas along a particular direction, the ensemble average of the momentum widths $\langle p_i^2\rangle_t$ converges to a stationary distribution in the long time limit $t\to\infty$. In particular, we observed that $\langle p_x^2\rangle_\infty = \langle p_y^2\rangle_\infty$ and in general $\langle p_x^2\rangle_\infty \neq \langle p_z^2\rangle_\infty$.

Calculating the final momentum widths $\langle p_i^2\rangle_\infty$ for a gas of atoms in the quadrupole potential from first principles is difficult without understanding the individual trajectories. Therefore, as mentioned above, it is a natural simplification to consider instead the case where we remove the anisotropy in the quadrupole potential:

$$V_{\varepsilon=0}(x,y,z) = \sqrt{x^2+y^2+z^2} = r, \tag{16}$$

where r is the radial coordinate (for the rest of this section we will drop the subscript $\varepsilon = 0$). Naïvely, one would expect that perturbing a gas along any direction in such an spherical potential will lead to an isotropic distribution at long times: $\langle p_x^2\rangle_\infty = \langle p_y^2\rangle_\infty = \langle p_z^2\rangle_\infty$. However, as we shall see, the final momentum width along the direction of the perturbation will be different to that along perpendicular directions. To anticipate some of the conclusions of this section: this is intuitively plausible: in a spherical potential all three components of angular momentum are conserved, so the motion of each atom is confined to a plane passing through $r = 0$ and perpendicular to its angular momentum. The population of each plane is therefore constant during the motion. In thermal equilibrium, this population is the same for all planes but a momentum kick will cause a transfer of atoms between planes, so that the population of each plane will depend on its angle relative to the kick direction. This anisotropy in populations in the distribution is preserved at long times again due to conservation of angular momentum and translates into different final temperatures along the different directions.

A. Averages over the motion in planes

With a particle in a central field [21, 22], the trajectory stays on the plane perpendicular to its angular momentum $\mathbf{L}$ which includes the origin $r = 0$. Using polar coordinates (r,θ) for the plane, the energy E is given by the usual expression:

$$E = \frac{1}{2}\left(\dot r^2 + r^2\dot\theta^2\right) + V(r) = \frac{1}{2}\left(\dot r^2 + \frac{L^2}{r^2}\right) + V(r) \tag{17}$$

where $L = |\mathbf{L}| = r^2\dot\theta =$ constant. In a potential such as (16), the motion is confined between two values of the radial coordinate $r_{\min} \le r \le r_{\max}$ which are solutions of $\dot r = 0$. During the time in which r varies from $r_{\max}$ to $r_{\min}$ and back, the radius vector turns through an angle $\Delta\theta$. The condition for the path to be closed is that this angle should be a rational fraction of 2π, i.e. that $\Delta\theta = 2\pi m/n$, where m and n are integers. But according to Bertrand's theorem [22] the only central potentials for which all paths are closed are Kepler's ($\propto -\frac{1}{r}$) and the harmonic potential ($\propto r^2$). For all other potentials (and excluding the particular case of trajectories with zero angular momentum), the trajectory will behave as in Fig. 4: it will become dense everywhere, filling the allowed annulus region isotropically so that the orbital density is only a function of the radius r as the propagation time tends to infinity.

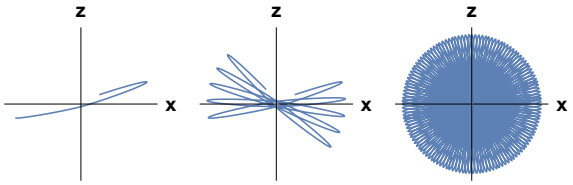

Figure 4. Orbit of atom in a plane with a central potential $V(r) = r$ after increasingly long times from left to right. Since the trajectory never closes, according to Bertrand's theorem, it fills the annular region between $r_{\max}$ and $r_{\min}$ in an isotropic, dense fashion as $t\to\infty$.

Using Bertrand's theorem, we would like to analyze the long time behavior of trajectories, in particular the time averages of different quantities. For a quantity $A(t)$, the time average of a quantity $\overline{A}$ is defined as, cf. (5):

$$\overline{A} \equiv \lim_{t\to\infty}\frac{1}{t}\int_0^t A(t')dt'. \tag{18}$$

We can convert the time average to one over the orbital density discussed above by a change of variables. We immediately conclude that, since Bertrand's theorem implies that the orbital density is isotropic, so will the time average also be:

$$\overline{x^2} = \overline{y^2} \tag{19}$$

$$\overline{p_x^2} = \overline{p_y^2}. \tag{20}$$

We will use this fact to calculate $\langle p_i^2\rangle_\infty$ for a gas of atoms.

B. Calculation of momentum averages in terms of integrals of planes

Although our purpose is to study the potential $V(r) = r$ as a limiting case of the family (15), it is straightforward to consider in this section a more general potential than (16), namely

$$V(r) = r^\alpha \tag{21}$$

with $0 < \alpha \neq 2$. This will allow us to examine qualitatively different behavior as a function of α. The case $\alpha = 2$ corresponds to the isotropic harmonic potential for which in general (19) and (20) are not true. For $\alpha = 1$ we recover (16).

For a gas in an spherical potential, the atoms belonging to the same plane in coordinate space are also confined to the

same plane in momentum space making each plane an independent system. So our strategy will be to treat the motion in each plane separately and then add over all of them at the end. For this we choose a coordinate system (see Appendix A) where two of the coordinates (the angles θ and ϕ) define the plane, and the remaining four correspond to the in-plane coordinates (u and v) and momenta (p_u and p_v). Then we can write the total energy as

$$\langle E\rangle = \int_0^\pi d\phi \int_0^\pi d\theta \langle E\rangle_{\text{plane}}. \tag{22}$$

where $\langle E\rangle_{\text{plane}}$ is the average energy of all the planes lying between θ and $\theta+d\theta$, ϕ and $\phi+d\phi$. Even though the probability density $f(\mathbf{r},\mathbf{p},t)$ is a function of time, the energy of each atom is constant in time as the potential is time-independent and there is no exchange of energy between the atoms, so the average energy is also a constant. Therefore if we know the probability density $f(\mathbf{r},\mathbf{p},t)$ at any one time, we will know the average energy for all time. This allows us to calculate the final momentum widths $\langle p_i^2\rangle_\infty$ from the distribution of energies at $t=0$ after the initial momentum kick.

Since the class of potentials (21) is homogeneous of order α we use the virial theorem,

$$\overline{K} = \frac{\alpha}{2}\overline{V}, \tag{23}$$

where K is the kinetic energy and the averages are over time as in (18). Note that the virial theorem is valid both for each atom individually as well as for the entire gas. If we assume that at long times, when the gas has reached a steady state, the ergodic hypothesis applies for such systems, we can replace the time average with the ensemble average

$$\langle K\rangle = \frac{\alpha}{2}\langle V\rangle. \tag{24}$$

As each plane is a closed individual system, (24) also applies to

$$\langle K\rangle_{\text{plane}} = \frac{\alpha}{2}\langle V\rangle_{\text{plane}}, \tag{25}$$

and using (25), $\langle E\rangle_{\text{plane}}$ can be written as

$$\begin{aligned}\langle E\rangle_{\text{plane}} &= \langle K\rangle_{\text{plane}} + \langle V\rangle_{\text{plane}}\\ &= \frac{2+\alpha}{\alpha}\langle K\rangle_{\text{plane}}\\ &= \frac{2+\alpha}{2\alpha}\left(\langle p_u^2\rangle + \langle p_v^2\rangle\right).\end{aligned} \tag{26}$$

According to Bertrand's Theorem, Kepler's potential $V(r) = -\frac{k}{r}$ and radial harmonic oscillator $V(r) = \frac{1}{2}kr^2$ are the only two types of central force potentials where all bound orbits are also closed orbits. Therefore, if we restrict ourselves to cases where $0<\alpha\neq 2$ where almost all orbits are open (except for the circular orbit), we see that $\langle p_u^2\rangle = \langle p_v^2\rangle$ as $t\to\infty$ so that, following the argument of Sec. III A,

$$\langle p_u^2\rangle = \langle p_v^2\rangle = \frac{\alpha}{2+\alpha}\langle E\rangle_{\text{plane}}. \tag{27}$$

We can now express the the averages of p_x^2, p_y^2 and p_z^2 through $\langle E\rangle_{\text{plane}}$ as shown in Appendix B (assuming that the final distribution does not depend on ϕ)

$$T_{x,y} = \langle p_{x,y}^2\rangle = \frac{\alpha\pi}{2(2+\alpha)}\int_0^\pi d\theta\langle E\rangle_{\text{plane}}(1+\sin^2\theta) \tag{28}$$

$$T_z = \langle p_z^2\rangle = \frac{\alpha\pi}{2+\alpha}\int_0^\pi d\theta\langle E\rangle_{\text{plane}}\cos^2\theta. \tag{29}$$

It remains now to calculate $\langle E\rangle_{\text{plane}}$ as a function of θ and ϕ after the momentum kick.

C. Momentum Kick

We perturb the Maxwell-Boltzmann distribution in a potential given by (21) at $t=0$ by applying a momentum kick q_z along the z-direction. The resulting initial distribution at temperature $k_BT_0=1$ is:

$$\begin{aligned}&f(\mathbf{r},\mathbf{p},t=0) =\\ &A\exp\left(-\frac{p_x^2+p_y^2+(p_z-q_z)^2}{2} - r^\alpha\right)\end{aligned} \tag{30}$$

where

$$A = \frac{3}{8\sqrt{2}\pi^{5/2}\Gamma\left(\frac{3+\alpha}{\alpha}\right)}. \tag{31}$$

If we transform (30) using (A3), we get:

$$\begin{aligned}&f = A\exp\left(-\frac{q_z^2}{2}\right)\\ &\exp\left(-r^\alpha\right)\exp\left(-\frac{p_r^2 - 2p_rq_z\cos\theta\sin\alpha_p}{2}\right).\end{aligned} \tag{32}$$

Using (32), we can calculate $\langle V\rangle_{\text{plane}} = \langle r^\alpha\rangle$, $\langle K\rangle_{\text{plane}} = \langle p_r^2\rangle/2m$, and finally $\langle E\rangle_{\text{plane}} = \langle V\rangle_{\text{plane}} + \langle K\rangle_{\text{plane}}$ as follows:

$$\begin{aligned}\langle V\rangle_{\text{plane}}(t=0) = &\frac{3|\cos\theta|}{\alpha\pi}e^{-\frac{q_z^2}{2}}e^{\frac{q_z^2\cos^2\theta}{4}}\\ &\times\left[I_1\left(\frac{q_z^2\cos^2\theta}{4}\right)\frac{q_z^2\cos^2\theta}{4}\right.\\ &\left.+I_0\left(\frac{q_z^2\cos^2\theta}{4}\right)\left(\frac{1}{2}+\frac{q_z^2\cos^2\theta}{4}\right)\right],\end{aligned} \tag{33}$$

$$\begin{aligned}&\langle K\rangle_{\text{plane}}(t=0) = \frac{|\cos\theta|}{8\pi}\exp\left(-\frac{q_z^2}{2}\right)\exp\left(\frac{q_z^2\cos^2\theta}{4}\right)\\ &\times\left[q_z^2I_1\left(\frac{q_z^2\cos^2\theta}{4}\right)\cos^2\theta(4+q_z^2\cos^2\theta)\right.\\ &\left.+I_0\left(\frac{q_z^2\cos^2\theta}{4}\right)(6+6q_z^2\cos^2\theta+q_z^4\cos^4\theta)\right],\end{aligned} \tag{34}$$

where I_0 and I_1 are modified Bessel functions of the first kind. Since $\langle E\rangle_{\text{plane}}$ does not change with time we can use this to

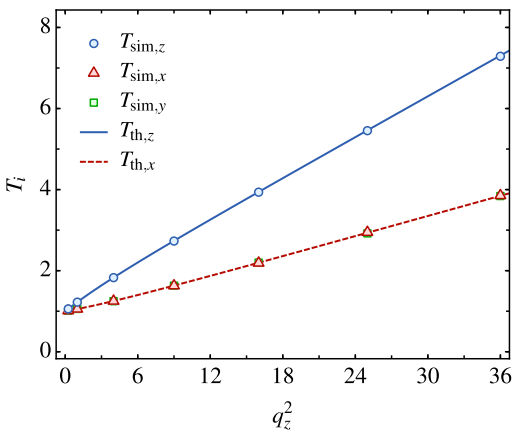

Figure 5. Comparison of the simulation results for $T_i = \langle p_i^2 \rangle_{t\to\infty}$ ($i = x, y, z$) with the analytical predictions (35) and (36) for an isotropic potential (21) with $\alpha = 1$ for different kick strengths q_z along the z-direction. Note that the predicted $\langle p_x^2 \rangle_\infty$ and $\langle p_y^2 \rangle_\infty$ are identical.

obtain the $\langle p_i^2 \rangle$ at $t \to \infty$ via Eqs. (28,29). For $\alpha = 1$ the resulting expressions read

$$\langle p_x^2 \rangle = \frac{q_z^2}{12} + \frac{5}{6} + \frac{1}{2q_z^2} - \frac{\sqrt{2}}{2q_z^3} F\left(\frac{q_z}{\sqrt{2}}\right), \tag{35}$$

$$\langle p_z^2 \rangle = \frac{q_z^2}{6} + \frac{4}{3} - \frac{1}{q_z^2} + \frac{\sqrt{2}}{q_z^3} F\left(\frac{q_z}{\sqrt{2}}\right), \tag{36}$$

where F is the Dawson function. In Fig. 5 we show the excellent agreement of the simulations with these analytical predictions.

For a small momentum kick, we can find some illuminating expressions. Expanding $\langle E \rangle_{\mathrm{plane}}$ about $q_z = 0$ up to $\mathscr{O}(q_z^2)$ we obtain from (28) and (29)

$$T_{x,y} \approx 1 + \frac{5\alpha - 2}{20(2+\alpha)} q_z^2 \tag{37}$$

$$T_z \approx 1 + \frac{2+5\alpha}{10(2+\alpha)} q_z^2. \tag{38}$$

For the case $\alpha = 1$ we find

$$T_{x,y} \approx 1 + \frac{1}{20} q_z^2 \Rightarrow \Delta T_{x,y} = \frac{1}{10} \Delta E, \tag{39}$$

$$T_z \approx 1 + \frac{7}{30} q_z^2 \Rightarrow \Delta T_{x,y} = \frac{7}{15} \Delta E. \tag{40}$$

which satisfies the virial theorem (11). Comparing with the quadrupole experiment (point 3. above) where $\Delta T_{x,y} = 0$ and $\Delta T_z = 2/3 \Delta E$, we see that the spherical case leads to some increased heating in the xy plane although small.

In terms of the matrix Θ_{ij} from (12), for a spherically symmetric case we can show that

$$\Theta_{ij} = \begin{pmatrix} \theta_1 & \theta_2 & \theta_2 \\ \theta_2 & \theta_1 & \theta_2 \\ \theta_2 & \theta_2 & \theta_1 \end{pmatrix} \tag{41}$$

so that e.g. $\Delta T_x = \theta_1 q_x^2/2$ and $\Delta T_x = \theta_2 q_y^2/2$. As before, using the sum rule, we find that $\theta_1 + 2\theta_2 = 2/3$ so that the matrix depends only on a single unknown parameter. Then (37) and (38) imply that

$$\theta_1 = \frac{2+5\alpha}{5(2+\alpha)} \text{ and } \theta_2 = \frac{5\alpha - 2}{10(2+\alpha)} \tag{42}$$

which satisfy the sum rule (13). For the case $\alpha = 1$ (16) we get $\theta_1 = 7/15$ and $\theta_2 = 1/10$.

D. Heating and cooling of transverse directions

These results allow us to answer an interesting question: if we kick the gas along a direction, do the transverse directions heat or cool?

For an interacting gas, we know collisions will distribute the energy along all directions, hence the transverse directions will be heated by the same amount as the kicked direction. For an ideal gas in e.g. a harmonic potential, the transverse directions will not be affected.

Using (37) and (38) we see that, for a noninteracting gas in a spherical potential of the form (21), we can have different types of behaviour (up to $\mathscr{O}(q_z^2)$) for the transverse directions:

- for $\alpha < \frac{2}{5}$: cooling;
- for $\alpha = \frac{2}{5}$: no change;
- for $\alpha > \frac{2}{5}$: heating.

This surprising result tells us that it is possible in some cases to *cool* the gas along some directions while heating it up along others. In fact, as we will see later the quadrupole potential is of this type: it cools along the x and y directions if kicked along z. Nevertheless, the spherical potential, which most closely resembles it, with $\alpha = 1$, behaves more conventionally since it heats up.

E. Population redistribution due to kick

We would like to gain some insight into why the final momentum widths are different $\langle p_x^2 \rangle = \langle p_y^2 \rangle \neq \langle p_z^2 \rangle$ for $q_z \neq 0$.

We can rewrite (28) using the fact that the total energy of the gas $E_{\mathrm{total}}(q=0) + \Delta E$ with ΔE given by (2), can be expressed as the sum of the plane energies:

$$E_{\mathrm{total}}(q=0) + \frac{q_z^2}{2} = \int_0^\pi d\phi \int_0^\pi d\theta \langle E \rangle_{\mathrm{plane}} = \pi \int_0^\pi d\theta \langle E \rangle_{\mathrm{plane}} \tag{43}$$

The term $E_{\mathrm{total}}(q=0)$ can be easily found from the $q_z = 0$ limit of (33) and (34). It follows that:

$$\begin{aligned} \langle p_{x,y}^2 \rangle &= \frac{\alpha\pi}{2(2+\alpha)} \int_0^\pi d\theta \langle E \rangle_{\mathrm{plane}} (1 + \sin^2\theta) \\ &= \frac{\alpha}{2(2+\alpha)} \left(\frac{q^2}{2} + \frac{6+3\alpha}{2\alpha} + \pi \int_0^\pi d\theta \langle E \rangle_{\mathrm{plane}} \sin^2\theta \right) \\ &\overset{\alpha=1}{=} \frac{1}{6} \left(\frac{q_z^2}{2} + \frac{9}{2} \right) + \frac{\pi}{6} \int_0^\pi d\theta \sin^2\theta \langle E \rangle_{\mathrm{plane}}. \end{aligned} \tag{44}$$

We can study how each of the terms in $\langle p_x^2 \rangle$ varies with q_z. In Fig. 6, we can see that the contribution of the integral term of (44) is small compared to the q_z^2 term and becomes less important as q_z increases.

To understand why the integral term becomes small, we can investigate how $\langle E \rangle_{\text{plane}}$ changes as a function of θ for different values of q_z. From Fig. 7, we can see that the value of $\langle E \rangle_{\text{plane}}$ near $\theta = 0$ and $\theta = \pi$ increases with increasing q_z and the opposite happens near $\theta = \pi/2$. As the integrand multiplies this factor by $\sin^2\theta$ which is 0 at $\theta = 0, \pi$ and peaks at $\theta = \pi/2$ the integral will decrease as q_z increases.

To make it even clearer, it is useful to plot not $\langle E \rangle_{\text{plane}}$ but $\langle E \rangle_{\text{plane}}/|\cos\theta|$ which removes the effect of the Jacobian (A2) which simply accounts for the variation of the density of planes as a function of θ, leaving us with the change in plane energy as a result of the kick.

From Fig. 8, we can see that when there is no momentum kick, the energy of all the planes are the same. When we apply a momentum kick along the z-axis, planes lying along that direction ($\theta = 0$ or π) gain energy whereas directions close $\theta = \pi/2$ lose it. This means that, when we project the energy of each plane to obtain the momentum widths, $\langle p_z^2 \rangle > \langle p_x^2 \rangle$.

We can also see that as $q_z \to \infty$, $\langle E \rangle_{\text{plane}}/|\cos\theta|$ is only non-zero at $\theta = 0$ and π which explains the momentum widths ratio constraint derived in (B10) (note that Fig. 9 agrees with the ratio constraint).

F. Memory loss in isotropic potentials

A natural question arising from the study of this section is whether a gas can remember in which direction it was kicked after a long time has passed. For example, we could start with a gas in thermal equilibrium in an isotropic potential, i.e. a spherically (3D) or circularly (2D) symmetric potential, apply a momentum kick along an arbitrary direction and wait for a very long time. Is the final gas distribution anisotropic? I.e. does it preserve a memory of the direction of the kick?

In a collisional gas, the extra energy from the momentum kick is redistributed along all directions equally, leading to isotropic heating and therefore a loss of memory.

A non-interacting gas in a harmonic oscillator preserves this memory because its center of mass oscillates along the kick direction indefinitely.

However, quite surprisingly, a non-interacting gas in a non-separable potential can also preserve it due to the existence of integrals of motion which encode the direction. For example in a 3D spherical potential the memory is associated with the three components of angular momentum $L_{x,y,z}$ being integrals of the motion, as we have seen.

An interesting question is: can there be memory loss with no interactions and a non-separable potential? Unexpectedly the answer is yes: for example a gas in a 2D circular symmetric potential has $\langle p_x^2 \rangle = \langle p_y^2 \rangle$ due to Bertrand's theorem, so memory is lost (excluding harmonic and Kepler's potential). There is only a single component of angular momentum so the direction cannot be encoded in the integrals of the motion. After the kick the extra energy is redistributed to all directions,

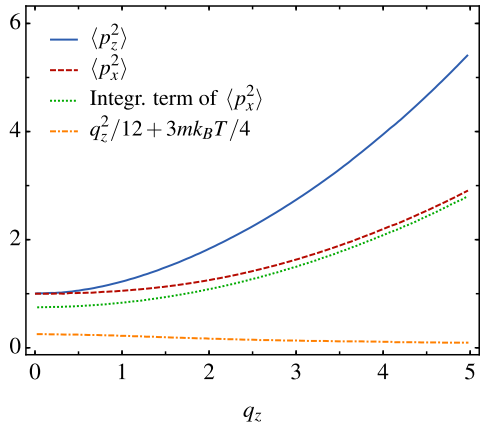

Figure 6. Comparing the different terms of $\langle p_x^2 \rangle$ in (44) with $\langle p_z^2 \rangle$ (36) for different values of momentum kick q_z with $m = k_BT = 1$.

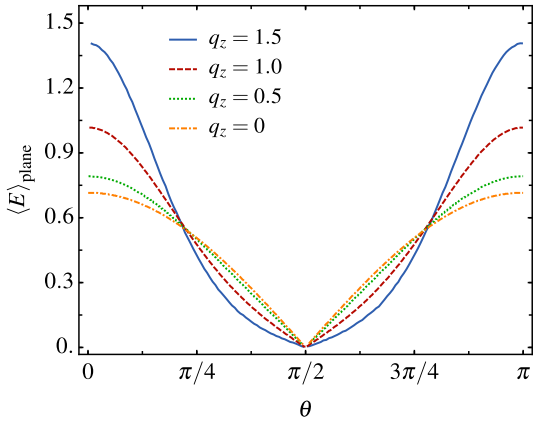

Figure 7. Using Eqs. (33) and (34) to plot $\langle E \rangle_{\text{plane}}(\theta)$ for different values of momentum kick q_z.

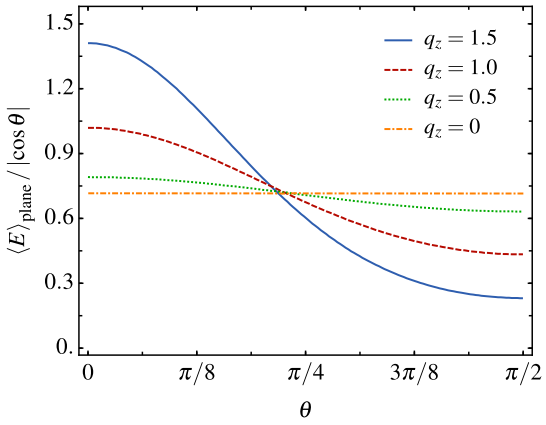

Figure 8. Using Eqs. (33) and (34) to plot $\langle E \rangle_{\text{plane}}(\theta)/|\cos\theta|$ for different values of momentum kick q_z.

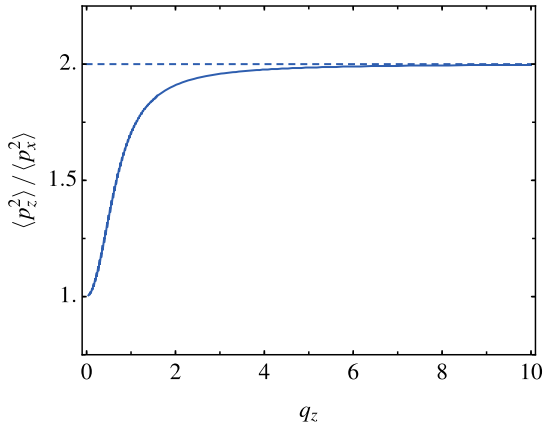

Figure 9. Using Eqs. (33) and (34) to plot the ratio between $\langle p_z^2 \rangle$ and $\langle p_x^2 \rangle$ for different values of momentum kick q_z.

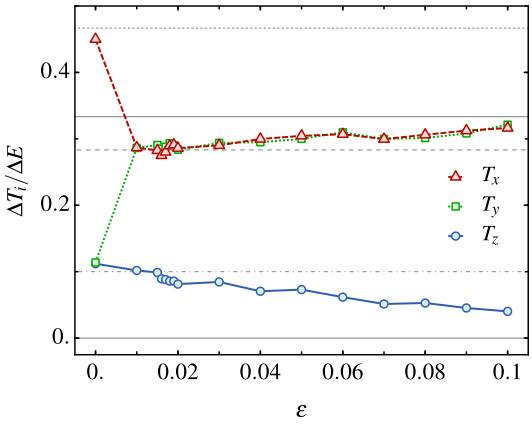

Figure 10. Behavior of the final temperatures $\Delta T_i/\Delta E$ as a function of the anisotropy ε near the spherical limit after a kick along x. At $\varepsilon = 0$, $T_z = T_y$ after which there is a discontinuous change in the temperatures due to the breaking of spherical symmetry along z. Data are obtained by numerical simulation over 100 000 atoms. Dashed, dotted and plain lines correspond to the theoretical expectations of the fully isotropic (39, 40), almost isotropic (38 and 50) and quadrupole geometries, respectively.

the "orbit density" becomes isotropic as $t \to \infty$ which leads to loss of memory. This macroscopic loss of information is due to ergodicity of the individual trajectories rather than to collisions. Of course, microscopically the memory is preserved since, if we reversed the momenta of all atoms at the same time, we could recover the initial kicked distribution.

G. First order transition due to breaking of the potential's spherical symmetry

As we have seen, if we start with an isotropic equilibrium thermal distribution in a spherical trap ($\varepsilon = 0$) and we kick the gas along the z direction then, when $t \to \infty$, we find that $T_x = T_y \neq T_z$. Likewise, by spherical symmetry, kicking along the x direction will lead to the temperatures along the perpendicular directions being equal ($T_y = T_z \neq T_x$, see Fig. 10).

However, this is in seeming contradiction with the experimental results for the quadrupole case ($\varepsilon = 3$), see point 2. above and Fig. 1, where a kick along the x direction leads to $T_x = T_y$. It seems that breaking the spherical symmetry by setting $\varepsilon > 0$ and making the z direction unequal, enforces a cylindrical symmetry of the steady state gas distribution along the perpendicular directions after the kick. This discrepancy in behaviour indicates a discontinuous (first order) transition in gas behavior as a function of ε when going from spherical to non-spherical potentials.

To study this better we plot the three final temperatures after a kick along x as a function of ε near $\varepsilon = 0$ (Fig. 10). We see that at $\varepsilon = 0$, $T_y = T_z < T_x$, as expected. However, for values of ε immediately above that, we find that $T_x = T_y > T_z$, the behavior of the quadrupole trap. In other words:

$$\lim_{\varepsilon \to 0} \lim_{t \to \infty} \langle p_x^2 - p_y^2 \rangle_t \neq \lim_{t \to \infty} \lim_{\varepsilon \to 0} \langle p_x^2 - p_y^2 \rangle_t, \tag{45}$$

the lhs being zero and the rhs not. We will see that the reason for this is due to $\langle p_x^2 - p_y^2 \rangle_t$ relaxing to zero with a relaxation or dephasing time scale $\tilde{\tau}$ which diverges as $\varepsilon \to 0$.

There is a characteristic relaxation time $\tilde{\tau}$ before the momentum widths reach their final steady state value during which there is a gradual dephasing of the orbits of atoms with different angular momenta and energy in each plane. This timescale is related to the width of the thermal distribution and does not depend on ε as $\varepsilon \to 0$. From dimensional analysis we see that $\tilde{\tau} \sim \sqrt{T_0} \sim 1$.

However, there is a second much longer characteristic relaxation time τ during which T_x and T_y converge to each other and which was not present in the perfectly spherical case. This timescale appears because of the rotation (precession) of the orbital planes of each atom around the z axis and is due to the potential's anisotropy. This phenomenon is known in astronomy when studying the orbit of satellites around slightly non-spherical planets, where it is called nodal precession [22].

For sufficiently small ε and at long times $t \gg \tau$, we expect that $\langle p_x^2 - p_y^2 \rangle_t$ will decay at long times as some function of t/τ, where the decay time scale is given by

$$\tau \sim \varepsilon^{\nu}. \tag{46}$$

The value of ν is independent of the kick strength if it is weak enough, and the dependence on $\sqrt{T_0}$ sets the dimensions of τ. We show in Appendix C that $\nu = -1$ so that $\tau \sim 1/\varepsilon$; this is confirmed in Fig. 11.

While Bertrand's equilibrium leads to a higher temperature along the kicked direction, the orbital precession redistributes the energy equally between the x- and y-axes, leading eventually to the equilibration of T_x and T_y. The first process takes place in about 40 time units, while the latter process is much slower as the anisotropy is smaller, as shown in Fig. 11.

This analysis leads to quantitative predictions for the final temperatures at small anisotropy, particular for the temperature discontinuities. For $\varepsilon \gtrsim 0$, the imparted energy gets first

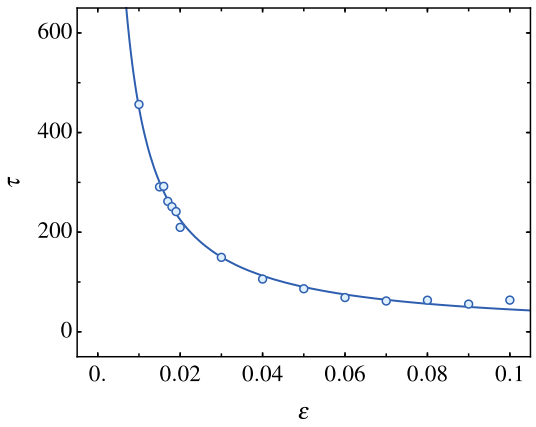

Figure 11. Equilibration time as a function of the trap anisotropy ε. The equilibration time is defined as the time required for T_y to reach 99% of the steady T_x value. The solid line is a fit $A \times \varepsilon^{-1}$ following the expression (46). The best fit leads to an R-squared value of 0.99.

redistributed in the plane, before the orbital precession slowly equilibrates temperatures so that we can express the final temperatures in terms of the spherical temperatures (39), (40):

$$\Delta T_x^{\varepsilon\to 0} = \Delta T_y^{\varepsilon\to 0} = \frac{1}{2}\left(\Delta T_x^{\varepsilon=0} + \Delta T_y^{\varepsilon=0}\right) \tag{47}$$

$$= \frac{17}{60}\Delta E \qquad \text{and} \tag{48}$$

$$\Delta T_z^{\varepsilon\to 0} = \Delta T_z^{\varepsilon=0} \tag{49}$$

$$= \frac{1}{10}\Delta E. \tag{50}$$

From here we can extract the matrix elements of (14) since in the above equations $\Delta E = q_x^2/2$: $\theta_1 = 17/60$, $\theta_2 = 1/10$, which means that $\theta_3 = 7/15$.

This prediction is in very good agreement with the results presented in Fig. 10 and is valid near $\varepsilon = 0$ as long as $\tau \gg \widetilde{\tau}$.

IV. PANCAKE LIMIT

In the previous section we analyzed the spherically symmetric case, which could be solved analytically. There is another case where the motion can be solved analytically, namely the limit when the confinement along the z-direction is strong ($\varepsilon \gg 1$). As we will see later, this case exhibits behavior which is much closer to the quadrupole.

We consider the case of strong confinement of the gas along the z direction of the potential (15) with $\varepsilon \gg 1$ so that

$$V(\mathbf{r}) = \sqrt{x^2+y^2+(1+\varepsilon)z^2} \simeq \sqrt{\rho^2+\varepsilon z^2}, \tag{51}$$

where we have used cylindrical coordinate $\rho = \sqrt{x^2+y^2}$. Since the potential is tightly confined, motion along the z direction is fast compared to that in the plane. To check this we compare t_z, the period of oscillation along z, with the period of oscillation along ρ, t_ρ, the characteristic timescales of the two motions.

An atom whose motion is along the x-axis experiences a potential $V = x$, whereas if the atom moves along the z-axis, it sees a potential $V = \sqrt{\varepsilon}z$. Assuming that both of these atoms have the same overall thermal energy T, then, in the first case, its period of oscillation is $\propto \sqrt{E}$ whereas in the second case it is $\propto \sqrt{E/\varepsilon}$, so that the ratio of the two periods is $\varepsilon \gg 1$ and therefore the approximation of considering the motion along z to be fast compared with that in the plane is justified.

We start by analyzing the motion of a single atom. We split up the energy as

$$E = \frac{p_\rho^2}{2} + \frac{p_\phi^2}{2\rho^2} + E_z, \tag{52}$$

where p_ρ and p_ϕ are the canonically conjugate momenta and $\phi = \arctan(y/x)$ is the angle with the x-axis in the xy plane. E and p_ϕ are constants of the motion (the latter being the angular momentum L_z which is always conserved due to the potential being independent of ϕ). Also,

$$E_z = \frac{p_z^2}{2} + \sqrt{\rho^2+\varepsilon z^2}. \tag{53}$$

We now replace p_z, z with the action-angle variables I, η in the usual way. In particular

$$\begin{aligned} I &= \oint p_z \frac{dz}{2\pi} = 4\int_0^{z_{\max}} p_z \frac{dz}{2\pi} \\ &= \frac{2\sqrt{2}}{\pi}\int_0^{\sqrt{\frac{E_z^2-\rho^2}{\varepsilon}}} \sqrt{E_z - \sqrt{\rho^2+\varepsilon z^2}}\,dz \\ &= \frac{2\sqrt{2}}{\pi\sqrt{\varepsilon}} I_0 \end{aligned} \tag{54}$$

with the definition

$$I_0 \equiv \int_0^{\sqrt{E_z^2-\rho^2}} \sqrt{E_z - \sqrt{\rho^2+z'^2}}\,dz' \tag{55}$$

where we made the substitution $z' = \sqrt{\varepsilon}z$ to show that $I \propto 1/\sqrt{\varepsilon}$, since I_0 does not depend on ε. Note that, for the same reason, in (55) E_z depends implicitly only on I_0 and ρ but not on ε.

The trajectory $p_z(z)$ is determined by (53) and therefore depends on E_z and ρ. Also, since ρ is slowly varying, by the standard arguments, I (or I_0) can be considered an adiabatic invariant (i.e. another constant) for the motion in the plane.

A simple approximate solution to (55) which allows us to express E_z explicitly in terms of I_0 and ρ is

$$E_z(I_0,\rho) = \left(\frac{3}{2}I_0 + \rho^{3/2}\right)^{2/3}, \tag{56}$$

which allows us to rewrite (52) as

$$E = \frac{p_\rho^2}{2} + \frac{p_\phi^2}{2\rho^2} + \left(\frac{3}{2}I_0 + \rho^{3/2}\right)^{2/3} \tag{57}$$

and we see that the effective potential for the radial motion is a sum of the centrifugal term plus a confining term increasing linearly at large distances.

Since we had originally three degrees of freedom, a particular trajectory is completely determined by the three integrals of the motion E, p_ϕ and I_0. Therefore, the time averaged in-plane kinetic energy

$$\overline{\frac{p_\rho^2}{2}+\frac{p_\phi^2}{2\rho^2}} \tag{58}$$

is also determined by these constants.

It is now clear that the averaged kinetic energy is only a function of the constants of the motion E, p_ϕ, and I_0 for that orbit.

The adiabatic principle tells us that the atom executes a motion in the plane under the effective potential E_z given by (56). Since I_0 is not the same for all atoms, each atom moves in slightly different potentials, labelled by their value of I_0.

When we apply a kick to an atom along z at a time t_0, its in-plane momenta p_ϕ, p_ρ and its position ρ, z are unchanged. What changes instead is its momentum p_z and therefore its corresponding kinetic energy $p_z^2/2 \to (p_z+q)^2/2 = p_z^2/2 + p_z q + q^2/2$. After averaging over the whole gas, the term $p_z q$ drops out so that only the third term remains, an average increase of kinetic energy of $q^2/2$ per atom (and so of $E_z(\rho_0)$ as we see from (53)). This has two effects: it changes the effective potential (56) and it increases the total energy E. Since I_0 is an increasing function of E_z, an increase of the kinetic energy along z at t_0 implies an instantaneous change $I_0 \to I_0 + \Delta I_0$, $\Delta I_0 > 0$. In the subsequent motion, the effective potential is changed $E_z(I_0,\rho) \to E_z(I_0+\Delta I_0,\rho)$, transforming it into a shallower effective 2D potential as we can see from (56). On the other hand, the increased kinetic energy also means an increased total energy $E \to E + \Delta E$:

$$\Delta E = E_z(I_0+\Delta I_0,\rho_0) - E_z(I_0,\rho_0). \tag{59}$$

The first effect leads naturally to a reduction in speed in the plane, i.e. a reduction in the average in-plane kinetic energy (58). However, the increase ΔE has the opposite effect, that of increasing the average kinetic energy. This latter effect is dominant for atoms which were near the bottom of the potential at the moment of the kick, whereas the reduction in ΔE is most felt by those which were away from the center.

To determine what happens to the gas as a whole, we use numerical simulations. We compare the results of the pancake case after a kick along z with a very large ε with the case of a 2D gas in the effective potential (56), with the same number of atoms, temperature, and kick momentum q.

For the simulation of the 2D gas, we use the same initialization of the system as for the regular pancake case, namely the kicked Boltzmann distribution with potential (51). Then for each individual atom we evaluate I_0 via Eq. (56), where E_z and ρ are determined by the initial position and momentum coordinates of the atom. The subsequent time-evolution of each atom is governed by Eq. (57), where the last term corresponds to the new effective potential (56) which replaces the regular pancake potential (51) (I_0 is assumed constant for each atom during the time-evolution). Note that we only evaluate the movement of the gas in the xy plane in this approximation—the position and momentum coordinates in z-direction do not appear in the equations.

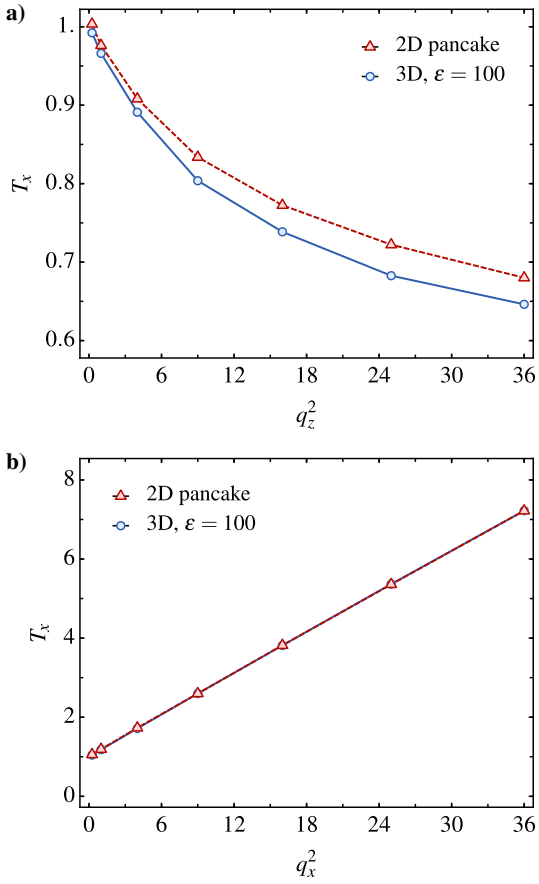

Figure 12. Comparison of the 2D potential given by (56) and the pancake potential. Here $\varepsilon = 100$, but larger ε values produced consistent results. The plots are for $\langle p_x^2 \rangle$ as a function of q_z^2 (top panel), and as a function of q_x^2 (bottom panel). Solid and dashed lines represent guides to the eye. Note that the two potentials give almost identical results for the heating along the kick direction and a small discrepancy for the orthogonal cooling.

We are also able to use the same method to study the change in average kinetic energy along z due to a kick in the plane along x.

Our findings are in Fig. 12. We see that there is excellent agreement between the 3D pancake gas and the 2D case, especially for the heating along the direction of the kick. Although both show cooling of the transverse directions, the agreement is less good there, a fact which we attribute to the inexact ansatz (56).

So the physical interpretation of the pancake case is clear: there is a slight overall cooling of the transverse directions when the gas is kicked along the z direction due to the effective potential becoming shallower for the atoms closer to the center of the trap. This effect dominates over the heating of

the atoms near the edges of the gas, although not by much so that the overall cooling is very small.

V. COMPARISON OF THE POTENTIALS

In Fig. 13 we compare the quadrupole potential with the two others we have discussed, the spherical and the pancake. It is clear that the quadrupole behavior is much closer to that of the pancake so that, in this respect, it seems that the $\varepsilon = 3$ is already very close to the limit of $\varepsilon = \infty$. There is a remarkably good quantitative agreement between the two cases. For example we obtain approximately the same heating and cooling in both the kicked and transverse directions. We find for the pancake $\Theta_{xx} = 0.38$ and $\Theta_{zx} = -0.09$ which can be compared with the very similar values for the quadrupole $\Theta_{xx} = 0.36$ and $\Theta_{zx} = -0.05$ mentioned in Sec. II.

In Sec. II we mentioned two puzzles: one was the anisotropy of the temperatures along the kicked and orthogonal directions in the quadrupole potential. Both the spherical and pancake potentials exhibit this. For the spherical case this is due to a geometric reason, the fact that the kick redistributes the atoms into planes which are more aligned with the direction of the kick. They will subsequently remain there due to the conservation of angular momentum. In the pancake case this is due to strong potential anisotropy coming from the large value of ε. This latter reason is responsible also for the anisotropy in the quadrupole potential.

Also, in the spherical case we saw that the temperatures of the kicked direction and of the plane orthogonal to it were different. In the quadrupole case we find generally in all simulations that $T_x = T_y \neq T_z$. This was interpreted in terms of the 2D effective description where Bertrand's theorem applies; it leads naturally to the isotropy of the distribution in the xy plane. Clearly the quadrupole gas has this behavior for the same reason.

The second puzzle was the apparent (near) separability of the kicked and orthogonal directions, i.e. that the kick energy is *not* redistributed into the momentum distributions of all directions but rather it is concentrated only in the kick direction. As we see from Fig. 13, the spherical and pancake potentials behave very differently: the pancake reproduces closely the quadrupole's separability (in fact a slight cooling of the orthogonal directions) while the spherical potential shows a clear heating of those directions. The reason for the separability in the quadrupole case can be traced to the 2D model where it is due to a near cancellation of the contributions of the atoms which, at the moment of the kick, are close to the center of the trap and are cooled and that of the atoms at the periphery which are heated.

VI. CONCLUSION

We began this analysis with some puzzling experimental results for a non-interacting classical gas in a quadrupole trap whereby momentum kicks along one spatial direction were found to mostly affect only that direction, despite the fact that

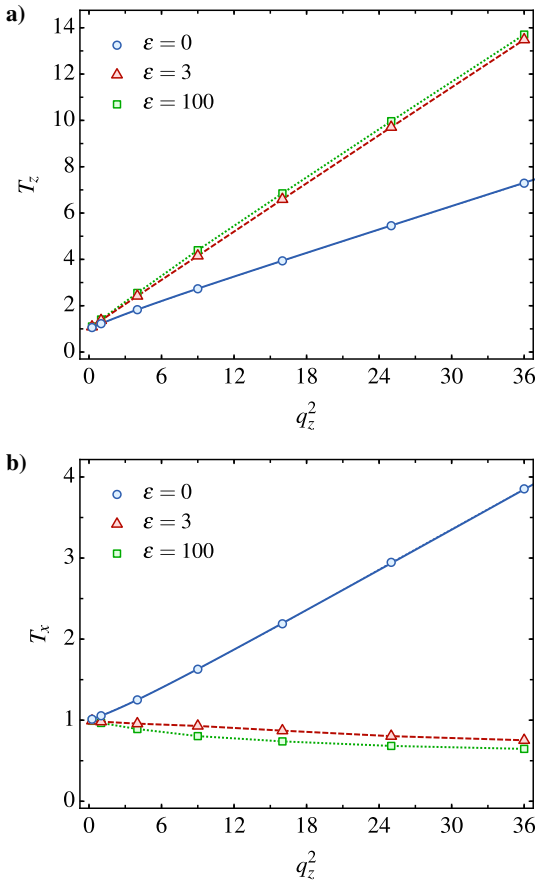

Figure 13. Comparison of the three types of potentials: spherical ($\varepsilon = 0$), quadrupole ($\varepsilon = 3$) and pancake ($\varepsilon = 100$) showing the much better agreement between the quadrupole and the pancake compared with the spherical case. The top panel shows $\langle p_z^2 \rangle$ and the bottom panel $\langle p_x^2 \rangle$ as a function of the momentum kick q_z^2 in z-direction. The blue solid lines are the analytical predictions (35) and (36) for the spherical potential. Dashed and dotted lines for the other potentials are guides to the eye.

the potential is non-separable. By analyzing the extreme case of the spherical potential ($\varepsilon = 0$) we understood that, in 3D, the constants of the motion (e.g. the angular momentum components) can allow the system to retain a memory of the direction of the kick. Consequently, the long time momentum distribution can remain anisotropic in this *isotropic* system. However, this effect strongly depends on the dimensionality of the problem, and the situation is completely different in 2D, where Bertrand's theorem leads to an isotropic distribution. Furthermore, as soon as the potential becomes slightly anisotropic ($0 < \varepsilon \ll 1$), the competition between the in-plane isotropic behavior and the symmetry-induced precession of orbital planes results in a qualitatively different steady-state, which we were able to characterize analytically. Finally, we investigated the pancake limit (large ε), which was shown numerically to be much closer to the experimental situation (i.e. the quadrupole potential). We were able to explain analytically, based on an effective potential, most of its characteristic

features, including the peculiar cooling effect experienced by the transverse degrees of freedom with respect to the kick direction.

For future analysis we would like to investigate the apparent "thermalization" of the gas after the kick as discussed in section II A as well as studying more in detail the region between the spherical to pancake limits.

[1] V. Arnol'd, *Mathematical Methods of Classical Mechanics* (Springer Science & Business Media, 2013) p. 520.
[2] J. Loschmidt, Sitzungsber. Kais. Akad. Wiss. Wien, Math. Naturwiss. **73**, 128 (1874).
[3] H. Poincaré, Acta mathematica **13**, A3 (1890).
[4] E. Fermi, P. Pasta, S. Ulam, and M. Tsingou, *Studies of the nonlinear problems*, Tech. Rep. (Los Alamos Scientific Lab., N. Mex., 1955).
[5] T. Dauxois, Physics Today **61**, 55 (2008).
[6] *Time's Arrows Today: Recent Physical and Philosophical Work on the Direction of Time* (Cambridge University Press, 1995).
[7] J. M. Deutsch, Phys. Rev. A **43**, 2046 (1991).
[8] M. Srednicki, Phys. Rev. E **50**, 888 (1994).
[9] M. Rigol, V. Dunjko, and M. Olshanii, Nature **452**, 854 (2008).
[10] F. Jin, T. Neuhaus, K. Michielsen, S. Miyashita, M. Novotny, M. I. Katsnelson, and H. De Raedt, New Journal of Physics **15**, 033009 (2013).
[11] C. Voisin, D. Christofilos, N. Del Fatti, F. Vallée, B. Prével, E. Cottancin, J. Lermé, M. Pellarin, and M. Broyer, Phys. Rev. Lett. **85**, 2200 (2000).
[12] N. Sarkar and P. Ghosh, Phys. Rev. C **96**, 044901 (2017).
[13] A. M. Kaufman, M. E. Tai, A. Lukin, M. Rispoli, R. Schittko, P. M. Preiss, and M. Greiner, Science **353**, 794 (2016).
[14] E. L. Surkov, J. T. M. Walraven, and G. V. Shlyapnikov, Phys. Rev. A **49**, 4778 (1994).
[15] K. B. Davis, M.-O. Mewes, M. A. Joffe, M. R. Andrews, and W. Ketterle, Phys. Rev. Lett. **74**, 5202 (1995).
[16] D. Suchet, M. Rabinovic, T. Reimann, N. Kretschmar, F. Sievers, C. Salomon, J. Lau, O. Goulko, C. Lobo, and F. Chevy, EPL (Europhysics Letters) **114**, 26005 (2016), arXiv:1507.02106.
[17] O. Goulko, F. Chevy, and C. Lobo, Phys. Rev. A **84**, 051605(R) (2011), arXiv:1106.5773.
[18] O. Goulko, F. Chevy, and C. Lobo, New Journal of Physics **14**, 073036 (2012), arXiv:1201.6235 [cond-mat.quant-gas].
[19] W. C. Swope, H. C. Andersen, P. H. Berens, and K. R. Wilson, The Journal of Chemical Physics **76**, 637 (1982).
[20] T. Lepers, D. Davesne, S. Chiacchiera, and M. Urban, Phys. Rev. A **82**, 023609 (2010), arXiv:1004.5241.
[21] L. D. Landau and E. Lifshitz, *Mechanics, Volume 1* (Elsevier, 1982) p. 224.
[22] H. Goldstein, C. P. Poole, and J. L. Safko, *Classical Mechanics* (Addison Wesley, 2002) p. 638.

Appendix A: Coordinate transformation for the spherical case

In a spherical potential the motion of each atom is confined to a plane through the origin and perpendicular to its angular momentum. To treat the gas in each plane as a separate system it is convenient to choose coordinates where the motion in each plane is described by in-plane 2D coordinates along orthogonal axes labelled (u,v) with corresponding momenta (p_u,p_v). To relate these to the rectangular coordinates we define two angles θ and ϕ. θ is the angle between the z axis and the v axis. ϕ is the angle between the x-axis and the projection of the v-axis onto the x-y plane. Both angles are in the interval $[0,\pi]$. The coordinate transformation is thus:

$$\begin{aligned} x &= u\sin\phi + v\sin\theta\cos\phi \\ y &= -u\cos\phi + v\sin\theta\sin\phi \\ z &= v\cos\theta \\ p_x &= p_u\sin\phi + p_v\sin\theta\cos\phi \\ p_y &= -p_u\cos\phi + p_v\sin\theta\sin\phi \\ p_z &= p_v\cos\theta. \end{aligned} \tag{A1}$$

Note that it is not a canonical transformation since the Jacobian is:

$$J_1 = |(p_u v - p_v u)\cos\theta|. \tag{A2}$$

The $\cos\theta$ term has a simple interpretation: the angular density of planes having an angle θ with the z-axis is largest for small θ and drops to zero when $\theta = \pi/2$ since then there is only one plane perpendicular to the z-axis. In most cases, the calculation becomes simpler if we use polar coordinates in the plane:

$$\begin{aligned} u &= r\cos\alpha_r \\ v &= r\sin\alpha_r \\ p_u &= p_r\cos\alpha_p \\ p_v &= p_r\sin\alpha_p, \end{aligned}$$

where α_r and α_p are in the interval $(0,2\pi]$. The transformation (A1) becomes:

$$\begin{aligned} x &= r\cos\alpha_r\sin\phi + r\sin\alpha_r\sin\theta\cos\phi \\ y &= -r\cos\alpha_r\cos\phi + r\sin\alpha_r\sin\theta\sin\phi \\ z &= r\sin\alpha_r\cos\theta \\ p_x &= p_r\cos\alpha_p\sin\phi + p_r\sin\alpha_p\sin\theta\cos\phi \\ p_y &= -p_r\cos\alpha_p\cos\phi + p_r\sin\alpha_p\sin\theta\sin\phi \\ p_z &= p_r\sin\alpha_p\cos\theta. \end{aligned} \tag{A3}$$

The Jacobian for the transformation (A3) is

$$J_2 = r^2 p_r^2 |\sin(\alpha_r - \alpha_p)\cos\theta|. \tag{A4}$$

As the Boltzmann function $f(x,y,z,p_x,p_y,p_z,t)$ is normalized to unity, if we apply the transformations (A1) or (A3), the following quantities will also normalize to unity either in the $(u,v,p_u,p_v,\theta,\phi)$ or in the $(r,\alpha_r,p_r,\alpha_p,\theta,\phi)$ coordinates:

$$\begin{aligned} 1 &= \int_0^\pi d\phi \int_0^\pi d\theta \int_{-\infty}^{\infty} dp_u \int_{-\infty}^{\infty} dp_v \int_{-\infty}^{\infty} du \int_{-\infty}^{\infty} dv J_1 f \\ &= \int_0^\pi d\phi \int_0^\pi d\theta \int_0^{2\pi} d\alpha_p \int_0^{\infty} dp_r \int_0^{2\pi} d\alpha_r \int_0^{\infty} dr J_2 f. \end{aligned}$$

The average energy $\langle E\rangle$ is given by

$$\langle E\rangle(t) \equiv \langle E\rangle_t = \int d^3\mathbf{r} \int d^3\mathbf{p} f(\mathbf{r},\mathbf{p},t) E(\mathbf{r},\mathbf{p}). \tag{A5}$$

It is useful to define an energy $\langle E\rangle_{\text{plane}}(\theta,\phi)$ which is the average energy of all the planes lying between θ and $\theta+d\theta$, ϕ and $\phi+d\phi$

$$\langle E\rangle_{\text{plane}}(\theta,\phi) \equiv \int_0^{2\pi} d\alpha_r \int_0^{2\pi} d\alpha_p \int_0^{\infty} dp_r \int_0^{\infty} dr J_2 f E \tag{A6}$$

so that the total energy is, cf. (22),

$$\langle E\rangle = \int_0^{\pi} d\phi \int_0^{\pi} d\theta \langle E\rangle_{\text{plane}}. \tag{A7}$$

Note that, after the kick, $\langle E\rangle_{\text{plane}}$ is independent of time as the number of atoms on each plane is constant.

Appendix B: Averages over momenta

Using the transformation (A1), we can write the averages of p_x^2, p_y^2 and p_z^2 as:

$$\langle p_x^2\rangle = \langle p_u^2 \sin^2\phi\rangle + \langle p_v^2 \sin^2\theta\cos^2\phi\rangle + 2\langle p_u p_v \sin\theta\sin\phi\cos\phi\rangle, \tag{B1}$$
$$\langle p_y^2\rangle = \langle p_u^2 \cos^2\phi\rangle + \langle p_v^2 \sin^2\theta\sin^2\phi\rangle - 2\langle p_u p_v \sin\theta\sin\phi\cos\phi\rangle, \tag{B2}$$
$$\langle p_z^2\rangle = \langle p_v^2 \cos^2\theta\rangle. \tag{B3}$$

The first term of (B1) can be written in terms of $\langle E\rangle_{\text{plane}}$ using (27),

$$\begin{aligned}\langle p_u^2 \sin^2\phi\rangle &= \int_0^{\pi} d\phi \sin^2\phi \int_0^{\pi} d\theta \int_{-\infty}^{\infty} dv \int_{-\infty}^{\infty} du \int_{-\infty}^{\infty} dp_v \int_{-\infty}^{\infty} dp_u J_1 f(u,v,p_u,p_v,\theta,\phi,t) p_u^2 \\ &= \int_0^{\pi} d\phi \sin^2\phi \int_0^{\pi} d\theta \frac{m\alpha}{2+\alpha} \langle E\rangle_{\text{plane}}.\end{aligned} \tag{B4}$$

Using similar technique, (B1), (B2) and (B3) can be written as:

$$\langle p_x^2\rangle = \frac{m\alpha}{2+\alpha}\int_0^{\pi} d\phi \sin^2\phi \int_0^{\pi} d\theta \langle E\rangle_{\text{plane}} + \frac{m\alpha}{2+\alpha}\int_0^{\pi} d\phi \cos^2\phi \int_0^{\pi} d\theta \sin^2\theta \langle E\rangle_{\text{plane}} + 2\langle p_u p_v \sin\theta\sin\phi\cos\phi\rangle \tag{B5}$$
$$\langle p_y^2\rangle = \frac{m\alpha}{2+\alpha}\int_0^{\pi} d\phi \cos^2\phi \int_0^{\pi} d\theta \langle E\rangle_{\text{plane}} + \frac{m\alpha}{2+\alpha}\int_0^{\pi} d\phi \sin^2\phi \int_0^{\pi} d\theta \sin^2\theta \langle E\rangle_{\text{plane}} - 2\langle p_u p_v \sin\theta\sin\phi\cos\phi\rangle \tag{B6}$$
$$\langle p_z^2\rangle = \frac{m\alpha}{2+\alpha}\int_0^{\pi} d\phi \int_0^{\pi} d\theta \cos^2\theta \langle E\rangle_{\text{plane}}. \tag{B7}$$

The third term in (B5) and (B6) when written explicitly is:

$$\langle p_u p_v \sin\theta\sin\phi\cos\phi\rangle = \int_0^{\pi} d\phi \sin\phi\cos\phi \int_0^{\pi} d\theta \sin\theta \int_{-\infty}^{\infty} dv \int_{-\infty}^{\infty} du \int_{-\infty}^{\infty} dp_v \int_{-\infty}^{\infty} dp_u J_1 f(u,v,p_u,p_v,\theta,\phi,t) p_u p_v. \tag{B8}$$

If $f(u,v,p_u,p_v,\theta,\phi,t)$ is independent of ϕ then (B8) equals to zero. If $\langle E\rangle_{\text{plane}}$ is also independent of ϕ, (B5), (B6) and (B7) will be reduced to:

$$\langle p_x^2\rangle = \frac{m\alpha\pi}{2(2+\alpha)}\int_0^{\pi} d\theta \langle E\rangle_{\text{plane}}(1+\sin^2\theta)$$
$$\langle p_y^2\rangle = \frac{m\alpha\pi}{2(2+\alpha)}\int_0^{\pi} d\theta \langle E\rangle_{\text{plane}}(1+\sin^2\theta)$$
$$\langle p_z^2\rangle = \frac{m\alpha\pi}{2+\alpha}\int_0^{\pi} d\theta \langle E\rangle_{\text{plane}}\cos^2\theta.$$

We can see that $\langle p_x^2\rangle$ and $\langle p_y^2\rangle$ are equal. If we look at the ratio between $\langle p_x^2\rangle$ and $\langle p_z^2\rangle$:

$$\frac{\langle p_z^2\rangle}{\langle p_x^2\rangle} = 2\frac{\int_0^{\pi}\langle E\rangle_{\text{plane}}\cos^2\theta}{\int_0^{\pi}\langle E\rangle_{\text{plane}}(1+\sin^2\theta)}, \tag{B9}$$

as $\langle E\rangle_{\text{plane}}(\theta) \geq 0$, the ratio of the integrals will be between 0 and 1, therefore we can derive an inequality:

$$\langle p_z^2\rangle \leq 2\langle p_x^2\rangle. \tag{B10}$$

Appendix C: Calculation of dephasing rate

1. Initial distribution

We wish to study

$$\langle p_x^2 - p_y^2\rangle_t = \int dr^3 dp^3 (p_x^2 - p_y^2) f(\mathbf{r},\mathbf{p},t). \tag{C1}$$

However, since the gas is noninteracting, we can find time-dependent averages by following the position of individual atoms starting from an initial distribution of the gas and then averaging over that distribution. For example, to find $\langle p_x^2 - p_y^2\rangle_t$, instead of finding the time dependence of the Boltzmann distribution f, we calculate the quantity $p_x^2(t) - p_y^2(t)$ for each atom starting at the initial position $(\mathbf{r}_0, \mathbf{p}_0)$ and then average over $\mathbf{r}_0, \mathbf{p}_0$ weighted by the initial distribution:

$$\langle p_x^2 - p_y^2\rangle_t = \int d\mathbf{r}_0 d\mathbf{p}_0 \left[p_x^2(t) - p_y^2(t)\right]_{\mathbf{r}_0,\mathbf{p}_0} \times f(\mathbf{r}_0, \mathbf{p}_0, t=0) \tag{C2}$$

We take the initial distribution from (6) and expand in powers of q:

$$f(t=0) \propto \exp\left(-\frac{(p_x-q)^2 + p_y^2 + p_z^2}{2T}\right)\exp\left(-\frac{V(x,y,z)}{T}\right)$$
$$= \left(1 + \frac{p_x q}{T} - \frac{q^2}{2T} + \frac{1}{2}\left(\frac{p_x q}{T}\right)^2 + O(q^3)\right) f_{q=0} \tag{C3}$$

The first and third terms in the brackets do not contribute to (C2) since they are spherically symmetric and remain so during time evolution. The second term $\propto p_x q$ is odd under the parity transformation $x, p_x \to -x, -p_x$. Since this parity is preserved under time evolution, the integral of this term is zero for all times. The only term that contributes to (C2) is the one proportional to $(p_x q)^2$. Therefore keeping the lowest nonzero term we obtain:

$$f(t=0) = \frac{1}{2}\left(\frac{p_x q}{T}\right)^2 f_{q=0}. \tag{C4}$$

2. Precession of the orbital planes

To find this contribution we will make the crucial assumption that its orbital plane precesses slowly around the z-axis compared with the fast motion in each plane so that we are allowed to use the virial theorem to calculate averages in the plane as in subsection III A.

An orbital plane which is precessing will be characterised by a constant angle θ and a rate of precession $\dot{\phi}$. To find this rate we consider a perturbation of the planar orbit in the limit of a small correction to the spherical potential. Since $|\varepsilon| \ll 1$, we expand the potential in (15) to order $\mathcal{O}(\varepsilon)$:

$$V = \sqrt{x^2 + y^2 + (1+\varepsilon)z^2} \simeq r + \Delta H \tag{C5}$$

with

$$\Delta H \equiv \frac{z^2}{2r}\varepsilon \tag{C6}$$

being the perturbation of the Hamiltonian.

The rate of rotation of the orbital plane $\dot{\phi}$ is given by [22]:

$$\dot{\phi} = \frac{1}{l}\frac{\partial \overline{\Delta H}}{\partial \cos i} \tag{C7}$$

where i is the inclination of the orbital plane and is related to θ via $i = \frac{\pi}{2} - \theta$, l is the magnitude of angular momentum. $\overline{\Delta H}$ is the time-averaged value of ΔH calculated using the orbits of the *unperturbed* Hamiltonian.

If the orbit in the plane were closed, the averaging would be over the period of the unperturbed orbit. In our potential, almost all orbits are open so the period is not well defined. However, if we average over a time on the order $\widetilde{\tau}$, then we can assume that the plane of the orbit (i.e. θ) remains fixed during that time but that the time average over the motion in the plane has achieved a stationary value:

$$\overline{\Delta H} \equiv \frac{1}{\widetilde{\tau}}\int_0^{\widetilde{\tau}} \Delta H dt \tag{C8}$$

and applying the co-ordinate transformation in (A1):

$$\overline{\frac{z^2}{\sqrt{x^2+y^2+z^2}}} = \overline{\frac{v^2\cos^2\theta}{\sqrt{u^2+v^2}}} \tag{C9}$$
$$= \overline{\frac{v^2}{\sqrt{u^2+v^2}}}\cos^2\theta. \tag{C10}$$

The last step uses the fact that the angle of the plane θ has not changed appreciably after a time t.

Assuming that the averages over the time $\widetilde{\tau}$ are well reproduced using the virial theorem (since the unperturbed potential is simply $V_{\varepsilon=0} = r$), we know that:

$$E = \frac{3}{2}\overline{V_{\varepsilon=0}}$$
$$= \frac{3}{2}\overline{\sqrt{u^2+v^2}}$$
$$= \frac{3}{2}\left(\overline{\frac{u^2}{\sqrt{u^2+v^2}}} + \overline{\frac{v^2}{\sqrt{u^2+v^2}}}\right). \tag{C11}$$

If we assume

$$\overline{\frac{u^2}{\sqrt{u^2+v^2}}} = \overline{\frac{v^2}{\sqrt{u^2+v^2}}} \tag{C12}$$

we get

$$\overline{\frac{v^2}{\sqrt{u^2+v^2}}} = \frac{E}{3}. \tag{C13}$$

Therefore the perturbed Hamiltonian averaged over $\widetilde{\tau}$ is:

$$\overline{\Delta H} = \frac{\varepsilon E}{6}\cos^2\theta$$
$$= \frac{\varepsilon E}{6}\sin^2 i \tag{C14}$$

and the rotation rate of the orbital plane is:

$$\dot{\phi} = \frac{\varepsilon E}{6l}\frac{\partial}{\partial\cos i}(\sin^2 i)$$
$$= -\frac{\varepsilon E}{3l}\cos i = -\frac{\varepsilon E}{3l}\sin\theta \tag{C15}$$

so that the plane precesses at a constant rate. For a single atom on a plane θ, ϕ (similarly to the calculations in B)

$$\langle p_x^2\rangle = \langle p_u^2\rangle \sin^2\phi + \langle p_v^2\rangle \sin^2\theta\cos^2\phi$$
$$+2\langle p_u p_v\rangle \sin\theta\sin\phi\cos\theta \tag{C16}$$

and similarly for $\langle p_y^2 \rangle$. The last term is zero $\langle p_u p_v \rangle \to 0$ because of the isotropy due to Bertrand's theorem. Using (28) with $\alpha = 1$ we get

$$\langle p_x^2 - p_y^2 \rangle_t = \frac{E}{3} \cos^2\theta (\sin^2\phi - \cos^2\phi) \tag{C17}$$

Here, θ is a constant whereas $\phi(t) = \phi_0 + \dot{\phi} t$.

To find the total value, we use (C2):

$$\begin{aligned} \langle p_x^2 - p_y^2 \rangle_t &= \int d\mathbf{r}_0 d\mathbf{p}_0 (p_x^2(t) - p_y^2(t)) \times \left(\frac{p_{x0} q}{T}\right)^2 f_{q=0}(\mathbf{r}_0, \mathbf{p}_0) \\ &= \int d\mathbf{r}_0 d\mathbf{p}_0 \frac{E(\mathbf{r}_0, \mathbf{p}_0)}{3} \cos^2\theta_0 (\sin^2\phi(t) - \cos^2\phi(t)) \\ &\quad \times \left(\frac{p_{x0} q}{T}\right)^2 f_{q=0}(\mathbf{r}_0, \mathbf{p}_0) \end{aligned} \tag{C18}$$

We see that $\langle p_x^2 - p_y^2 \rangle_t$ is a function of εt so $\tau \sim 1/\varepsilon$ since the only time dependence is through $\dot{\phi}$. So we conclude that in (46), $\nu = -1$.

References

[1] Yuri Manin. *Computable and Uncomputable (in Russian)*. Sov.Radio, 1980.

[2] I. M. Georgescu, S. Ashhab, and Franco Nori. Quantum simulation. *Rev. Mod. Phys.*, 86:153–185, Mar 2014.

[3] Immanuel Bloch, Jean Dalibard, and Sylvain Nascimbène. Quantum simulations with ultracold quantum gases. *Nature Physics*, 8(4):267–276, 2012.

[4] R. Blatt and C. F. Roos. Quantum simulations with trapped ions. *Nature Physics*, 8:277–284, April 2012.

[5] Juan Zurita, Charles Creffield, and Gloria Platero. Topology and interactions: using photonic systems as quantum simulators, 2019.

[6] S. Aigner, L. D. Pietra, Y. Japha, O. Entin-Wohlman, T. David, R. Salem, R. Folman, and J. Schmiedmayer. Long-range order in electronic transport through disordered metal films. *Science*, 319(5867):1226–1229, Feb 2008.

[7] Oren Lahav, Amir Itah, Alex Blumkin, Carmit Gordon, Shahar Rinott, Alona Zayats, and Jeff Steinhauer. Realization of a sonic black hole analog in a Bose-Einstein condensate. *Physical Review Letters*, 105(24):1–4, 2010.

[8] Richard P Feynman. Simulating Physics with Computers. *International Journal of Theoretical Physics*, 21:467–488, 1982.

[9] J. J. Sakurai. *Modern Quantum Physics*. Pearson, 1993.

[10] M. E. Peskin and D. V. Schroeder. *An introduction to Quantum Field Theory*. Westview Press, 1995.

[11] S Bose. Plancks Gesetz und Lichtquantenhypothese. *Zeitschrift für Physik*, 26(1):178–181, 1924.

[12] Albert Einstein. Quantentheorie des einatomigen idealen Gases. *Sitzungs- berichte der Preussischen Akademie der Wissenschaften*, 6:261–267, 1924.

[13] Luca Salasnich. Fermionic condensation in ultracold atoms, nuclear matter and neutron stars. *Journal of Physics: Conference Series*, 497:012026, Apr 2014.

[14] E. R. Dobbs. What happens to liquid helium 3 at very low temperatures? *Physikalische Blätter*, 32(12):591–600, 1976.

[15] Leon N. Cooper. Bound electron pairs in a degenerate fermi gas. *Phys. Rev.*, 104:1189–1190, Nov 1956.

[16] J. Bardeen, L. N. Cooper, and J. R. Schrieffer. Theory of superconductivity. *Phys. Rev.*, 108:1175–1204, 1957.

[17] L. D. Landau. The theory of fermi liquid. *JETP*, 3(6):920, 1956.

[18] L. D. Landau. Oscillations in a Fermi Liquid. *JETP*, 5(1):101, 1957.

[19] L. D. Landau. On the Theory of the Fermi Liquid. *JETP*, 8(1):70, 1957.

[20] H. J. Schulz. Fermi liquids and non–fermi liquids, 1995.

[21] Iulia Buluta and Franco Nori. Quantum simulators. *Science*, 326(5949):108–111, 2009.

[22] Zi-Xiang Li and Hong Yao. Sign-problem-free fermionic quantum monte carlo: Developments and applications. *Annual Review of Condensed Matter Physics*, 10(1):337–356, Mar 2019.

[23] Philip W Anderson. Twenty-five years of high-temperature superconductivity – a personal review. *Journal of Physics: Conference Series*, 449:012001, jul 2013.

[24] A P Ramirez. Strongly geometrically frustrated magnets. *Annual Review of Materials Science*, 24(1):453–480, 1994.

[25] Rajan Gupta, Gregory W. Kilcup, and Stephen R. Sharpe. Tuning the hybrid monte carlo algorithm. *Phys. Rev. D*, 38:1278–1287, Aug 1988.

[26] William D. Phillips and Harold Metcalf. Laser deceleration of an atomic beam. *Phys. Rev. Lett.*, 48:596–599, Mar 1982.

[27] E. L. Raab, M. Prentiss, Alex Cable, Steven Chu, and D. E. Pritchard. Trapping of Neutral Sodium Atoms with Radiation Pressure. *Physical Review Letters*, 59(23):2631–2634, 1987.

[28] S. Chu, J. E. Bjorkholm, A. Ashkin, and A. Cable. Experimental observation of optically trapped atoms. *Physical Review Letters*, 57:314–317, July 1986.

[29] Alan L. Migdall, John V. Prodan, and William D. Phillips. First Observation of Magnetically Trapped Neutral Atoms. *Physical Review Letters*, 54(24):2596–2599, 1985.

[30] Wolfgang Ketterle, S Durfee, and M Stamper-Kurn. Making, probing and understanding Bose-Einstein condensates. In M. Inguscio, S. Stringari, and C.E. Wieman, editors, *Bose-Einstein condensation in atomic gases, Proceedings of the International School of Physics "Enrico Fermi", Course CXL*, pages 67–176. IOS Press, Amsterdam,, 1999.

[31] M. R. Andrews, C. G. Townsend, H.-J. Miesner, D. S. Durfee, D. M. Kurn, and W. Ketterle. Observation of interference between two bose condensates. *Science*, 275(5300):637–641, 1997.

[32] J. Denschlag, J. E. Simsarian, D. L. Feder, Charles W. Clark, L. A. Collins, J. Cubizolles, L. Deng, E. W. Hagley, K. Helmerson, W. P. Reinhardt, S. L. Rolston, B. I. Schneider, and W. D. Phillips. Generating solitons by phase engineering of a bose-einstein condensate. *Science*, 287(5450):97–101, 2000.

[33] Kevin E. Strecker, Guthrie B. Partridge, Andrew G. Truscott, and Randall G. Hulet. Formation and propagation of matter-wave soliton trains. *nature*, 417(6885):150–153, May 2002.

[34] K.W. Madison, F. Chevy, and W. Wohlleben. Vortex formation in a stirred Bose-Einstein condensate. *Physical Review letters*, 84(5):806–809, 2000.

[35] J R Abo-Shaeer, C Raman, J M Vogels, and W Ketterle. Observation of vortex lattices in Bose-Einstein condensates. *Science*, 292(5516):476–479, 2001.

[36] B DeMarco and D S Jin. Onset of Fermi degeneracy in a trapped atomic gas. *Science*, 285(5434):1703–1706, 1999.

[37] Wolfgang Ketterle and Martin Zwierlein. Making, probing and understanding ultracold Fermi gases. In M. Inguscio, W. Ketterle, and C. Salomon, editors, *Ultra-cold Fermi Gases, Proceedings of the International School of Physics "Enrico Fermi", Course CLXIV*, number June 2006, pages 20–30. IOS Press, Amsterdam, 2008.

[38] W Hofstetter and T Qin. Quantum simulation of strongly correlated condensed matter systems. *Journal of Physics B: Atomic, Molecular and Optical Physics*, 51(8):082001, mar 2018.

[39] U. Fano. Effects of configuration interaction on intensities and phase shifts. *Phys. Rev.*, 124:1866–1878, Dec 1961.

[40] Herman Feshbach. Unified theory of nuclear reactions. *Reviews of Modern Physics*, 36(4):1076–1078, 1964.

[41] A. Perali, P. Pieri, L. Pisani, and G. C. Strinati. Bcs-bec crossover at finite temperature for superfluid trapped fermi atoms. *Phys. Rev. Lett.*, 92:220404, Jun 2004.

[42] M. Randeria, W. Zwerger, and M. Zwierlein. *The BCS–BEC Crossover and the Unitary Fermi Gas*, pages 1–32. Springer Berlin Heidelberg, Berlin, Heidelberg, 2012.

[43] C. A. R. Sá de Melo, Mohit Randeria, and Jan R. Engelbrecht. Crossover from bcs to bose superconductivity: Transition temperature and time-dependent ginzburg-landau theory. *Phys. Rev. Lett.*, 71:3202–3205, Nov 1993.

[44] Rudolf Grimm. Ultracold Fermi gases in the BEC-BCS crossover: a review from the Innsbruck perspective. *arXiv e-prints*, pages cond–mat/0703091, Mar 2007.

[45] Frédéric Chevy and Christophe Mora. Ultra-cold polarized fermi gases. *Reports on Progress in Physics*, 73(11):112401, oct 2010.

[46] Cheng Chin, Rudolf Grimm, Paul Julienne, and Eite Tiesinga. Feshbach resonances in ultracold gases. *Reviews of Modern Physics*, 82(2):1225–1286, 2010.

[47] M W Zwierlein, A Schirotzek, C H Schunck, and W Ketterle. Vortices and superfluidity in a strongly interacting Fermi gas. *Nature*, 435(June):1047–1051, 2005.

[48] M W Zwierlein, C H Schunck, a Schirotzek, and W Ketterle. Direct observation of the superfluid phase transition in ultracold Fermi gases. *Nature*, 442(July):54–58, 2006.

[49] Mark J. H. Ku, Ariel T. Sommer, Lawrence W. Cheuk, and Martin W. Zwierlein. Revealing the superfluid lambda transition in the universal thermodynamics of a unitary fermi gas. *Science*, 335(6068):563–567, 2012.

[50] Guthrie B. Partridge, Wenhui Li, Ramsey I. Kamar, Yean-an Liao, and Randall G. Hulet. Pairing and phase separation in a polarized fermi gas. *Science*, 311(5760):503–505, 2006.

[51] Yong-Il Shin, Christian H Schunck, André Schirotzek, and Wolfgang Ketterle. Phase diagram of a two-component Fermi gas with resonant interactions. *Nature*, 451(7179):689–693, 2008.

[52] Tin-Lun Ho. Universal thermodynamics of degenerate quantum gases in the unitarity limit. *Phys. Rev. Lett.*, 92:090402, Mar 2004.

[53] J. T. Stewart, J. P. Gaebler, T. E. Drake, and D. S. Jin. Verification of universal relations in a strongly interacting fermi gas. *Phys. Rev. Lett.*, 104:235301, Jun 2010.

[54] *Recent Progress in Many-Body Theories - Proceedings of the 10th International Conference*, Jan 2000.

[55] Jr. Baker, George A. Neutron matter model. *Phys. Rev. C*, 60(5):054311, Nov 1999.

[56] Giancarlo Calvanese Strinati, Pierbiagio Pieri, Gerd Röpke, Peter Schuck, and Michael Urban. The bcs–bec crossover: From ultra-cold fermi gases to nuclear systems. *Physics Reports*, 738:1–76, Apr 2018.

[57] Jesper Levinsen, Pietro Massignan, Shimpei Endo, and Meera M Parish. Universality of the unitary fermi gas: a few-body perspective. *Journal of Physics B: Atomic, Molecular and Optical Physics*, 50(7):072001, Mar 2017.

[58] C. Cao, E. Elliott, J. Joseph, H. Wu, J. Petricka, T. Schäfer, and J. E. Thomas. Universal quantum viscosity in a unitary fermi gas. *Science*, 331(6013):58–61, 2011.

[59] Enrico Vogt, Michael Feld, Bernd Fröhlich, Daniel Pertot, Marco Koschorreck, and Michael Köhl. Scale invariance and viscosity of a two-dimensional fermi gas. *Phys. Rev. Lett.*, 108:070404, Feb 2012.

[60] A. Sommer, M. Ku, G. Roati, and M. W. Zwierlein. Universal spin transport in a strongly interacting Fermi gas. *nature*, 472:201–204, April 2011.

[61] M. Koschorreck, D. Pertot, E. Vogt, and M. Köhl. Universal spin dynamics in two-dimensional Fermi gases. *Nature Physics*, 9:405–409, July 2013.

[62] Z. Hadzibabic and J. Dalibard. Two-dimensional Bose fluids: An atomic physics perspective. *Rivista del Nuovo Cimento*, 34(6):389–434, 2011.

[63] N. D. Mermin and H. Wagner. Absence of ferromagnetism or antiferromagnetism in one- or two-dimensional isotropic heisenberg models. *Phys. Rev. Lett.*, 17:1133–1136, Nov 1966.

[64] Sumio Iijima. Helical microtubules of graphitic carbon. *Nature*, 354:56–58, Nov 1991.

[65] M. Greiner. *Ultracold quantum gases in three-dimensional optical lattice potentials*. PhD thesis, 2003.

[66] M. Greiner, O. Mandel, T. Esslinger, T.W. Hänsch, and I. Bloch. Quantum phase transition from a superfluid to a Mott insulator in a gas of ultracold atoms. *Nature*, 415(6867):39–44, 2002.

[67] Zoran Hadzibabic, Peter Krüger, Marc Cheneau, Baptiste Battelier, and Jean Dalibard. Berezinskii-Kosterlitz-Thouless crossover in a trapped atomic gas. *Nature*, 441(7097):1118–1121, 2006.

[68] B Paredes, a Widera, V Murg, O Mandel, S Folling, I Cirac, G V Shlyapnikov, T W Hansch, and I Bloch. Tonks – Girardeau gas of ultracold atoms in an optical lattice. *Nature*, 429:277, 2004.

[69] B. Yang, Y.-Y. Chen, Y.-G. Zheng, H. Sun, H.-N. Dai, X.-W. Guan, Z.-S. Yuan, and J.-W. Pan. Observation of Quantum Criticality and Luttinger Liquid in One-dimensional Bose Gases. *Physical Review Letters*, November 2016.

[70] Armin Ridinger. *Towards quantum degenerate Fermi mixtures : Photoassociation of weakly bound 6 Li 40 K molecules*. PhD thesis, 2011.

[71] Franz Sievers. *Ultracold Fermi mixtures and simultaneous sub-Doppler laser cooling of fermionic ^{6}Li and ^{40}K*. PhD thesis, 2014.

[72] Norman Kretzschmar. *Experiments with Ultracold Fermi Gases : Quantum Degeneracy of Potassium-40 and All-solid-state Laser Sources for Lithium*. PhD thesis, 2015.

[73] Mihail Rabinovic. *Quasithermalization of Fermions in a Quadrupole Potential and Evaporative Cooling of 40K to Quantum Degeneracy*. PhD thesis, 2017.

[74] Thomas Reimann. *Resonant spin dynamics and 3D-1D dimensional crossovers in ultracold Fermi gases.* PhD thesis, Université Paris Sciences et Lettres, 2018.

[75] Franz Sievers, Norman Kretzschmar, Diogo Rio Fernandes, Daniel Suchet, Michael Rabinovic, Saijun Wu, Colin V. Parker, Lev Khaykovich, Christophe Salomon, and Frédéric Chevy. Simultaneous sub-Doppler laser cooling of fermionic ^{6}Li and ^{40}K on the D_1 line: Thoery and experiment. *Phys. Rev. A*, 91(2):023426, 2015.

[76] D R Fernandes, F Sievers, N Kretzschmar, S Wu, C Salomon, and F Chevy. Sub-Doppler laser cooling of fermionic 40 K atoms in three-dimensional gray optical molasses. *Europhysics Letters*, 100:63001, 2012.

[77] Diogo Rio Fernandes. *Trapping and cooling of fermionic alkali atoms to quantum degeneracy . Sub-Doppler cooling of Potassium-40 and Lithium-6 in gray molasses.* PhD thesis, Université Pierre et Marie Curie, 2014.

[78] Thomas Salez. *Towards quantum degenerate atomic Fermi mixtures*. PhD thesis, 2011.

[79] Daniel Suchet. *Simulating the dynamics of harmonically trapped Weyl particles with cold atoms.* PhD thesis, Université Pierre et Marie Curie, 2016.

[80] E. A. Donley, Levi F. heavner, T. P. Tataw, and S. R. Jefferts. Double-pass acousto-optic modulator system. *Review of Scientific Instruments*, 76(76):063112, 2005.

[81] Stephan Falke, Eberhard Tiemann, Christian Lisdat, Harald Schnatz, and Gesine Grosche. Transition frequencies of the *d* lines of ^{39}K, ^{40}K, and ^{41}K measured with a femtosecond laser frequency comb. *Phys. Rev. A*, 74:032503, Sep 2006.

[82] T G Tiecke. Properties of Potassium. *unpublised*, pages 1–14, 2010.

[83] E. Arimondo, M. Inguscio, and P. Violino. Experimental determinations of the hyperfine structure in the alkali atoms. *Reviews of Modern Physics*, 49(1):31, 1977.

[84] B. DeMarco, J. Bohn, J. Burke, M. Holland, and D. Jin. Measurement of p-Wave Threshold Law Using Evaporatively Cooled Fermionic Atoms. *Physical Review Letters*, 82(21):4208–4211, may 1999.

[85] B DeMarco. *Quantum Behavior of an Atomic Fermi Gas*. PhD thesis, JILA, 2001.

[86] M. Berglund and M Wieser. Isotopic compositions of the elements 2009 (iupac technical report). *Pure and Applied Chemistry*, 83(2):397–410, 2011.

[87] B. DeMarco, H. Rohner, and D. S. Jin. An enriched 40k source for fermionic atom studies. *Review of Scientific Instruments*, 70(4):1967–1969, 1999.

[88] Emmanuel Mimoun, Luigi De Sarlo, David Jacob, Jean Dalibard, and Fabrice Gerbier. Fast production of ultracold sodium gases using light-induced desorption and optical trapping. *Physical Review. A*, 81(2), 2 2010.

[89] C. Klempt, T. van Zoest, T. Henninger, O. Topic, E. Rasel, W. Ertmer, and J. Arlt. Ultraviolet light-induced atom desorption for large rubidium and potassium magneto-optical traps. *Physical Review. A*, 73(1):013410, January 2006.

[90] C. B. Alcock, V. P. Itkin, and M. K. Horrigan. Vapour pressure equations for the metallic elements: 298–2500k. *Canadian Metallurgical Quarterly*, 23(3):309–313, 1984.

[91] Claude Cohen-Tannoudji and David Guery Odelin. *Advances In Atomic Physics: An Overview*. 2011.

[92] J. P. Gordon and A. Ashkin. Motion of atoms in a radiation trap. *Phys. Rev. A*, 21(5):1606–1617, 1980.

[93] Harlod J Metcalf and Peter van der Straten. *Laser Cooling and Trapping*. Springer, 1999.

[94] Jean Dalibard. A Brief History of Cold Atoms. *Cours au College de France*, 2015.

[95] J. Dalibard and C. Cohen-Tannoudji. Laser cooling below the Doppler limit by polarization gradients: simple theoretical models. *Journal of the Optical Society of America B*, 6(11):2023, nov 1989.

[96] G. Modugno, C. Benkő, P. Hannaford, G. Roati, and M. Inguscio. Sub-Doppler laser cooling of fermionic ^{40}K atoms. *Phys. Rev. A*, 60(5):R3373–R3376, nov 1999.

[97] Vandna Gokhroo, G Rajalakshmi, R Kollengode Easwaran, and C S Unnikrishnan. Sub-Doppler deep-cooled bosonic and fermionic isotopes of potassium in a compact 2D +–3D MOT set-up. *Journal of Physics B: Atomic, Molecular and Optical Physics*, 44(11):115307, 2011.

[98] M.A. Ol'shaniî and V.G. Minogin. Three-dimensional velocity-selective coherent population trapping of a (3+3)-level atom. *Optics Communications*, 89(5-6):393, 1992.

[99] R. Wynands and A. Nagel. Precision spectroscopy with coherent dark states. *Applied Physics B: Lasers and Optics*, 68:1–25, 1999.

[100] M S Shahriar, P R Hemmer, M G Prentiss, P Marte, J Mervis, D P Katz, N P Bigelow, and T Cai. Continuous polarization-gradient precooling-assisted velocity-selective coherent population trapping. *Phys. Rev. A*, 48(6):R4035—-R4038, 1993.

[101] M Weidemuller, T Esslinger, M A Ol'Shanii, A Hemmerich, and T W Hansch. A Novel Scheme for Efficient Cooling below the Photon Recoil Limit . *Europhyscs letters*, 27(2):109, 1994.

[102] C Valentin, M.-C. Gagné, J Yu, and P Pillet. One-Dimension Sub-Doppler Molasses in the Presence of Static Magnetic Field. *EPL (Europhysics Letters)*, 17(2):133, 1992.

[103] D. Boiron, C. Triché, D. R. Meacher, P. Verkerk, and G. Grynberg. Three-dimensional cooling of cesium atoms in four-beam gray optical molasses. *Phys. Rev. A*, 52:R3425–R3428, Nov 1995.

[104] Dipankar Nath, R Kollengode Easwaran, G. Rajalakshmi, and C. S. Unnikrishnan. Quantum-interference-enhanced deep sub-Doppler cooling of ^{39}K atoms in gray molasses. *Phys. Rev. A*, 88(5):053407, 2013.

[105] G Salomon, L Fouché, P Wang, A Aspect, P Bouyer, and T Bourdel. Gray-molasses cooling of 39 K to a high phase-space density. *EPL (Europhysics Letters)*, 104(6):63002, 2013.

[106] Andrew T. Grier, Igor Ferrier-Barbut, Benno S. Rem, Marion Delehaye, Lev Khaykovich, Frédéric Chevy, and Christophe Salomon. Λ-enhanced sub-Doppler cooling of lithium atoms in D1 gray molasses. *Phys. Rev. A*, 87(6):63411, 2013.

[107] A. Burchianti, G. Valtolina, J. A. Seman, E. Pace, M. De Pas, M. Inguscio, M. Zaccanti, and G. Roati. Efficient all-optical production of large Li6 quantum gases using D1 gray-molasses cooling. *Phys. Rev. A*, 90(4):043408, 2014.

[108] Q. Bouton, R. Chang, A. L. Hoendervanger, F. Nogrette, A. Aspect, C. I. Westbrook, and D. Clément. Fast production of bose-einstein condensates of metastable helium. *Phys. Rev. A*, 91:061402, 2015.

[109] Giacomo Colzi, Gianmaria Durastante, Eleonora Fava, Simone Serafini, Giacomo Lamporesi, and Gabriele Ferrari. Sub-doppler cooling of sodium atoms in gray molasses. *Phys. Rev. A*, 93:023421, Feb 2016.

[110] G D Bruce, E Haller, B Peaudecerf, D A Cotta, M Andia, S Wu, M Y H Johnson, B W Lovett, and S Kuhr. Sub-doppler laser cooling of 40k with raman gray molasses on the d_2 line. *Journal of Physics B: Atomic, Molecular and Optical Physics*, 50(9):095002, 2017.

[111] S. Rosi, A. Burchianti, S. Conclave, D. S. Naik, G. Roati, C. Fort, and F. Minardi. Λ-enhanced grey molasses on the D_2 transition of Rubidium-87 atoms. *Scientific Reports*, 8:1301, 2018.

[112] Ettore Majorana. Atomi orientati in campo magnetico variabile. *Il Nuovo Cimento*, 9(2):43–50, 1932.

[113] Wolfgang Petrich, Michael Anderson, Jason Ensher, and Eric Cornell. Stable, Tightly Confining Magnetic Trap for Evaporative Cooling of Neutral Atoms. *Physical Review Letters*, 74(17):3352–3355, 1995.

[114] R Chicireanu, Q Beaufils, A Pouderous, B Laburthe-Tolra, E Marechal, J V Porto, L Vernac, J C Keller, and O Gorceix. Accumulation and thermalization of cold atoms in a finite-depth magnetic trap. *Phys. Rev. A*, 76(2):23406, 2007.

[115] Myoung-Sun Heo, Jae-yoon Choi, and Yong-il Shin. Fast production of large 23Na Bose-Einstein condensates in an optically plugged magnetic quadrupole trap. *Phys. Rev. A*, 83(1):6, 2010.

[116] R. Dubessy, K. Merloti, L. Longchambon, P.-E. Pottie, T. Liennard, A. Perrin, V. Lorent, and H. Perrin. Rubidium-87 Bose-Einstein condensate in an optically plugged quadrupole trap. *Phys. Rev. A*, 85(1):013643, jan 2012.

[117] T L Gustavson, A P Chikkatur, A E Leanhardt, A Görlitz, S Gupta, D E Pritchard, and W Ketterle. Transport of Bose-Einstein Condensates with Optical Tweezers. *Physical Review Letters*, 88(2):3–6, 2002.

[118] Julian Léonard, Moonjoo Lee, Andrea Morales, Thomas M Karg, Tilman Esslinger, and Tobias Donner. Optical transport and manipulation of an ultracold atomic cloud using focus-tunable lenses. *New Journal of Physics*, 16(093028), 2014.

[119] H. Lewandowski. *Coherences and correlations in an ultracold Bose gas*. PhD thesis, JILA, 2002.

[120] S. Handel, A. L. Marchant, T. P. Wiles, S. A. Hopkins, and S. L. Cornish. Magnetic transport apparatus for the production of ultracold atomic gases in the vicinity of a dielectric surface. *Review of Scientific Instruments*, 83(1):013105, 2012.

[121] K. B. Davis, M. O. Mewes, and W. Ketterle. An analytical model for evaporative cooling of atoms. *Applied Physics B Laser and Optics*, 60(2-3):155–159, 1995.

[122] Claude Cohen-Tannoudji. Atomes ultrafroids - Piégeage non dissipatif et refroidissement évaporatif. *Cours au College de France*, 1996.

[123] K. O'Hara, M. Gehm, S. Granade, and J. Thomas. Scaling laws for evaporative cooling in time-dependent optical traps. *Phys. Rev. A*, 64(5):1–4, 2001.

[124] Antje Ludewig. *Feshbach Resonances in 40 K*. PhD thesis.

[125] Cindy a Regal, Christopher Ticknor, John L Bohn, and Deborah S Jin. Creation of ultracold molecules from a Fermi gas of atoms. *Nature*, 424(6944):47–50, 2003.

[126] C. a. Regal, M. Greiner, and D. S. Jin. Observation of Resonance Condensation of Fermionic Atom Pairs. *Physical Review Letters*, 92(4):040403, jan 2004.

[127] Rudolf Grimm, Matthias Weidemüller, and Yurii B Ovchinnikov. Optical dipole traps for neutral atoms. *Advances In Atomic, Molecular, and Optical Physics*, 42:95, 2000.

[128] Y. J. Lin, A. R. Perry, R. L. Compton, I. B. Spielman, and J. V. Porto. Rapid production of R 87 b Bose-Einstein condensates in a combined magnetic and optical potential. *Phys. Rev. A*, 79(6):1–8, 2009.

[129] Tobias Tiecke. *Feshbach resonances in ultracold mixtures of the fermionic quantum gases*. PhD thesis, 2009.

[130] Claude Cohen-Tannoudji, Bernard Diu, and Franck Laloe. *Mécanique quantique I*. Editions Hermann, 1997.

[131] L. Landau. On the theory of transfer of energy at collisions II'. *Phys. Z. Sowjetunion*, 2(46), 1932.

[132] Clarence Zener. Non-adiabatic crossing of energy levels. *Proceedings of the Royal Society of London A: Mathematical, Physical and Engineering Sciences*, 137(833):696–702, 1932.

[133] Jan R. Rubbmark, Michael M. Kash, Michael G. Littman, and Daniel Kleppner. Dynamical effects at avoided level crossings: A study of the landau-zener effect using rydberg atoms. *Phys. Rev. A*, 23:3107–3117, Jun 1981.

[134] Daniel Steck. Quantum and Atom Optics. *http://steck.us/teaching*, 2012.

[135] S Will. *Interacting bosons and fermions inthree-dimensional optical lattice potentials*. PhD thesis, Johannes Gutenberg-Universität Mainz, 2011.

[136] Thierry Giamarchi. *Quantum Physics in one dimension*. Oxford University Press, 2003.

[137] F. D. M. Haldane. 'Luttinger liquid theory' of one-dimensional quantum fluids. I. Properties of the Luttinger model and their extension to the general 1D interacting spinless Fermi gas. *Journal of Physics C Solid State Physics*, 14:2585–2609, July 1981.

[138] T. Giamarchi. *From Luttinger to Fermi Liquids in Organic Conductors*, page 719. 2008.

[139] Leo Radzihovsky and Daniel E Sheehy. Imbalanced feshbach-resonant fermi gases. *Reports on Progress in Physics*, 73(7):076501, jun 2010.

[140] Stefano Giorgini and Sandro Stringari. Theory of ultracold atomic Fermi gases. *Reviews of Modern Physics*, 80(4):1215–1274, oct 2008.

[141] I. Bausmerth, A. Recati, and S. Stringari. Chandrasekhar-clogston limit and phase separation in fermi mixtures at unitarity. *Phys. Rev. A*, 79:043622, Apr 2009.

[142] A. M. Clogston. Upper limit for the critical field in hard superconductors. *Phys. Rev. Lett.*, 9:266–267, Sep 1962.

[143] B. S. Chandrasekhar. A note on the maximum critical field of high-field superconductors. *Applied Physics Letters*, 1(1):7–8, 1962.

[144] S. Nascimbène, N. Navon, S. Pilati, F. Chevy, S. Giorgini, A. Georges, and C. Salomon. Fermi-liquid behavior of the normal phase of a strongly interacting gas of cold atoms. *Phys. Rev. Lett.*, 106:215303, May 2011.

[145] André Schirotzek, Cheng-Hsun Wu, Ariel Sommer, and Martin W. Zwierlein. Observation of fermi polarons in a tunable fermi liquid of ultracold atoms. *Phys. Rev. Lett.*, 102:230402, Jun 2009.

[146] S Nascimbene, N Navon, K J Jiang, F Chevy, and C Salomon. Exploring the thermodynamics of a universal Fermi gas. *Nature*, 463(7284):1057–U73, 2010.

[147] N Navon, S Nascimbène, F Chevy, and C Salomon. The equation of state of a low-temperature Fermi gas with tunable interactions. *Science*, 328(5979):729–732, 2010.

[148] Yoav Sagi, Tara E. Drake, Rabin Paudel, Roman Chapurin, and Deborah S. Jin. Breakdown of the fermi liquid description for strongly interacting fermions. *Phys. Rev. Lett.*, 114:075301, Feb 2015.

[149] N. Dupuis. Fermi liquid theory. Lecture Notes, Université Pierre et Marie Curie, LPTMS, 2014.

[150] Päivi Törmä. Physics of ultracold fermi gases revealed by spectroscopies. *Physica Scripta*, 91(4):043006, mar 2016.

[151] H. J. Schulz, G. Cuniberti, and P. Pieri. Fermi liquids and luttinger liquids, 1998.

[152] D. Petrov. *Bose-Einstein condensation in low-dimensional trapped gases*. PhD thesis, 2003.

[153] Elliott H. Lieb and Werner Liniger. Exact analysis of an interacting bose gas. i. the general solution and the ground state. *Phys. Rev.*, 130:1605–1616, May 1963.

[154] D. S. Petrov, G. V. Shlyapnikov, and J. T. M. Walraven. Regimes of quantum degeneracy in trapped 1d gases. *Phys. Rev. Lett.*, 85:3745–3749, Oct 2000.

[155] T. Bergeman, M. G. Moore, and M. Olshanii. Atom-atom scattering under cylindrical harmonic confinement: Numerical and analytic studies of the confinement induced resonance. *Phys. Rev. Lett.*, 91:163201, Oct 2003.

[156] A Recati, P O Fedichev, W Zwerger, and P Zoller. Fermi one-dimensional quantum gas: Luttinger liquid approach and spin charge separation. *Journal of Optics B: Quantum and Semiclassical Optics*, 5(2):S55–S64, apr 2003.

[157] A. Sedeki, D. Bergeron, and C. Bourbonnais. Interfering antiferromagnetism and superconductivity in quasi-one-dimensional organic conductors. *Physica B: Condensed Matter*, 405(11, Supplement):S89 – S91, 2010. Proceeding of the 8th International Symposium on Crystalline Organic Metals, Superconductors and Ferromagnets; Yamada Conference LXIV.

[158] M Moreno, C. J. B. Ford, Y. Jin, J. P. Griffiths, I. Farrer, G. A. C. Jones, D. A. Ritchie, O. Tsyplyatyev, and A. J. Schofield. Nonlinear spectra of spinons and holons in short gaas quantum wires. *Nature Communications*, 7, 2016.

[159] M. Klanjšek, H. Mayaffre, C. Berthier, M. Horvatić, B. Chiari, O. Piovesana, P. Bouillot, C. Kollath, E. Orignac, R. Citro, and T. Giamarchi. Controlling luttinger liquid physics in spin ladders under a magnetic field. *Phys. Rev. Lett.*, 101:137207, Sep 2008.

[160] Henning Moritz, Thilo Stöferle, Michael Köhl, and Tilman Esslinger. Exciting collective oscillations in a trapped 1d gas. *Phys. Rev. Lett.*, 91:250402, Dec 2003.

[161] I. Bloch. Ultracold quantum gases in optical lattices. *Nature Physics*, 1:23–30, October 2005.

[162] Yean-an Liao, Ann Sophie C. Rittner, Tobias Paprotta, Wenhui Li, Guthrie B. Partridge, Randall G. Hulet, Stefan K. Baur, and Erich J. Mueller. Spin-imbalance in a one-dimensional fermi gas. *Nature*, 467:567–569, 2010.

[163] Maxim Olshanii. Atomic Scattering in Presence of an External Confinement and a Gas of Impenetrable Bosons. *Physical review letters*, 81(5):5, 1998.

[164] B. Paredes, A. Widera, V. Murg, O. Mandel, S. Fölling, I. Cirac, G. V. Shlyapnikov, T. W. Hänsch, and I. Bloch. Tonks-Girardeau gas of ultracold atoms in an optical lattice. *nature*, 429:277–281, May 2004.

[165] G. E. Astrakharchik, D. Blume, S. Giorgini, and B. E. Granger. Quasi-One-Dimensional Bose Gases with a Large Scattering Length. *Physical Review Letters*, 92(3):030402, January 2004.

[166] Toshiya Kinoshita, Trevor Wenger, and David S. Weiss. Observation of a one-dimensional tonks-girardeau gas. *Science*, 305(5687):1125–1128, 2004.

[167] Lewi Tonks. The complete equation of state of one, two and three-dimensional gases of hard elastic spheres. *Phys. Rev.*, 50:955–963, Nov 1936.

[168] M. Girardeau. Relationship between Systems of Impenetrable Bosons and Fermions in One Dimension. *Journal of Mathematical Physics*, 1:516–523, November 1960.

[169] J. N. Fuchs, A. Recati, and W. Zwerger. Exactly solvable model of the bcs-bec crossover. *Phys. Rev. Lett.*, 93:090408, Aug 2004.

[170] G. E. Astrakharchik, D. Blume, S. Giorgini, and L. P. Pitaevskii. Interacting fermions in highly elongated harmonic traps. *Phys. Rev. Lett.*, 93:050402, Jul 2004.

[171] X.-W. Guan, M. T. Batchelor, and C. Lee. Fermi gases in one dimension: From Bethe ansatz to experiments. *Reviews of Modern Physics*, 85:1633–1691, October 2013.

[172] Henning Moritz, Thilo Stöferle, Kenneth Günter, Michael Köhl, and Tilman Esslinger. Confinement induced molecules in a 1D fermi gas. *Physical Review Letters*, 94(21):1–4, 2005.

[173] I. V. Tokatly. Dilute fermi gas in quasi-one-dimensional traps: From weakly interacting fermions via hard core bosons to a weakly interacting bose gas. *Phys. Rev. Lett.*, 93:090405, Aug 2004.

[174] C. N. Yang. Some exact results for the many-body problem in one dimension with repulsive delta-function interaction. *Phys. Rev. Lett.*, 19:1312–1315, Dec 1967.

[175] M. Gaudin. Un systeme a une dimension de fermions en interaction. *Physics Letters A*, 24(1):55 – 56, 1967.

[176] H. Bethe. Zur theorie der metalle. *Zeitschrift für Physik*, 71(3):205–226, Mar 1931.

[177] H. Guan and N. Andrei. Quench Dynamics of the Gaudin-Yang Model. *arXiv e-prints*, March 2018.

[178] G. Orso. Attractive Fermi Gases with Unequal Spin Populations in Highly Elongated Traps. *Physical Review Letters*, 98(7):070402, February 2007.

[179] M. Colomé-Tatché. Two-component repulsive fermi gases with population imbalance in elongated harmonic traps. *Phys. Rev. A*, 78:033612, Sep 2008.

[180] Y. A. Liao, M. Revelle, T. Paprotta, A. S. C. Rittner, W. Li, G. B. Partridge, and R. G. Hulet. Metastability in Spin-Polarized Fermi Gases. *Physical Review Letters*, 107(14):145305, September 2011.

[181] O. I. Pâtu and A. Klümper. Thermodynamics, contact, and density profiles of the repulsive Gaudin-Yang model. *Phys. Rev. A*, 93(3):033616, March 2016.

[182] Thierry Giamarchi. *Quantum Physics in One Dimension*. Oxford University Press, 2004.

[183] Lars Kecke, Hermann Grabert, and Wolfgang Häusler. Charge and spin dynamics of interacting fermions in a one-dimensional harmonic trap. *Phys. Rev. Lett.*, 94:176802, May 2005.

[184] A. Kleine, C. Kollath, I. P. McCulloch, T. Giamarchi, and U. Schollwöck. Spin-charge separation in two-component bose gases. *Phys. Rev. A*, 77:013607, Jan 2008.

[185] Timon A. Hilker, Guillaume Salomon, Fabian Grusdt, Ahmed Omran, Martin Boll, Eugene Demler, Immanuel Bloch, and Christian Gross. Revealing hidden antiferromagnetic correlations in doped hubbard chains via string correlators. *Science*, 357(6350):484–487, 2017.

[186] Erhai Zhao and W. Vincent Liu. Theory of quasi-one-dimensional imbalanced fermi gases. *Phys. Rev. A*, 78:063605, Dec 2008.

[187] M. A. Cazalilla, R. Citro, T. Giamarchi, E. Orignac, and M. Rigol. One dimensional bosons: From condensed matter systems to ultracold gases. *Rev. Mod. Phys.*, 83:1405–1466, Dec 2011.

[188] Ch. Rüegg, K. Kiefer, B. Thielemann, D. F. McMorrow, V. Zapf, B. Normand, M. B. Zvonarev, P. Bouillot, C. Kollath, T. Giamarchi, S. Capponi, D. Poilblanc, D. Biner, and K. W. Krämer. Thermodynamics of the spin luttinger liquid in a model ladder material. *Phys. Rev. Lett.*, 101:247202, Dec 2008.

[189] Y. Kono, T. Sakakibara, C. P. Aoyama, C. Hotta, M. M. Turnbull, C. P. Landee, and Y. Takano. Field-induced quantum criticality and universal temperature dependence of the magnetization of a spin-$1/2$ heisenberg chain. *Phys. Rev. Lett.*, 114:037202, Jan 2015.

[190] G. A. Fiete. Colloquium: The spin-incoherent Luttinger liquid. *Reviews of Modern Physics*, 79:801–820, July 2007.

[191] H. H. Jen and S.-K. Yip. Spin-incoherent luttinger liquid of one-dimensional spin-1 tonks-girardeau bose gases: Spin-dependent properties. *Phys. Rev. A*, 95:053631, May 2017.

[192] Melissa Revelle. *Quasi-One-Dimensional Ultracold Fermi Gases*. PhD thesis, Rice University, 2016.

[193] Andreas Vogler, Ralf Labouvie, Giovanni Barontini, Sebastian Eggert, Vera Guarrera, and Herwig Ott. Dimensional phase transition from an array of 1d luttinger liquids to a 3d bose-einstein condensate. *Physical Review Letters*, 113(21), Nov 2014.

[194] S. A. Wolf, D. D. Awschalom, R. A. Buhrman, J. M. Daughton, S. von Molnár, M. L. Roukes, A. Y. Chtchelkanova, and D. M. Treger. Spintronics: A Spin-Based Electronics Vision for the Future. *Science*, 294:1488–1495, November 2001.

[195] J.-P. Brantut, C. Grenier, J. Meineke, D. Stadler, S. Krinner, C. Kollath, T. Esslinger, and A. Georges. A Thermoelectric Heat Engine with Ultracold Atoms. *Science*, 342:713–715, November 2013.

[196] Peter T. Brown, Debayan Mitra, Elmer Guardado-Sanchez, Reza Nourafkan, Alexis Reymbaut, Charles-David Hébert, Simon Bergeron, A.-M. S. Tremblay, Jure Kokalj, David A. Huse, Peter Schauß, and Waseem S. Bakr. Bad metallic transport in a cold atom fermi-hubbard system. *Science*, 363(6425):379–382, 2019.

[197] Matthew A. Nichols, Lawrence W. Cheuk, Melih Okan, Thomas R. Hartke, Enrique Mendez, T. Senthil, Ehsan Khatami, Hao Zhang, and Martin W. Zwierlein. Spin transport in a mott insulator of ultracold fermions. *Science*, 363(6425):383–387, 2019.

[198] D. T. Son. Vanishing bulk viscosities and conformal invariance of the unitary fermi gas. *Phys. Rev. Lett.*, 98:020604, Jan 2007.

[199] Edward Taylor and Mohit Randeria. Viscosity of strongly interacting quantum fluids: Spectral functions and sum rules. *Phys. Rev. A*, 81:053610, May 2010.

[200] P. K. Kovtun, D. T. Son, and A. O. Starinets. Viscosity in strongly interacting quantum field theories from black hole physics. *Phys. Rev. Lett.*, 94:111601, Mar 2005.

[201] Thomas Schäfer and Derek Teaney. Nearly perfect fluidity: from cold atomic gases to hot quark gluon plasmas. *Reports on Progress in Physics*, 72(12):126001, nov 2009.

[202] I. D'amico and G. Vignale. Theory of spin Coulomb drag in spin-polarized transport. *Phys. Rev. B*, 62:4853–4857, August 2000.

[203] K. Flensberg, T. Stibius Jensen, and N. Asger Mortensen. Diffusion equation and spin drag in spin-polarized transport. *Phys. Rev. B*, 64(24):245308, December 2001.

[204] A J Leggett. Spin diffusion and spin echoes in liquid3he at low temperature. *Journal of Physics C: Solid State Physics*, 3(2):448–459, feb 1970.

[205] Alma Bardon. *Dynamics of a unitary Fermi gas*. PhD thesis, University of Toronto, 2014.

[206] Tilman Enss. Transverse spin diffusion in strongly interacting fermi gases. *Phys. Rev. A*, 88:033630, Sep 2013.

[207] A. J. Leggett and M. J. Rice. Spin echoes in liquid he^3 and mixtures: A predicted new effect. *Phys. Rev. Lett.*, 20:586–589, Mar 1968.

[208] L. R. Corruccini, D. D. Osheroff, D. M. Lee, and R. C. Richardson. Spin diffusion in liquid ^{3}He: The effect of leggett and rice. *Phys. Rev. Lett.*, 27:650–653, Sep 1971.

[209] A. B. Bardon, S. Beattie, C. Luciuk, W. Cairncross, D. Fine, N. S. Cheng, G. J. A. Edge, E. Taylor, S. Zhang, S. Trotzky, and J. H. Thywissen. Transverse demagnetization dynamics of a unitary fermi gas. *Science*, 344(6185):722–724, 2014.

[210] G M Bruun. Spin diffusion in fermi gases. *New Journal of Physics*, 13(3):035005, mar 2011.

[211] T. Enss and R. Haussmann. Quantum Mechanical Limitations to Spin Diffusion in the Unitary Fermi Gas. *Physical Review Letters*, 109(19):195303, November 2012.

[212] R. A. Duine, Marco Polini, H. T. C. Stoof, and G. Vignale. Spin drag in an ultracold fermi gas on the verge of ferromagnetic instability. *Phys. Rev. Lett.*, 104:220403, Jun 2010.

[213] T. Schäfer. Ratio of shear viscosity to entropy density for trapped fermions in the unitarity limit. *Phys. Rev. A*, 76:063618, Dec 2007.

[214] C. Luciuk, S. Smale, F. Böttcher, H. Sharum, B. A. Olsen, S. Trotzky, T. Enss, and J. H. Thywissen. Observation of quantum-limited spin transport in strongly interacting two-dimensional fermi gases. *Phys. Rev. Lett.*, 118:130405, Mar 2017.

[215] G. M. Bruun. Shear viscosity and spin-diffusion coefficient of a two-dimensional fermi gas. *Phys. Rev. A*, 85:013636, Jan 2012.

[216] M Punk and W Zwerger. Collective mode damping and viscosity in a 1d unitary fermi gas. *New Journal of Physics*, 8(8):168–168, aug 2006.

[217] Adilet Imambekov, Thomas L. Schmidt, and Leonid I. Glazman. One-dimensional quantum liquids: Beyond the luttinger liquid paradigm. *Reviews of Modern Physics*, 84(3):1253–1306, Sep 2012.

[218] N. W. Ashcroft and N. D. Mermin. *Solid State Physics*. Wesley, 1976.

[219] C. Kittel. *Introduction to Solid State Physics*. Wesley, 2005.

[220] Jean Dalibard. Des cages de lumière pour les atomes : la physique des pièges et des réseaux optiques. *Cours au College de France*, 2013.

[221] Wilhelm Zwerger. Mott hubbard transition of cold atoms in optical lattices. *Journal of Optics B: Quantum and Semiclassical Optics*, 5(2):S9–S16, apr 2003.

[222] R.A Williams. *Vortex nucleation in a rotating optical lattice of ultracold atoms*. PhD thesis, University of Oxford, 2009.

[223] Xavier Michalet and Shimon Weiss. Using photon statistics to boost microscopy resolution. *Proceedings of the National Academy of Sciences*, 103(13):4797–4798, 2006.

[224] L. M. Bennie, P. T. Starkey, M. Jasperse, C. J. Billington, R. P. Anderson, and L. D. Turner. A versatile high resolution objective for imaging quantum gases. *Opt. Express*, 21(7):9011–9016, Apr 2013.

[225] J. D. Pritchard, J. A. Isaacs, and M. Saffman. Long working distance objective lenses for single atom trapping and imaging. *Review of Scientific Instruments*, 87(7):073107, 2016.

[226] Carsten Robens, Stefan Brakhane, Wolfgang Alt, Felix Kleissler, Dieter Meschede, Geol Moon, Gautam Ramola, and Andrea Alberti. High numerical aperture (na=0.92) objective lens for imaging and addressing of cold atoms. *Opt. Lett.*, 42(6):1043–1046, Mar 2017.

[227] Wolfgang Alt. An objective lens for efficient fluorescence detection of single atoms. *Optik*, 113(3):142 – 144, 2002.

[228] J Hecker Denschlag, J E Simsarian, H Haffner, C McKenzie, A Browaeys, D Cho, K Helmerson, S L Rolston, and W D Phillips. A bose-einstein condensate in an optical lattice. *Journal of Physics B: Atomic, Molecular and Optical Physics*, 35(14):3095–3110, jul 2002.

[229] P. B. Blakie and J. V. Porto. Adiabatic loading of bosons into optical lattices. 69(1):013603, January 2004.

[230] M. Köhl, H. Moritz, T. Stöferle, K. Günter, and T. Esslinger. Fermionic Atoms in a Three Dimensional Optical Lattice: Observing Fermi Surfaces, Dynamics, and Interactions. *Physical Review Letters*, 94(8):080403, March 2005.

[231] U. Schneider. *Interacting Fermionic Atoms in Optical Lattices - A Quantum Simulator for Condensed Matter Physics*. PhD thesis, 2010.

[232] Thilo. Stöferle. *Exploring atomic quantum gases in optical lattices.* PhD thesis, ETH Zürich, 2005.

[233] C. Keller, J. Schmiedmayer, A. Zeilinger, T. Nonn, S. Dürr, and G. Rempe. Adiabatic following in standing-wave diffraction of atoms. *Applied Physics B: Lasers and Optics*, 69:303–309, October 1999.

[234] Philip E. Moskowitz, Phillip L. Gould, Susan R. Atlas, and David E. Pritchard. Diffraction of an atomic beam by standing-wave radiation. *Phys. Rev. Lett.*, 51:370–373, Aug 1983.

[235] M. Kozuma, L. Deng, E. W. Hagley, J. Wen, R. Lutwak, K. Helmerson, S.L. Rolston, and W.D. Phillips. Coherent splitting of bose-einstein condensed atoms with optically induced bragg diffraction, 1999.

[236] P. J. Martin, B. G. Oldaker, A. H. Miklich, and D. E. Pritchard. Bragg scattering of atoms from a standing light wave. *Physical Review Letters*, 60:515–518, February 1988.

[237] Phillip L. Gould, George A. Ruff, and David E. Pritchard. Diffraction of atoms by light: The near-resonant kapitza-dirac effect. *Phys. Rev. Lett.*, 56:827–830, Feb 1986.

[238] M. E. Gehm, K. M. O'Hara, T. A. Savard, and J. E. Thomas. Dynamics of noise-induced heating in atom traps. *Phys. Rev. A*, 58:3914–3921, Nov 1998.

[239] Yijun Tang, Wil Kao, Kuan-Yu Li, Sangwon Seo, Krishnanand Mallayya, Marcos Rigol, Sarang Gopalakrishnan, and Benjamin L. Lev. Thermalization near integrability in a dipolar quantum newton's cradle. *Physical Review X*, 8(2), May 2018.

[240] I. E. Mazets, T. Schumm, and J. Schmiedmayer. Breakdown of integrability in a quasi-1d ultracold bosonic gas. *Phys. Rev. Lett.*, 100:210403, May 2008.

[241] D. S. Petrov, V. Lebedev, and J. T. M. Walraven. Controlling integrability in a quasi-one-dimensional atom-dimer mixture. *Phys. Rev. A*, 85:062711, Jun 2012.

[242] I E Mazets and J Schmiedmayer. Thermalization in a quasi-one-dimensional ultracold bosonic gas. *New Journal of Physics*, 12(5):055023, may 2010.

[243] Yuzhu Jiang, D. V. Kurlov, Xi-Wen Guan, F. Schreck, and G. V. Shlyapnikov. Itinerant ferromagnetism in one-dimensional two-component fermi gases. *Phys. Rev. A*, 94:011601, Jul 2016.

[244] Edmund C. Stoner Ph.D. Lxxx. atomic moments in ferromagnetic metals and alloys with non-ferromagnetic elements. *The London, Edinburgh, and Dublin Philosophical Magazine and Journal of Science*, 15(101):1018–1034, 1933.

[245] Gyu-Boong Jo, Ye-Ryoung Lee, Jae-Hoon Choi, Caleb A. Christensen, Tony H. Kim, Joseph H. Thywissen, David E. Pritchard, and Wolfgang Ketterle. Itinerant ferromagnetism in a fermi gas of ultracold atoms. *Science*, 325(5947):1521–1524, 2009.

[246] David Pekker, Mehrtash Babadi, Rajdeep Sensarma, Nikolaj Zinner, Lode Pollet, Martin W. Zwierlein, and Eugene Demler. Competition between pairing and ferromagnetic instabilities in ultracold fermi gases near feshbach resonances. *Phys. Rev. Lett.*, 106:050402, Feb 2011.

[247] Christian Sanner, Edward J. Su, Wujie Huang, Aviv Keshet, Jonathon Gillen, and Wolfgang Ketterle. Correlations and pair formation in a repulsively interacting fermi gas. *Phys. Rev. Lett.*, 108:240404, Jun 2012.

[248] Zaiyao Fei, Bevin Huang, Paul Malinowski, Wenbo Wang, Tiancheng Song, Joshua Sanchez, Wang Yao, Di Xiao, Xiaoyang Zhu, Andrew F. May, Weida Wu, David H. Cobden, Jiun-Haw Chu, and Xiaodong Xu. Two-dimensional itinerant ferromagnetism in atomically thin Fe_3GeTe_2. *Nature Materials*, 17(9):778–782, Aug 2018.

[249] Claude Cohen-Tannoudji, Jacques Dupont-Roc, and Gilbert Grynberg. *Processus d'interaction entre photons et atomes*. EDP Sciences, CNRS édition, 2001.

[250] G. Breit and I. I. Rabi. Measurement of Nuclear Spin. *Physical Review*, 38(11):2082–2083, 1931.

[251] Herman Feshbach. A unified theory of nuclear reactions. II. *Annals of Physics*, 19(2):287–313, 1962.

[252] A. J. Moerdijk, B. J. Verhaar, and A. Axelsson. Resonances in ultracold collisions of ^{6}Li, ^{7}Li, and ^{23}Na. *Phys. Rev. A*, 51:4852–4861, Jun 1995.

[253] C. A. Regal, C. Ticknor, J. L. Bohn, and D. S. Jin. Tuningp-wave interactions in an ultracold fermi gas of atoms. *Physical Review Letters*, 90(5), Feb 2003.

[254] JTM Walraven. Elements of Quantum Gases : Thermodynamic and Collisional Properties of Trapped Atomic Gases. *Cold-Atoms PreDoc School*, 2010.

[255] Alessandro Zenesini, Bo Huang, Martin Berninger, Stefan Besler, Hanns-Christoph Nägerl, Francesca Ferlaino, Rudolf Grimm, Chris H Greene, and Javier von Stecher. Resonant five-body recombination in an ultracold gas of bosonic atoms. *New Journal of Physics*, 15(4):043040, apr 2013.

[256] Q. Beaufils, A. Crubellier, T. Zanon, B. Laburthe-Tolra, E. Maréchal, L. Vernac, and O. Gorceix. Feshbach resonance in *d*-wave collisions. *Phys. Rev. A*, 79:032706, Mar 2009.

[257] C. Ticknor, C. A. Regal, D. S. Jin, and J. L. Bohn. Multiplet structure of feshbach resonances in nonzero partial waves. *Phys. Rev. A*, 69:042712, Apr 2004.

[258] Yue Cui, Chuyang Shen, Min Deng, Shen Dong, Cheng Chen, Rong Lü, Bo Gao, Meng Khoon Tey, and Li You. Observation of broad d -wave feshbach resonances with a triplet structure. *Physical Review Letters*, 119(20), Nov 2017.

RÉSUMÉ

Cette thèse décrit les récents résultats de l'expérience FerMix, expérience dédiée à l'étude des systèmes fermioniques quantiques à N corps à ultra basse température. Pour cela, des ensembles d'atomes de ^{40}K sont utilisés. Nous présentons ici deux principaux résultats.

En premier lieu, nous décrivons le dispositif expérimental ainsi que les étapes menant à la préparation d'un gaz fermionique fortement dégénéré composé de 1.5×10^4 atomes de ^{40}K à une température de $T/T_F = 0.14$, soit juste en-dessous de la température critique de superfluidité.

En second lieu, nous rapportons nos progrès pour explorer le croisement dimensonnel entre les liquides de Tomonaga-Luttinger à 1D et ceux de Landau-Fermi à 3D. Pour ce faire, nous confinons notre gaz de Fermi ultrafroid au sein d'un réseau optique 2D à grand pas. Après la description du dispositif utilisé et la caractérisation du potentiel périodique, nous discutons de la stratégie mise en oeuvre pour transférer les atomes dans le réseau 1D puis au sein de l'onde stationnaire 2D. Le chargement du réseau 1D représente l'accomplissement final présenté dans ce manuscrit : la réalisation d'un gaz de Fermi dégénéré à deux dimensions, composé de 250 atomes par état de spin et à une témperature de $T/T_F = 0.34$.

MOTS CLÉS

Gaz de Fermi ultrafroids, gaz quantiques, physique atomique, systèmes quantiques à N corps fortement corrélés, physique en dimensions réduites

ABSTRACT

This thesis reports on the recent results of the FerMix experiment, which is dedicated to the study of fermionic quantum many-body systems at ultralow temperatures using ensemble of ^{40}K. The main achievements are twofold.

First, we describe the experimental apparatus and the successive stages leading to the preparation of a deeply degenerate Fermi gas of 1.5×10^4 atoms of ^{40}K at a temperature of $T/T_F = 0.14$, just below the critical temperature of superfluidity.

Second, we summarize our progress towards the exploration of the dimensional crossover between the Tomonaga-Luttinger liquid in 1D and the Landau-Fermi liquid in 3D. To that end, we confine our ultracold Fermi gas in a large spacing optical lattice. The experimental considerations regarding the tunability of the dimensionality of our system as well as the apparatus used to generate the 2D lattice are described in detail. Following the characterization of the optical periodic potential, the strategy employed to transfer atoms into a single 1D lattice before loading them into the 2D standing wave is discussed. The loading of the 1D lattice represents the final milestone presented in this work: the realization of a degenerate Fermi gas in two dimensions composed of 250 atoms per spin state at a temperature $T/T_F = 0.34$.

KEYWORDS

Ultracold Fermi gases, quantum gases, atomic physics, strongly correlated quantum manybody systems, physics in reduced dimensions